



Theses and Dissertations

2024-04-16

The Generation of Terahertz Light and its Applications in the Study of Vibrational Motion

Aldair Alejandro
Brigham Young University

Follow this and additional works at: <https://scholarsarchive.byu.edu/etd>



Part of the [Physical Sciences and Mathematics Commons](#)

BYU ScholarsArchive Citation

Alejandro, Aldair, "The Generation of Terahertz Light and its Applications in the Study of Vibrational Motion" (2024). *Theses and Dissertations*. 10330.

<https://scholarsarchive.byu.edu/etd/10330>

This Dissertation is brought to you for free and open access by BYU ScholarsArchive. It has been accepted for inclusion in Theses and Dissertations by an authorized administrator of BYU ScholarsArchive. For more information, please contact ellen_amatangelo@byu.edu.

The Generation of Terahertz Light and its Applications
in the Study of Vibrational Motion

Aldair Alejandro

A dissertation submitted to the faculty of
Brigham Young University
in partial fulfillment of the requirements for the degree of

Doctor of Philosophy

Jeremy A. Johnson, Chair
Eric T. Sevy
James E. Patterson
David J. Michaelis

Department of Chemistry and Biochemistry
Brigham Young University

Copyright © 2024 Aldair Alejandro

All Rights Reserved

ABSTRACT

The Generation of Terahertz Light and its Applications in the Study of Vibrational Motion

Aldair Alejandro
Department of Chemistry and Biochemistry, BYU
Doctor of Philosophy

Terahertz (THz) spectroscopy is a powerful tool that uses ultrashort pulses of light to study the properties of materials on picosecond time scales. THz light can be generated through a variety of methods. In our lab, we generate THz through the process of optical rectification in nonlinear optical (NLO) organic crystals. THz light can be used to study several phenomena in materials, such as spin precession, electron acceleration, vibrational and rotational motion. The work presented in this dissertation is divided into two parts: (1) the generation of THz light and (2) applications of THz light. The first portion of this work shows how THz light is generated, with an emphasis on the generation through optical rectification. We also show how to improve the generation of THz light by creating heterogenous multi-layer structures with yellow organic THz generation crystals. Additionally, we show that crystals used for THz generation can also be used to generate second-harmonic light. In the second half of this work, we show that THz light can be used to study the vibrational motion of molecular systems. We model how resonant vibrational modes in a fluorobenzene molecule can be excited with a multi-THz pump to transfer energy anharmonically to non-resonant modes. We also show that we can use two-dimensional (2D) THz spectroscopy to excite infrared-active vibrational modes and probe Raman-active modes in a CdWO_4 crystal to obtain a nonlinear response. We show that the nonlinear response is due to anharmonic coupling between vibrational modes and we can quantify the relative strengths of these anharmonic couplings, which previously was only accessible through first-principles calculations.

Keywords: Terahertz, terahertz generation, optical rectification, ultrafast, second-harmonic generation, vibrational motion, anharmonic coupling, terahertz bandwidth, 2D terahertz spectroscopy.

ACKNOWLEDGEMENTS

I cannot believe that this is the end of a long journey and I know it would have not been possible with the support of great mentors, family and friends.

Firstly, I would like to acknowledge the support, love and encouragement from my family: Margarito, Analine, Anuar, Adilene and Michael. They have always been there for me during the toughest times of my PhD. I appreciate all the phone calls, prayers, visits and words of encouragement.

Secondly, I want to acknowledge and thank everyone in my lab. I will start by saying that this is all possible thanks to the support, mentorship and guidance of my PI, Dr. Jeremy Johnson. He is an excellent mentor, always encouraging me to learn and grow. He was always available to answer questions or have discussions on subjects that were complicated in nature. I appreciate a lot his patient with me as I was trying to learn and understand about THz spectroscopy. When I started in the lab, I had no knowledge of THz light and no experience working with lasers. I can gladly say today that I have grown as a scientist and it is all thanks to Jeremy. I would also like to acknowledge the professors and members of my committee that I have collaborated with and/or have helped me in this journey: Dr. Sevy, Dr. Patterson, Dr. Michaelis, Dr. Woolley, Dr. Watt and Dr. Wood. Additionally, I want to acknowledge all the members of my lab for their help in answering questions, having discussions, laser aligning training, MATLAB programming questions, among many other things. Particularly, I want to thank: Dr. Clayton Moss, Dr. Brittany Knighton, Megan Biggs, Enoch (Sin Hang) Ho, Emma Nelson, Lauren Davis, Daisy Ludlow, Natalie Green, Claire Rader, Matthew Lutz, Tanner Manwaring and Tanner Hardy. In addition to collaborators from other labs: Kayla Holland and Paige Petersen.

Thirdly, I would like to acknowledge all my friends that have supported me in these last few years: Todd Hall, Courtney Hall, Colten Brown, Peter Seely, Alma (Suhwan Seo), Jason Crouch, Aidan Goble, Saul Alvarado, Josue Alvarado, Christina Mira, Sarah Boyce, Rebekah Phillips, Conner Nelson, and Gustavo Preciado. I also want to thank everyone from my volleyball group and from all my wards during my time at BYU for the support and encouragement.

TABLE OF CONTENTS

TITLE PAGE	i
ABSTRACT.....	ii
ACKNOWLEDGEMENTS.....	iii
TABLE OF CONTENTS.....	v
LIST OF TABLES.....	x
LIST OF FIGURES	xi
CHAPTER 1: Overview	1
1.1 Introduction.....	1
1.2 Chapter Breakdown	2
1.3 References.....	3
CHAPTER 2: Introduction to Terahertz Generation in Nonlinear Optical Organic Crystals	5
2.1 Terahertz Light.....	5
2.2 Methods Used for Generation of Terahertz Light.....	5
2.2.1 THz Generation Through Photoconductive Antennas.....	6
2.2.2 THz Generation Through Gas Lasers	7
2.3 Generation of THz Light Through Optical Rectification (OR)	9
2.3.1 Nonlinear Polarization	10
2.3.2 Properties of Materials Related to Second Order Susceptibility ($\chi(2)$)	11
2.3.3 Phase Matching Condition.....	13
2.4 Summary.....	16
2.5 References.....	16
CHAPTER 3: THz Spectroscopy Methods.....	22

3.1	Introduction.....	22
3.2	Ti:sapphire Laser and Optical Parametric Amplifier (OPA)	22
3.3	Initial Laser Alignment: Infrared Light	24
3.4	The Green Laser Alignment.....	26
3.5	The 800 nm Probe Alignment.....	28
3.6	Detection Scheme Alignment	31
3.7	Alignment of the THz Light	33
3.8	Collection of a THz Time Trace	37
3.9	Conclusion	40
3.10	References.....	40
CHAPTER 4: Improved Generation of Terahertz Light Through Heterogeneous Multi Layered		
Organic Crystal Structures.....		
4.1	Introduction.....	43
4.2	Methods.....	46
4.2.1	Fusing Crystals to Sapphire	46
4.2.2	Heterogeneous Multi-layer “Sandwich” Structures.....	47
4.2.3	Damage Threshold and THz Generation Output Efficiency Measurements	49
4.3	Results & Discussion	51
4.3.1	Damage Threshold.....	51
4.3.2	THz Output Efficiency.....	53
4.3.3	Longevity of Sandwich Structures.....	61
4.4	Conclusion	62
4.5	Appendix.....	63

4.6	References.....	67
CHAPTER 5: Characterization of Organic Crystals for Second Harmonic Generation		72
5.1	Abstract.....	72
5.2	Introduction.....	73
5.3	Methods.....	75
5.4	Results and Discussion	79
5.5	Conclusion	82
5.6	Appendix.....	82
5.7	References.....	91
CHAPTER 6: Vibrational Control Through THz Light		97
6.1	Introduction.....	97
6.2	Vibrational Motion.....	97
6.3	The Harmonic Oscillator.....	100
6.4	The Potential Energy Surface (PES).....	102
6.5	Equations of Motion	104
6.6	Conclusion	106
6.7	References.....	107
CHAPTER 7: Modeling Ultrafast Anharmonic Vibrational Coupling in the Gas-Phase.....		110
7.1	Abstract.....	110
7.2	Introduction.....	110
7.3	Methods.....	113
7.4	Results.....	116
7.5	Discussion.....	122

7.6	Conclusion	126
7.7	Acknowledgments.....	127
7.8	Appendix.....	127
CHAPTER 8: Pump-Pulse Bandwidth-Activated Nonlinear Phononic Coupling in CdWO ₄		138
8.1	Abstract.....	138
8.2	Introduction.....	139
8.3	Materials and Methods.....	143
8.4	Results and Discussion	152
8.4.1	Electronic Raman Scattering (ERS) Signal in Frequency Correlation Spectrum.	153
8.4.2	Anharmonic Coupling Signal in Frequency Correlation Spectrum.....	156
8.4.3	Shutting off ERS to Isolate the Anharmonic Coupling Features in 2D THz Spectrum.....	159
8.4.4	Comparison Between Experimental and First-Principles Anharmonic Coupling	160
8.4.5	The Inefficiency in Anharmonic Coupling can be Supplied by the THz Bandwidth.....	161
8.5	Conclusions.....	164
8.6	Appendix.....	165
8.6.1	Coupled Equations of Motion.....	165
8.6.2	Group Theory and Pathways of Excitation.....	167
8.6.3	Dependence of the THz Field-Strength	170
8.6.4	Turning off Electronic Raman Scattering Signal.....	172
8.6.5	Chi-Squared Fitting.....	174
8.6.6	First-Principles Calculations.....	177

8.7 References..... 180

LIST OF TABLES

Table 4-1. Comparison of laser damage threshold for NMBA, MNA and BNA for both bare and fused crystals.....	52
Table 5-1: Parameters related to nonlinear optical processes in DSTMS, PNPA and DAST and physical parameters of test samples.....	83
Table 7-1. Quantum parameters used to model intramolecular vibrational energy transfer through anharmonic coupling in a fluorobenzene molecule.	127
Table 7-1. Continued	128
Table 8-1: CdWO ₄ Vibrational Modes	140
Table 8-1: Continued	141
Table 8-2: Frequency Mixing of Relevant Anharmonic Coupling in CdWO ₄	162
Table 8-3: Properties of IR-active Phonons in CdWO ₄ ¹⁴	167
Table 8-4: Properties of Raman-active Phonons in CdWO ₄	167
Table 8-5: Character Table of C2h	168
Table 8-6: Symmetry Products	168
Table 8-7: Overview of all Symmetry Products and Driving Mechanisms.....	169
Table 8-7: Continued	170
Table 8-8: Extracted values of the anharmonic coupling constants along with their corresponding Raman scattering tensors for CdWO ₄	177
Table 8-9: Frequencies from first-principles and literature along with experimental damping rates ^{8, 14}	179

LIST OF FIGURES

Figure 2-1: Example of a common THz photoconductive antenna, as seen in Ref. 25.....	6
Figure 2-2: Experimental setup for THz generation through a gas laser pumped by a MIR-QCL from Ref. 28. In this setup, the medium used is NH ₃ gas.	8
Figure 3-1: Diagram that shows the main components of our Ti:sapphire laser: (1) laser pump, (2) oscillator, (3) regenerative amplifier, (4) stretcher and (5 & 6) compressors 1 and 2. The red arrows show the 800 nm outputs from compressors 1 and 2.....	23
Figure 3-2: The setup used to perform 1D THz spectroscopy. The output light (purple) from the OPA is split through the wavelength separator, into signal (blue) and idler. The THz light (green) is generated in the NLO organic crystal through OR and the 800 nm probe (red) measures the THz signal. The signal pump light goes through a chopper and the timing of the 800 nm pulse is controlled by a delay stage. List of components in the setup: filter (F), irises (labeled as ia, where a=1-9), mirrors (labeled as Mb, where b=1-10), telescope (L1, L2), lenses (L3, L4), polarizers (P1, P2, P3), $\lambda/4$ wave plate (QWP), Wollaston prism (WP) and photodiodes (PD1, PD2). The frequency of the chopper is set to 500 Hz.....	25
Figure 3-3: Picture of the CMOS camera used to assist in the alignment of the green laser through the 3-parabolic mirror setup (a) and the image produced from the camera to show an ideal alignment of the green laser focused onto the camera (b).	28
Figure 3-4: Images of the 800 nm IR light obtained through the beam profiling camera. a) Shows an IR beam that is not aligned due to the red regions not being symmetrically distributed, while b) shows an IR beam that is aligned as the red regions are symmetrically distributed.	29

Figure 3-5: Screenshot of the LabView software used to collect data. The signals of channel 1 and 2 are shown in red and black on the top, respectively. The difference signal, channel 3, is shown in orange on the bottom. 32

Figure 3-6: LabView screen showing a near single cycle THz pulse. The THz pulse is shown in orange in channel 3. A blue arrow shows the highest peak of the pulse, while a red arrow shows a small peak that was used as a reference peak for the initial alignment..... 35

Figure 3-7: LabView screen showing the scanning of the THz pulse (orange) in channel 3 around the position of the new reference peak, which is the maximum peak. 37

Figure 3-8: Picture of our 1D THz setup. The IR light (blue line) generated from the OPA goes inside the box, hits the NLO organic crystal to generate THz light (green line), which is then directed through a GM and the 3-parabolic mirror setup to focus into the 100- μm GaP crystal or the sample. The 800 nm probe (red line) hits the sample through a hole in the back of the third parabolic mirror and is then directed to the detection scheme. The box around the setup is used to create a dry air atmosphere by purging out the humidity. 38

Figure 3-9: THz signal generated from a 300- μm (110) GaP. a) The electric field (kV/cm) of the single cycle THz pulse as function of delay time (ps). b) THz spectrum of the pulse in a). 39

Figure 4-1. UV-vis transmission spectra for yellow organic crystals BNA, NMBA and MNA (solid lines purple, blue and green, respectively) along with the transmission of red crystals PNPA (dashed yellow) and DAST (dotted pink)..... 44

Figure 4-2. THz refractive indices for the yellow organic crystals BNA, MNA, NMBA (solid lines magenta, green and blue, respectively). Refractive indices for the index-matching fluid MBBA and the Teflon are shown as dotted lines (black and red, respectively)..... 48

Figure 4-3. Layout of the heterogeneous multi-layer structures for improved THz output (not to scale). The pump IR light (blue) generates the THz frequency light (red) in the organic crystals through optical rectification. The dotted lines indicate material interfaces where Fresnel losses can occur, but are reduced in this structure..... 49

Figure 4-4. Setups used to measure the THz generation of yellow organic crystals for (a) damage threshold and (b) THz output efficiency..... 50

Figure 4-5. Damage threshold of (a) NMBA crystals and (b) MNA crystals. The averaged damage threshold for bare crystals (red dotted line) and the averaged damage threshold for crystals fused to sapphire (blue dotted line) are shown. Shaded regions show standard deviations for the averaged damage threshold measurements. The open circles (bare crystal) and closed squares (crystal fused to sapphire) show an example of the electric field as a function of the increasing laser fluence..... 52

Figure 4-6. Comparison between the averaged THz spectrum of a sapphire-fused BNA crystal before (blue) and after (yellow) inclusion into a multi-layered structure..... 54

Figure 4-7. The normalized THz output intensity of the layered structure (yellow bar) compared to the sapphire-fused crystal (blue bar) for the average of six NMBA and BNA crystals, and three MNA crystals. The error bars for the sandwich structure are shown in brown. 55

Figure 4-8. The normalized THz output intensity of the sandwich structure (yellow bar) compared to the sapphire-fused crystal (blue bar) for two different NMBA crystals. The error bars for the sandwich structures are shown in brown. The red dotted line is the modeled normalized THz intensity of the sandwich structure. 56

Figure 4-9. Representation of the sandwich structure used for the modeling of the THz output, ***E₀ωk***. The incident field (***E₀ωk***) travels through (1) the organic crystal with a surface roughness

represented by multiple rectangles of length dk (yellow), (2) the liquid crystal MBBA with length l to $l - dk$, (3) the Teflon filter (gray). At the end, the $E_{i\omega}$ exits to air. The red dotted line represents the portion of the organic crystal that is considered to be smooth. The propagation of $E_{i\omega}$ through the crystal is shown as red arrows ($P1, P2, P3$), while the transmission is shown as green arrows (t_{12}, t_{23}, t_{3air}). 58

Figure 4-10. The THz electric field as a function of time in days for one sandwich structure for (a) NMBA, (b) BNA and (c) MNA. Some data points are averages of multiple measurements and have error bars. 61

Figure 4-11. The normalized ratio of the THz output intensity of the sandwich structures (yellow bar) compared to the sapphire-fused crystal (blue bar) for six NMBA samples. NMBA samples 1-3 (a-c) came from batches of aged crystals, while NMBA samples 4-6 (d-f) came from batches of recent crystals. The error bars for the sandwich structures are shown in brown. The red dotted line is the modeled normalized ratio of the THz intensity for the sandwich structure. For NMBA crystals a-c, the surface roughness (σd) was determined to be 24.5, 17.7 and 12.8 μm ; however, the surface roughness for the model of NMBA samples d-f was set to zero because these crystals were assumed to have a smooth surface due to coming from recently made crystal batches. 63

Figure 4-12. The normalized ratio of the THz output intensity of the sandwich structures (yellow bar) compared to the sapphire-fused crystals (blue bar) for six BNA samples. BNA samples 1-3 (a-c) came from batches of aged crystals, while BNA samples 4-6 (d-f) came from batches of recent crystals. The error bars for the sandwich structures are shown in brown. The red dotted line is the modeled normalized THz intensity of the sandwich structure. For the recently made BNA crystals a-c the surface roughness was determined to be 15.2, 12.7 and 5.5 μm , respectively. The surface roughness for the model of BNA samples d-f was set to zero because

these crystals were assumed to have a smooth surface due to coming from recently made crystal batches..... 65

Figure 4-13. The normalized THz output intensity of the sandwich structures (yellow bar) compared to the sapphire-fused crystals (blue bar) for three MNA samples. All MNA samples came from recently made crystal batches. The error bars for the sandwich structures are shown in brown. The red dotted line is the modeled normalized THz intensity of the sandwich structure. The surface roughness (σd) for the model of all MNA samples was set to zero because these crystals were assumed to have a smooth surface due to all of them coming from recently made crystal batches..... 66

Figure 4-14. The THz electric field as a function of time in days for one sandwich structure for (a) NMBA, (b) BNA and (c) MNA. The number of measurements for each data point varied and are listed in the legend as: one (black square), two (blue circle), three (red star) and four (green diamond). 67

Figure 5-1: Schematic of the SHG experimental setup. The OPA produces signal and idler beams of 1200–1550 nm and 1800-2000 nm, respectively. The idler beam passes through a half-waveplate (WP) to rotate polarization. A variable neutral density (ND) filter controls the power. The dashed line indicates the position of the power meter to measure incident power. The incident background light is removed from the path via a short pass filter. The generated SH light is measured by the power meter (PM). 76

Figure 5-2: Transmission spectra of SHG crystals with their THz generation axis (for the organic crystals) perpendicular (dotted lines) and parallel (solid lines) to the polarization of the light: BBO (blue), DAST (green), PNPA (purple) and DSTMS (orange). The jump at 850 nm is an instrumental artifact. 77

Figure 5-3: Average SHG efficiency as a function of laser fluences in mJ/cm^2 at (a) 1450 nm for the signal and (b) 2000 nm for the idler. The crystals were: BBO (blue circles), DAST (green stars), PNPA (purple diamonds) and DSTMS (orange squares)..... 79

Figure 5-4: Average SHG efficiencies as a function of incident wavelength in nm. Signal wavelengths were collected from 1200-1550 nm (1500 nm for BBO) at $\sim 0.88 \text{ mJ}/\text{cm}^2$ and idler wavelengths were collected from 1800-2000 nm at $\sim 0.66 \text{ mJ}/\text{cm}^2$ ($\sim 0.44 \text{ mJ}/\text{cm}^2$ for some of the DAST crystals). The crystals were: BBO (blue circles), DAST (green stars), PNPA (purple diamonds) and DSTMS (orange squares). 81

Figure 5-5: Unit cells with the polar axis in blue, the hyperpolarizability (β) vector in red and the angle between them for DSTMS (a), PNPA (b) and DAST (c)..... 83

Figure 5-6: The SHG efficiency as a function of laser fluences in mJ/cm^2 at 1450 nm. Only a single set of scans of the crystals during this initial screening is shown. The crystals measured were: DSTMS (red squares), PNPA (magenta diamonds), DAST (green stars), BBO (blue circles), MNA (brown hexagrams) and NMBA (light blue asterisks)..... 84

Figure 5-7: The SHG efficiency as a function of laser fluences in mJ/cm^2 at 1450 nm. Only a single set of scans of the crystals during this initial screening is shown. The crystals measured were: DSTMS (red squares), PNPA (magenta diamonds), DAST (green stars), BBO (blue circles), MNA (brown hexagrams) and NMBA (light blue asterisks)..... 85

Figure 5-8: Transmission spectrum of the short-pass filters used for the (a) signal wavelengths (1200-1550 nm) and (b) idler wavelengths (1800-2000 nm)..... 86

Figure 5-9: Normalized spectrum of newly generated SH light from DSTMS, PNPA and DAST crystals obtained using a fiber optics spectrometer with incident signal (1450 nm) and idler (1800 nm) wavelengths. 86

Figure 5-10: The SHG efficiency as a function of incident laser fluences in mJ/cm^2 at 1450 and 2000 nm for the individual measurements of (a) DSTMS (squares), (b) PNPA (diamonds), (c) DAST (stars) and (d) BBO (circles). Two different PNPA and DAST crystals were measured at certain wavelengths. The thicknesses for each crystal are listed in the legend. 87

Figure 5-11: The SHG efficiencies as a function of the incident wavelength in nm for the individual measurements of (a) DSTMS (squares), (b) PNPA (diamonds), (c) DAST (stars) and (d) BBO (circles). The signal wavelength measurements were performed with 1200-1550 nm incident light at ~ 400 mW; however, BBO measurements were only recorded from 1200-1500 nm. The idler wavelength measurements were performed with 1800-2000 nm incident light at ~ 300 mW. The thicknesses for each crystal are listed in the legend. 88

Figure 5-12: The refractive index of DSTMS (solid light blue line) and DAST (solid light red line) as a function of wavelength. The data was extracted from Fig. 5a from Ref. 39. The fundamental wavelength at 1500 nm (dotted blue line) with its respective SHG wavelength at 750 nm (dotted red line) are shown as an example to compare their respective refractive indices. 89

Figure 6-1: Vibrational modes and phonons. a) Three vibrational modes for a BF_3 molecule. b) Three phonons for a unit cell of LiNbO_3 . The arrows in both represent the direction of the eigenvectors of motion..... 98

Figure 6-2: Potential energy surface. (a) Potential energy as a function of mode coordinate Q_1 and (b) as a function of mode coordinates Q_1 and Q_2 104

Figure 7-1: (a) The IR Intensity as a function of the harmonic frequency of each vibrational mode in fluorobenzene. The frequencies are listed in wavenumber (top axis) and in THz (bottom axis) units. The legend shows the symmetries of the vibrational modes: A_1 (red), A_2 (yellow), B_1

(green) and B₂ (blue). The light blue curve shows a scaled 96 THz pump excitation spectrum with a ~5.3 THz bandwidth. (b) Pictorial representation of a resonantly excited 95.7 THz vibrational mode (left) transferring energy to an anharmonically coupled non-resonant 12.2 THz mode (right). The vectors show the respective motion of the atoms. (c) Modeled time trace depicting a 96 THz pump pulse (black) that excites a resonant 95.7 THz vibrational mode (red) that lies within its pump bandwidth. The oscillations of the resonantly excited mode(s) anharmonically excite a 12.2 THz non-resonant mode (blue). (d) The oscillation motion of the non-resonant 12.2 THz mode (blue) from (c) is zoomed in because it is two orders of magnitude smaller in amplitude than the resonantly excited 95.7 THz mode..... 115

Figure 7-2: Maximum oscillation amplitude for each vibrational mode in fluorobenzene as a function of their mode frequency after excitation with a (a) 96 THz and (b) 49 THz pump. The maximum oscillation amplitudes were also converted in terms of energy for both the (c) 96 THz and (d) 49 THz pump. The center frequency for each pump is shown as an orange stripe. The width of the orange stripe was set to match the bandwidth of the THz pump (~5.3 THz). The frequencies are shown in both wavenumber (top axis) and in THz (bottom axis) units. The legend shows the symmetries of the vibrational modes: A₁ (circles, red), A₂ (squares, yellow), B₁ (stars, green) and B₂ (triangles, blue). A logarithmic amplitude scale was used to better distinguish the oscillation amplitudes of the non-resonant vibrational modes. 117

Figure 7-3: The maximum oscillation amplitude for each vibrational mode Q_i modeled as a function of the sum of the Fourier amplitude of each product $\phi_{ijk}\cos\omega_j t \cos\omega_k t$ at the mode frequency after excitation with a 96 THz pump. The legend shows the symmetries of the vibrational modes: A₁ (circles, red), A₂ (squares, yellow), B₁ (stars, green) and B₂ (triangles, blue). The frequency of each vibrational mode is displayed under its respective marker..... 118

Figure 7-4: The maximum oscillation amplitude for each vibrational mode Q_i modeled as a function of the sum of the Fourier amplitude of each product ($\phi_{ijk}Q_jQ_k$) at a 96 THz pump frequency. The legend shows the symmetries of the vibrational modes: A₁ (circles, red), A₂ (squares, yellow), B₁ (stars, green) and B₂ (triangles, blue). The frequency of each vibrational mode is displayed under its respective marker. 120

Figure 7-5: The maximum oscillation amplitude as function of mode and pump frequency in THz. A light orange stripe highlights the region where modes are resonantly excited and a light red stripe highlights where the mode frequency is equal to twice the pump frequency. Arrows are used to point out off-diagonal vibrational modes. The legend shows the symmetries of the vibrational modes: A₁ (circles, red), A₂ (squares, yellow), B₁ (stars, green) and B₂ (triangles, blue). 122

Figure 7-6: Extracted data from Ref 43. After resonantly exciting liquid fluorobenzene with a 3068 cm⁻¹ pump (~92 THz), we show the energy deposited in the vibrational modes. The pump is shown as an orange line with a bandwidth of 25 cm⁻¹ (~0.7 THz). The energy deposited in this liquid-phase fluorobenzene experiment from Ref 43 can be directly compared to Fig. 7-2c above showing differences in the modeled energy transfer for fluorobenzene in gas-phase. 125

Figure 7-7: Maximum oscillation amplitude for each vibrational mode Q_i in fluorobenzene as a function of their respective harmonic frequencies after excitation with a (a) 40, (b) 33, (c) 28, (d) 21, (e) 15 and (f) 7 THz pump pulse. The maximum oscillation amplitude converted in terms of energy are shown for these same THz pumps in (g) 40, (h) 33, (i) 28, (j) 21, (k) 15 and (l) 7. The center frequency for each pump is shown as an orange stripe. The mode frequencies are shown in both wavenumber (top axis) and in THz (bottom axis) units. The legend in (a) shows the symmetries of the vibrational modes for each THz pump: A₁ (circles, red), A₂ (squares, yellow),

B₁ (stars, green) and B₂ (triangles, blue). A logarithmic amplitude scale was used to better distinguish the oscillation amplitudes of the non-resonant vibrational modes. 129

Figure 7-8: The maximum oscillation amplitude for each vibrational mode Q_i modeled as a function of the sum of the Fourier amplitude of each product $\phi_{ijk}\cos\omega_j t \cos\omega_k t$ at the mode frequency after excitation with a (a) 96, (c) 28 and (e) 7 THz pump pulse. The maximum oscillation amplitude was also modeled as a function of the sum of the Fourier amplitude of each product $\phi_{ijkl}\cos\omega_j t \cos\omega_k t \cos\omega_l t$ at the mode frequency after excitation with a (b) 96, (d) 28 and (f) 7 THz pump pulse. The legend in (a) shows the symmetries of the vibrational modes for each THz pump: A₁ (circles, red), A₂ (squares, yellow), B₁ (stars, green) and B₂ (triangles, blue). The frequency of each vibrational mode is displayed under the respective marker. 130

Figure 7-9: The maximum oscillation amplitude for each vibrational mode Q_i modeled as a function of the sum of the Fourier amplitude of each product $\phi_{ijk}Q_j Q_k$ after excitation with a (a) 96, (c) 28 and (e) 7 THz pump pulse. The maximum oscillation amplitude was also modeled as a function of the sum of the Fourier amplitude of each product $\phi_{ijkl}Q_j Q_k Q_l$ at the same pumps: (b) 96, (d) 28 and (f) 7 THz. The legend in (a) shows the symmetries of the vibrational modes: A₁ (circles, red), A₂ (squares, yellow), B₁ (stars, green) and B₂ (triangles, blue). The frequency of each vibrational mode is displayed under the respective marker. 131

Figure 8-1: Important details of our 2D THz spectroscopy setup. a) The orthogonally polarized THz pump pulses, shown in blue and green, are separated by time delay (τ) and by delay (t) with respect to the 800 nm probe pulse, shown in red. b) Dual chopping scheme. The 250 Hz chopper (green) allows two pulses to go through and blocks two pulses; meanwhile, the 500 Hz chopper (blue) allows one pulse through and blocks one pulse. In the end, the chopping creates four different combinations of the THz pump pulses: both THz pulses allowed, the horizontal THz

pulse allowed while the vertical pulse is blocked, the vertical THz pulse allowed while the horizontal pulse is blocked and finally both THz pulses blocked. c) The extracted nonlinear time signal from the 2D THz measurements, where the y-axis is the pump delay τ and the x-axis is the probe delay t 145

Figure 8-2: 2D THz setup with both THz pump pulses vertically polarized. The setup shows the 1450 nm output signal light (blue) and the 1790 nm output idler light (purple) generated from the OPA after being separated by a wavelength separator. A d-mirror reflects and allows the THz light that is generated from the signal and idler beam inputs to be directed to the parabolic mirror scheme, respectively. The parabolic mirror scheme focuses both THz beams unto the CdWO₄ sample. The 800 nm probe (red) focuses unto the sample through the back of the last parabolic mirror and is then guided to the heterodyne detection scheme..... 147

Figure 8-3: Time and frequency domain responses from CdWO₄ acquired through 2D THz spectroscopy with a parallel polarization setup of the THz pump pulses. (a) The time domain response, where the vertical stripes are the responses from the stationary THz pump pulse (signal) and the diagonal stripes are the responses from the variable delay THz pump pulse. (b) The isolated time domain nonlinear response from CdWO₄ after chopping the THz pump pulses and (c) the nonlinear response converted into the frequency domain, which are known as frequency correlation spectrum..... 148

Figure 8-4: 2D THz setup with the THz pump pulses perpendicularly polarized. The setup shows the 1450 nm output signal light (blue) and the 1790 nm output idler light (purple) generated from the OPA after being separated by a wavelength separator. A polarizer reflects and transmits the THz light that is generated from the signal and idler beam inputs to be directed to the parabolic mirror scheme, respectively. The parabolic mirror scheme focuses both THz beams unto the

CdWO₄ sample. The 800 nm probe (red) focuses onto the sample through the back of the last parabolic mirror and is then guided to the heterodyne detection scheme..... 149

Figure 8-5: Time and frequency domain responses from CdWO₄ acquired through 2D THz spectroscopy with a perpendicular polarization setup of the THz pump pulses. a) The time domain response, where the vertical stripes are the responses from the stationary THz pump pulse (signal) and the diagonal stripes are the responses from the variable delay THz pump pulse. (b) The isolated time domain nonlinear response from CdWO₄ after chopping the THz pump pulses and (c) the nonlinear response converted into the frequency domain, which are known as frequency correlation spectrum..... 151

Figure 8-6: Modeled and experimental frequency correlation spectrum highlighting the ERS signals. a) Frequency correlation plot generated by only modeling mode 4 driven by ERS. b) Experimental frequency correlation plot generated from the isolated nonlinear signal. The red box highlights the ERS signal at the frequency of mode 4..... 154

Figure 8-7: Contributions from ERS are observed as vertical bands in the 2D THz correlation spectrums. a) THz spectrum of the DAST crystal used for THz generation. The solid red line indicates the Raman-active mode 4 at its resonant frequency, while the dotted lines in pairs represent four possible combinations that can be mixed through addition or subtraction to match the frequency of the Raman-active mode that is being driven. b) Modeled frequency correlation spectrum by exciting mode 4 through ERS. Along the THz pump axis, the possible sum and difference combinations of the frequency pairs in a) are shown as circles that are found on the vertical band at the resonant frequency of the mode that is being drive at 2.33 THz in the THz probe axis..... 155

Figure 8-8: Modeled nonlinear features generated through anharmonic coupling and frequency assignments of the features. a) Example of spectrum generated through anharmonic coupling of three arbitrary phonons. b) Modeled spectrum of the coupling of phonons in CdWO₄ where the stationary pump pulse was model with a vertical polarization and the variable delay pump pulse with a horizontal polarization. c) The modeled CdWO₄ spectrum has the reverse order of the THz polarizations that were used to generate the spectrum in b). The frequency elements across the pump axis are found at: 1) the resonant frequencies of the IR-active modes (squares), 2) sum frequencies (triangles) and 3) difference frequencies (circles) that match the frequency of the Raman-active mode. 157

Figure 8-9: Frequency correlation plot of the nonlinear response in CdWO₄. The nonlinear features are highlighted with shapes depending on the following frequencies: 1) resonant frequency of the IR-active modes (circles), sum- (diamonds) and difference-frequencies (squares). Responses originating from the coupling of modes 4, 6, 8 and 4, 8, 10 are shown in gray and white, respectively. In the case that the signal is influence by both sets of couplings, the shape contains white lines with dashed gray lines..... 159

Figure 8-10: THz pump bandwidth adds additional frequency content to the motion of the vibrational modes, thus contributing to trilinear coupling. In the middle, the energy diagram shows the frequency difference (1.32 THz) needed from the coupling motion between the A_u mode 8 and B_u mode 10 to nonlinearly drive the B_g mode 4 at 2.33 THz. The orange box shows the motion of the A_u mode by the vertical THz pulse 6 ps prior to the excitation of the B_u mode by the horizontal THz pulse, which is shown in the green box. The vertical dotted lines in a) and c) show the arrival of the THz pump pulses. a) Shows the oscillations of the A_u mode, while b) shows the Fourier transform of the late motion of the A_u mode (oscillations in orange). c) Shows

the early oscillation of the B_u mode when it is initially driven by the second THz pulse and d) shows the Fourier transform of that early motion (oscillations in purple), which shows more frequency content besides the resonant frequency of the B_u mode. The spectrum in d) shows frequency content from the THz pump bandwidth and the frequency content needed to drive the B_g mode is shown in a dotted green line at 1.32 THz. 163

Figure 8-11: Frequency correlation spectrum with field strength dependence. 2D spectrum with parallel THz pump pulses were collected with increasing field strengths (right to left) of 0.455 MV/cm, 0.646 MV/cm, 0.826 MV/cm, 0.972 MV/cm and 1.101 MV/cm. The nonlinear response shows up as yellow features and start to increase with the increasing field strength. 171

Figure 8-12: Quadratic dependence of nonlinear signal of 2D frequency correlation spectrum. a) Frequency correlation spectrum at 1.101 MV/cm, where a region is highlighted in a red box. b) Extracted average of the Fourier amplitude spectral signal from the region in red in a) as a function of electric field strength of idler THz pump pulse..... 172

Figure 8-13: Modeled nonlinear signal from the Raman-active mode 4 of $CdWO_4$ generated by ERS and trilinear coupling with different polarization of the THz pulses. The top panels show the modeled oscillation amplitude of mode 4 driven by ERS (left) and trilinear coupling (right) with parallel THz pump pulses. The bottom panels show the modeled oscillation amplitude by ERS (left) and trilinear coupling (left) with perpendicular THz pump pulses. Mode 4 is basically not driven by ERS when both THz pulses are orthogonal and the pulses are not overlapped in time. 173

Figure 8-14: Summary of Chi-squared fitting process. (I) Values for the ERS and the anharmonic coupling parameters of $CdWO_4$, with the range of $\phi_4, \mathbf{8}, \mathbf{10}$ magnitudes used to find the minimum RMSE for $\phi_4, \mathbf{8}, \mathbf{10}$ shown in A). B) The modeled frequency correlation spectrum

according to the values of I and the optimal $\phi 4, 8, 10$. (II) Values of fit parameters with the range of $R4\alpha\beta$ magnitudes used to find the minimum RMSE for $R4\alpha\beta$ shown in C). D) The modeled frequency correlation spectrum with the values of II and the optimal $R4\alpha\beta$. (III) Values of fit parameters with the range of $R7\alpha\beta$ magnitudes used to find the minimum RMSE for $R7\alpha\beta$ shown in E). F) The modeled frequency correlation spectrum with the values of III and the optimal $R7\alpha\beta$. The multiple small arrows after III, E) and F) shows multiple steps that are not shown. (IV) Final values of all fit parameters after one round of fitting. G) The minimization of the RMSE to find the optimal value of the last parameter, $\phi 11, 8, 10$. H) Final modeled frequency correlation plot after one round of adjusting all the parameters, which are shown in IV. I) Final modeled frequency correlation spectrum after two rounds of adjusting all the parameters. J) Experimental frequency correlation plot. 175

Figure 8-15: Unit cells of CdWO₄. a) The unit cells with all the atomic positions at rest. b) The unit cell showing an excited IR-active mode along with eigenvectors of each atom and the mode effective charge vector (blue arrow). c) The unit cell showing an excited Raman-active mode along with the eigenvectors of each atom. 178

CHAPTER 1: Overview

1.1 Introduction

Electromagnetic waves with frequencies of 10^{12} Hz that lie between the infrared (IR) and microwave regions of the electromagnetic spectrum are known as terahertz (THz) light. Generally, the frequencies of the THz light region range from ~ 0.3 -10 THz. In recent years, high-field THz spectroscopy has garnered some attention as an ultrafast technique capable of studying nonlinear phenomena in materials.¹ In the field of solid-state physics, THz light has been used to study phenomena such as the motion of phonons,^{2,3} the precession of spins,⁴ as well as the electronic transitions in materials.⁵ There are also applications in the molecular realm, such as the study of vibrational and rotational motion in both liquids and gasses.⁶⁻⁹ These examples show the versatility that THz spectroscopy offers to the study of properties of materials/molecules.

Our study of THz light could be split into two categories that can answer the following two questions: (1) how can we efficiently generate THz light? and (2) what can we study with this region of the electromagnetic spectrum? In regards to generating THz light, we need to consider characteristics such as, broadband vs narrowband THz pulses, the generated THz frequency range and how to optimize the generation of large intensities.¹⁰⁻¹² These characteristics depend on several factors, such as the THz generation material and method of THz generation. Concerning what we can study with THz light, we will present here two examples of using THz light to investigate anharmonic coupling that results from intense THz excitation.

1.2 Chapter Breakdown

The first portion of this dissertation, which covers chapters 2 through 5, primarily focuses on the generation of THz light. Chapter 2 introduces what THz light is and some methods used to generate it, with a particular emphasis on generating THz through the process of optical rectification in organic crystals. It also covers what properties make organic crystals efficient at generating THz light. Chapter 3 goes through the entire process of aligning the laser to optimize the generation of THz light through optical rectification and the last section of this chapter finalizes by showing how to collect a THz time trace. Chapter 4 discusses a project in collaboration with the Michaelis lab at BYU, where we created heterogenous multi-layered structures to improve the damage threshold and the THz output in yellow organic crystals. Finally, chapter 5 addresses a project that was a collaboration with the Patterson and Michaelis labs at BYU. In chapter 5, we show the efficiency of several organic crystals, which are usually used to generate THz light, in second-harmonic generation (SHG). We show the SHG efficiency depending on wavelengths and laser fluences. The work presented in this chapter was published in *Optics Letters*.¹³

The second portion of this dissertation in chapters 6 through 8 focuses on using THz light to control vibrational properties in molecules and materials. Chapter 6 functions as an introduction to both chapters 7 and 8 because it presents background concepts such as how to describe vibrational motion, the importance of the anharmonic potential energy surface (PES) and classical equations of motion, which are needed to understand the work presented in those chapters. The work presented in chapter 7, which is a collaboration with the Sevy lab at BYU, delves into the study of vibrational motion in the energy transfer process that occurs when one molecule of fluorobenzene is excited by a multi-THz pump. Specifically, this work shows the

specific roles of anharmonic coupling and the symmetry of the vibrational modes in the intramolecular energy transfer process. Finally, in chapter 8 we show the nonlinear response in CdWO₄ after excitation with two THz pump pulses and isolate the portion of the response coming from anharmonic coupling from that of electronic Raman scattering (ERS) by changing the configuration of the THz pulses.

1.3 References

1. H. Y. Hwang, S. Fleischer, N. C. Brandt, B. G. Perkins Jr, M. Liu, K. Fan, A. Sternbach, X. Zhang, R. D. Averitt, and K. A. Nelson, "A review of non-linear terahertz spectroscopy with ultrashort tabletop-laser pulses," *Journal of Modern Optics* **62**, 1447-1479 (2015).
2. A. von Hoegen, R. Mankowsky, M. Fechner, M. Först, and A. Cavalleri, "Probing the interatomic potential of solids with strong-field nonlinear phononics," *Nature* **555**, 79-82 (2018).
3. M. Henstridge, M. Först, E. Rowe, M. Fechner, and A. Cavalleri, "Nonlocal nonlinear phononics," *Nature Physics* **18**, 457-461 (2022).
4. T. Kampfrath, M. Battiato, A. Sell, F. Freimuth, A. Leitenstorfer, M. Wolf, R. Huber, P. Oppeneer, and M. Münzenberg. *Ultrafast spin precession and transport controlled and probed with terahertz radiation*; SPIE, 2014.
5. S. Houver, L. Huber, M. Savoini, E. Abreu, and S. L. Johnson, "2D THz spectroscopic investigation of ballistic conduction-band electron dynamics in InSb," *Optics Express* **27**, 10854-10865 (2019).
6. S. Fleischer, Y. Zhou, R. W. Field, and K. A. Nelson, "Molecular Orientation and Alignment by Intense Single-Cycle THz Pulses," *Physical Review Letters* **107**, 163603 (2011).

7. J. Lu, Y. Zhang, H. Y. Hwang, B. K. Ofori-Okai, S. Fleischer, and K. A. Nelson, “Nonlinear two-dimensional terahertz photon echo and rotational spectroscopy in the gas phase,” *Proceedings of the National Academy of Sciences* **113**, 11800-11805 (2016).
8. E. H. G. Backus, K.-J. Tielrooij, M. Bonn, and H. J. Bakker, “Probing ultrafast temperature changes of aqueous solutions with coherent terahertz pulses,” *Optics Letters* **39**, 1717-1720 (2014).
9. I. A. Finneran, R. Welsch, M. A. Allodi, T. F. Miller, and G. A. Blake, “Coherent two-dimensional terahertz-terahertz-Raman spectroscopy,” *Proceedings of the National Academy of Sciences* **113**, 6857-6861 (2016).
10. G. A. Valdivia-Berroeta, Z. B. Zaccardi, S. K. F. Pettit, S.-H. Ho, B. W. Palmer, M. J. Lutz, C. Rader, B. P. Hunter, N. K. Green, C. Barlow, C. Z. Wayment, D. J. Ludlow, P. Petersen, S. J. Smith, D. J. Michaelis, and J. A. Johnson, “Data Mining for Terahertz Generation Crystals,” *Advanced Materials* **34**, 2107900 (2022).
11. O. V. Chefonov, A. V. Ovchinnikov, C. P. Hauri, and M. B. Agranat, “Broadband and narrowband laser-based terahertz source and its application for resonant and non-resonant excitation of antiferromagnetic modes in NiO,” *Optics Express* **27**, 27273-27281 (2019).
12. B. E. Knighton, R. Tanner Hardy, C. L. Johnson, L. M. Rawlings, J. T. Woolley, C. Calderon, A. Urrea, and J. A. Johnson, “Terahertz waveform considerations for nonlinearly driving lattice vibrations,” *Journal of Applied Physics* **125**, (2019).
13. K. M. Holland, A. Alejandro, D. J. H. Ludlow, P. K. Petersen, M. A. Wright, C. C. Chartrand, D. J. Michaelis, J. A. Johnson, and J. E. Patterson, “Characterization of organic crystals for second-harmonic generation,” *Optics Letters* **48**, 5855-5858 (2023).

CHAPTER 2: Introduction to Terahertz Generation in Nonlinear Optical Organic Crystals

2.1 Terahertz Light

Light is an electromagnetic wave that can be used to study a variety of phenomena or processes, depending on the frequency of the light. This chapter primarily focuses on how to generate and use light with frequencies of 10^{12} Hz, which is known as terahertz (THz) light. THz light is found between the infrared (IR) and microwave regions of the electromagnetic spectrum of light, and it typically ranges from $\sim 0.3 - 10$ THz. In other units, 1 THz of light equals $300 \mu\text{m}$ in wavelength, which corresponds to 33 cm^{-1} in wavenumbers or 4 meV in electronvolts. Due to its unique frequency range, THz light is uniquely suited to study several phenomena in materials/molecules, such as vibrational (phonon) and rotational motion,¹⁻⁵ spin precession,⁶ electron acceleration,⁷ and magnetic and electronic properties.⁸⁻¹¹ Due to the inherent interactions of THz light with these material degrees of freedom, THz light has a broad range of applications, including security and imaging,¹²⁻¹⁴ nondestructive studies of biological systems,¹⁵⁻¹⁷ atomic lattice manipulation in materials,¹⁸⁻²⁰ and creation of high-speed devices.²¹ Some of these applications are relevant to the projects that I have worked on and will be described in more detail in this dissertation. The remainder of this chapter will focus on methods used to generate THz light, starting with brief descriptions of photoconductive antennas and gas lasers, and then having a more complete description of THz generation via optical rectification (OR).

2.2 Methods Used for Generation of Terahertz Light

In this section, we will briefly explain two common methods used to generate THz light, photoconductive antennas (PCAs) and gas lasers. It should be noted that laser-induced plasma

sources are another common method used to generate THz light;²²⁻²⁴ however, we will not go over the specifics of this method in this dissertation.

2.2.1 THz Generation Through Photoconductive Antennas

Emission of THz pulses can be produced using photoconductive antennas, as seen in Fig. 2-1.²⁵ Typically, PCAs consists of two metal semi-conductor contacts that act as on-chip THz antennas. There is a spacing or gap between the two metal contacts, which are mounted on a photoconductive semiconductor substrate that is attached to a silicon lens.

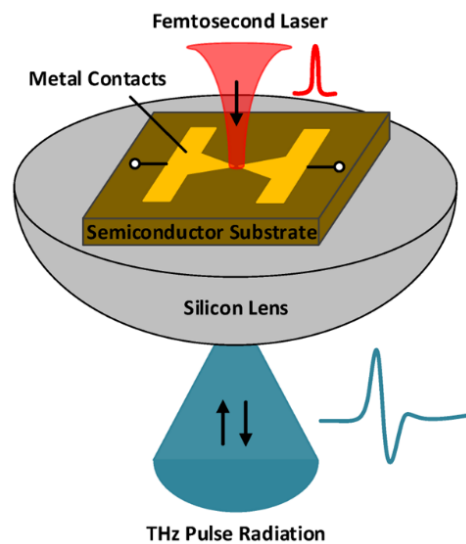


Figure 2-1: Example of a common THz photoconductive antenna, as seen in Ref. 25.

The gap is a crucial component of the PCAs for two reasons: (1) it offers a point of intersection between the femtosecond laser pulses and the substrate, and (2) it can withstand and permit the travel of a low DC voltage between both of the metal contacts, thus allowing for the generation of electric fields in the substrate beneath the gap. Additionally, the options for selecting the semiconductor substrate are limited because its energy bandgap needs to be appropriate for the absorption of femtosecond laser pulses to produce photoexcited electrical

carriers. The metal contacts will eventually collect the drifted photocarriers prior to their recombination. When the pump laser light is absorbed, creating mobile conduction band electrons, those carriers are accelerated in one direction by the DC voltage. This voltage-induced asymmetry produces a femtosecond photocurrent that emits THz light through the on-chip THz antennas. A silicon lens is often connected to the substrate to help improve the efficiency of outcoupling the THz light.

Although PCAs can generate THz light, the generated THz light is typically limited to the low frequency range (less than ~ 1.1 THz) of the THz spectrum and the generated spectrum is narrowband.^{25,26} However, there are a few cases where high THz frequencies (up to ~ 15 THz) were generated through PCAs.²⁷ Two of the main difficulties that arise when generating THz light with PCAs are: (1) selecting the appropriate substrate and (2) challenges with aligning the pump laser in the gap between the contacts. The substrate requires two important properties, a short photocarrier lifetime and a great carrier mobility capacity, that allows it to be an efficient ultrafast photoconductive medium. The properties of the substrate also limit the wavelengths that can be used for the generation of THz light. Working around some of these issues usually only tends to make the PCAs less cost efficient for the generation of THz light pulses. Additionally, the small gap needed for the PCAs introduces difficulties in the alignment due to its small size and it also limits the ability to use PCAs in a phased array manner as the gap requires the use of mechanical stage for alignment of the signal.²⁵

2.2.2 THz Generation Through Gas Lasers

Another technique used to generate THz light, besides PCAs, is through gas lasers. Fig. 2-2 shows a typical setup for THz generation with an ammonia laser pumped by a mid-infrared

(MIR) quantum cascade laser (QCL).²⁸ In this setup, pumping with a MIR-QCL provides several benefits, such as a having the ability to be used in a continuous-wave (CW) mode, being single-mode, having wavelength tunability, operational at room temperature, and high average power output. To then be able to generate coherent THz light, an important part of these types of setups is the medium, which is a molecular gas present in the laser waveguide. Depending on the molecular properties of the medium gas, the setup allows for the adjustment of qualities like the levels of the gain, threshold, and efficiency of the conversion, which are needed to efficiently produce THz light.

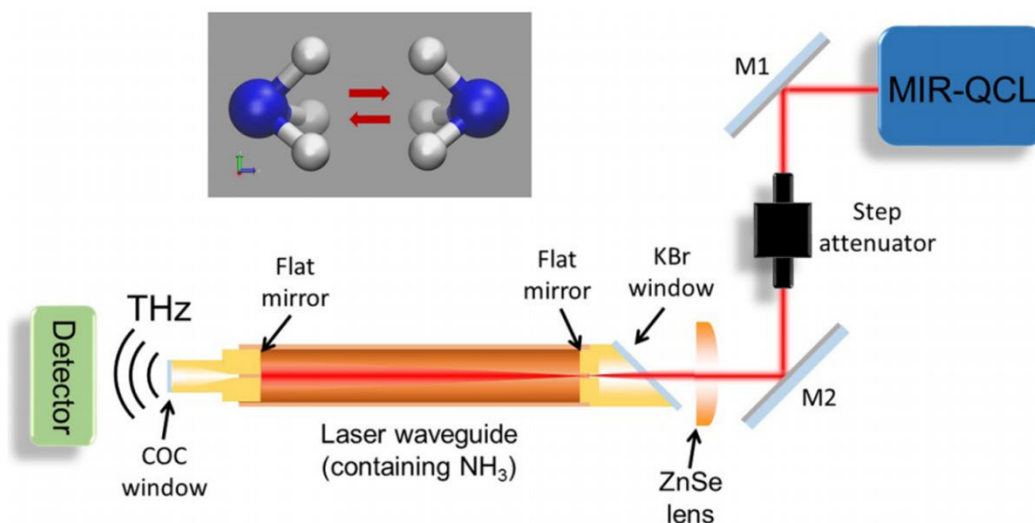


Figure 2-2: Experimental setup for THz generation through a gas laser pumped by a MIR-QCL from Ref. 28. In this setup, the medium used is NH₃ gas.

Similar to PCAs, gas lasers are also limited to the generation of narrowband, low frequency THz light, which is close to one THz in this case. This is primarily due to the gas medium being limited by the allowed transitions of its rotational states. The setup shown in Fig. 2-2, used NH₃ as the medium, which allowed for the generation of THz light at 1.073 THz. If other frequencies are needed, then a different medium needs to be selected that has the allowed

rotational transitions to access such desired frequencies, which could make the generation of THz more tedious through gas lasers.

As previously mentioned, both PCAs and gas lasers are great methods to generate narrowband THz light in the lower frequency range of the THz spectrum. However, if one requires higher and a broader range of THz frequencies, then other methods would need to be considered. Due to these limitations, optical rectification in a nonlinear material is a great option to generate THz light.

2.3 Generation of THz Light Through Optical Rectification (OR)

Optical rectification (OR) is a nonlinear optical (NLO) process that can generate new frequencies of light when a pulse of incident light interacts with a nonlinear optical material and induces a nonlinear polarization (P_{NL}) in the material.²³ The NLO material used for OR can be defined as a material that generates an electric field (E_{gen}) response that is not proportional to the incident electric field (E_i), but rather the relationship is $E_{gen} \propto P_{NL} \propto E_i^2$ prior to saturation. This induced nonlinear polarization in the NLO material contains additional frequency components compared to the incident light, which results in emitted light containing these new frequencies. OR can be thought of as a type of difference frequency generation (DFG) because two photons of light interact within a nonlinear material and generate new frequency that is the difference in energy between the two incident photons. If a narrowband pump laser is used so that all photons have nearly identical energy, then optical rectification in the traditional sense leads to a zero frequency (DC) electric field in the crystal. However, since our incident light comes from a femtosecond laser,²⁹ the newly generated light lies within the frequencies of the THz region.

The nonlinear materials used for optical rectification can either be of inorganic or organic nature. In the case of inorganic materials, GaP³⁰ or ZnTe^{31, 32} are crystals often used to generate THz light. Inorganic crystals can be useful for producing THz pulses with THz frequencies ranging from 1-3 THz; however, the THz efficiency at higher THz frequencies (> 3 THz) diminishes.^{29, 33} In contrast to inorganic crystals, organic crystals can be used for optical rectification to generate short and broadband THz pulses with high intensities and a broader bandwidth with THz frequencies extending to 6 THz or beyond, depending on the pump pulse duration.³⁴ In the following subsections, several properties related to the nonlinear materials will be described to understand the properties that influence the efficient generation of THz light through optical rectification. There will be a special emphasis on the characteristics of the organic nonlinear optical materials that are central to this work.

2.3.1 Nonlinear Polarization

To generate THz light, the incident pulse of light will cause a change in the nonlinear polarization of the material,²³ which is proportional to the generated THz electric field output. The nonlinear polarization ($P_{NL}(\Omega)$) and the THz electric field output ($E_{THz}(\Omega)$) can be described by Eq. 2-1 and Eq. 2-2, respectively:

$$\mathbf{P}_{NL}(\Omega) = \epsilon_0 \chi^{(2)} \int_0^\infty \mathbf{E}(\omega + \Omega) \mathbf{E}^*(\omega) d\omega, \quad (2-1)$$

$$\mathbf{E}_{THz}(\Omega) \propto -\omega^2 \mathbf{P}_{NL}(\Omega) \quad (2-2)$$

In Eqs. 2-1 and 2-2, Ω is the frequency of the generated THz pulse, ϵ_0 is the vacuum permittivity constant, $\chi^{(2)}$ is the second order susceptibility, and $E(\omega)$ is the incident electric field as a function of angular frequency, ω . We can learn two important elements from Eq. 2-1 regarding the generation of THz light. First, the $\chi^{(2)}$ is a measure of the nonlinearity of the

material and ideally needs to have a large value. As it will become apparent in chapter 5 of this dissertation, the second order susceptibility is also crucial for other nonlinear processes, such as second-harmonic generation (SHG).^{35, 36} Second, this equation shows that the bandwidth of the incident pulse is key to determining how broad the generated THz spectrum will be and what frequencies it can reach because it integrates along all the frequencies (ω) present in the incident pulse. For instance, if the incident pulse is narrowband, then the frequency content in the THz spectrum will be narrow and of low frequency; however, if the pulse is broadband, then the frequency content will be broad and may reach higher frequencies.

2.3.2 Properties of Materials Related to Second Order Susceptibility ($\chi^{(2)}$)

In Eq. 2-1, the second order susceptibility, $\chi^{(2)}$, quantifies the nonlinearity of a material. The second order susceptibility for organic crystals can be described in more detail using the 1D chromophore approximation by the following equation:³⁷

$$\chi^{(2)} = NF_{ijk}\beta \cos^3(\theta_p), \quad (2-3)$$

In Eq. 2-3, N is defined as the chromophore density of the unit cells, F_{ijk} is the factor of the local field that is related to the refractive index of the material, β is the magnitude of the molecular hyperpolarizability, and θ_p is the angle between the β vector and the polar axis of the material. For the rest of this subsection, we will discuss the properties of the NLO materials that are associated to the $\chi^{(2)}$, as shown in Eq. 2-3.

We will begin with the molecular hyperpolarizability, β , which specifies a molecule's ability to change its dipole moment when being influenced by an incident electric field. The hyperpolarizability is closely related to the structure of the organic molecules. Organic molecules can generate THz light because the structures usually consist of conjugated π -systems with

electron donating and electron withdrawing groups. The magnitude of the hyperpolarizability depends on the location and strength of interaction of these groups, as well as the alignment and length of the conjugated π -systems.³⁷

Despite the hyperpolarizability being a good measure of the strength of the second order susceptibility of a material to predict its ability to generate THz light, it should be noted that one cannot only rely on this or any other parameter alone for such predictions. For example, the organic crystal DAST has a larger value for the calculated molecular hyperpolarizability compared to the crystal HMQ-TMS, which are 157 and 143, respectively; however, the second order susceptibility for both crystal ends up being similar, which are 1.05 and 1.00, respectively.³⁷ This example, like many others, can be explained by analyzing other crucial properties used to determine the second order susceptibility of a material.

The similarity in the second order susceptibility for the previous two organic crystals can be explained by analyzing another property, the order parameter. The order parameter of a material is shown in Eq. 2-3 as $\cos^3(\theta_p)$. The angle θ_p is defined as the angle between the hyperpolarizability vector and the polar axis of the crystal, which is the axis that is oriented towards the dipole moment of the crystal. The orientation of the polar axis is important because it needs to be parallel to the incident light for maximum generation of either THz light or second harmonic light. In regards to DAST and HMQ-TMS, the magnitude of their order parameters, which are 0.83 ($\theta_p = 0.35$) and 1.00 ($\theta_p = 0$), respectively, compensate for their differences in hyperpolarizability and thus allows them to have similar values for the second order susceptibility.

By paying attention to the expression of the order parameter, it can be noticed that if the angle between the hyperpolarizability and the polar axis is 90° , then the order parameter will be

zero. When the order parameter is zero, the second order susceptibility becomes zero (see Eq. 2-3) and this in turn results in a nonlinear polarization of zero as well (see Eq. 2-1). This means that the material will have a linear response when interacting with incident light and thus not generating THz light, SHG or any other nonlinear process. Physically, this means that the crystal contains an inversion center and is centrosymmetric. For nonlinear interactions, the crystal needs to be non-centrosymmetric, which means that the order parameter is not equal to zero.

We will end this subsection by discussing the chromophore or packing density (N) of the unit cells, which is another property of the material crucial to having an ideal second order susceptibility for THz generation, as seen in Eq. 2-3. The hyperpolarizability and the order parameter could have ideal magnitudes to contribute to the second order susceptibility tensor of a material but if the material does not contain a significant number of chromophores in the unit cells tightly packed, then the generation of THz light will be small. The generation of THz light increases due to two reasons: (1) the more chromophores present per unit cell in the crystal, the more it is able to generate THz light, and (2) the less free space between the chromophores in the crystal reduces the magnitude of the phonons present in the crystal and also self-absorption of the generated THz light.²⁶ In fact, this is one of the benefits of using organic crystal to generate THz light instead of inorganic crystals, as organic crystals have smaller vibrational amplitudes from the phonons compared to inorganic crystals, which in turn allows for the generation of ultra-broadband THz light.²⁶

2.3.3 Phase Matching Condition

The last property that we will discuss related to efficient THz generation is the phase matching condition. The phase matching condition is fulfilled when the incident IR light and the

newly generated THz pulse travel at the same speed inside the THz generation crystal, which reduces destructive interference to efficiently generate THz light. THz generation through optical rectification can be maximized when the phase matching condition is met, as described in the following equation:

$$\Delta\kappa(\Omega) = \kappa(\Omega) + \kappa(\omega) - \kappa(\Omega + \omega) = 0 \quad (2-4)$$

In Eq. 2-4,²³ κ is the wavevector as a function of either the fundamental frequency of the incident pump pulse, ω , or of the frequency of the generated THz pulse in the nonlinear material, Ω . To simplify the phase matching condition equation, we can modify it by considering that the pump frequency is larger than the THz frequency ($\Omega \ll \omega$) and thus the term $\kappa(\Omega + \omega) - \kappa(\omega)$ can be estimated by the derivative, $\partial\kappa/\partial\omega|_{\omega_0} \cdot \Omega$, where ω_0 is the average frequency of the pump pulse. The following three equations will also be needed to simplify Eq. 2-4 (λ is the wavelength, v is the phase velocity and n is the refractive index):

$$\kappa = 2\pi\lambda, \quad (2-5)$$

$$v = \omega/\kappa \quad (2-6)$$

$$n = c/v \quad (2-7)$$

The phase matching condition can then be re-written in terms of the refractive index, n and the group refractive index of the generated THz light n_g , as seen in Eq. 2-8:

$$\Delta\kappa = [n(\Omega) - n_g(\omega_0)]\Omega/c \quad (2-8)$$

From Eq. 2-8, we can see that the ideal phase matching condition can only be achieved when both the THz refractive index and the pump group refractive index are the same, making $\Delta\kappa$ equal to zero. This can also be written in terms of the phase velocity of the generated THz pulse, v , and the group velocity of the pump pulse, v_g by properly applying Eqs. 2-6 and 2-7 into Eq. 2-8.

$$\mathbf{v}(\boldsymbol{\Omega}) = \mathbf{v}_g(\omega_0) \quad (2-9)$$

Equivalent to Eq. 2-8, the phase matching condition is optimized when the group velocity of the incident pump pulse and the phase velocity of the generated THz pulse are the same. This can be challenging, if not impossible, as it would require the finding of materials with group refractive indices equal to or close to the refractive index of the incident pump light at all THz frequencies. Despite this challenge, THz light can still be generated although it is limited to certain frequencies, which depends on the refractive index of the material used. However, it is worth mentioning that having similar refractive indices does not guarantee that a material will be efficient for THz generation because all of the previously mentioned properties also need to be considered for optical rectification. Additionally, the wavelength of the pump pulse is also limited to the absorption cutoff wavelength of the THz generation material because strong absorbances will decrease the generation of THz light depending on the frequency of the phonon(s) in the material.

There are some ways to circumvent the limitations from phase matching, such as building a setup with a tilted pump pulse front²³ or creating a multilayer of different materials to compensate the difference in refractive indices.³⁹ However, the former option has been mostly done in inorganic crystals, such as lithium niobate (LN)²³ but requires a setup that is complex and as previously mentioned, the generated THz spectrum is narrowband and limited to low frequencies. The latter option is also challenging as it requires finding materials that can generate THz with appropriate refractive indices to either increase or decrease the group phase velocity to match the phase velocity of the pump pulse.

2.4 Summary

In this chapter, we briefly mentioned some techniques commonly used to generate THz light in nonlinear materials. We then shifted our discussion on THz generation through optical rectification in a nonlinear material because this method is primarily used to generate THz pulses in our laboratory. The generation of THz light can be achieved by optimizing properties related to the nonlinear material, such as: the nonlinear polarization, the molecular hyperpolarizability, the order parameter, the chromophore density, and by fulfilling phase matching condition. It is worth noting that materials able to generate THz light, do not always strongly fulfill each of these requirements. In some cases, the material may have a small magnitude for a particular property but can compensate for this with another property and thus be able to generate the desired THz light. It is for this reason that one should consider collectively all these properties when determining the potential for an organic material to generate THz light.

2.5 References

1. C. L. Johnson, B. E. Knighton, and J. A. Johnson, "Distinguishing Nonlinear Terahertz Excitation Pathways with Two-Dimensional Spectroscopy," *Physical Review Letters* **122**, 073901 (2019).
2. S. Maehrlein, A. Paarmann, M. Wolf, and T. Kampfrath, "Terahertz Sum-Frequency Excitation of a Raman-Active Phonon," *Physical Review Letters* **119**, 127402 (2017).
3. J. Lu, Y. Zhang, H. Y. Hwang, B. K. Ofori-Okai, S. Fleischer, and K. A. Nelson, "Nonlinear two-dimensional terahertz photon echo and rotational spectroscopy in the gas phase," *Proceedings of the National Academy of Sciences* **113**, 11800-11805 (2016).

4. S. Fleischer, R. W. Field, and K. A. Nelson, “Commensurate Two-Quantum Coherences Induced by Time-Delayed THz Fields,” *Physical Review Letters* **109**, 123603 (2012).
5. S. Fleischer, Y. Zhou, R. W. Field, and K. A. Nelson, “Molecular Orientation and Alignment by Intense Single-Cycle THz Pulses,” *Physical Review Letters* **107**, 163603 (2011).
6. T. Kampfrath, M. Battiato, A. Sell, F. Freimuth, A. Leitenstorfer, M. Wolf, R. Huber, P. M. Oppeneer, and M. Münzenberg, “Ultrafast spin precession and transport controlled and probed with terahertz radiation,” In *Proc.SPIE*, p 898415 (2014).
7. E. A. Nanni, W. R. Huang, K.-H. Hong, K. Ravi, A. Fallahi, G. Moriena, R. J. Dwayne Miller, and F. X. Kärtner, “Terahertz-driven linear electron acceleration,” *Nature Communications* **6**, 8486 (2015).
8. O. H.-C. Cheng, D. H. Son, and M. Sheldon, “Light-induced magnetism in plasmonic gold nanoparticles,” *Nature Photonics* **14**, 365-368 (2020).
9. Y.-L. Li, D. Zhang, M. Luo, Q.-H. Yang, F. Fan, S.-J. Chang, and Q.-Y. Wen, “Terahertz magneto-optical response of bismuth-gadolinium-substituted rare-earth garnet film,” *Optics Express* **29**, 23540-23548 (2021).
10. T. F. Nova, A. Cartella, A. Cantaluppi, M. Först, D. Bossini, R. V. Mikhaylovskiy, A. V. Kimel, R. Merlin, and A. Cavalleri, “An effective magnetic field from optically driven phonons,” *Nature Physics* **13**, 132-136 (2017).
11. S. Houver, L. Huber, M. Savoini, E. Abreu, and S. L. Johnson, “2D THz spectroscopic investigation of ballistic conduction-band electron dynamics in InSb,” *Optics Express* **27**, 10854-10865 (2019).
12. J. Shi, D. Yoo, F. Vidal-Codina, C.-W. Baik, K.-S. Cho, N.-C. Nguyen, H. Utzat, J. Han, A. M. Lindenberg, V. Bulović, M. G. Bawendi, J. Paire, S.-H. Oh, and K. A. Nelson, “A room-

- temperature polarization-sensitive CMOS terahertz camera based on quantum-dot-enhanced terahertz-to-visible photon upconversion,” *Nature Nanotechnology* **17**, 1288-1293 (2022).
13. Q. Song, Y. Zhao, A. Redo-Sanchez, C. Zhang, and X. Liu, “Fast continuous terahertz wave imaging system for security,” *Optics Communications* **282**, 2019-2022 (2009).
14. H.-B. Liu, Y. Chen, G. J. Bastiaans, and X. C. Zhang, “Detection and identification of explosive RDX by THz diffuse reflection spectroscopy,” *Optics Express* **14**, 415-423 (2006).
15. Q. Sun, Y. He, K. Liu, S. Fan, E. P. J. Parrott, and E. Pickwell-MacPherson, “Recent advances in terahertz technology for biomedical applications,” *Quantitative Imaging in Medicine and Surgery* **7**, 345-355 (2017).
16. M. Mizuno, A. Yamada, K. Fukunaga, and H. Kojima, “Far-infrared spectroscopy of salt penetration into a collagen fiber scaffold,” *Journal of Biological Physics* **41**, 293-301 (2015).
17. M. A. Brun, F. Formanek, A. Yasuda, M. Sekine, N. Ando, and Y. Eishii, “Terahertz imaging applied to cancer diagnosis,” *Physics in Medicine & Biology* **55**, 4615 (2010).
18. X. Li, T. Qiu, J. Zhang, E. Baldini, J. Lu, A. M. Rappe, and K. A. Nelson, “Terahertz field-induced ferroelectricity in quantum paraelectric SrTiO₃,” *Science* **364**, 1079-1082 (2019).
19. M. Kozina, M. Fechner, P. Marsik, T. van Driel, J. M. Glowonia, C. Bernhard, M. Radovic, D. Zhu, S. Bonetti, U. Staub, and M. C. Hoffmann, “Terahertz-driven phonon upconversion in SrTiO₃,” *Nature Physics* **15**, 387-392 (2019).
20. L. Luo, D. Cheng, B. Song, L.-L. Wang, C. Vaswani, P. M. Lozano, G. Gu, C. Huang, R. H. J. Kim, Z. Liu, J.-M. Park, Y. Yao, K. Ho, I. E. Perakis, Q. Li, and J. Wang, “A light-induced phononic symmetry switch and giant dissipationless topological photocurrent in ZrTe₅,” *Nature Materials* **20**, 329-334 (2021).

21. L. Viti, and M. S. Vitiello, "Tailored nano-electronics and photonics with two-dimensional materials at terahertz frequencies," *Journal of Applied Physics* **130**, 170903 (2021).
22. C. D. Moss, S. A. Sorenson, and J. A. Johnson. Wavelength and phase considerations for multi-pulse plasma generation of terahertz. *Optica Open*: 2023.
23. M. C. Hoffmann, and J. A. Fülöp, "Intense ultrashort terahertz pulses: generation and applications," *Journal of Physics D: Applied Physics* **44**, 083001 (2011).
24. W. Sun, X. Wang, and Y. Zhang, "Terahertz generation from laser-induced plasma," *Opto-Electronic Science* **1**, 220003-220001-220003-220027 (2022).
25. P. Chen, M. Hosseini, and A. Babakhani. An Integrated Germanium-Based THz Impulse Radiator with an Optical Waveguide Coupled Photoconductive Switch in Silicon. In *Micromachines*, 2019; Vol. 10.
26. J.-H. Seok, U. Puc, S.-J. Kim, W. Yoon, H. Yun, I. C. Yu, F. Rotermund, D. Kim, M. Jazbinsek, and O. P. Kwon, "High-Density Organic Electro-Optic Crystals for Ultra-Broadband THz Spectroscopy," *Advanced Optical Materials* **9**, 2100618 (2021).
27. Y. C. Shen, P. C. Upadhy, H. E. Beere, E. H. Linfield, A. G. Davies, I. S. Gregory, C. Baker, W. R. Tribe, and M. J. Evans, "Generation and detection of ultrabroadband terahertz radiation using photoconductive emitters and receivers," *Applied Physics Letters* **85**, 164-166 (2004).
28. A. Pagies, G. Ducournau, and J. F. Lampin, "Low-threshold terahertz molecular laser optically pumped by a quantum cascade laser," *APL Photonics* **1**, 031302 (2016).
29. F. D. J. Brunner, S.-H. Lee, O. P. Kwon, and T. Feurer, "THz generation by optical rectification of near-infrared laser pulses in the organic nonlinear optical crystal HMQ-TMS," *Optical Materials Express* **4**, 1586-1592 (2014).

30. N. Hekmat, T. Vogel, Y. Wang, S. Mansourzadeh, F. Aslani, A. Omar, M. Hoffmann, F. Meyer, and C. J. Saraceno, “Cryogenically cooled GaP for optical rectification at high excitation average powers,” *Optical Materials Express* **10**, 2768-2782 (2020).
31. G. Polónyi, B. Monoszlai, G. Gäumann, E. J. Rohwer, G. Andriukaitis, T. Balciunas, A. Pugzlys, A. Baltuska, T. Feurer, J. Hebling, and J. A. Fülöp, “High-energy terahertz pulses from semiconductors pumped beyond the three-photon absorption edge,” *Optics Express* **24**, 23872-23882 (2016).
32. J. A. Fülöp, G. Polónyi, B. Monoszlai, G. Andriukaitis, T. Balciunas, A. Pugzlys, G. Arthur, A. Baltuska, and J. Hebling, “Highly efficient scalable monolithic semiconductor terahertz pulse source,” *Optica* **3**, 1075-1078 (2016).
33. T. Tanabe, K. Suto, J. Nishizawa, K. Saito, and T. Kimura, “Tunable terahertz wave generation in the 3- to 7-THz region from GaP,” *Applied Physics Letters* **83**, 237-239 (2003).
34. G. A. Valdivia-Berroeta, Z. B. Zaccardi, S. K. F. Pettit, S.-H. Ho, B. W. Palmer, M. J. Lutz, C. Rader, B. P. Hunter, N. K. Green, C. Barlow, C. Z. Wayment, D. J. Ludlow, P. Petersen, S. J. Smith, D. J. Michaelis, and J. A. Johnson, “Data Mining for Terahertz Generation Crystals,” *Advanced Materials* **34**, 2107900 (2022).
35. Y. R. Shen, “Surface properties probed by second-harmonic and sum-frequency generation,” *Nature* **337**, 519-525 (1989).
36. K. M. Holland, A. Alejandro, D. J. H. Ludlow, P. K. Petersen, M. A. Wright, C. C. Chartrand, D. J. Michaelis, J. A. Johnson, and J. E. Patterson, “Characterization of organic crystals for second-harmonic generation,” *Optics Letters* **48**, 5855-5858 (2023).

37. G. A. Valdivia-Berroeta, L. K. Heki, E. A. McMurray, L. A. Foote, S. H. Nazari, L. Y. Serafin, S. J. Smith, D. J. Michaelis, and J. A. Johnson, "Alkynyl Pyridinium Crystals for Terahertz Generation," *Advanced Optical Materials* **6**, 1800383 (2018).
38. G. A. Valdivia-Berroeta, K. C. Kenney, E. W. Jackson, J. C. Bloxham, A. X. Wayment, D. J. Brock, S. J. Smith, J. A. Johnson, and D. J. Michaelis, "6MNEP: a molecular cation with large hyperpolarizability and promise for nonlinear optical applications," *Journal of Materials Chemistry C* **8**, 11079-11087 (2020).
39. A. G. Stepanov, L. Bonacina, and J.-P. Wolf, "DAST/SiO₂ multilayer structure for efficient generation of 6 THz quasi-single-cycle electromagnetic pulses," *Optics Letters* **37**, 2439-2441 (2012).

CHAPTER 3: THz Spectroscopy Methods

3.1 Introduction

In the previous chapter, we discussed important aspects of the THz light, its applications and several methods used to generate THz with an emphasis in optical rectification (OR). We also talked about the important properties that make an organic crystal efficient at generating pulses of THz light. In this chapter, we will discuss the process of collecting time trace data with a THz spectroscopy setup consisting of a THz pump and an 800 nm probe. To describe this process, we will first discuss the laser system used to generate a pump and probe light beam. We will then explain how to properly align the different laser paths in the setup, which includes: (1) the infrared (IR) pump light that is generated in an optical parametric amplifier (OPA) and used to generate THz light through OR; (2) the visible green laser that sets the path for the THz light through the setup; (3) the 800 nm probe light along with (4) the path that leads to the detection scheme used to measure the THz signal; and (5) how to optimize the THz light itself. We will then finalize by explaining how to collect a THz time trace.

3.2 Ti:sapphire Laser and Optical Parametric Amplifier (OPA)

To generate THz light through optical rectification, we use incident IR light to produce light with frequencies in the THz region by inducing a change in polarization in a nonlinear optical (NLO) material.¹ For the incident light, we use a Coherent Libra Ti:sapphire laser that generates 800 nm light with a 100 fs pulse duration and 1 kHz repetition rate. The diagram in Fig. 3-1 shows the different components that form part of our laser system: the pump laser, the oscillator, the regenerative amplifier, the stretcher, and compressors 1 and 2. In short, green laser

pulses from the pump laser are directed into the Ti:sapphire gain medium in the regenerative amplifier. Simultaneously, seeded oscillator pulses, which were lengthened in time in the stretcher, are also directed into the gain medium to amplify the generated light. The amplified 800 nm light is then divided into two portions by a beam splitter: the larger portion (~98% of the light) goes into compressor 1 and comes out with a pulse energy of ~3.3-4.0 mJ, while the smaller portion (~2% of the light) goes into compressor 2 and comes out with a pulse energy of ~0.06 mJ. The 800 nm light from both pulses has a repetition rate of 1 kHz, a beam diameter of ~0.9 cm and a pulse duration of 100 fs. The 800 nm output light from compressor 1 is used as the input beam for the OPA, which eventually is used primarily as the pump pulse, whereas the output from compressor 2 is often used as the probe pulse.

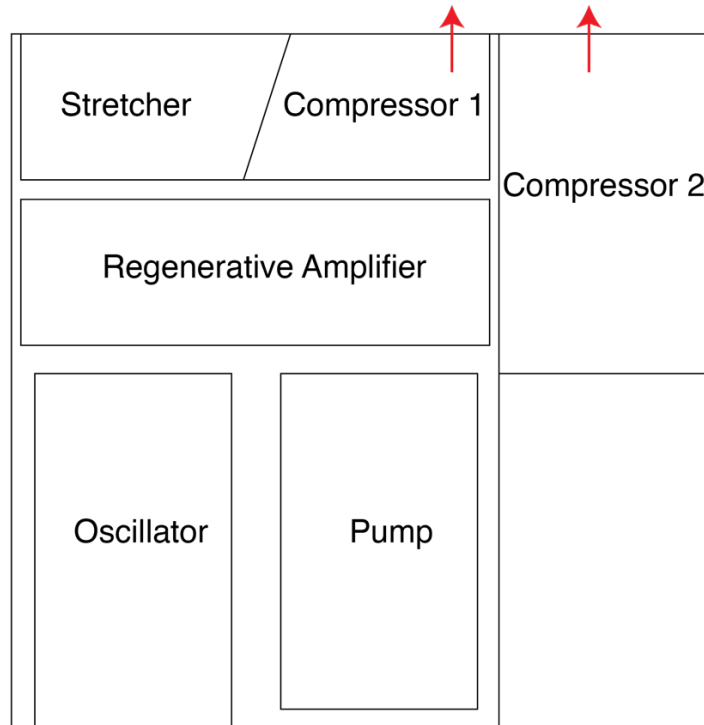


Figure 3-1: Diagram that shows the main components of our Ti:sapphire laser: (1) laser pump, (2) oscillator, (3) regenerative amplifier, (4) stretcher and (5 & 6) compressors 1 and 2. The red arrows show the 800 nm outputs from compressors 1 and 2.

The 800 nm output light that goes into the OPA is used to generate longer IR wavelengths, which are then separated by using a wavelength separator. The wavelength separator splits the output light from the OPA into two beams: the signal beam ranging from ~1250-1600 nm with a vertical polarization and the idler beam ranging from ~1600-2100 nm with a horizontal polarization. The THz spectroscopy setup described for the rest of this chapter is a one-dimensional (1D) THz setup because it only requires the use of a single THz pulse (signal beam). However, it is important to point out that having two IR pump pulses (signal and idler) opens up the possibility to perform two-dimensional (2D) THz spectroscopy,²⁻⁴ which is the setup that we used for the work presented in chapter 8 of this dissertation.

3.3 Initial Laser Alignment: Infrared Light

The setup that we use to perform 1D THz spectroscopy is shown in Fig. 3-2, which follows a pump-probe scheme,⁵⁻⁷ where the role of the THz pump is to excite the sample and the probe measures the sample's nonlinear response. In Fig. 3-2, the 800 nm light (purple) from the OPA output goes into the wavelength separator, where the light is split into two IR pump beams, a signal and idler beam. The signal pump light (blue) is directed through three mirrors into an NLO organic crystal to generate broadband THz light through OR after going through a 500 Hz chopper. The generated THz light (green) is focused and then collimated through a gold mirror (GM) and a 3-parabolic mirror scheme, and eventually focuses into the sample. Meanwhile, through the back of the third parabolic mirror, the 800 nm probe beam (red) goes through a filter (F), a telescope (L1, L2), a delay stage, and is then focused into the sample through a lens (L3). The probe beam is recollimated through another lens (L4) and then directed to the detection scheme consisting of a $\lambda/4$ wave plate (QWP), a Wollaston prism (WP) and two photodiodes

(PD1, PD2). The QWP converts the probe light into circularly polarized light, which is then split into horizontally and vertically polarized light that are directed into PD1 and PD2 for detection, respectively.

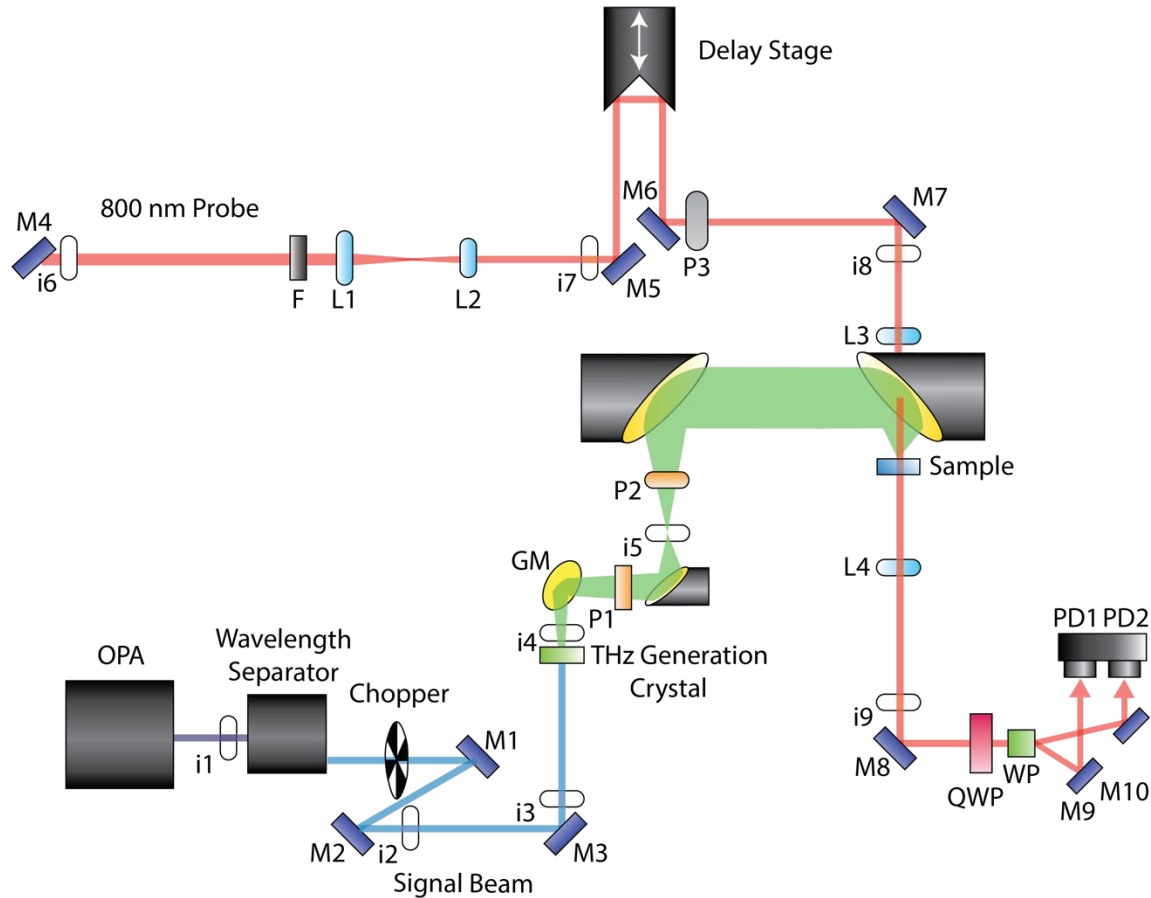


Figure 3-2: The setup used to perform 1D THz spectroscopy. The output light (purple) from the OPA is split through the wavelength separator, into signal (blue) and idler. The THz light (green) is generated in the NLO organic crystal through OR and the 800 nm probe (red) measures the THz signal. The signal pump light goes through a chopper and the timing of the 800 nm pulse is controlled by a delay stage. List of components in the setup: filter (F), irises (labeled as ia, where a=1-9), mirrors (labeled as Mb, where b=1-10), telescope (L1, L2), lenses (L3, L4), polarizers (P1, P2, P3), $\lambda/4$ wave plate (QWP), Wollaston prism (WP) and photodiodes (PD1, PD2). The frequency of the chopper is set to 500 Hz.

To perform measurements of good quality, the 1D THz setup needs to be properly aligned to maximize the generation and detection of the THz signal. The alignment process that we perform can be divided into five parts, which are: (1) the alignment of the IR signal light generated from the OPA; (2) the green laser alignment that sets the path for the THz light

through the GM and the 3-parabolic mirror scheme; (3) the alignment of the 800 nm probe path to the THz detection crystal; (4) the alignment of the probe beam through the detection scheme; and (5) the alignment of the THz light. For the remainder of this section, we will talk about the alignment of the IR light.

As part of the initial alignment, we center the vertically polarized IR light output from the signal OPA on iris i1 by adjusting the height and lateral position of the iris. Setting this iris correctly is crucial because it will later be used for the green visible laser alignment, which we will discuss in the next section. We then align the IR signal light output beam to irises i2, i3 and i4. The IR light is aligned by centering the light onto the iris with a mirror that is found before the iris. As a good rule of thumb, the mirror used to align an iris needs to be two optics away from the iris of interest. We use an IR viewer to view and align the actual IR light rather than the visible light coming out of the wavelength separator because this is a more efficient way of aligning the IR light. This alignment is done in this manner for irises i2 and i3; however, for iris 4, we only use the mirror (M3) right before it because this is the end of the alignment of the IR light. The reason we align the IR light with these three irises is because we want to set up an initial path for a green laser that is going to be used in the next step of the alignment.

3.4 The Green Laser Alignment

Before going into the details of the green visible laser alignment, we will go over the reasons why we use it as part of the alignment process. The alignment of the IR light, as mentioned in the previous section, ends on the path where iris i4 is found and right before iris i4 there is a mount to place the organic NLO crystal that is used for THz generation. Due to the THz light being invisible to the naked eye and the lack of any optical instrument capable of

seeing the THz light, it becomes too difficult to do a proper alignment of the THz light generated after the IR light goes through the THz generation crystal. It is for this reason that we opted for using a visible green laser to align all the optics after the THz generation crystal position, prior to placing the THz crystal in its mount and aligning the THz light. More importantly, the green laser also sets up the path for the THz light into the GM and the 3-parabolic mirror scheme, as seen in Fig. 3-2.

We will now go over the process of aligning with the green laser. The green laser is placed before iris i1, after closing the shutter of the input 800 nm light coming from the OPA. The height and position of the green laser is set in a way that the light is centered at both irises i1 and i2 as best as possible. Minor adjustments may be done to align the green laser on iris i2 by adjusting its proper mirror (M1). In a similar manner to the alignment done for the initial IR light, the green laser is also aligned to irises i3 and i4.

The next part of the setup alignment is the three off-axis parabolic mirror scheme as seen in Fig. 3-2. Just as a clarification, polarizers P1 and P2 are not present when we do the alignment with the green laser and a temporary iris is placed prior to the second parabolic mirror to assist in aligning with the green laser. The three parabolic mirrors, in the order that they are placed in the setup, have the following dimensions and effective focal lengths (EFL): (1) 1-inch diameter with a 1-inch EFL, (2) 3-inch diameter with a 5-inch EFL and (3) 3-inch diameter with a 2-inch EFL. The green laser is then aligned at the focus of iris i5 and through the temporary iris, by adjusting the gold mirror (GM) and the first parabolic mirror, respectively. The green laser is then recollimated through the second parabolic mirror and then focused into the sample position by the third parabolic mirror, as seen in Fig. 3-2. Once this alignment is accomplished, a Thorlabs CMOS camera (DCC1545M-GL) is placed on the motorized stage mount (see Fig. 3-3a) that is

found at the sample position, in order to adjust the camera position and ensure that the green laser hits its center. This setup with the camera is necessary to perform a proper alignment of the parabolic mirrors. The knobs of the second and third parabolic mirror are adjusted to make sure the beam looks as circular as possible on the image projected from the camera unto the computer, as seen in Fig. 3-3b. The shape of the beam ensures that the alignment has been properly done and that it can aid in finishing the alignment when we introduce the THz light. The temporary iris can be removed because it is not needed for the remainder of the aligning process. The next step requires us to overlap the green laser with the 800 nm probe at the sample position by using the CMOS camera. However, to do this we first need to align the 800 nm probe light, which is what we are going to discuss in the following section.

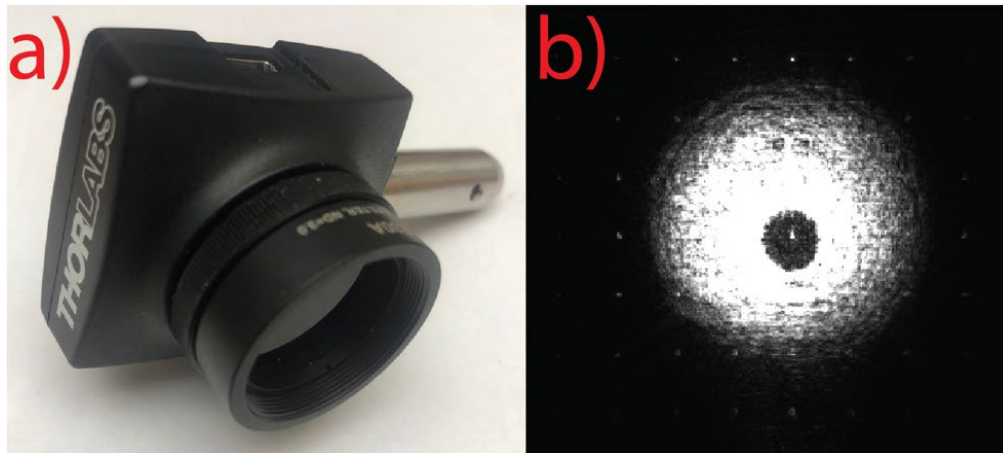


Figure 3-3: Picture of the CMOS camera used to assist in the alignment of the green laser through the 3-parabolic mirror setup (a) and the image produced from the camera to show an ideal alignment of the green laser focused onto the camera (b).

3.5 The 800 nm Probe Alignment

The probe beam used for our 1D THz measurements originates from the 800 nm output light generated in compressor 2 and its alignment is crucial because it will eventually need to be overlapped with the THz pump pulse and it will then be directed to the detection scheme. The

output from compressor 2 is directed to mirror M4, which is the start of the probe line that is shown in red in Fig. 3-2. We will first go over how to properly align the probe line and then we will cover the roles of some of the optics present in the path of the probe beam.

To align the probe beam, we use three irises (i7, i8, i9) along with their respective mirrors (M4, M5, M7) and a beam profiling camera. The camera that we use is a Gentec-EO Beamage-4M (P/N 202880) and is placed after mirror M8 in the setup shown in Fig. 3-2. The purpose of the camera is to simplify the alignment by being able to visualize the beam through the computer screen and ensure that the 800 nm is centered at the irises prior to going through the detection scheme. We began by aligning the 800 nm probe light to iris i7 by adjusting mirror M4 and by looking at the camera image on the screen. We adjust the mirror knobs to make sure that the image of the beam on the camera looks as symmetric as possible. In Fig. 3-4a, we show the image of the 800 nm beam not centered, which can be noticed by the uneven red regions; however, in Fig. 3-4b, we show the beam more centered by having the red regions evenly distributed.

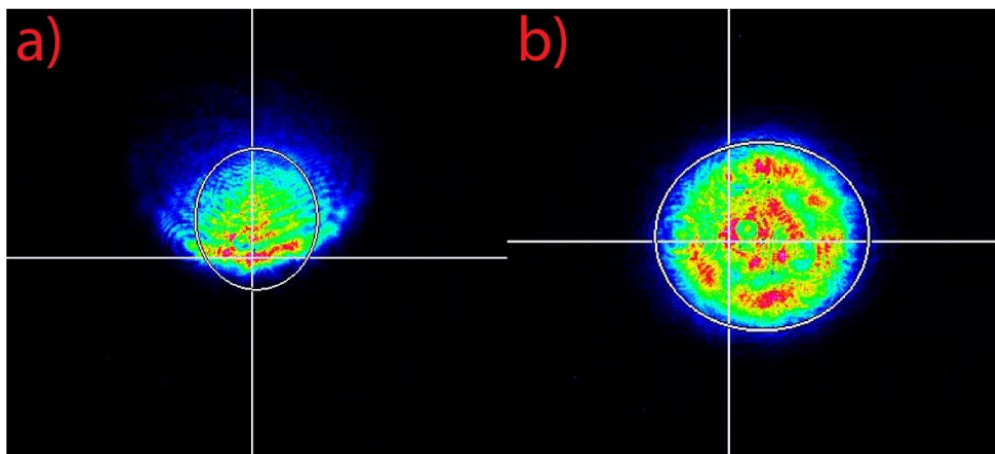


Figure 3-4: Images of the 800 nm IR light obtained through the beam profiling camera. a) Shows an IR beam that is not aligned due to the red regions not being symmetrically distributed, while b) shows an IR beam that is aligned as the red regions are symmetrically distributed.

The alignment follows this pattern for the remaining irises. Irises i8 and i9 are aligned by adjusting mirrors M5 and M7, respectively, and by always assuring that the image of the beam looks centered in the camera. It should be noted that this process can and should be repeated several times as this guarantees that the beam is properly aligned and maximized for the detection of the THz signal eventually. The beam profiling camera is then removed once the probe beam has been aligned.

As it can be noted in Fig. 3-2, there are several optics present in the probe beam path and we will now go over their respective roles. The 800 nm beam from the compressor 2 output is somewhat large and intense, which can cause some difficulties when aligning the probe beam and can also saturate the beam profiling camera or the photodiodes used for detection. It is for this reason that we added a filter (F), which consists of a NDUV 30A reflective filter and a NE20A absorptive filter, to reduce the beam intensity and two lenses (L1, L2) that make a telescope to reduce the size of the 800 nm beam, as seen in Fig. 3-2. Along the 800 nm probe beam path, we have a motorized variable delay stage that has a step size of 0.005 mm, which is a fundamental part of the setup because it allows us to adjust the path length of the probe beam to be able to overlap the probe and pump beams in time at the sample position. Following the delay stage, there is a polarizer (P3) that is optimized to minimize vertically polarized light since the 800 nm light is horizontally polarized. Finally, the light will then be focused, through a hole in the back of the third parabolic mirror, into a spot at the sample with lens L3. The 800 nm probe light is then recollimated by lens L4, and directed to the detection scheme. The alignment through the detection scheme will be explained later in section 3.6.

Finally, by having the 800 nm probe and the green laser (section 3.4) aligned, we can now overlap both of these pulses in space at the sample position. As mentioned before, we

placed a CMOS camera at the sample position and the green laser was aligned and focused properly into this camera. We can now allow the 800 nm probe to hit the camera through the hole in the back of the parabolic mirror; however, the 800 nm is still too intense for the CMOS camera and so an additional NE40A absorptive filter is added to filter F. By having the dimmer probe and the green laser beams focused into the CMOS camera, we can overlap both pulses in space by looking at the visual image of the pulses on the computer screen and adjusting the vertical and horizontal position of the probe beam with mirror M7 to overlap it with the green laser. It should be mentioned that if the alignment has been properly done, the adjustments with mirror M7 will be minor. Once both pulses are overlapped in space, we can remove the CMOS camera and finish aligning the 800 nm probe through the detection scheme.

3.6 Detection Scheme Alignment

Prior to going over how to properly finish aligning the 800 nm probe through the detection scheme, we will go over the detection scheme path and the relevant optics in it. Once the 800 nm probe beam has been recollimated with the assistance of lens L4, the beam is directed by mirror M8 into a $\lambda/4$ wave plate (QWP). Since the probe beam is horizontally polarized, the QWP is adjusted to 45° to ensure that the light output becomes circularly polarized. Following the QWP, the probe goes through the Wollaston prism (WP), which divides the probe light into horizontally and vertically polarized light and directs them into photodiodes PD1 and PD2 through mirrors M9 and M10, respectively (see Fig. 3-2). The signals from photodiodes PD1 and PD2 correspond to the signals displayed in channels 1 and 2 of the LabView program on the computer screen, respectively. The LabView program also shows channel 3, which is the difference channel between channels 1 and 2. Fig. 3-5 shows a screenshot of the LabView

software used to see the signals recorded from the photodiode channels 1 (red), 2 (black) and 3 (orange).

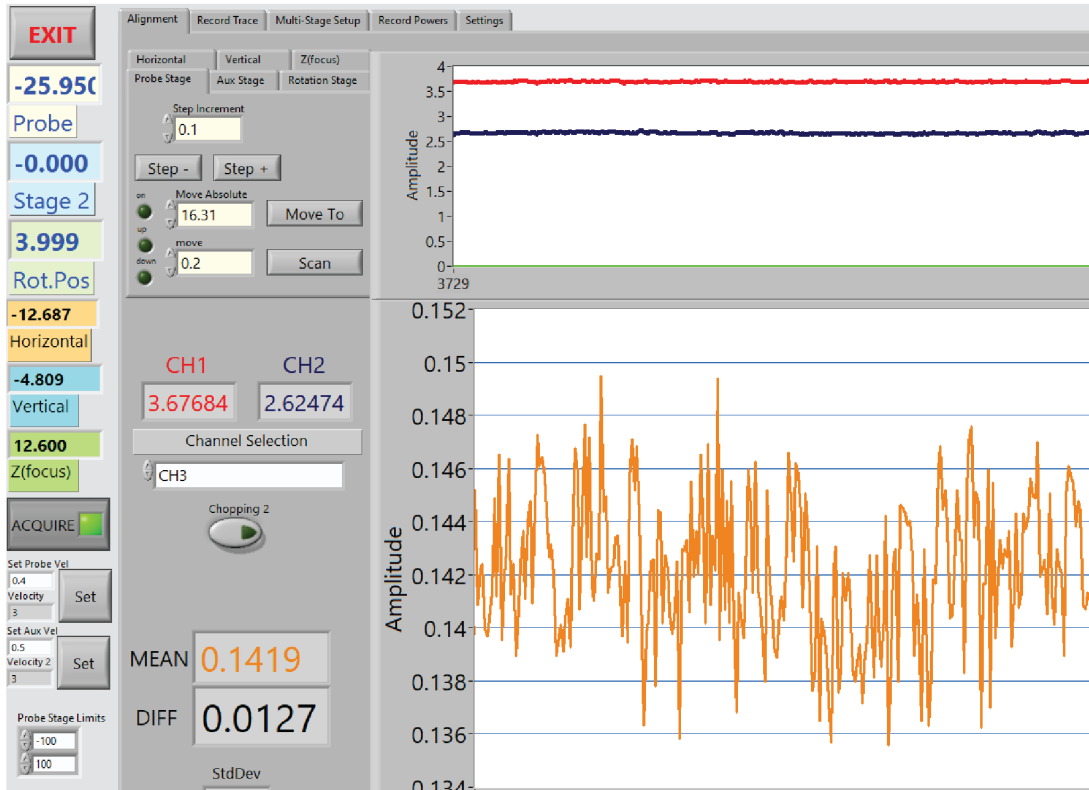


Figure 3-5: Screenshot of the LabView software used to collect data. The signals of channel 1 and 2 are shown in red and black on the top, respectively. The difference signal, channel 3, is shown in orange on the bottom.

We will now finish explaining how to properly align the 800 nm probe beam. The 800 nm probe light signal can be optimized by adjusting the generated signal that is recorded through the photodiodes and visually observed through the LabView program. First, the probe is optimized by adjusting the vertical and horizontal knobs of mirror M8 to maximize the observed signal on channel 1 of the LabView screen. Subsequently, the $\lambda/4$ wave plate is optimized by maximizing the signal in channel 3 displayed on LabView, which ensures that the wave plate is being set to 45° and thus maximizes the circular polarization of the 800 nm probe light. The probe light then travels through the Wollaston prism, which splits the light into horizontally and

vertically polarized light. The horizontally and vertically polarized beams are aligned into PD1 and PD2 by maximizing the signals in channel 1 and 2 by optimizing mirrors M9 and M10, respectively. Due to the saturation of the signal in PD1, a variable filter is used to assist in blocking some of the light while aligning the probe line. Once the alignment has been completed, the LabView is set to the difference channel 3 and the variable filter is adjusted to zero the incoming signal from the 800 nm light. We have now finished our discussion on aligning the 800 nm probe beam and are ready to move forward and align the THz light.

3.7 Alignment of the THz Light

In section 3.4, we aligned the green laser at the focus of the sample position with the assistance of a CMOS camera that was placed at this position, which was crucial as it sets up the pump path that is going to be used for the THz light. THz light is generated through the process of OR, which was explained in chapter 2 of this dissertation, by having the 800 nm light from the OPA output go through the NLO organic crystal to generate longer pulses of light, which lie within the THz frequency range. We use a variety of THz generators in this lab, such as DAST,⁸ OH-1,^{9, 10} DSTMS,^{8, 10} NMBA,¹¹ MNA,¹² and PNPA.^{11, 13} The THz generation crystal is chosen depending on the frequencies that we are interested in exciting and probing in our sample, which are limited to 0.5-6 THz. For the purposes of this chapter, we will use a standard (110) GaP crystal (300- μ m thick) to generate THz light¹⁴ with signal light at 1450 nm wavelength. We use 1450 nm light as a convenient reference wavelength because many of the NLO organic crystals have an optimal phase matching and generate the most power at this wavelength. The pulse energy of the 1450 nm light is ~0.4-0.7 mJ after going through a 500 Hz chopper, which allows us to subtract a background from the measured signal. We then place the 300- μ m GaP on a

rotating mount before the 3-parabolic mirror scheme (see Fig. 3-2) and we are now ready to find the THz pulse, which we need to do before we fully align and optimize the THz light.

To detect and optimize the THz pulse through electro-optic sampling, we place a (110) GaP crystal (100- μm thick) attached to a (100) GaP (1-mm thick) substrate on a mount at the sample position, which is on a motorized stage. The reason why we have the thin (100- μm) GaP attached to a thick (1-mm) GaP for detection is to remove echoes from the THz signal, which would be caused by the drastic changes in refractive index between the thin GaP and air, if the thick GaP was not present. However, the refractive index of the thick GaP is similar to that of the thin GaP and thus reduces echoes in the signal. Also, the thick GaP functions as an additional support due to the fragility of the thin GaP. To avoid any confusion between the GaP crystals used for generation and detection, we will refer to them with their respective thicknesses of 300- μm (generation) and 100- μm (detection), respectively.

It is now necessary to first find an ideal spot on the 100- μm GaP crystal because due to extensive use there might be burn spots at the surface that are not ideal to detect THz signal. To find an ideal spot, we direct the 800 nm probe light that focuses with a spot size of $\sim 50 \mu\text{m}$ into the GaP crystal, and then move the GaP mount horizontally and vertically to find a spot where the signal maximizes and is relatively consistent in the channel 1 output of the LabView screen (see Fig. 3-5). The THz light is then allowed to go through the 3-parabolic mirror setup, where the THz light is focused, recollimated and focused for a second time into the 100- μm GaP detection crystal (see Fig. 3-2) with a spot size of $\sim 250 \mu\text{m}$.

Prior to start optimizing the THz light, we need to place polarizers P1 and P2 in their proper position, according to Fig. 3-2. P1 is a rotating polarizer that allows us to block a certain amount of the THz light by rotating the angle of the polarizer (0° = full vertically polarized

beam), which is useful because allowing the full THz beam to hit the sample can sometimes saturate the signal and/or induce undesirable nonlinear responses. To find the THz signal, we set P1 at 0° because it allows the entire beam to go through and it makes it easier to see the THz signal. P2 simply allows for vertically polarized THz light to go through and reach the $100\text{-}\mu\text{m}$ GaP crystal. Once both polarizers are placed and the THz pump pulse is focused into the $100\text{-}\mu\text{m}$ GaP, we can move the motorized delay stage position until we can observe the near single cycle THz pulse, as seen in Fig. 3-6. We then find a peak (red arrow) of the single cycle THz pulse to use as a reference peak for the initial alignment of the THz signal; however, we do not choose the highest peak (blue arrow) because that peak could potentially saturate the THz signal at 0° of P1.

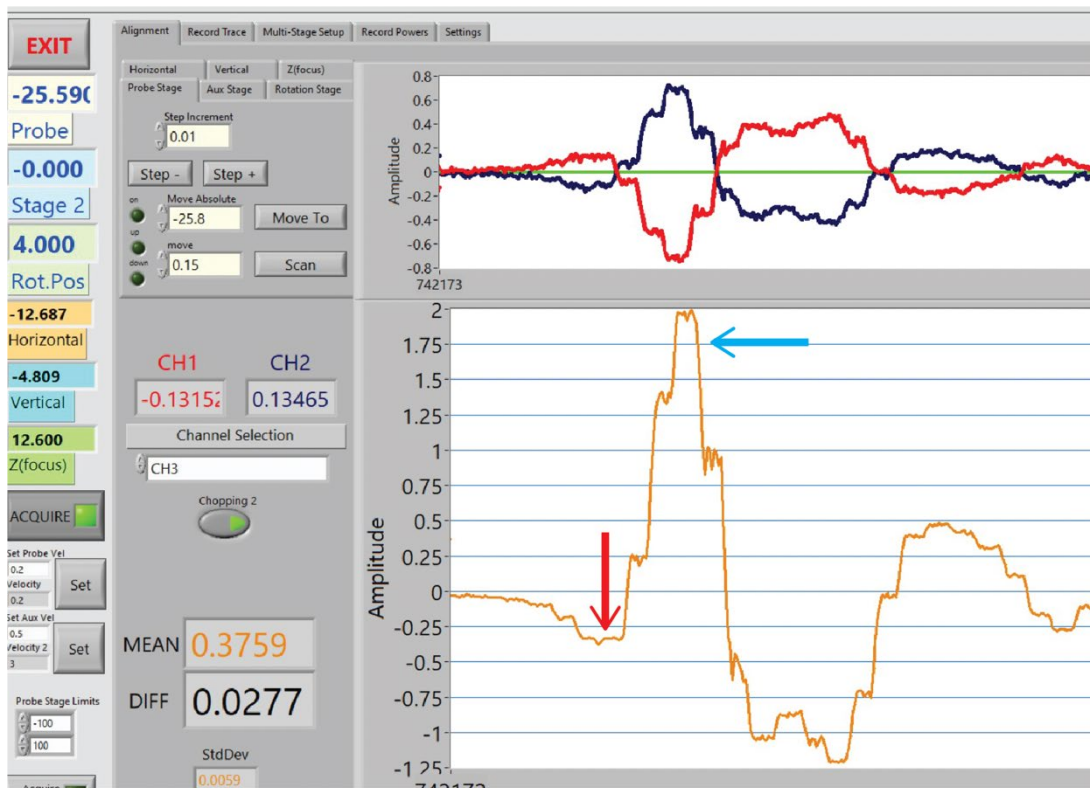


Figure 3-6: LabView screen showing a near single cycle THz pulse. The THz pulse is shown in orange in channel 3. A blue arrow shows the highest peak of the pulse, while a red arrow shows a small peak that was used as a reference peak for the initial alignment.

We will now go over how to properly optimize the generated THz pulse. As mentioned before, the 300- μm GaP THz generation crystal was placed on a rotating mount at the position that is shown in Fig. 3-2. Once signal was found by moving the delay stage, it is necessary to ensure that the polar axis of the THz generation crystal, which is commonly known as the THz generation axis, is aligned parallel to the polarization axis of the incoming IR light. This is accomplished by rotating the THz crystal and maximizing the reference peak (see red arrow in Fig. 3-6) that was previously found. Once we properly set the THz generation axis of the THz crystal, we can set the angle of P1 to 60° to avoid saturation and find the maximum peak of the single cycle THz pulse (see blue arrow in Fig. 3-6) and use it as the new reference peak for the remaining alignment of the THz pulse. After finding the THz generation axis, we can focus on optimizing the vertical and horizontal position of the THz crystal by changing the height and horizontal position of the THz crystal and maximizing the THz signal at the position of the reference peak that we observe on the LabView screen, as seen in Fig. 3-6. To further maximize the THz pulse, we can optimize the focus into the 100- μm GaP detection crystal along with the overlap with the 800 nm probe pulse by adjusting the vertical and horizontal knobs of the third parabolic mirror. It should be noted that prior to optimizing with the parabolic mirror, it is necessary to scan the THz pulse in channel 3, which can be done automatically by shifting the delay stage around the position of the reference peak that we selected. We need to scan the THz pulse because when we adjust the parabolic mirror, we can also shift the position of the reference peak in time, which would cause the alignment to be inaccurate. In Fig. 3-7, we show the scanning of the THz pulse in channel 3 (orange pulse) of the LabView software around the position of the new reference peak that we selected. After optimizing with the parabolic mirror, we can adjust the position of the 100- μm GaP crystal through the focus (z-position) to enhance

the signal of the THz pulse by moving the motorized mount stage by 0.1 mm steps. Iterations of the three actions that were just discussed in this paragraph (crystal position, parabolic mirror and z-position) are performed multiple times until the THz signal is fully optimized. By performing these last adjustments, we have managed to aligned and optimized the THz signal generated in the NLO organic crystal.

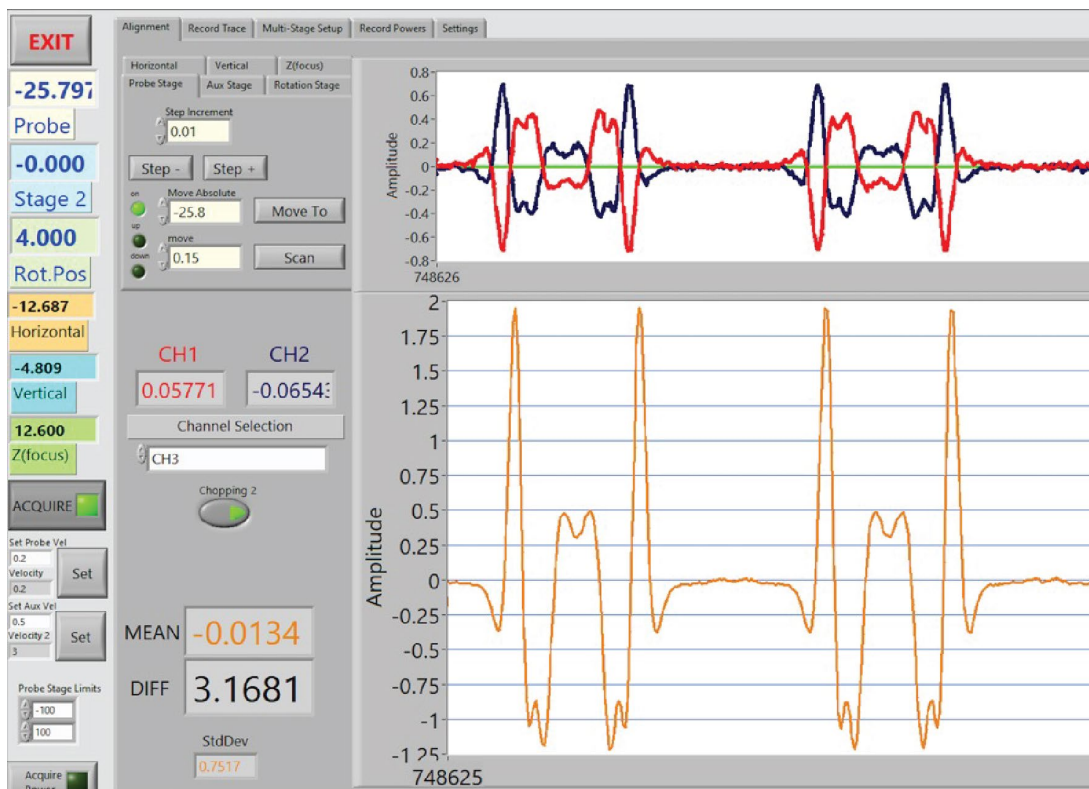


Figure 3-7: LabView screen showing the scanning of the THz pulse (orange) in channel 3 around the position of the new reference peak, which is the maximum peak.

3.8 Collection of a THz Time Trace

With the 1D THz setup properly aligned, we can start to collect a THz time trace. One of the challenges when working with THz light is that water can strongly absorb the THz light generated from the organic crystal,¹⁵ in particular at the low frequencies that we work with. By the time the THz light reaches the GaP detection crystal or sample, the THz signal has already

been strongly reduced. Due to this issue, we have built a box around the THz setup to purge out the atmospheric humidity with dry air, specifically around the area that contains the organic THz generator and the sample, as seen in Fig. 3-8. In Fig. 3-8, we show the THz setup inside the box and highlight the THz generation crystal and the sample, as well as the paths of the IR (blue), THz (green) and 800 nm probe (red) light. We purge the inside of the box for several minutes until the relative humidity is $\sim 3.00\%$ to maximize the THz signal as much as possible.

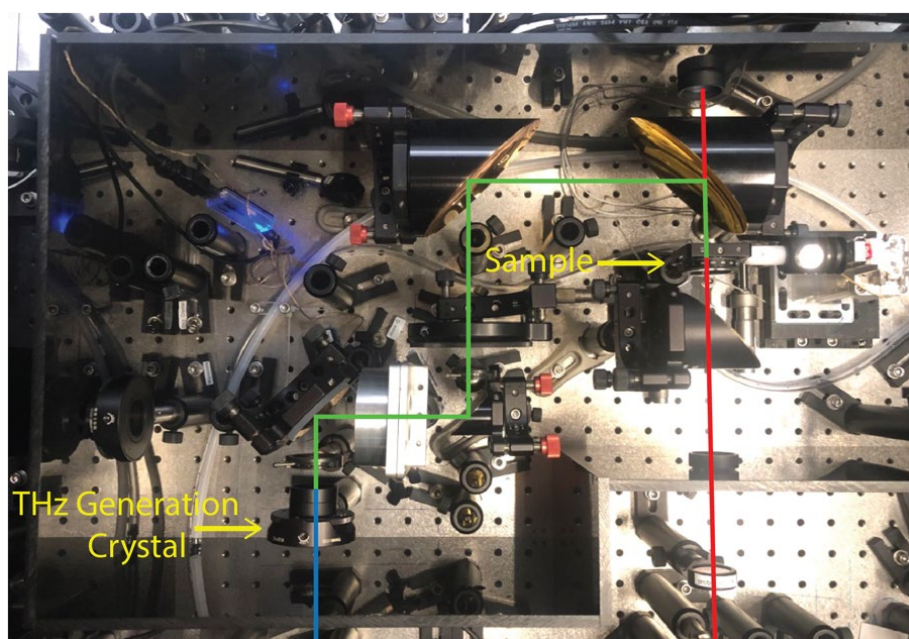


Figure 3-8: Picture of our 1D THz setup. The IR light (blue line) generated from the OPA goes inside the box, hits the NLO organic crystal to generate THz light (green line), which is then directed through a GM and the 3-parabolic mirror setup to focus into the $100\text{-}\mu\text{m}$ GaP crystal or the sample. The 800 nm probe (red line) hits the sample through a hole in the back of the third parabolic mirror and is then directed to the detection scheme. The box around the setup is used to create a dry air atmosphere by purging out the humidity.

Once the inside of the box has been purged with dry air, we need to make sure the position of the maximum peak of the single cycle THz pulse is still in the same location because the purging process can sometimes cause minor shifts in time of the THz pulse. We can simply move the delay stage to verify or move to the new peak position. For the time trace, we set the LabView program to start collecting data ~ 0.2 mm steps away from the position of the maximum

peak because it is usually enough to cover the beginning of the THz pulse. We can then select a step size (usually 0.005 mm) and an appropriate number of steps to cover the entire range of the THz pulse. When all of this has been set up, we can simply collect the THz time trace through the LabView software. An example of a time trace is shown in Fig. 3-9a, where the extracted electric field (kV/cm) is plotted as function of the time delay (ps). This THz time trace was obtained by measuring the generated THz from the 300- μm (110) GaP, which was then detected by the 100- μm GaP through electro-optic sampling. We can then Fourier transform the time axis to convert it into the frequency domain and obtain the THz spectrum that is shown in Fig. 3-9b. Fig. 3-9b shows the Fourier amplitude of the generated THz light from the 300- μm (110) GaP as a function of frequency in THz. The THz spectrum shows high amplitudes at frequencies between ~ 0.5 -4 THz. Prior to characterizing the generated THz light from other organic crystals or a sample (which replaces the detection crystal at the sample position), we always obtain a reference trace with the 300- μm (110) GaP as a standard THz generator.

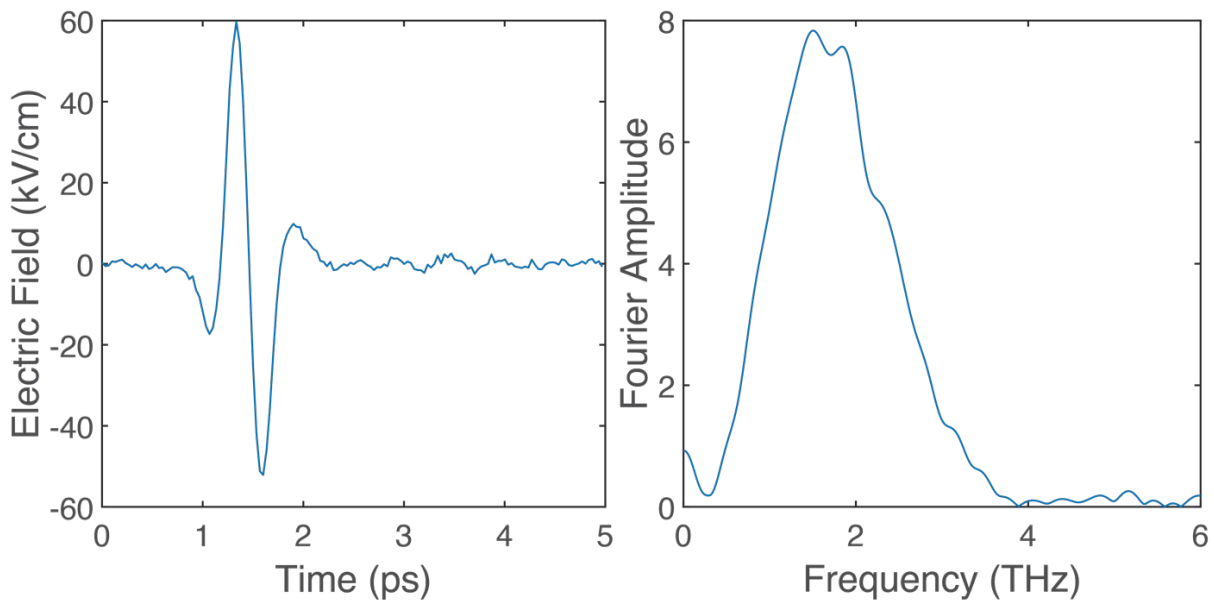


Figure 3-9: THz signal generated from a 300- μm (110) GaP. a) The electric field (kV/cm) of the single cycle THz pulse as function of delay time (ps). b) THz spectrum of the pulse in a).

3.9 Conclusion

In this chapter, we have discussed the entire process that is required to properly align a 1D THz setup to measure and characterize the THz pulse that is generated in a NLO organic crystal through OR. We started by briefly introducing the Ti:sapphire laser and its components, which are crucial to generate the 800 nm light that we use to generate the IR pump and probe beams. To properly align the pump pulse of this setup, we start by performing an initial alignment with the IR light, which is then followed by using a visible green laser to align the optics that focus the THz light into the sample. We then align the 800 nm probe, which is also focused into the sample, and then goes through the detection scheme. In the end the pump and probe pulses are overlapped in time and in space, and we then complete the process by aligning the THz light. Once all of the alignment has been properly done, we can then measure a THz time trace generated from the NLO crystal, which was a 300- μm (110) GaP crystal in this case. In the end, this chapter shows the hard work required to obtain a good quality THz spectrum.

3.10 References

1. M. C. Hoffmann, and J. A. Fülöp, “Intense ultrashort terahertz pulses: generation and applications,” *Journal of Physics D: Applied Physics* **44**, 083001 (2011).
2. B. E. Knighton, S. A. Sorenson, and J. A. Johnson, “Simple experimental setup for double-pulse and two-dimensional terahertz spectroscopy,” *Journal of Applied Physics* **128**, (2020).
3. C. L. Johnson, B. E. Knighton, and J. A. Johnson, “Distinguishing Nonlinear Terahertz Excitation Pathways with Two-Dimensional Spectroscopy,” *Physical Review Letters* **122**, 073901 (2019).

4. M. F. Biggs, B. E. Knighton, A. Alejandro, L. M. Davis, C. Rader, and J. A. Johnson, “Pump Pulse Bandwidth-Activated Nonlinear Phononic Coupling in CdWO₄,” (2023).
5. M. C. Hoffmann, J. Hebling, H. Y. Hwang, K.-L. Yeh, and K. A. Nelson, “THz-pump/THz-probe spectroscopy of semiconductors at high field strengths [Invited],” *Journal of the Optical Society of America B* **26**, A29-A34 (2009).
6. J. Hebling, M. C. Hoffmann, H. Y. Hwang, K.-L. Yeh, and K. A. Nelson, “Observation of nonequilibrium carrier distribution in Ge, Si, and GaAs by terahertz pump--terahertz probe measurements,” *Physical Review B* **81**, 035201 (2010).
7. G. Sharma, L. Razzari, F. H. Su, F. Blanchard, A. Ayesheshim, T. L. Cocker, L. V. Titova, H. C. Bandulet, T. Ozaki, J. C. Kieffer, R. Morandotti, M. Reid, and F. A. Hegmann, “Time-Resolved Terahertz Spectroscopy of Free Carrier Nonlinear Dynamics in Semiconductors,” *IEEE Photonics Journal* **2**, 578-592 (2010).
8. B. Monozslai, C. Vicario, M. Jazbinsek, and C. P. Hauri, “High-energy terahertz pulses from organic crystals: DAST and DSTMS pumped at Ti:sapphire wavelength,” *Optics Letters* **38**, 5106-5109 (2013).
9. B. S. Dastrup, J. R. Hall, and J. A. Johnson, “Experimental determination of the interatomic potential in LiNbO₃ via ultrafast lattice control,” *Applied Physics Letters* **110**, (2017).
10. B. E. Knighton, R. Tanner Hardy, C. L. Johnson, L. M. Rawlings, J. T. Woolley, C. Calderon, A. Urrea, and J. A. Johnson, “Terahertz waveform considerations for nonlinearly driving lattice vibrations,” *Journal of Applied Physics* **125**, (2019).
11. G. A. Valdivia-Berroeta, Z. B. Zaccardi, S. K. F. Pettit, S.-H. Ho, B. W. Palmer, M. J. Lutz, C. Rader, B. P. Hunter, N. K. Green, C. Barlow, C. Z. Wayment, D. J. Ludlow, P. Petersen, S. J.

Smith, D. J. Michaelis, and J. A. Johnson, “Data Mining for Terahertz Generation Crystals,” *Advanced Materials* **34**, 2107900 (2022).

12. B. W. H. Palmer, C. Rader, E. S.-H. Ho, Z. B. Zaccardi, D. J. Ludlow, N. K. Green, M. J. Lutz, A. Alejandro, M. F. Nielson, G. A. Valdivia-Berroeta, C. C. Chartrand, K. M. Holland, S. J. Smith, J. A. Johnson, and D. J. Michaelis, “Large Crystal Growth and THz Generation Properties of 2-Amino-5-Nitrotoluene (MNA),” *ACS Applied Electronic Materials* **4**, 4316-4321 (2022).

13. C. Rader, Z. B. Zaccardi, S.-H. E. Ho, K. G. Harrell, P. K. Petersen, M. F. Nielson, H. Stephan, N. K. Green, D. J. H. Ludlow, M. J. Lutz, S. J. Smith, D. J. Michaelis, and J. A. Johnson, “A New Standard in High-Field Terahertz Generation: the Organic Nonlinear Optical Crystal PNPA,” *ACS Photonics* **9**, 3720-3726 (2022).

14. K. Aoki, J. Savolainen, and M. Havenith, “Broadband terahertz pulse generation by optical rectification in GaP crystals,” *Applied Physics Letters* **110**, (2017).

15. H. Ge, M. Lv, X. Lu, Y. Jiang, G. Wu, G. Li, L. Li, Z. Li, and Y. Zhang, “Applications of THz Spectral Imaging in the Detection of Agricultural Products,” *Photonics* **8**, 518 (2021).

CHAPTER 4: Improved Generation of Terahertz Light Through Heterogeneous Multi Layered Organic Crystal Structures

4.1 Introduction

In recent years, terahertz (THz) light has gained special interest due to its applications in biological and security imaging,¹⁻⁴ in high-speed electronic devices,⁵ and its ability to study ultrafast processes like phonon coupling⁶⁻⁸ and magnetism.⁹⁻¹¹ Because of these applications, the development and improvement of sources that generate THz-frequency light is of ongoing importance. THz light can be generated using photoconductive antennas (PCAs),¹² THz molecular gas lasers,¹³⁻¹⁵ plasma sources,¹⁶⁻¹⁸ and through optical rectification (OR) in nonlinear optical (NLO) materials.¹⁹ Inorganic crystals like ZnTe^{20, 21} or GaP²² have traditionally been used to generate low-intensity THz light. Organic NLO crystals are currently the strongest THz generators^{23, 24} they possess high second-order nonlinearity^{25, 26} and better phase-matching when compared to inorganic materials.²⁷ The use of organic materials for high intensity THz generation through OR is also attractive because these materials can generate intense, short, and broadband THz light (0.5-6 THz) without requiring high laser powers that are needed for plasma sources for THz radiation.¹⁶

Common organic crystals used for THz generation through OR include DAST,^{28, 29} DSTMS,²⁸ OH-1,³⁰ PNPA,²⁴ and BNA.^{31, 32} An important observation of these THz sources is that red crystals (DAST, DSTMS, OH-1, and PNPA) have higher absorption cutoffs in the IR frequencies than yellow-colored crystals (BNA) that have low absorption cutoffs. The lower absorption cutoffs of yellow crystals allows them to be pumped with the 800 nm output light produced by common Ti:sapphire laser systems. Recently, we discovered and optimized the growth methods for additional yellow organic crystals like BNA, including MNA,³³ and NMBA,²³

all of which generate THz frequency light efficiently when pumped at 800 nm. The transmission spectra from Fig. 4-1 shows the absorption cutoffs for these three yellow organic crystals that are at shorter wavelengths compared to PNPA²⁴ and DAST (below 500 nm for the yellow crystals compared to ~600 nm for the red crystals). This shorter wavelength absorption cutoff makes the yellow crystals easier to pump at 800 nm, and even better at 1030 nm with increasingly popular Ytterbium-based laser systems due to less two-photon absorption.

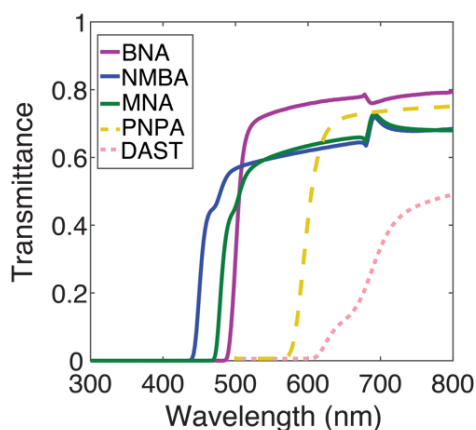


Figure 4-1. UV-vis transmission spectra for yellow organic crystals BNA, NMBA and MNA (solid lines purple, blue and green, respectively) along with the transmission of red crystals PNPA (dashed yellow) and DAST (dotted pink).

One drawback of organic crystals is that they often have low melting points, which limits the irradiation intensity that can be used and the subsequent THz generation intensity that a crystal can produce. For example, the melting points for BNA, NMBA and MNA are ~104 °C, ~122 °C and ~130 °C, respectively. The low melting points of these crystals may lead to damage as multi-photon absorption can lead to heating the material above the melting point.³⁴ We reduced the heating in NLO crystals by developing a method to fuse BNA crystals directly (without glue or adhesive) to sapphire plates that have high thermal conductivity and can dissipate the heat generated at the crystal from the pump laser.³⁴ Fusing BNA crystals to sapphire allow them to

withstand higher laser fluences without raising the crystal temperature above the melting point, and consequently the THz output is increased.

Fresnel reflection losses that result when the incident laser light passes from air into materials with drastically different refractive index can also lower the efficiency of THz generation crystals. A typical THz generation setup utilizing an organic crystal includes the crystal itself and a material like Teflon (PTFE), high-density polyethylene (HDPE), or semiconductors like silicon after the THz crystal to transmit the THz and filter the remaining IR light. This type of setup includes several interfaces between the THz crystal, the layer of air, and the IR filter, which lead to reductions in the THz output efficiency due to Fresnel reflection losses at each interface. We previously showed with the organic crystal DAST that by creating heterogeneous multi-layered “sandwich” structures, Fresnel reflection losses were reduced. These layered structures included the addition of index-matching fluids at each interface between the air, the crystal, and the IR filter.³⁵ The overall intensity of the THz output from DAST crystals in these sandwich structures was improved by as much as 50%.

In this work, we expand upon our previous work on improving the stability and THz output of BNA to include the other yellow organic crystals NMBA and MNA. To achieve this, we fuse each organic crystal to sapphire plates to create tight interfaces that minimize Fresnel losses and effectively dissipate heat. Next, we create multi-layered structures with index-matching liquid crystal MBBA (N-(4-methoxybenzylidene)-4-butylaniline) and a Teflon IR filter. Creating these improved sandwich structures leads to significant increases in the THz output of each yellow organic crystal by increasing the damage threshold and reducing reflective losses at the transmission interfaces. We report that by fusing NMBA and MNA crystals to sapphire plates, their damage thresholds increase by $\sim 1.6\times$ and $\sim 2\times$, respectively. We also report that assembling

these yellow organic crystals, NMBA, MNA and BNA into sandwich structures improves the THz output by $\sim 1.5\times$, $\sim 1.2\times$ and $\sim 1.2\times$, respectively.

4.2 Methods

4.2.1 Fusing Crystals to Sapphire

We have previously reported a method for fusing low-melting point organic crystals of BNA to sapphire.³⁴ This method involves heating the sapphire window to just below the melting point of the crystals, which causes a partial melting and fusing of the crystal with the sapphire to create a tight contact between the two materials. Due to the similarities in absorption cutoff and melting temperature between BNA and the two new yellow crystals MNA and NMBA (see Fig. 4-1), we theorized that these additional yellow crystals could benefit from fusing to sapphire. While both MNA and NMBA have higher melting points than BNA, we found that the same fusing protocol used to fuse BNA crystals to sapphire were amenable to fusing both MNA and NMBA, but at higher temperatures.

The fusing process involves a heat treatment that affects each of the crystals in different ways and three factors were considered to verify the quality of crystals fused to sapphire plates. The first factor is how each crystal is affected by overheating, which can cause the crystal to fully melt and become polycrystalline or to become cloudy and opaque. The second factor is how well each kind of crystal stays fused to sapphire when force is applied to the edges. The final factor is the frequency of delamination, which occurs when individual layers of the crystal itself begin to separate from each other.

These three factors differed between each crystal and will be briefly discussed. The low melting point of BNA causes the crystal to melt very easily. Overheating BNA to the point where it begins to liquify causes it to cool in a completely opaque, polycrystalline manner. BNA delaminates minimally, mostly in areas on the edge of the crystal that may have been put under stress during the cleaving process. MNA has the highest melting point yet the crystal quickly becomes cloudy around the edges when excess heat is applied. MNA also fuses less tightly to the sapphire than BNA and has a greater chance of becoming unfused after processing. Additionally, MNA has a high tendency to delaminate, causing imperfections in the single crystalline windows needed for THz generation. Finally, NMBA also becomes cloudy with overheating and forms the least tight bond with sapphire. This means that NMBA crystals are prone to come unfused more often after heating. One way to mitigate this is to ensure that the crystal face being fused is perfectly smooth and no imperfections (dust, etc.) are between the crystal and the sapphire surface. NMBA also exhibits the least amount of delamination. For this work, we used only crystals for THz generation that did not show any cloudiness or delamination and that were securely fused to the sapphire plate.

4.2.2 Heterogeneous Multi-layer “Sandwich” Structures

We have previously shown that THz output from organic crystals (DAST) can be improved by layering materials with similar refractive indices to reduce Fresnel reflection losses. During THz light generation, the IR pump light and generated THz frequency light must travel through several interfaces before entering the THz crystal (pump) or exiting through the Teflon filter (THz). Creating tight interfaces (no air) at each of these material transitions by the introduction of materials with intermediate refractive indices can minimize Fresnel losses. The refractive indices

for the yellow organic crystals BNA, MNA and NMBA, along with the refractive indices of the liquid crystal MBBA and Teflon are shown in Fig. 4-2. The three yellow crystals used in this study have a refractive index greater than 2, with MNA having a refractive index at ~ 2.5 for all the shown frequencies. The difference in refractive indices between these three crystals and air ($n = 1.00027$) results in significant reflective losses in the IR pump light and the generated THz light. As we designed previously with DAST,³⁵ we chose the layer materials with refractive indices that gradually decrease going from the organic crystal, to liquid crystal MBBA, to the Teflon filter, and finally to air. By gradually stepping down the refractive indices between the multiple layers (MBBA has an intermediate refractive index between the two other layers), the Fresnel reflective losses will be reduced and thus increase the THz generation output.

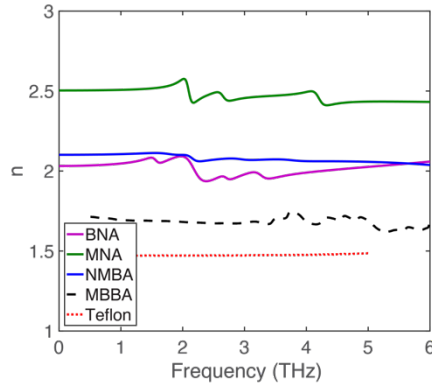


Figure 4-2. THz refractive indices for the yellow organic crystals BNA, MNA, NMBA (solid lines magenta, green and blue, respectively). Refractive indices for the index-matching fluid MBBA and the Teflon are shown as dotted lines (black and red, respectively).

The new sandwich structures were assembled by taking each organic crystal and fusing it directly to a sapphire plate by our partial melting procedure. The fused crystal was then placed into a 1-inch lens tube with the crystal facing the inside. A small layer (\sim two drops) of liquid crystal MBBA was used to cover the entire surface of the crystal and a layer of Teflon (~ 1.5 mm) was

added to close the back side of the layered structure. The layout of our sandwich structures can be seen in Fig. 4-3.

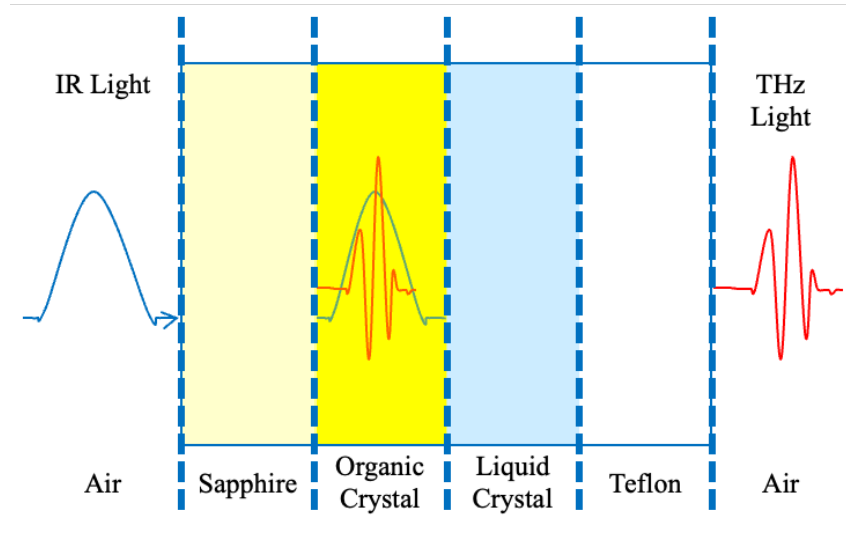


Figure 4-3. Layout of the heterogeneous multi-layer structures for improved THz output (not to scale). The pump IR light (blue) generates the THz frequency light (red) in the organic crystals through optical rectification. The dotted lines indicate material interfaces where Fresnel losses can occur, but are reduced in this structure.

2.2.3 Damage Threshold and THz Generation Output Efficiency Measurements

The setup used to measure the damage threshold of these organic crystals has previously been described in depth.³⁴ For damage threshold measurements, we used the 800 nm output beam from our Ti:sapphire laser with a repetition rate of 1000 Hz mechanically chopped to 500 Hz, a pulse duration of 100 fs and a pulse energy of 3.8 mJ per pulse. To guarantee that the full laser beam was interacting with our sample crystals, we used a telescope to shrink the beam size to a $1/e^2$ beam diameter between ~ 3.6 mm and ~ 5.1 mm, depending on the size of the crystal.

In these measurements, the laser power (fluence) was gradually increased until the THz output from the crystal began to decrease. This fluence point was designated as the damage threshold of the crystal. At each pump power, the generated THz output was focused tightly using

a three-parabolic mirror focusing scheme (see Fig. 4-4) with the following diameters (d) and effective focal lengths (EFL): (1) 1-in d with a 1-in EFL, (2) 3-in d with a 5-in EFL and (3) 3-in d with a 2-in EFL. The THz output was detected via electro-optic (EO) sampling with an 800 nm probe using a 100- μm (110) GaP crystal bonded to a 1-mm (100) GaP crystal as the detection crystal. The pulse duration of the probe pulse limits our detection bandwidth to ~ 6 THz. Additionally, two wire-grid polarizers were used to attenuate the THz light as it can saturate the detector. The attenuated THz was then scaled up to its true amplitude. A full picture of this setup can be seen in Fig. 4-4a. Three bare crystals (not fused to sapphire plates) and three crystals fused to sapphire were tested only for MNA and NMBA, as BNA had been tested before.³⁴ The crystals used in these measurements had a variety of thicknesses ranging from 300-900 μm for NMBA and 400 μm to 1.4 mm for MNA.

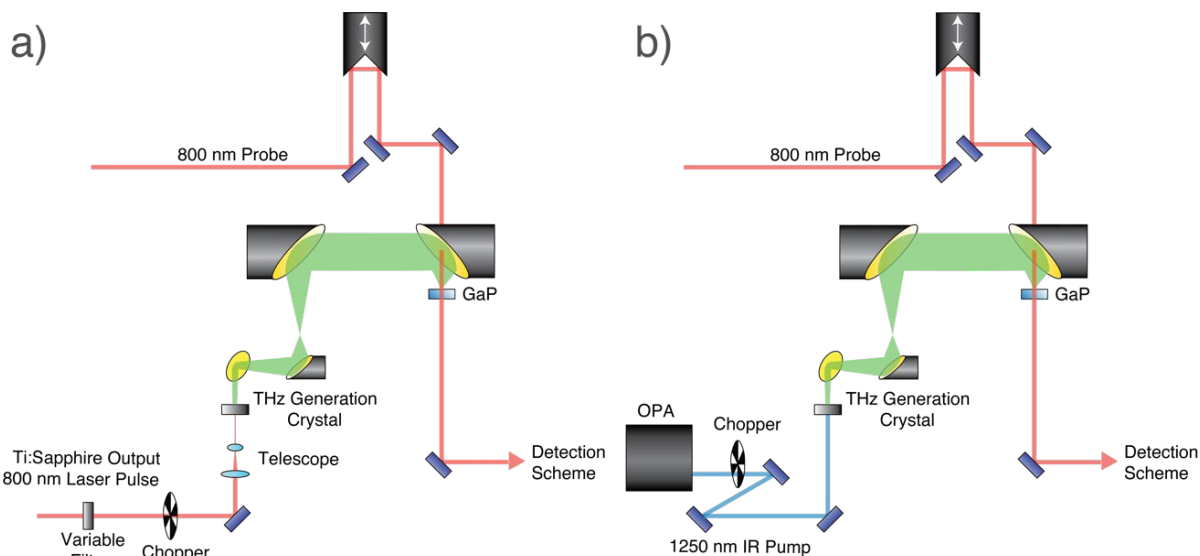


Figure 4-4. Setups used to measure the THz generation of yellow organic crystals for (a) damage threshold and (b) THz output efficiency.

THz output efficiency measurements were also performed, where the THz generation of crystals fused to sapphire were measured several times before and after being constructed into

multi-layered “sandwich” structures. These before and after sandwich structure measurements were done on the same day in order to maintain consistent laser powers. The setup used for these measurements was similar to the one briefly described for damage threshold measurements, minus a few key differences (see Fig. 4-4b). A 1250-nm output of an optical parametric amplifier (OPA) was used to pump the organic crystals. This wavelength has a pulse energy of ~ 0.65 mJ per pulse and a $1/e^2$ beam diameter of ~ 7.6 mm. This wavelength was selected because it is the optimally phase-matched wavelength for yellow organic crystals that the OPA outputs.

4.3 Results & Discussion

4.3.1 Damage Threshold

Fig. 4-5 shows the results of the damage threshold measurements for (a) NMBA and (b) MNA crystals. The comparison between the averaged damage threshold of bare crystals (red shaded region) and crystals fused to sapphire (blue shaded region) for both (a) NMBA and (b) MNA crystals. In Fig. 4-5, the y-axis shows the generated electric field of the crystals and the x-axis shows the increasing laser fluences in mJ/cm^2 . The averaged laser fluence at the damage threshold is shown as dotted vertical lines for the bare crystal (red) and the crystal fused to sapphire (blue). The shaded regions around the vertical lines are the standard deviation for the laser fluence at the damage threshold. A sample of one measurement for a bare crystal (open circles) and for a crystal fused to sapphire (closed squares) are also shown. The thicknesses of the crystals used for these samples were ~ 400 μm for NMBA and ~ 1.2 mm for MNA.

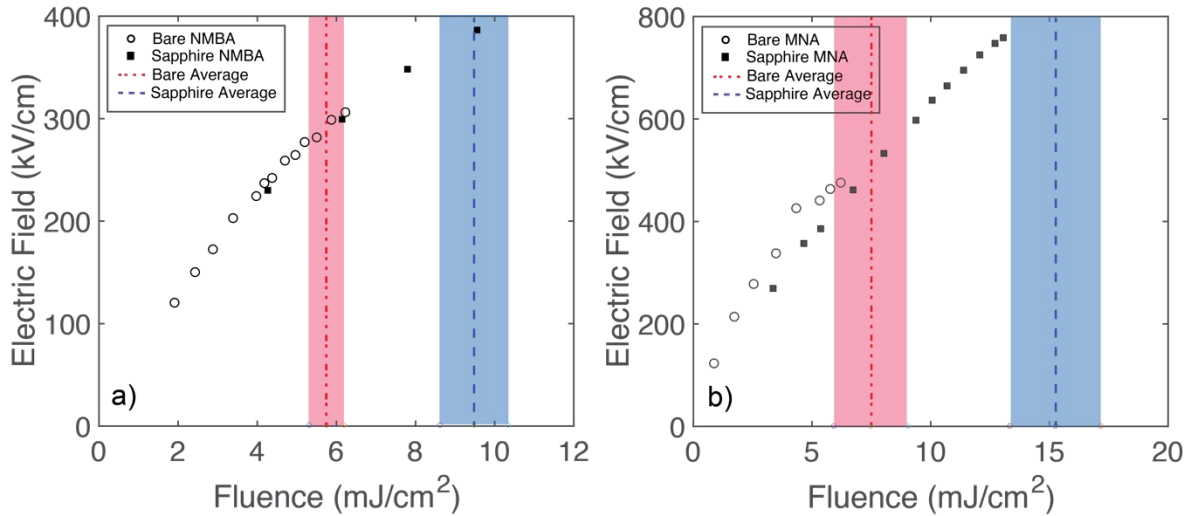


Figure 4-5. Damage threshold of (a) NMBA crystals and (b) MNA crystals. The averaged damage threshold for bare crystals (red dotted line) and the averaged damage threshold for crystals fused to sapphire (blue dotted line) are shown. Shaded regions show standard deviations for the averaged damage threshold measurements. The open circles (bare crystal) and closed squares (crystal fused to sapphire) show an example of the electric field as a function of the increasing laser fluence.

Fig. 4-5 shows that the damage thresholds for the bare NMBA and MNA are ~ 5.8 and ~ 7.5 mJ/cm^2 , respectively, while fusing the crystals to sapphire increases their damage threshold to ~ 9.5 and ~ 15.3 mJ/cm^2 , respectively. In terms of electric field strengths, NMBA can generate $\sim 30\%$ more when the crystals are fused to sapphire, while MNA can generate $\sim 40\%$ more. Table 4-1 shows a comparison of NMBA and MNA damage thresholds with our previous work on BNA crystals.³⁴

Table 4-1. Comparison of laser damage threshold for NMBA, MNA and BNA for both bare and fused crystals.

Crystal	Bare Damage Threshold (mJ/cm^2)	Fused Damage Threshold (mJ/cm^2)	Ratio of Fused to Bare
NMBA	5.8	9.5	1.6
MNA	7.5	15.3	2.0
BNA	4.4	12.4	2.8

Fusing these organic crystals to sapphire plates increases the damage threshold significantly. BNA fused to sapphire experiences a $\sim 2.8\times$ increase,³⁴ MNA a $\sim 2\times$ increase, and NMBA a $\sim 1.6\times$ increase. The differences in damage threshold appear to be due to the melting points, where BNA has the lowest melting point and experiences the largest increase in damage threshold. The observed higher damage threshold of the crystals fused to sapphire over the bare crystals means that higher intensity THz light can be accessed by pumping with higher laser fluences (see Fig. 4-5). The lifetime of each organic crystal is also extended by minimizing the irradiation-induced crystal damage.

4.3.2 THz Output Efficiency

Our next objective was to demonstrate that an additional increase in THz output could be accomplished by inclusion of our sapphire-fused crystals into layered structures designed to minimize Fresnel reflection losses. To show the improved THz output efficiency from NMBA, BNA and MNA, we measured the THz generation output for the sapphire-fused crystals before and after assembling them into layered (sandwich) structures (see Fig. 4-3) according to the setup in Fig. 4-4b. For this study, we measured a total of six NMBA crystals, six BNA crystals, and three MNA crystals. Each crystal was measured at least three times (some up to five times) before and after being assembled into sandwich structures.

As an example, Fig. 4-6 shows the average THz spectrum of a sapphire-fused BNA crystal before (blue) and after (yellow) it was assembled into a sandwich structure. These data clearly show that assembly of BNA into a layered structure significantly increases the THz output at all frequencies. However, the increase is more apparent between ~ 1 -4.5 THz.

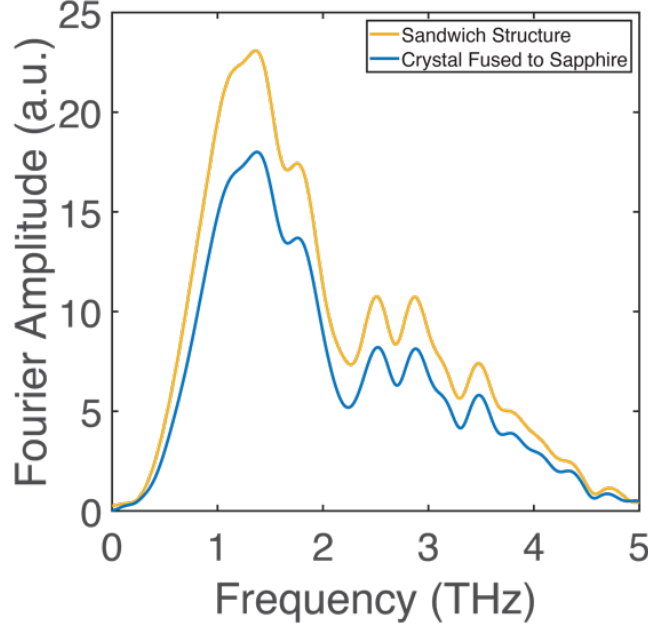


Figure 4-6. Comparison between the averaged THz spectrum of a sapphire-fused BNA crystal before (blue) and after (yellow) inclusion into a multi-layered structure.

To make a more direct comparison between the sapphire-fused crystals and the newly made layered structures, the THz spectra were integrated using Eq. 4-1 from ~0.5–6 THz to provide a measure of the THz strength for each measurement. The THz intensity of the layered structures was normalized with respect to the sapphire-fused crystals according to the ratio in Eq. 4-2.

$$\epsilon = \int_{0.5}^6 E_o(\omega) d\omega \quad (4-1)$$

$$\mathbf{Ratio} = \left(\epsilon_{\text{Sandwich Structure}} / \epsilon_{\text{Sapphire-fused crystal}} \right)^2 \quad (4-2)$$

We first determined the average ratio for each set of measurements on individual NMBA, BNA and MNA sandwich structures, and then calculated an overall average per crystal type. Fig. 4-7 shows the averages for the normalized ratios of the THz intensity for all six NMBA and BNA crystals, and the three MNA crystals. The normalized ratios of the THz output intensity of the sandwich structure are shown as yellow bars with their respective error bars in brown and the normalized THz intensity for the sapphire-fused crystals are shown as blue bars.

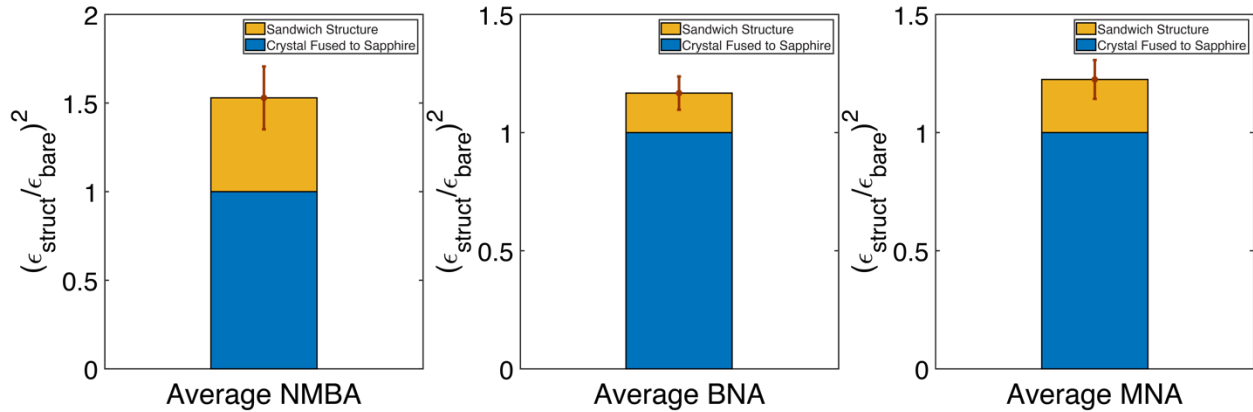


Figure 4-7. The normalized THz output intensity of the layered structure (yellow bar) compared to the sapphire-fused crystal (blue bar) for the average of six NMBA and BNA crystals, and three MNA crystals. The error bars for the sandwich structure are shown in brown.

In Fig. 4-7, we see that the averaged THz output for each crystal type improves when the sapphire-fused crystal is made into a layered structure. For NMBA we see an increase of $\sim 1.5\times$ in the THz output, while we see an increase of $\sim 1.2\times$ for BNA and MNA.

We also noticed an interesting result when comparing the THz output efficiency between crystals of the same type. In Fig. 4-8, we show a comparison for two different sapphire-fused NMBA crystals before and after inclusion into a layered structure. Figs. 4-11 to 4-13 in the Appendix section show a comparison between all NMBA, BNA and MNA layered structures. In this comparison with NMBA, we notice a large difference between the improvements in THz output efficiency for each crystal; NMBA-A increases by a factor of ~ 1.9 while NMBA-B increases only by a factor of ~ 1.2 . This discrepancy between crystals of the same type was also observed with other NMBA crystals and BNA samples. Upon further analysis, we realized that the crystals that experienced significant increase in THz output in layered structures came from different batches than those that didn't increase as much. Those crystals that experienced larger increases were produced several months previously, while those that exhibited smaller increases

had recently been made (< 1 month). In the following discussion, we will refer to the former crystals as “aged crystals” and to the latter ones as “recent crystals”.

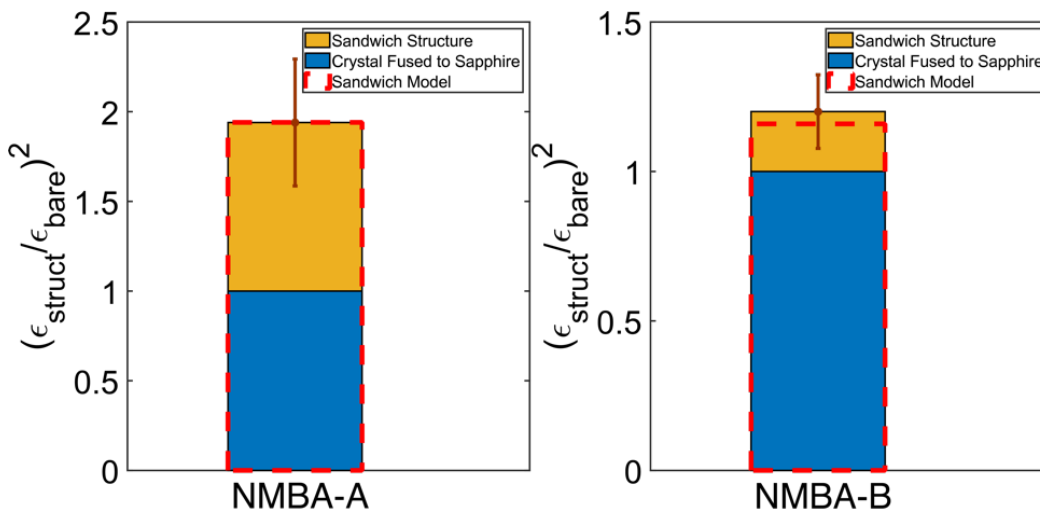


Figure 4-8. The normalized THz output intensity of the sandwich structure (yellow bar) compared to the sapphire-fused crystal (blue bar) for two different NMBA crystals. The error bars for the sandwich structures are shown in brown. The red dotted line is the modeled normalized THz intensity of the sandwich structure.

We noticed that the crystals with higher increases in THz output came from batches of aged crystals, while the ones with lower or non-distinguishable increases in THz output came from recent crystals. Our initial explanation for this phenomenon is related to the surface roughness of the organic crystals. We have observed that organic crystals degrade over time due to water absorption and/or small photochemical reactions that occur at the surface or inside the crystal. For the aged crystals with larger improvements than we would expect, we believe that the MBBA fluid fills in the gaps in the crystal due to surface roughness. The improved crystal surface reduces the scattering of the THz light upon exiting the crystal and thus increases the THz output.

To support our hypothesis that the surface roughness of the organic crystals affects the THz output, we modeled the THz output through a rough surface. Our modeling was initially inspired

by the work of Yang Yu et al.³⁶ in which they modeled the transmitted THz light ($E_o(\omega)$) through a sample with a rough surface, according to the following equation:

$$\mathbf{E}_o(\omega)_k = \mathbf{E}_i(\omega) \frac{4n(\omega)}{(1+n(\omega))^2} \langle \mathbf{exp} \left(-\frac{i\tilde{n}(\omega)\omega d(k)}{c} \right) \rangle, \quad (4-3)$$

where E_i is the incident electric field, n is the refractive index, ω is the angular frequency, \tilde{n} is the complex refractive index, $d(k)$ is the height of the surface roughness and c is the speed of light.

In their modeling, they assumed that the surface roughness is made up of multiple regions with different heights and thus included an ensemble average in Eq. 4-3, which is the term in angled brackets. The ensemble average can be simplified as follows:

$$\langle \mathbf{exp} \left(-\frac{i\tilde{n}(\omega)\omega d(k)}{c} \right) \rangle = \mathbf{exp} \left(-\frac{i\tilde{n}(\omega)\omega\mu}{c} \right) \mathbf{exp} \left(-\frac{\tilde{n}^2(\omega)\omega^2\sigma^2}{2c^2} \right) \quad (4-4)$$

Eq. 4-4 includes the mean (μ) and the standard deviation (σ) of the surface height, which are necessary to accurately model the transmission of THz light through a rough surface.

To model the THz output ($E_o(\omega)_k$), we took a similar approach in including the surface roughness; however, we also expanded their model to include multiple interfaces due the nature of our layered sandwich structures. In Fig. 4-9, the incident field ($E_i(\omega)$) completely generated towards the end of the organic crystal (yellow), and then as it exits the crystal, it traverses the region with a surface roughness represented as multiple steps of length d_k . This is followed by a layer of either air or MBBA liquid crystal layer (blue) of length l that compliments the surface roughness of the crystal. The THz then enters the polymer filter (gray) of length s and exits into air. The red dotted line represents the portion of the crystal that is considered to be smooth. On the right side of Fig. 4-9, we also show that the incident field will propagate through different thicknesses of the layers (red arrows) and transmit through the interfaces (green arrows). The three propagations of the incident field are denoted as P_1 , P_2 and P_3 , while the three transmission

coefficients are denoted as t_{12} , t_{23} and t_{3air} . In these propagation and transmission terms, the subscripts 1, 2 and 3 represent the organic crystal, the MBBA fluid or air, and the Teflon filter, respectively.

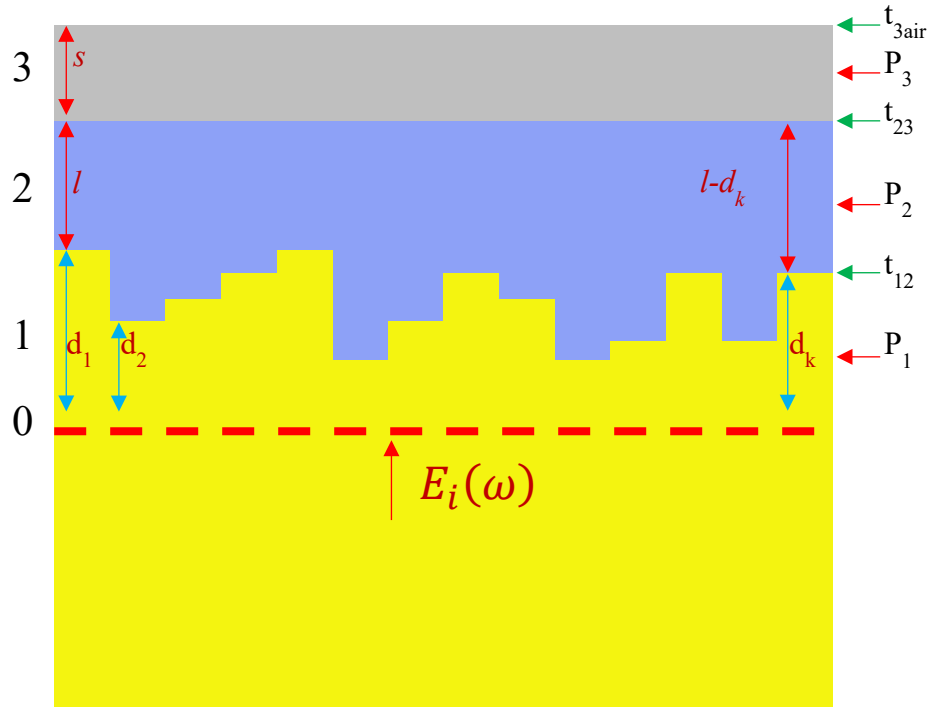


Figure 4-9. Representation of the sandwich structure used for the modeling of the THz output, $E_o(\omega)_k$. The incident field ($E_i(\omega)$) travels through (1) the organic crystal with a surface roughness represented by multiple rectangles of length d_k (yellow), (2) the liquid crystal MBBA with length l to $l - d_k$, (3) the Teflon filter (gray). At the end, the $E_i(\omega)$ exits to air. The red dotted line represents the portion of the organic crystal that is considered to be smooth. The propagation of $E_i(\omega)$ through the crystal is shown as red arrows (P_1, P_2, P_3), while the transmission is shown as green arrows (t_{12}, t_{23}, t_{3air}).

The modeled THz output light ($(E_o(\omega)_k)$), generated after going through the sandwich structure composed of multiple layers (organic crystal, MBBA fluid, Teflon, air), can be written as follows:

$$E_o(\omega)_k = E_i(\omega)t_{3air}P_3t_{23}P_2t_{12}P_1 \quad (4-5)$$

The incident field can be determined from the measured THz output from the crystal fused to sapphire, $E_{FS}(\omega)_k$, prior to becoming a sandwich structure, according to Eq. 4-6:

$$\mathbf{E}_{FS}(\omega)_k = \mathbf{E}_i(\omega) \mathbf{t}_{3air} \mathbf{t}_{23} \mathbf{t}_{12} \quad (4-6)$$

From Eq. 4-6, we solve for $E_i(\omega)$ and substitute it into Eq. 4-5 to determine the THz output of the sandwich structure. Additionally, we replace all the propagation and transmission coefficient terms in Eq. 4-5 with their respective equations to get the following expression:

$$\mathbf{E}_o(\omega)_k = \left(\frac{\mathbf{E}_{FS}(\omega)_k}{\mathbf{t}_{3air} \mathbf{t}_{23} \mathbf{t}_{12}} \right) \frac{2\tilde{n}_3}{1+\tilde{n}_3} \left(e^{\frac{-i\tilde{n}_3\omega s}{c}} \right) \frac{2\tilde{n}_2}{\tilde{n}_2+\tilde{n}_3} \left(e^{\frac{-i\tilde{n}_2\omega(l-d_k)}{c}} \right) \frac{2\tilde{n}_1}{\tilde{n}_1+\tilde{n}_2} \left(e^{\frac{-i\tilde{n}_1\omega d_k}{c}} \right) \quad (4-7)$$

In Eq. 4-7 the terms for the propagation of light through the THz crystal and the liquid crystal, P_1 and P_2 , can be combined according to the rules of exponents and an ensemble average like in Eq. 4-4 to obtain:

$$\mathbf{E}_o(\omega)_k = \left(\frac{\mathbf{E}_{Bare}(\omega)_k}{\mathbf{t}_{3air} \mathbf{t}_{23} \mathbf{t}_{12}} \right) \frac{2\tilde{n}_3}{1+\tilde{n}_3} \left(e^{\frac{-i\tilde{n}_3\omega s}{c}} \right) \frac{2\tilde{n}_2}{\tilde{n}_2+\tilde{n}_3} \frac{2\tilde{n}_1}{\tilde{n}_1+\tilde{n}_2} \left(e^{\frac{-i\omega\tilde{n}_2 l}{c}} \right) \left(e^{\frac{-i\omega(\tilde{n}_1-\tilde{n}_2)\mu_d}{c}} e^{\frac{-\omega^2(\tilde{n}_1-\tilde{n}_2)^2\sigma_d^2}{2c^2}} \right) \quad (4-8)$$

Ultimately, Eq. 4-8 models the THz output of our sandwich structure after an incident field propagates and transmits through the organic crystal, the liquid crystal MBBA, the Teflon filter and finally exits to air before being detected. Similar to Eq. 4-4 that was used in Ref 31, our Eq. 4-8 also includes μ_d and σ_d , which are the average and standard deviation of the surface roughness of the organic crystal, respectively. We can also use Eq. 4-8 to model what the THz output would look like for the organic crystal fused to sapphire, which is needed in order to model the normalized THz intensity ratio between the sandwich structure and the crystal fused to sapphire, according to Eq. 4-2. This was simply done by replacing the refractive index of the liquid crystal MBBA, \tilde{n}_2 , by that of air. The benefit of using Eq. 4-8 for modeling the normalized THz intensity ratio, is that we can model this ratio as a function of the standard deviation, σ_d , since it can be considered as a measure of the crystal's roughness. Modeling in this way, allowed us to determine an optimal roughness that works to model our data. The normalized modeled THz intensity ratio can be seen in Fig. 4-8 as red dotted lines. From Fig. 4-8, we can see that there is good agreement between the

data and the model for NMBA-A, which is an aged crystal, after determining a value of $17.7 \mu\text{m}$ for the surface roughness. However, due to the THz output improvement being small on NMBA-B, which is a recent crystal, the surface roughness was too small to determine and so for the model we assumed a perfect smoothness by setting σ_d equal to zero. Nonetheless, we can observe that the error bars for the sandwich structure THz output data for NMBA-B lie within our model. This modeling was also applied to all the other NMBA, BNA and MNA crystals. Their THz output efficiency along with the model and their determined surface roughness, σ_d , can be found in Figs. 4-11 to 4-13 in the Appendix section.

To summarize the results of the THz output efficiency measurements, the THz output increases when the yellow organic crystals, NMBA, BNA and MNA, fused to sapphire are converted into sandwich structures. In theory, this should be possible because the index-matching fluid MBBA has a refractive index between the yellow organic crystals and the Teflon filter, and thus Fresnel reflection losses are reduced. Our data shows that on average the THz output efficiency increases for each crystal; however, interesting results were observed when looking at each crystal individually. The crystals that came from aged batches had a significant THz output improvement, while the ones that came from recent batches had small or non-distinguishable improvement. The large improvement in aged crystals can be explained by understanding that over time, the surface roughness of the organic crystals increases and inclusion into a layered structure significantly reduces the Fresnel reflection losses from the rougher surfaces. To further support this, we included the effects of surface roughness into the modeled THz output efficiency and observed good agreement between the data and the model. In principle, all crystals should improve when being made into a sandwich structure; however, the recent crystals showed low or no improvement at all. Due to the recent crystals being measured almost immediately after their

creation, the surface of the crystals was smooth and thus they did not have strong losses due to Fresnel reflections. This final observation made us consider whether inclusion of our crystals into a layered structure would not only enhance THz output by minimizing Fresnel losses but also increase the robustness of the crystal toward degradation and THz intensity loss over time. Thus, we quantified the crystal stability over time for our layered structures.

4.3.3 Longevity of Sandwich Structures

To study the performance of these sandwich structure over time, we took one sandwich structure of an NMBA, BNA and MNA and measured its THz electric field according to the setup shown in Fig. 4-4b. Due to having a high availability of NMBA and BNA crystals, we were able to measure their electric field for a longer period of time (~470 days) compared to MNA (~180 days). Fig. 4-10 shows the measured electric field, according to Eq. 4-1, as a function of time in days for a sandwich structure of (a) NMBA, (b) BNA and (c) MNA. In some of the days, we performed multiple measurements and results were averaged, which are shown with error bars in Fig. 4-10 (for more details on the longevity measurements see Fig. 4-14 in the Appendix section.

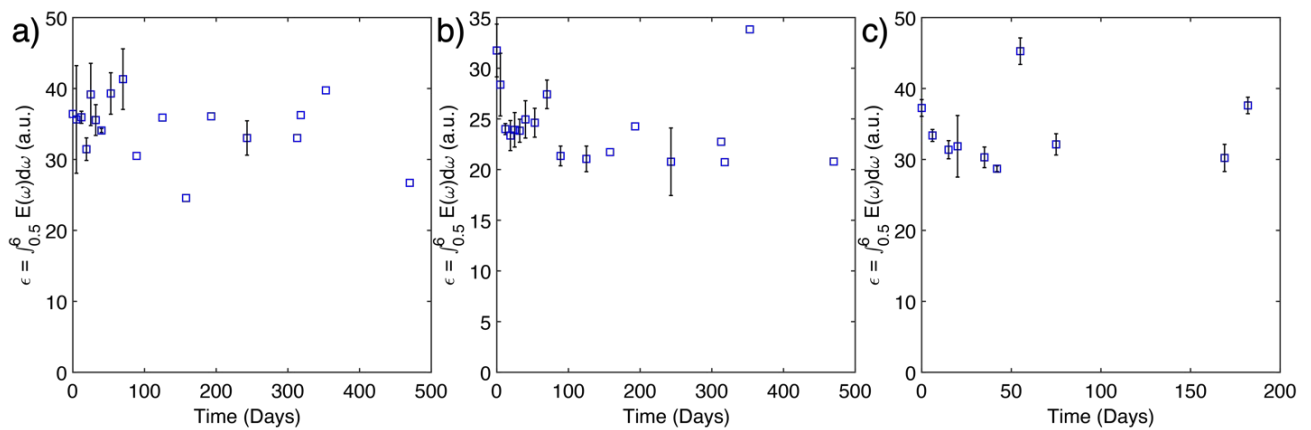


Figure 4-10. The THz electric field as a function of time in days for one sandwich structure for (a) NMBA, (b) BNA and (c) MNA. Some data points are averages of multiple measurements and have error bars.

In Fig. 4-10, we can see that the electric field amplitude is fairly consistent for all sandwich structures (NMBA and BNA structures after >400 days and the MNA structure after >150 days). The few outlier points in our data could result from laser power fluctuations as well as aligning the measurement on a damaged region of the GaP detection crystal. This shows that the crystals do not degrade in the layered structure, and may even receive extra protection from the environment compared to exposed crystals.

4.4 Conclusion

In conclusion, we show that the THz output generation of yellow organic crystals BNA, NMBA and MNA, can be improved in two different ways. First, fusing an organic crystal to a sapphire plate by our partial melting process helps increase the damage threshold of the crystal. This fusing allows the crystal to withstand higher laser fluences because the sapphire plate dissipates the heat, which in turn leads to greater THz light output. Second, assembling the sapphire-fused crystals into layered structures with a refractive index-matching fluid improves in THz generation because Fresnel reflections are reduced. The THz output efficiency of the organic crystal with high surface roughness (aged crystals) is improved dramatically when made into a sandwich structure and inclusion into a layered structure protects the crystal surface from degradation.

Our studies show that the THz output from these sandwich structures is stable over long periods of time. These results provide new methods for enhancing the THz output of many common organic crystals, and for improving their robustness and lifetimes under irradiation.

4.5 Appendix

We measured the THz output for six NMBA crystals fused to sapphire before and after being assembled into a sandwich structure. As mentioned above, we determined the THz intensity for all the NMBA sandwich structures and normalized them with respect to the sapphire-fused crystals (see Eq. 4-2). In Fig. 4-11, we show the normalized THz output for all six NMBA sandwich structures.

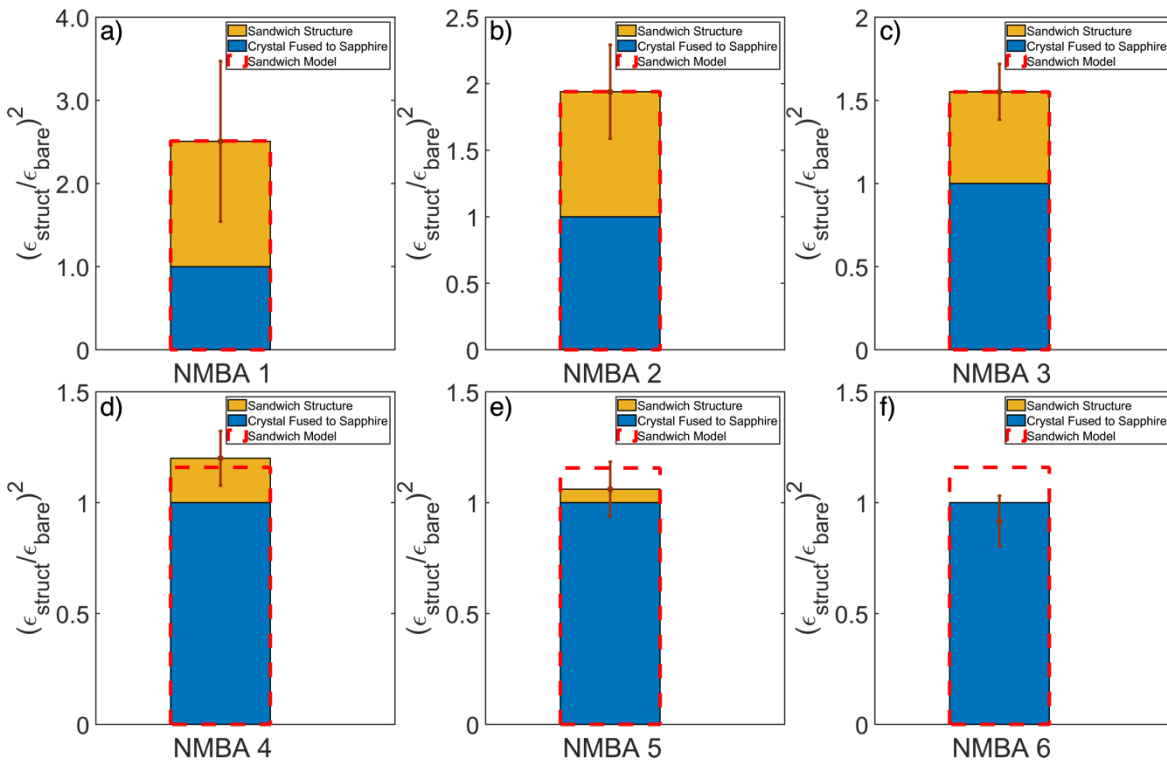


Figure 4-11. The normalized ratio of the THz output intensity of the sandwich structures (yellow bar) compared to the sapphire-fused crystal (blue bar) for six NMBA samples. NMBA samples 1-3 (a-c) came from batches of aged crystals, while NMBA samples 4-6 (d-f) came from batches of recent crystals. The error bars for the sandwich structures are shown in brown. The red dotted line is the modeled normalized ratio of the THz intensity for the sandwich structure. For NMBA crystals a-c, the surface roughness (σ_d) was determined to be 24.5, 17.7 and 12.8 μm ; however, the surface roughness for the model of NMBA samples d-f was set to zero because these crystals were assumed to have a smooth surface due to coming from recently made crystal batches.

The normalized THz output intensities of the sandwich structures are shown as yellow bars with their respective error bars in brown and the normalized THz intensities for the sapphire-fused

crystals are shown as blue bars. In Fig. 4-11, the NMBA crystals 1-3 (a-c) in the sandwich structures were from “aged” batches while the NMBA crystals 4-6 (d-f) were from “recent” batches. The modeled normalized THz output intensities for the sandwich structures, according to the modeling explained in section 4.3.2, are shown as red dotted lines. For the aged NMBA crystals 1, 2 and 3, the surface roughness (σ_d) for the model was determined to be 24.5, 17.7 and 12.8 μm , respectively. In the case of the recently made NMBA crystals (4-6), the normalized THz output intensity model assumed a smooth surface by setting the surface roughness to zero. It can be noticed that the THz output for the recently made samples is significantly lower when compared to that of the aged crystals. In fact, NMBA 6 shows no distinguishable increase but the error bar does suggest there is a small increase. Additionally, Fig. 4-8 shows a comparison between NMBA-A and NMBA-B, which are labeled as NMBA 2 and NMBA 4 in the Appendix section, respectively.

We also determined the normalized THz output intensity for all BNA samples, as seen in Fig. 4-12. In Fig. 4-12, we show the normalized THz output intensities of the sandwich structures as yellow bars with their respective error bars in brown and the normalized THz intensities for the sapphire-fused crystals as blue bars. Fig. 4-12 shows this information for aged (a-c) and recent (d-f) BNA crystals. The modeled normalized THz output intensities are shown as red dotted lines. For the aged BNA crystals 1-3, the surface roughness was determined to be 15.2, 12.7 and 5.5 μm , respectively. However, for the recently made BNA samples 4-6, the model assumed a smooth surface. From Fig. 4-12, we can see that there is no increase in THz output from the recently made crystals; however, the error bars for BNA 4 and 6 do suggest that there is a small increase. BNA 5 seems to perform worse as a sandwich structure. This could be explained due to difficulty of aligning the sandwich structure for efficient THz generation combined with the fact that recently

made crystals are more likely to have smooth surfaces and thus have a lower increase in THz generation when made into sandwich structures.

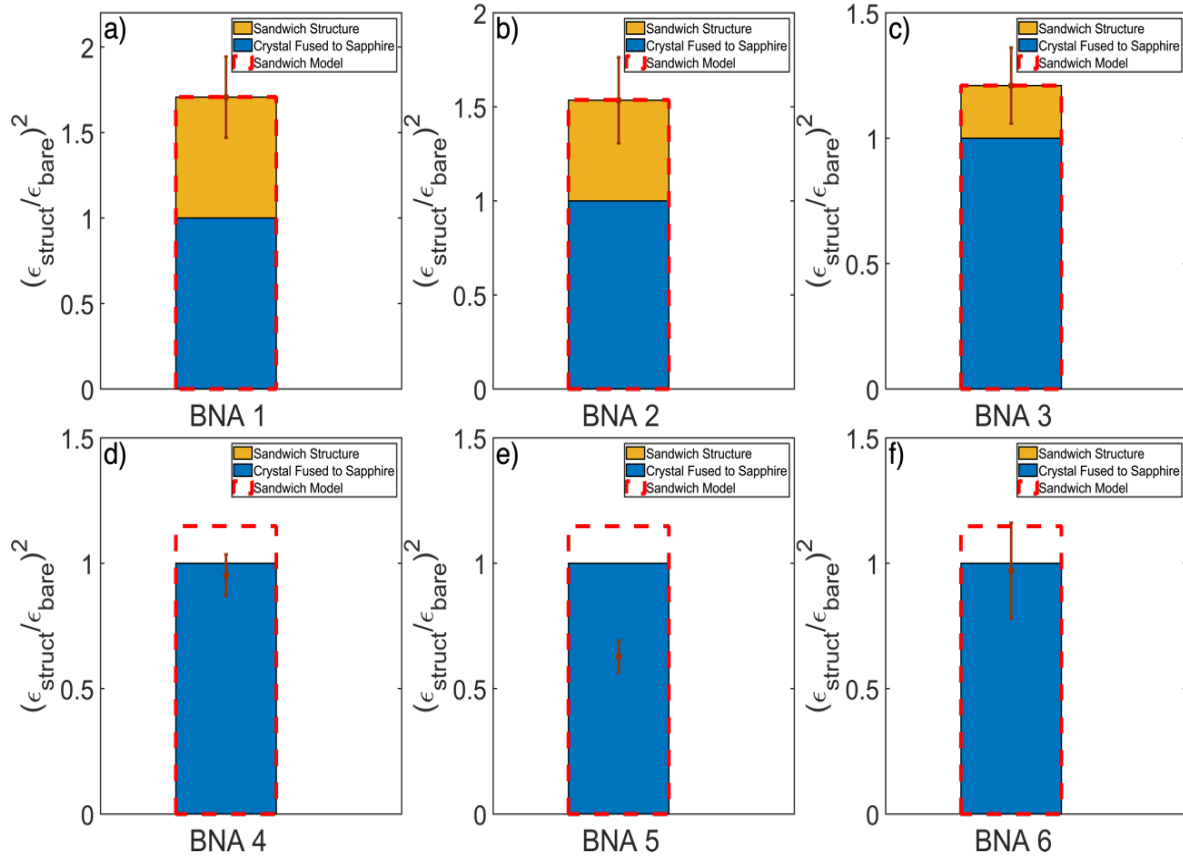


Figure 4-12. The normalized ratio of the THz output intensity of the sandwich structures (yellow bar) compared to the sapphire-fused crystals (blue bar) for six BNA samples. BNA samples 1-3 (a-c) came from batches of aged crystals, while BNA samples 4-6 (d-f) came from batches of recent crystals. The error bars for the sandwich structures are shown in brown. The red dotted line is the modeled normalized THz intensity of the sandwich structure. For the recently made BNA crystals a-c the surface roughness was determined to be 15.2, 12.7 and 5.5 μm , respectively. The surface roughness for the model of BNA samples d-f was set to zero because these crystals were assumed to have a smooth surface due to coming from recently made crystal batches.

Lastly, Fig. 4-13 shows the normalized THz output intensity for all of the MNA samples (1-3), which came from recently made crystal batches. In Fig. 4-13, we show the normalized THz output intensities of the sandwich structures as yellow bars with their respective error bars in brown and the normalized THz intensities for the sapphire-fused crystals as blue bars. The normalized

THz output intensities for the model assumed a smooth surface due to all the MNA crystals coming from recently made batches and the models are shown as red dotted lines.

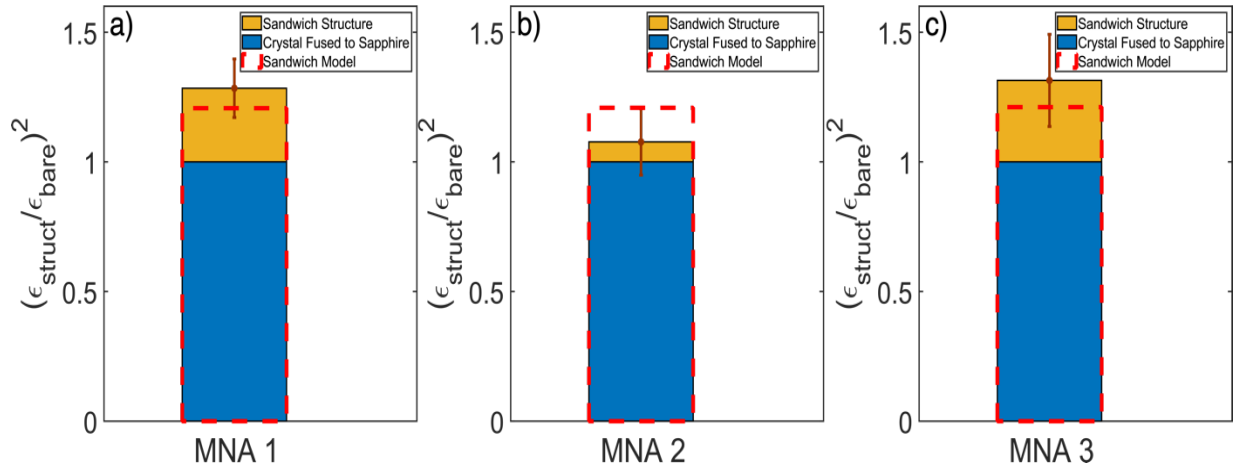


Figure 4-13. The normalized THz output intensity of the sandwich structures (yellow bar) compared to the sapphire-fused crystals (blue bar) for three MNA samples. All MNA samples came from recently made crystal batches. The error bars for the sandwich structures are shown in brown. The red dotted line is the modeled normalized THz intensity of the sandwich structure. The surface roughness (σ_d) for the model of all MNA samples was set to zero because these crystals were assumed to have a smooth surface due to all of them coming from recently made crystal batches.

Measurements to test the longevity of our sandwich structures were performed over long periods of time. In Fig. 4-14, we show the electric field (see Eq. 4-1) of three individual sandwich structures as function of time in days: (a) NMBA, (b) BNA and (c) MNA. At the beginning of these measurements (mostly NMBA and BNA), we measured electric field of the sandwich structures two to three times and in some cases four times to make sure we were consistent. After some time, due to the tedious nature of aligning the sandwich structures for optimal THz generation measurements, we decided to only perform single measurements for BNA and NMBA. This figure is exactly the same as Fig. 4-10 with the difference that the markers in the legend of Fig. 4-14 indicate the number of measurements of the data for each crystal.

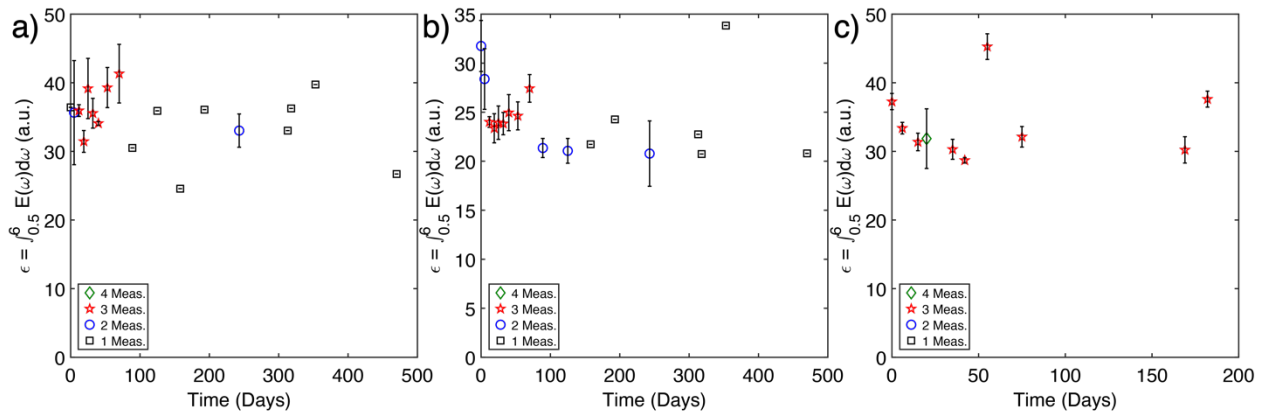


Figure 4-14. The THz electric field as a function of time in days for one sandwich structure for (a) NMBA, (b) BNA and (c) MNA. The number of measurements for each data point varied and are listed in the legend as: one (black square), two (blue circle), three (red star) and four (green diamond).

4.6 References

1. M. A. Brun, F. Formanek, A. Yasuda, M. Sekine, N. Ando, and Y. Eishii, “Terahertz imaging applied to cancer diagnosis,” *Phys Med Biol* **55**, 4615-4623 (2010).
2. D. Chakraborty, B. N. Mills, J. Cheng, I. Komissarov, S. A. Gerber, and R. Sobolewski, “Development of Terahertz Imaging Markers for Pancreatic Ductal Adenocarcinoma using Maximum A Posteriori Probability (MAP) Estimation,” *ACS Omega* **8**, 9925-9933 (2023).
3. H.-B. Liu, Y. Chen, G. J. Bastiaans, and X. C. Zhang, “Detection and identification of explosive RDX by THz diffuse reflection spectroscopy,” *Optics Express* **14**, 415-423 (2006).
4. M. E. Granger, A. Urrea, D. T. Arnold, A. B. Hoopes, and J. A. Johnson, “Combining Spectral Amplitude and Phase Improves Terahertz Hyperspectral Imaging,” *ACS Photonics* **11**, 745-751 (2024).
5. R. Mankowsky, A. von Hoegen, M. Först, and A. Cavalleri, “Ultrafast Reversal of the Ferroelectric Polarization,” *Physical Review Letters* **118**, 197601 (2017).

6. M. Kozina, M. Fechner, P. Marsik, T. van Driel, J. M. Glowonia, C. Bernhard, M. Radovic, D. Zhu, S. Bonetti, U. Staub, and M. C. Hoffmann, "Terahertz-driven phonon upconversion in SrTiO₃," *Nature Physics* **15**, 387-392 (2019).
7. D. M. Juraschek, and S. F. Maehrlein, "Sum-frequency ionic Raman scattering," *Physical Review B* **97**, 174302 (2018).
8. C. L. Johnson, B. E. Knighton, and J. A. Johnson, "Distinguishing Nonlinear Terahertz Excitation Pathways with Two-Dimensional Spectroscopy," *Physical Review Letters* **122**, 073901 (2019).
9. D. M. Juraschek, P. Narang, and N. A. Spaldin, "Phono-magnetic analogs to opto-magnetic effects," *Physical Review Research* **2**, 043035 (2020).
10. T. F. Nova, A. Cartella, A. Cantaluppi, M. Först, D. Bossini, R. V. Mikhaylovskiy, A. V. Kimel, R. Merlin, and A. Cavalleri, "An effective magnetic field from optically driven phonons," *Nature Physics* **13**, 132-136 (2017).
11. Y.-L. Li, D. Zhang, M. Luo, Q.-H. Yang, F. Fan, S.-J. Chang, and Q.-Y. Wen, "Terahertz magneto-optical response of bismuth-gadolinium-substituted rare-earth garnet film," *Optics Express* **29**, 23540-23548 (2021).
12. P. Chen, M. Hosseini, and A. Babakhani. An Integrated Germanium-Based THz Impulse Radiator with an Optical Waveguide Coupled Photoconductive Switch in Silicon. In *Micromachines*, 2019; Vol. 10.
13. A. Pagies, G. Ducournau, and J. F. Lampin, "Low-threshold terahertz molecular laser optically pumped by a quantum cascade laser," *APL Photonics* **1**, 031302 (2016).
14. S. Jung, J. H. Kim, Y. Jiang, K. Vijayaraghavan, and M. A. Belkin, "Terahertz difference-frequency quantum cascade laser sources on silicon," *Optica* **4**, 38-43 (2017).

15. U. Senica, A. Forrer, T. Olariu, P. Micheletti, S. Cibella, G. Torrioli, M. Beck, J. Faist, and G. Scalari, "Planarized THz quantum cascade lasers for broadband coherent photonics," *Light: Science & Applications* **11**, 347 (2022).
16. W. Sun, X. Wang, and Y. Zhang, "Terahertz generation from laser-induced plasma," *Opto-Electronic Science* **1**, 220003-220001-220003-220027 (2022).
17. S. A. Sorenson, C. D. Moss, S. K. Kauwe, J. D. Bagley, and J. A. Johnson, "Enhancing terahertz generation from a two-color plasma using optical parametric amplifier waste light," *Applied Physics Letters* **114**, (2019).
18. J. D. Bagley, C. D. Moss, S. A. Sorenson, and J. A. Johnson, "Laser-induced plasma generation of terahertz radiation using three incommensurate wavelengths," *Journal of Physics B: Atomic, Molecular and Optical Physics* **51**, 144004 (2018).
19. K. L. Yeh, M. C. Hoffmann, J. Hebling, and K. A. Nelson, "Generation of 10 μ J ultrashort terahertz pulses by optical rectification," *Applied Physics Letters* **90**, 171121 (2007).
20. G. Polónyi, B. Monoszlai, G. Gäumann, E. J. Rohwer, G. Andriukaitis, T. Balciunas, A. Pugzlys, A. Baltuska, T. Feurer, J. Hebling, and J. A. Fülöp, "High-energy terahertz pulses from semiconductors pumped beyond the three-photon absorption edge," *Optics Express* **24**, 23872-23882 (2016).
21. J. A. Fülöp, G. Polónyi, B. Monoszlai, G. Andriukaitis, T. Balciunas, A. Pugzlys, G. Arthur, A. Baltuska, and J. Hebling, "Highly efficient scalable monolithic semiconductor terahertz pulse source," *Optica* **3**, 1075-1078 (2016).
22. N. Hekmat, T. Vogel, Y. Wang, S. Mansourzadeh, F. Aslani, A. Omar, M. Hoffmann, F. Meyer, and C. J. Saraceno, "Cryogenically cooled GaP for optical rectification at high excitation average powers," *Optical Materials Express* **10**, 2768-2782 (2020).

23. G. A. Valdivia-Berroeta, Z. B. Zaccardi, S. K. F. Pettit, S.-H. Ho, B. W. Palmer, M. J. Lutz, C. Rader, B. P. Hunter, N. K. Green, C. Barlow, C. Z. Wayment, D. J. Ludlow, P. Petersen, S. J. Smith, D. J. Michaelis, and J. A. Johnson, "Data Mining for Terahertz Generation Crystals," *Advanced Materials* **34**, 2107900 (2022).
24. C. Rader, Z. B. Zaccardi, S.-H. E. Ho, K. G. Harrell, P. K. Petersen, M. F. Nielson, H. Stephan, N. K. Green, D. J. H. Ludlow, M. J. Lutz, S. J. Smith, D. J. Michaelis, and J. A. Johnson, "A New Standard in High-Field Terahertz Generation: the Organic Nonlinear Optical Crystal PNPA," *ACS Photonics* **9**, 3720-3726 (2022).
25. O. P. Kwon, S.-J. Kwon, M. Jazbinsek, F. D. J. Brunner, J.-I. Seo, C. Hunziker, A. Schneider, H. Yun, Y.-S. Lee, and P. Günter, "Organic Phenolic Configurationally Locked Polyene Single Crystals for Electro-optic and Terahertz Wave Applications," *Advanced Functional Materials* **18**, 3242-3250 (2008).
26. G. A. Valdivia-Berroeta, L. K. Heki, E. A. McMurray, L. A. Foote, S. H. Nazari, L. Y. Serafin, S. J. Smith, D. J. Michaelis, and J. A. Johnson, "Alkynyl Pyridinium Crystals for Terahertz Generation," *Advanced Optical Materials* **6**, 1800383 (2018).
27. M. C. Hoffmann, and J. A. Fülöp, "Intense ultrashort terahertz pulses: generation and applications," *Journal of Physics D: Applied Physics* **44**, 083001 (2011).
28. B. Monozslai, C. Vicario, M. Jazbinsek, and C. P. Hauri, "High-energy terahertz pulses from organic crystals: DAST and DSTMS pumped at Ti:sapphire wavelength," *Optics Letters* **38**, 5106-5109 (2013).
29. P. D. Cunningham, and L. M. Hayden, "Optical properties of DAST in the THz range," *Optics Express* **18**, 23620-23625 (2010).

30. F. D. J. Brunner, O. P. Kwon, S.-J. Kwon, M. Jazbinšek, A. Schneider, and P. Günter, “A hydrogen-bonded organic nonlinear optical crystal for high-efficiency terahertz generation and detection,” *Optics Express* **16**, 16496-16508 (2008).
31. I. C. Tangen, G. A. Valdivia-Berroeta, L. K. Heki, Z. B. Zaccardi, E. W. Jackson, C. B. Bahr, S.-H. Ho, D. J. Michaelis, and J. A. Johnson, “Comprehensive characterization of terahertz generation with the organic crystal BNA,” *Journal of the Optical Society of America B* **38**, 2780-2785 (2021).
32. M. Shalaby, C. Vicario, K. Thirupugalmani, S. Brahadeeswaran, and C. P. Hauri, “Intense THz source based on BNA organic crystal pumped at Ti:sapphire wavelength,” *Optics Letters* **41**, 1777-1780 (2016).
33. B. W. H. Palmer, C. Rader, E. S.-H. Ho, Z. B. Zaccardi, D. J. Ludlow, N. K. Green, M. J. Lutz, A. Alejandro, M. F. Nielson, G. A. Valdivia-Berroeta, C. C. Chartrand, K. M. Holland, S. J. Smith, J. A. Johnson, and D. J. Michaelis, “Large Crystal Growth and THz Generation Properties of 2-Amino-5-Nitrotoluene (MNA),” *ACS Applied Electronic Materials* **4**, 4316-4321 (2022).
34. Z. B. Zaccardi, I. C. Tangen, G. A. Valdivia-Berroeta, C. B. Bahr, K. C. Kenney, C. Rader, M. J. Lutz, B. P. Hunter, D. J. Michaelis, and J. A. Johnson, “Enabling high-power, broadband THz generation with 800-nm pump wavelength,” *Optics Express* **29**, 38084-38094 (2021).
35. C. B. Bahr, N. K. Green, L. K. Heki, E. McMurray, I. C. Tangen, G. A. Valdivia-Berroeta, E. W. Jackson, D. J. Michaelis, and J. A. Johnson, “Heterogeneous layered structures for improved terahertz generation,” *Optics Letters* **45**, 2054-2057 (2020).
36. Y. Yu, Z. Zhang, T. Zhang, X. Zhao, Y. Chen, C. Cao, Y. Li, and K. Xu, “Effects of surface roughness on terahertz transmission spectra,” *Optical and Quantum Electronics* **52**, 240 (2020).

CHAPTER 5: Characterization of Organic Crystals for Second Harmonic Generation

Adapted from K. M. Holland, A. Alejandro, D. J. H. Ludlow, P. K. Petersen, M. A. Wright, C. C. Chartrand, D. J. Michaelis, J. A. Johnson, and J. E. Patterson, *Opt. Lett.* **48**, 5855-5858 (2023)

I hereby confirm that the use of this article is compliant with all publishing agreements.

5.1 Abstract

Second harmonic generation (SHG) is a common technique with many applications. Common inorganic single-crystalline materials used to produce SHG light are effective using short IR/visible wavelengths but generally do not perform well at longer, technologically relevant IR wavelengths such as 1300, 1550 and 2000 nm. Efficient SHG materials possess many of the same key material properties as terahertz (THz) generators, and certain single-crystalline organic THz generation materials have been reported to perform at longer IR wavelengths. Consequently, this work focuses on characterizing three efficient organic THz generators for SHG, namely DAST (trans-4-[4-(dimethylamino)-N-methylstilbazolium] p-tosylate), DSTMS (4-N,N-dimethylamino-4'-N'-methyl-stilbazolium 2,4,6-trimethylbenzenesulfonate), and the recently discovered generator PNPA ((E)-4-((4-nitrobenzylidene)amino)-N-phenylaniline). All three of these crystals outperform beta-barium borate (BBO), an inorganic material commonly used for SHG, using IR pump wavelengths (1200–2000 nm).

5.2 Introduction

Nonlinear optical (NLO) processes, including second harmonic generation (SHG), are central to modern laser technology. SHG is a phenomenon that occurs when two photons from a single laser beam interact within a NLO material to produce one photon containing double the energy of each initial photon. Most materials cannot produce SHG in the bulk, but materials that are capable of SHG are valuable because they enable access to new wavelengths of light. In addition to doubling the fundamental wavelength, as with Nd:YAG lasers, many modern laser systems contain a SHG material as part of the optical parametric oscillators or amplifiers to generate tunable wavelengths. SHG materials used in industry are most commonly inorganic materials with noncentrosymmetric structures, such as beta-barium borate (BBO).¹⁻³ BBO crystals have largely been used to generate new SHG wavelengths in the UV-Vis region using incident wavelengths of 1030 nm,⁴ 800 nm,^{5,6} 626 nm,⁷ and 532 nm.^{3,8} Other nonlinear optical inorganic crystals commonly used to generate second-harmonic light include lithium triborate (LBO),⁹⁻¹¹ potassium dideuterium phosphate (KDP),^{12,13} potassium titanyl phosphate (KTP),^{10,14} and cesium lithium borate (CLBO).^{15,16} These inorganic crystals are efficient generators in the visible and near IR region, but poorly generate SH light from longer IR incident wavelengths (1200-2000 nm).¹⁷⁻²¹ Effective SHG materials that generate at 1300, 1550 and 2000 nm could be very beneficial because new, increasingly common industrial lasers operate at these wavelengths. Accessing shorter visible and near-infrared wavelengths through SHG could enhance imaging and other applications where use of infrared light has detection limitations. Therefore, there is significant value in identifying and evaluating materials that could efficiently produce SHG at incident wavelengths >1000 nm.

In the range of pump wavelengths between 1200-2000 nm, various single-crystalline NLO organic materials are used to generate terahertz (THz) frequency light via optical rectification.²² Although there can be challenges in crystallizing noncentrosymmetric organic generators, they can be optimized by fine tuning the structure of the molecular building blocks. Consequently, we hypothesized that these organic crystals could also serve as powerful alternatives to their inorganic counterparts for second harmonic generation with longer input wavelengths. In addition, some organic crystals have already been used for SHG and THz generation, such as kainate crystals with incident wavelengths of 1000–1500 nm.²³ In this work, we study and compare known organic terahertz generators for their ability to efficiently produce SHG with input wavelengths from 1200-2000 nm.

SHG results from an induced second-harmonic dipole per unit volume, $P^{(2)}$, which depends on the incident electric field $E(\omega)$ and the material's nonlinear susceptibility, $\chi^{(2)}$ (Eq. 5-1).²⁴

$$P^{(2)}(2\omega) = \chi^{(2)} E(\omega)E(\omega) \quad (5-1)$$

The magnitude of the nonlinear susceptibility, $\chi^{(2)}$, is also responsible for an organic material's ability to generate THz light.²⁴⁻²⁶ The value of $\chi^{(2)}$ for any material is determined by certain key properties, including noncentrosymmetric crystal packing, number density and molecular hyperpolarizability.²⁷⁻²⁹ Compared to inorganic materials, the molecular hyperpolarizability is greater for organic molecules with long conjugated π systems. Similar to THz generators,³⁰⁻³² effective SHG materials must also be robust, single crystalline, transparent for all relevant wavelengths, and noncentrosymmetric to efficiently generate SH light; they must also exhibit proper phase matching.³³ In recent years, many novel single-crystalline organic materials have been developed as efficient THz generators.³⁰ Thus, these new materials

developed for THz generation research may provide alternative and more efficient materials for SHG.

5.3 Methods

We studied seven known THz generation materials and explored their potential to also produce SHG. Specifically, MNA, BNA, NMBA, ZPAN, DAST, DSTMS, and PNPA^{30, 34-37} were tested for SHG efficiency. The latter three crystals, *trans*-4-[4-(dimethylamino)-*N*-methylstilbazolium] *p*-tosylate (DAST), 4-*N,N*-dimethylamino-4'-*N'*-methyl-stilbazolium 2,4,6-trimethylbenzenesulfonate (DSTMS), and (E)-4-((4-nitrobenzylidene)amino)-*N*-phenylaniline (PNPA), were found to be more efficient than BBO, a common industry standard. (See Fig. 5-5 in the Appendix section for unit cells of each crystal.) For example, in the wavelength range of 1200-2000 nm, DSTMS converted up to 19.2% of the incident light to second-harmonic frequency light, whereas BBO only reached a 3.1% efficiency.

Measurements were performed with a Ti:sapphire laser with a 1 kHz repetition rate and a pulse duration of ~100 fs. The Ti:sapphire laser was used to pump an optical parametric amplifier (OPA) to generate near-IR pulses. A wavelength separator was then used to separate the IR light into both signal (1200-1550 nm) and idler (1800-2000 nm) wavelengths with a $1/e^2$ beam diameter of 7.6 mm. For our measurements, the signal light from the wavelength separator was vertically polarized. For the idler beam, a half-waveplate was used to rotate the beam to have the same vertical polarization as the signal beam (Fig. 5-1). The organic crystals were aligned to have their polar axis parallel to the polarization of the incident light, as is done for THz generation. A neutral density (ND) filter was used to adjust the incoming laser power to the power meter (Gentec-EO). Laser power was measured before and after the SHG crystal to

calculate the incoming fluence and the output fluence produced from the SHG crystal. Short-pass filters were used to prevent transmission of the incident signal or idler light and to allow transmission of the newly generated SHG light. The generated SHG power was averaged over 10 seconds and recorded.

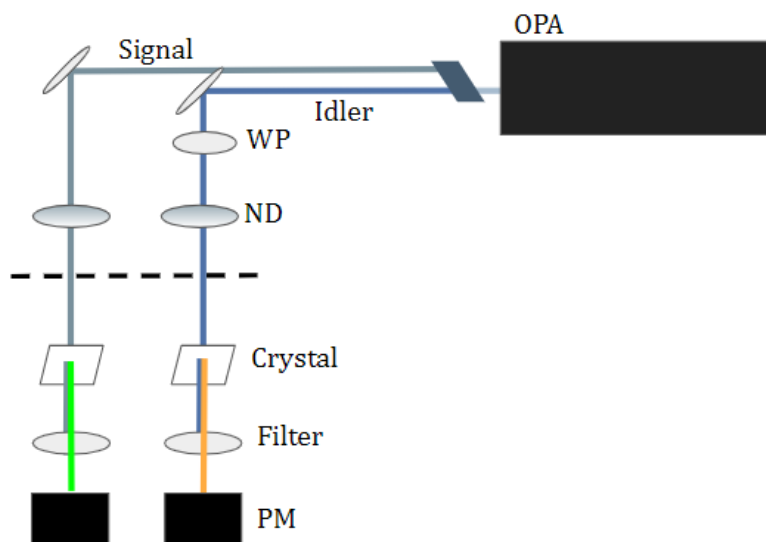


Figure 5-1: Schematic of the SHG experimental setup. The OPA produces signal and idler beams of 1200–1550 nm and 1800–2000 nm, respectively. The idler beam passes through a half-waveplate (WP) to rotate polarization. A variable neutral density (ND) filter controls the power. The dashed line indicates the position of the power meter to measure incident power. The incident background light is removed from the path via a short pass filter. The generated SH light is measured by the power meter (PM).

For our SHG studies, single crystals of MNA, BNA, NMBA, ZPAN, DAST, DSTMS, and PNPA were selected for testing. The crystals were mounted on apertures with a 5 mm diameter hole to ensure consistency between measurements; the crystals had lateral dimensions greater than 5 mm x 5 mm to ensure that the crystal covered the entire aperture. An initial screening was performed using crystals with thicknesses of 480–860 μm . (See Table 5-1 in the Appendix section for the thicknesses of all DSTMS, PNPA and DAST crystals.) We first tested five samples of each crystal with an incident energy of $\sim 400 \mu\text{J}$ (corresponding fluence of $\sim 0.88 \text{ mJ}/\text{cm}^2$) at 1200–1550 nm. MNA, BNA, NMBA, and ZPAN generated at less than $\sim 5\%$ at this

range of wavelengths, as shown in Figs. 5-6 and 5-7 in the Appendix section. PNPA, DAST, and DSTMS, however, were all significantly more efficient than the industry standard, BBO, with DSTMS being the most efficient.

To help us understand the wavelengths at which these organic materials can operate effectively as SHG crystals, transmission spectra of the three most efficient SHG crystals (DAST, DSTMS, and PNPA) and a reference inorganic crystal, BBO (cut at $\theta = 19.8^\circ$ for SHG at 1550 nm, 5x5x0.1 mm), were collected using a v-770 Jasco UV-VIS spectrometer. A polarizer was placed in the beam path to obtain spectra of the crystals with the THz generation axis of the organic crystals perpendicular (off-axis) and parallel (on-axis) to the polarization of the light (Fig. 5-2). For the organic crystals, the transmission is generally lower when light is polarized along the generation axis, due to the stronger interaction with the incident light. For BBO, its orientation did not affect the transmission as seen with the overlapping spectra, likely due to the uniaxial nature of the material.

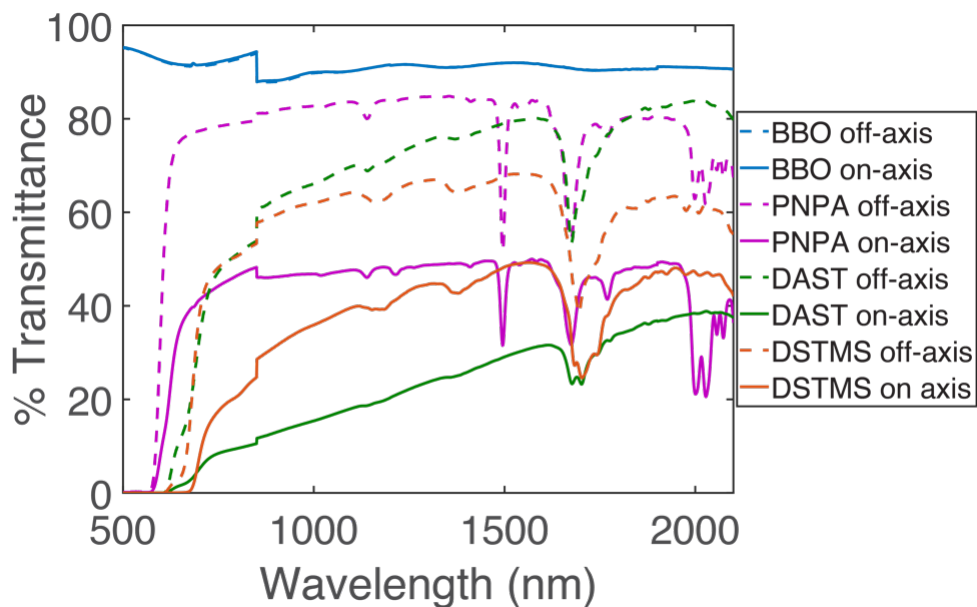


Figure 5-2: Transmission spectra of SHG crystals with their THz generation axis (for the organic crystals) perpendicular (dotted lines) and parallel (solid lines) to the polarization of the light: BBO (blue), DAST (green), PNPA (purple) and DSTMS (orange). The jump at 850 nm is an instrumental artifact.

Due to the restricted availability of short-pass filters for certain wavelength ranges, we could evaluate only part of the possible OPA signal and idler wavelength ranges (see Fig. 5-8 in the Appendix section). We irradiated NLO crystals using 1200-1550 nm and 1800-2000 nm light, and the corresponding emission was collected for wavelengths between 600-725 nm and 900-1000 nm. A spectrometer was used to confirm the SHG wavelengths (see Fig. 5-9 in the Appendix section).

To characterize the SHG of each crystal, we performed wavelength and fluence dependence measurements. During the wavelength dependence measurements, the pulse energy was set to $\sim 400 \mu\text{J}$ ($\sim 0.88 \text{ mJ/cm}^2$) and $\sim 300 \mu\text{J}$ ($\sim 0.66 \text{ mJ/cm}^2$) for both signal and idler beams, respectively. The fluence dependence measurements were performed at 1450 nm and 2000 nm for both signal and idler beams, respectively. To determine the SHG efficiency, the power of both the incident and the generated SH light from the NLO crystal were measured. It was observed that the organic crystals would most efficiently produce SHG if the incident light interacted parallel to the crystal's THz generation axis, as in THz generation experiments. Note that the organic crystals have type 0 phase matching with incident and generated light both having vertical polarization, whereas BBO has type I phase matching. To calculate the SHG efficiency (ϵ) of the crystals (see Eq. 5-2), the sample power measurement (I_s) was divided by the % transmission of the short-pass filter at the newly generated wavelength (f_g) (see Fig. 5-8 from the Appendix section). The background was found by multiplying the incident power (I_0) by the % transmission of the short-pass filter at the original incident wavelength (f_i). The sample power quotient was then subtracted by the background and the difference was divided by the original incident power.

$$\epsilon = \frac{I_s/f_g - I_0*f_i}{I_0} \quad (5-2)$$

5.4 Results and Discussion

We measured the fluence dependence of each of the three high performing crystal types and BBO with an incident wavelengths of 1450 nm and 2000 nm for the signal and idler beams, respectively (Fig. 5-3; see Fig. 5-10 from the Appendix section for details on individual measurements).

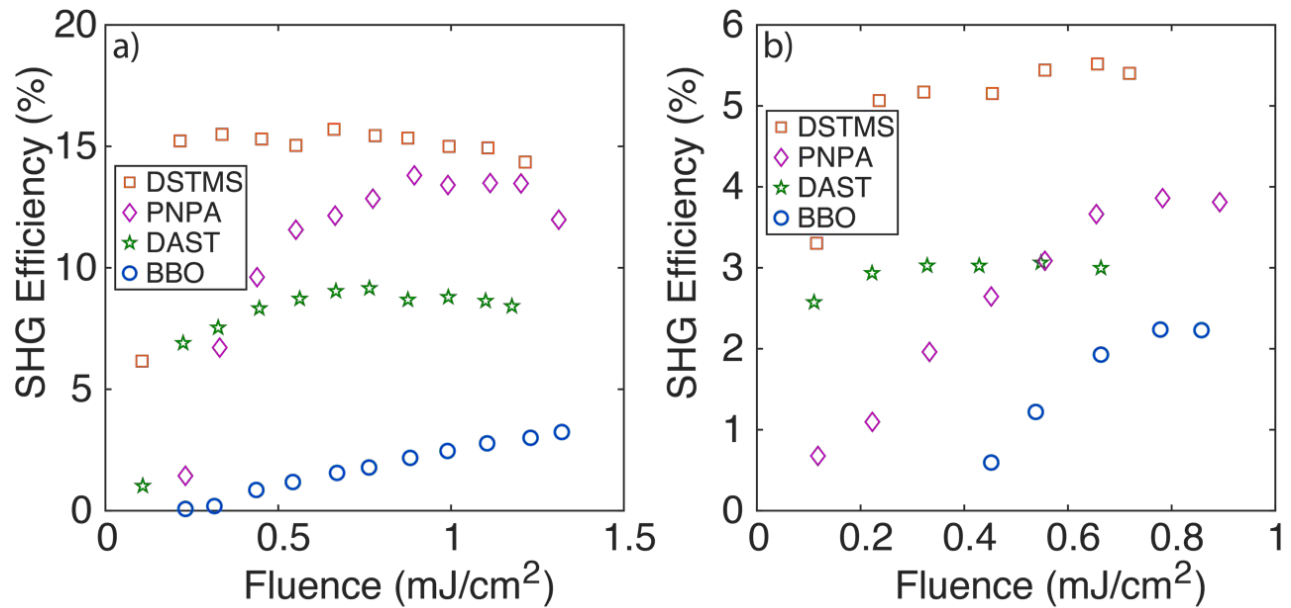


Figure 5-3: Average SHG efficiency as a function of laser fluences in mJ/cm² at (a) 1450 nm for the signal and (b) 2000 nm for the idler. The crystals were: BBO (blue circles), DAST (green stars), PNPA (purple diamonds) and DSTMS (orange squares).

In Fig. 5-3a, it is shown that the SHG efficiency of DAST and DSTMS remains largely consistent after ~ 0.22 mJ/cm² fluence (~ 100 μ J pulse energy), although DSTMS starts to gradually decrease in efficiency as the laser fluence increases. The SHG efficiency of PNPA remains consistent after ~ 0.55 mJ/cm² (~ 250 μ J). On the other hand, the efficiency of BBO steadily increases with fluence yet its SHG efficiency is consistently much lower than the other crystals. At 2000 nm, however, we observe some major differences in the trends, as seen in Fig. 5-3b. The SHG efficiency of DAST starts to remain consistent at incident fluences as low as

$\sim 0.11 \text{ mJ/cm}^2$ ($\sim 50 \text{ }\mu\text{J}$) and DSTMS at $\sim 0.22 \text{ mJ/cm}^2$ ($\sim 100 \text{ }\mu\text{J}$). Interestingly, PNPA continues to increase as the laser fluence increases and levels off after $\sim 0.77 \text{ mJ/cm}^2$ ($\sim 350 \text{ }\mu\text{J}$). The BBO standard appeared to behave similarly to PNPA, although SHG could not be detected until after $\sim 0.44 \text{ mJ/cm}^2$ ($\sim 200 \text{ }\mu\text{J}$) and it was not as efficient as any of the organic crystals. As is commonly observed with these crystals when used for THz generation, the saturation effect at higher fluences is due to a greater prevalence of multiphoton absorption.

The SHG efficiencies of the crystals were also evaluated at varied wavelengths and with a constant fluence of $0.88 \pm .02 \text{ mJ/cm}^2$ ($400 \pm 10 \text{ }\mu\text{J}$) for signal wavelengths and $0.66 \pm .02 \text{ mJ/cm}^2$ ($300 \pm 7 \text{ }\mu\text{J}$) for idler wavelengths (Fig. 5-4; see Fig. 5-11 from the Appendix section for details on individual measurements). For signal wavelengths (1200-1550 nm), all three organic crystals consistently performed more efficiently than BBO. Each organic crystal generated more efficiently as the incident wavelength increased. DSTMS was the most efficient, with an averaged maximum SHG efficiency of $\sim 19.2\%$ followed by PNPA with $\sim 18.7\%$ and DAST with $\sim 12.1\%$. The BBO crystal had a maximum efficiency at 1200 nm with $\sim 3.1\%$ and a minimum efficiency at 1500 nm with $\sim 2.4\%$; (the efficiency at 1550 nm was too low to accurately measure). Similarly, for idler wavelengths (1800-2000 nm), all three organic crystals are again more efficient than the BBO crystal; however, the efficiencies are not as great as with the signal wavelengths. The DAST crystals seem to only slightly outperform BBO with SHG efficiencies of $\sim 2.2\%$ at 1800 nm and $\sim 2.3\%$ at 2000 nm compared to 1.5% and 1.9% for BBO at these same wavelengths, respectively. Both PNPA and DSTMS are more efficient than BBO at any of these wavelengths, with PNPA being most efficient at 1800 nm with $\sim 4\%$ measured conversion and DSTMS at 2000 nm with $\sim 3.8\%$ conversion. One possible mechanism for the peak in SHG efficiency near 1600 nm is a resonant enhancement from the absorption feature in this region.

Other contributing factors are molecular hyperpolarizability and order parameter, as shown in Table 5-1. As discussed further in the Appendix section, considerations of phase matching show that the generation length in the BBO crystal is approximately the thickness of the sample, whereas the coherence length of the organic crystals is only a few μm . In other words, the thickness of the organic crystals has little influence on their performance, which is again an advantage over BBO, which must be carefully prepared.

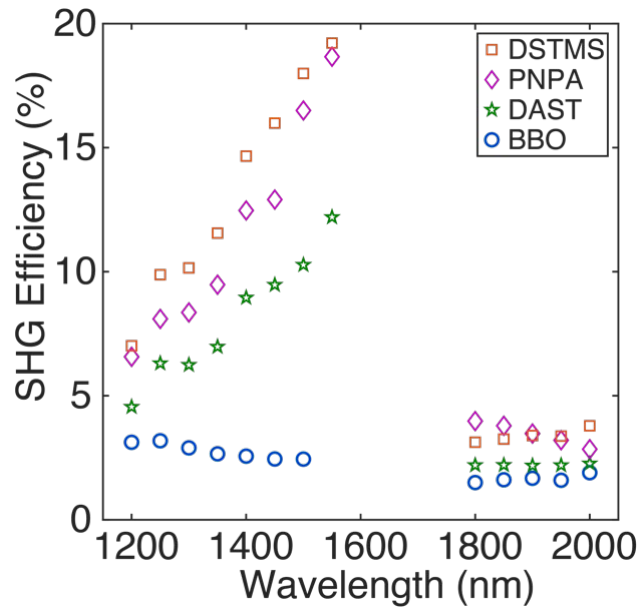


Figure 5-4: Average SHG efficiencies as a function of incident wavelength in nm. Signal wavelengths were collected from 1200-1550 nm (1500 nm for BBO) at $\sim 0.88 \text{ mJ/cm}^2$ and idler wavelengths were collected from 1800-2000 nm at $\sim 0.66 \text{ mJ/cm}^2$ ($\sim 0.44 \text{ mJ/cm}^2$ for some of the DAST crystals). The crystals were: BBO (blue circles), DAST (green stars), PNPA (purple diamonds) and DSTMS (orange squares).

It is worth noting that although DSTMS performs slightly higher than PNPA, both DSTMS and DAST are more brittle and often broke when mounting, handling, and adjusting. Damage thresholds for SHG processes are identical for THz generation using these crystals, and have been reported in the literature.^{30, 36} PNPA is a new material³⁰ that was more robust and

mechanically stable. Although it is not the best performer, PNPA was highly efficient and the most robust organic material, making it attractive for SHG.

5.5 Conclusion

In conclusion, terahertz and second harmonic generating materials have several overlapping qualities including noncentrosymmetric structures, large hyperpolarizabilities, and transparency. Organic crystals DSTMS, DAST, and PNPA efficiently produce SHG for incident wavelengths of 1200-1550 nm and 1800-2000 nm. Although these crystals have different efficiencies at different wavelengths, laser fluences do not greatly affect the proficiency of the crystals until the fluence is less than $\sim 0.44 \text{ mJ/cm}^2$, depending on the crystal. The most efficient SHG crystal is DSTMS, but PNPA is a close second and far more robust. Overall, these organic crystals outperform their inorganic counterpart, which may broaden the possibilities for a whole class of materials as effective SH generators, especially in industries that utilize IR wavelengths such as 1300, 1550 and 2000 nm.

5.6 Appendix

First principles calculations were used to determine several key parameters related to nonlinear optical processes (THz and SH generation) of the three most efficient SH generators, DSTMS, PNPA and DAST. Table 5-1, shows the relative nonlinear susceptibility ($\chi^{(2)}$), hyperpolarizability (β), order parameter ($\cos^3(\theta_p)$, where θ_p is the angle between the β vector and the polar axis of the crystal), crystal face, and the symmetry for each organic crystal. As a clarification, we use the term relative for the nonlinear susceptibility because to determine the actual nonlinear susceptibility value, we would also need to include the local field factor in

addition to the chromophore density, the hyperpolarizability and the order parameter of the unit cell. For these relative comparisons, therefore, we have assumed a similar value for the local field factor for each crystal, as has been done previously.³⁸ Table 5-1 also includes the thicknesses for each organic crystal used in this work.

Table 5-1: Parameters related to nonlinear optical processes in DSTMS, PNPA and DAST and physical parameters of test samples.

Crystal	$\chi^{(2)}$ (<i>esu</i> / \AA^3)	β (<i>esu</i>)	$\cos^3(\theta_p)$	Thickness (μm)	Crystal Face	Symmetry
DSTMS	6.60E-31	4.19E-28	0.8911	800	(001)	C _c
				860		
				720		
				480		
PNPA	8.21E-31	3.16E-28	0.9998	780	(010)	C _c
				750		
				690		
				520		
DAST	3.17E-31	2.01E-28	0.8281	700	(001)	C _c
				600		

In Fig. 5-5, the unit cells for each crystal are shown with their polar axis (blue), hyperpolarizability vector (red) and the angle between them. In this work, the pumping axis is along the polar axis of the crystal, as is often optimal for THz generation.

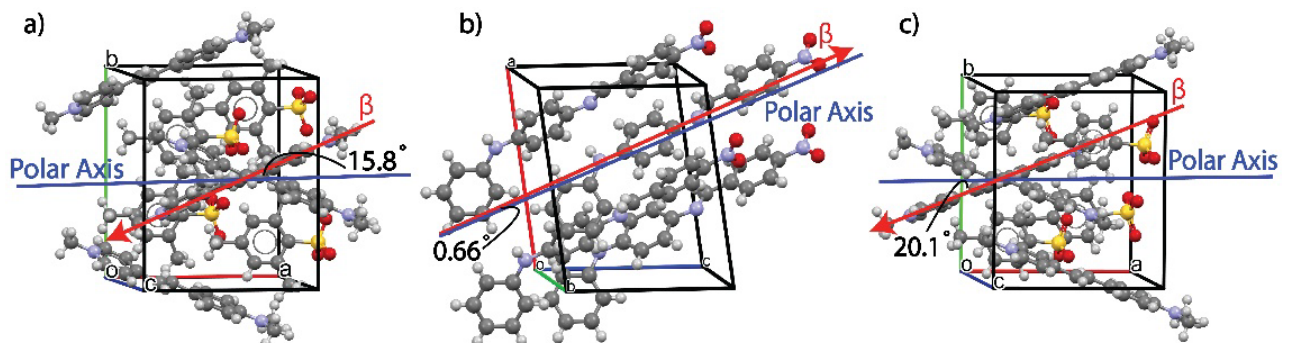


Figure 5-5: Unit cells with the polar axis in blue, the hyperpolarizability (β) vector in red and the angle between them for DSTMS (a), PNPA (b) and DAST (c).

We performed an initial screening of seven organic THz generators with a range of thicknesses of 480-700 μm to determine the viability of these crystals: MNA, BNA, NMBA, ZPAN, DAST, DSTMS, and PNPA. No SHG was detected from BNA and ZPAN crystals. The SHG efficiency of the 5 remaining crystals along with the BBO standard was determined with increasing laser fluences in mJ/cm^2 at 1450 nm, as seen in Fig. 5-6. In Fig. 5-6, we can observe that both MNA and NMBA do not perform better than the BBO standard, therefore no further testing was performed with these crystals. The three other crystals, DSTMS, PNPA and DAST, were more efficient SH generators compared to the BBO standard. The averaged scans in Figs. 5-3 and 5-4 were slightly higher as the method included further optimization.

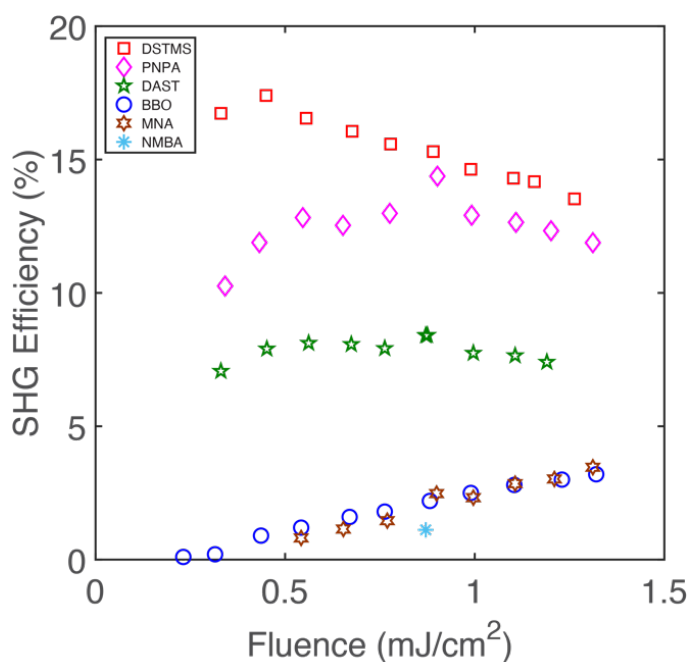


Figure 5-6: The SHG efficiency as a function of laser fluences in mJ/cm^2 at 1450 nm. Only a single set of scans of the crystals during this initial screening is shown. The crystals measured were: DSTMS (red squares), PNPA (magenta diamonds), DAST (green stars), BBO (blue circles), MNA (brown hexagons) and NMBA (light blue asterisks).

As part of the initial screening, we also performed wavelength dependence measurements of the seven organic crystals at ~ 400 mW and again we did not observe significant SHG for the

BNA and ZPAN organic crystals. The SHG efficiency of the 5 remaining crystals along with the BBO standard was determined as a function of wavelength in nm, as seen in Fig. 5-7. Similar to the laser fluence dependence measurements in Fig. 5-6, Fig. 5-7 shows that MNA and NMBA do not perform better than the BBO standard, while DSTMS, PNPA and DAST have higher SHG efficiency as the wavelength increases.

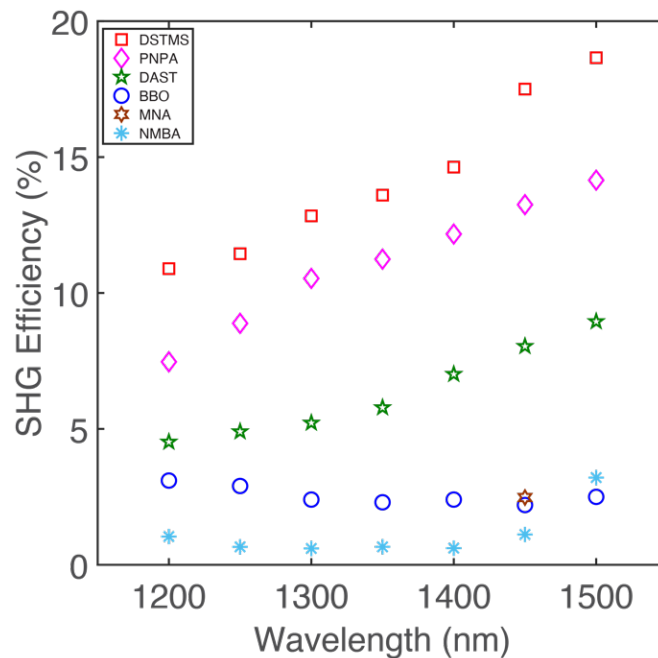


Figure 5-7: The SHG efficiency as a function of laser fluences in mJ/cm^2 at 1450 nm. Only a single set of scans of the crystals during this initial screening is shown. The crystals measured were: DSTMS (red squares), PNPA (magenta diamonds), DAST (green stars), BBO (blue circles), MNA (brown hexagrams) and NMBA (light blue asterisks).

The emitted second-harmonic generation (SHG) wavelengths, 600-725 nm and 900-1000 nm, generated from incident signal (1200-1550 nm) and idler (1800-2000 nm) wavelengths, respectively, were isolated with short-pass filters. Fig. 5-8 shows the transmission spectrum of these short-pass filters.

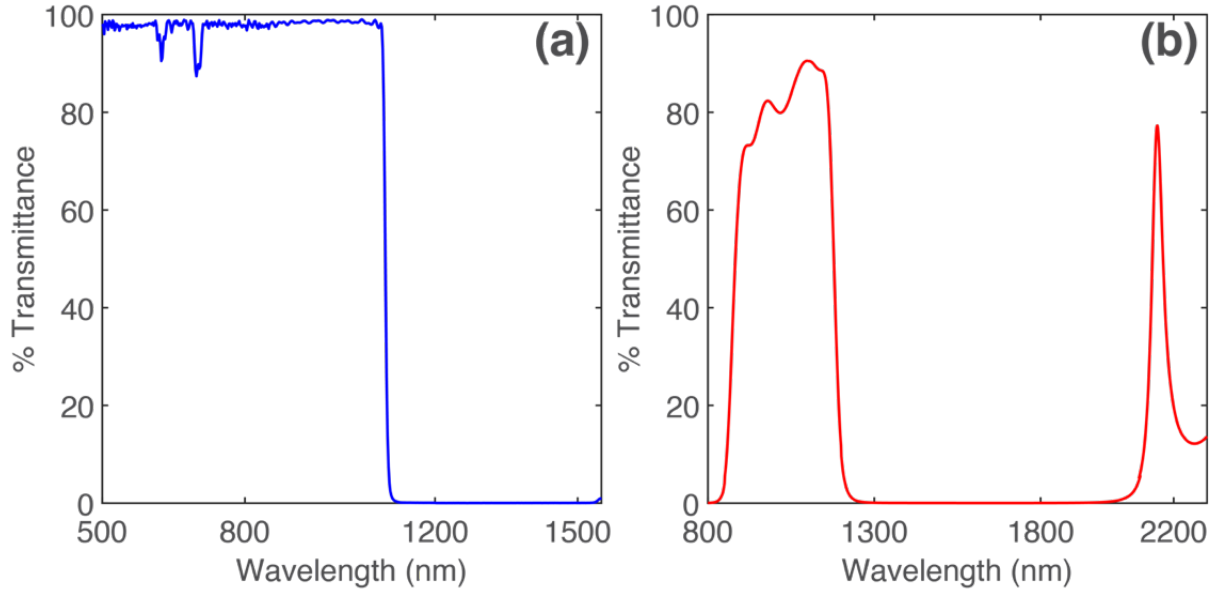


Figure 5-8: Transmission spectrum of the short-pass filters used for the (a) signal wavelengths (1200-1550 nm) and (b) idler wavelengths (1800-2000 nm).

We used a fiber optics spectrometer to verify the generation of SH wavelengths from the NMBA, MNA, DSTMS, PNPA and DAST. Fig. 5-9 shows the spectrum of the SH wavelengths generated by the latter three, efficient crystals.

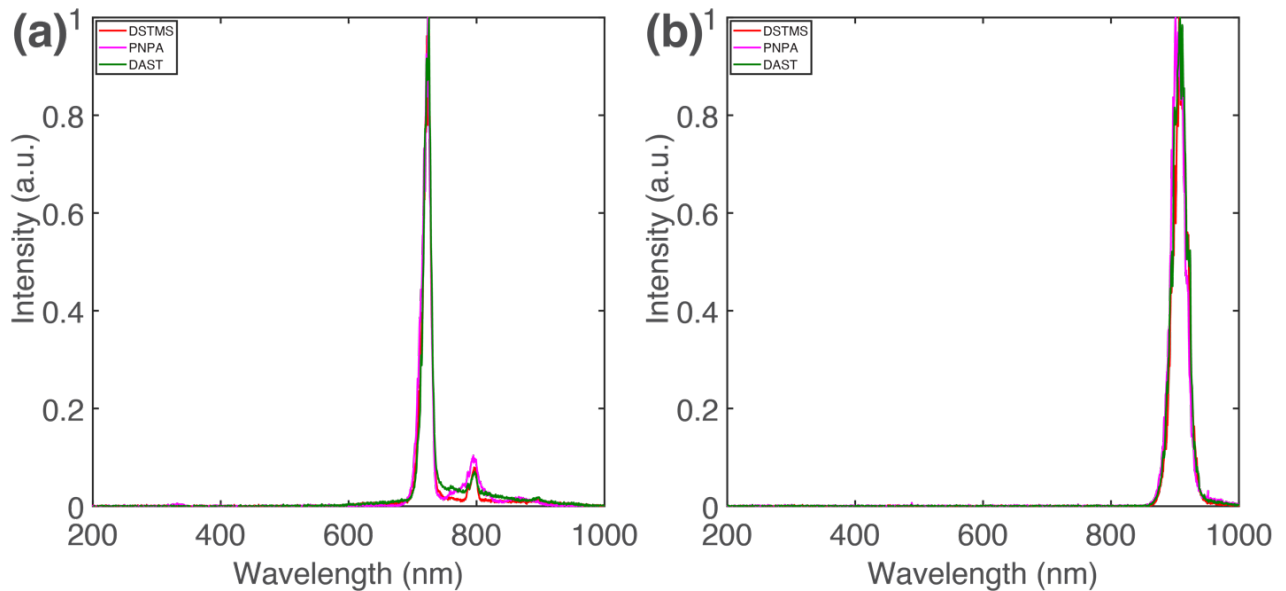


Figure 5-9: Normalized spectrum of newly generated SH light from DSTMS, PNPA and DAST crystals obtained using a fiber optics spectrometer with incident signal (1450 nm) and idler (1800 nm) wavelengths.

In Fig. 5-3, we show the average SHG efficiency as function of incident laser fluences in mJ/cm^2 for DSTMS, PNPA, DAST and BBO at 1450 nm and 2000 nm for the signal and idler, respectively. Fig. 5-10 shows the sets of the detected SHG efficiencies for the laser fluence dependence measurements for these crystals. Due to the availability of certain crystals, multiple measurements were performed for some of the generators.

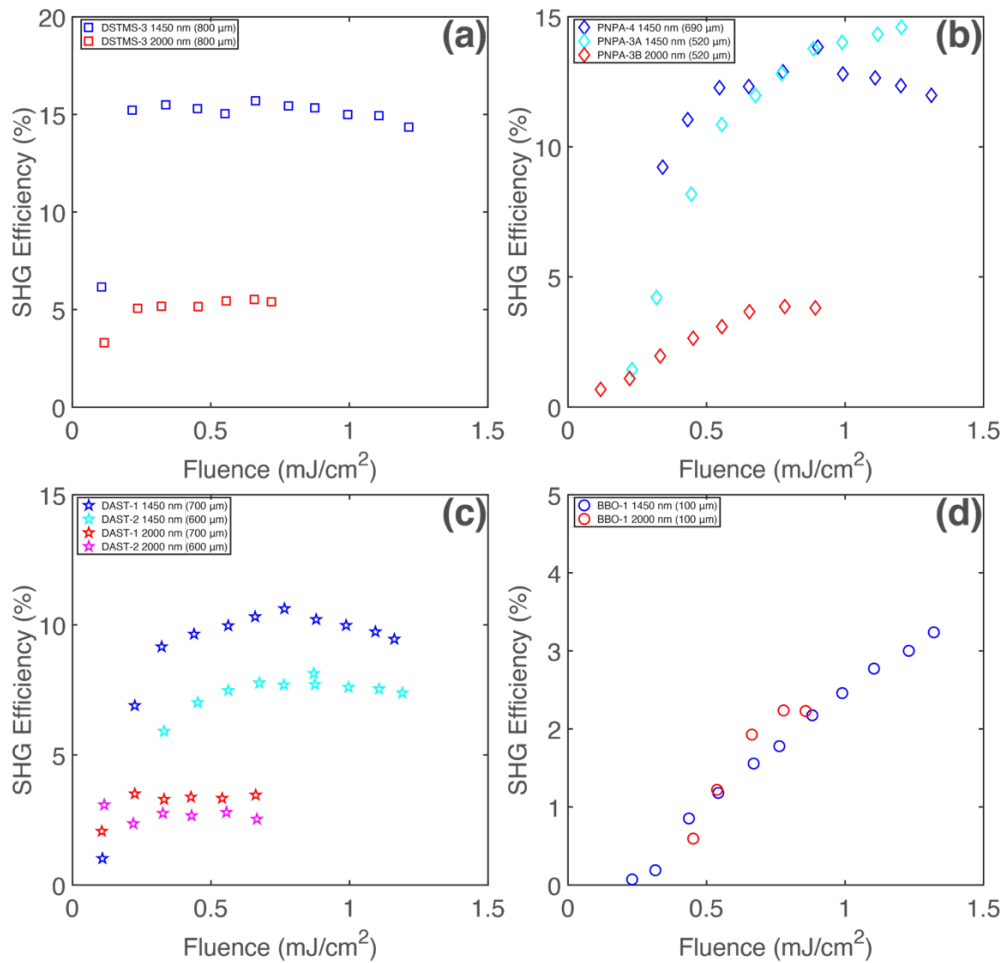


Figure 5-10: The SHG efficiency as a function of incident laser fluences in mJ/cm^2 at 1450 and 2000 nm for the individual measurements of (a) DSTMS (squares), (b) PNPA (diamonds), (c) DAST (stars) and (d) BBO (circles). Two different PNPA and DAST crystals were measured at certain wavelengths. The thicknesses for each crystal are listed in the legend.

In Fig. 5-4, we show the average SHG efficiency as function of incident wavelength in nm for DSTMS, PNPA, DAST and BBO. The incident power was set to ~ 400 mW for the signal

wavelengths and ~300 mW for the idler wavelengths. Fig. 5-11 shows the sets of the detected SHG efficiencies for the wavelength dependence measurements for these crystals. Due to the availability of certain crystals, multiple measurements were performed for some of the generators.

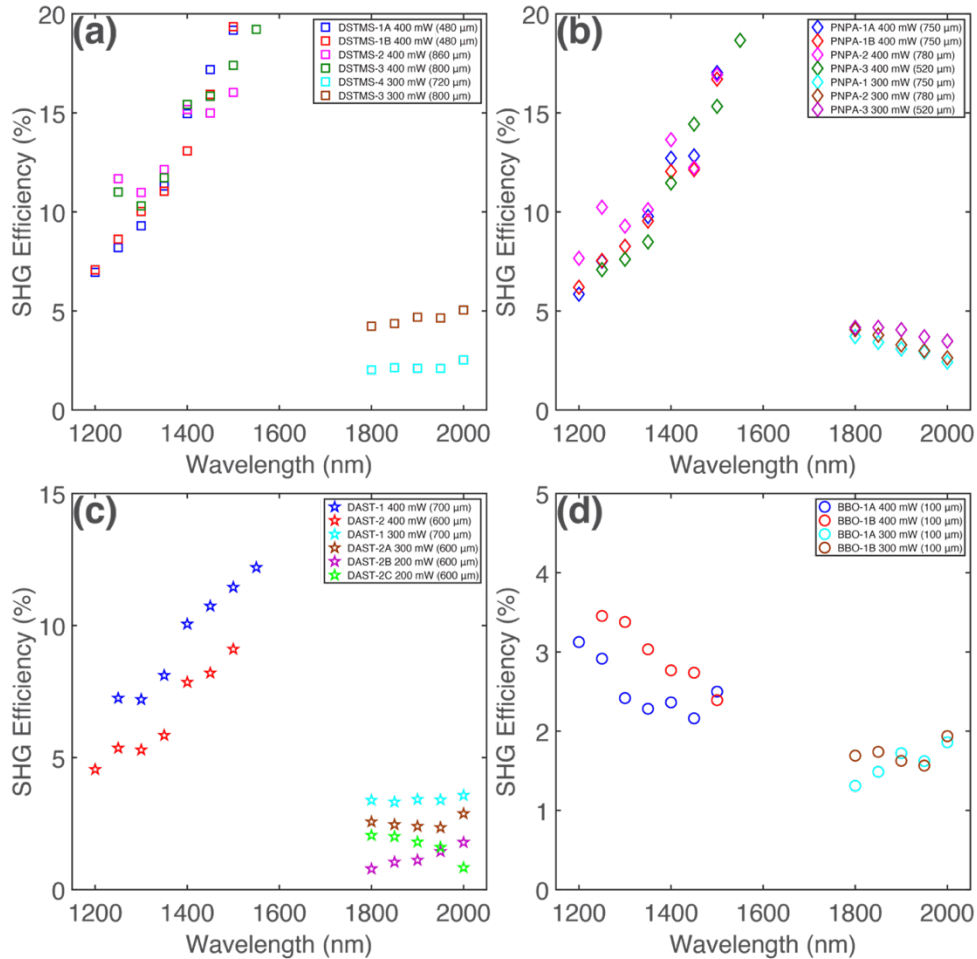


Figure 5-11: The SHG efficiencies as a function of the incident wavelength in nm for the individual measurements of (a) DSTMS (squares), (b) PNPA (diamonds), (c) DAST (stars) and (d) BBO (circles). The signal wavelength measurements were performed with 1200-1550 nm incident light at ~400 mW; however, BBO measurements were only recorded from 1200-1500 nm. The idler wavelength measurements were performed with 1800-2000 nm incident light at ~300 mW. The thicknesses for each crystal are listed in the legend.

To be able to efficiently generate THz or SHG light, the phase matching condition has to be met. This means that the refractive index of the fundamental light (n_f) has to be the same as

the refractive index of the generated SHG light (n_{shg}) or THz light, which minimizes destructive interference and maximizes the generation of the new light. Since our organic crystals have a variety of thicknesses, as seen in Figs. 5-10 and 5-11 for DSTMS, PNPA and DAST, and to verify their phase matching condition for SHG, we calculated the coherence length of the crystals. We extracted the refractive index data from Fig. 5a of Ref. 39 for DSTMS and DAST,³⁹ which covers the range of our fundamental signal (1200-1550 nm) and idler (1800-2000 nm) wavelengths, and their respective SHG wavelengths. Fig. 5-12 shows the extracted refractive index as a function of wavelength for DSTMS (solid light blue line) and DAST (solid light red line) and it also highlights the 1500 nm fundamental wavelength (blue dotted line) with its respective 750 nm SHG wavelength (red dotted line) as an example.

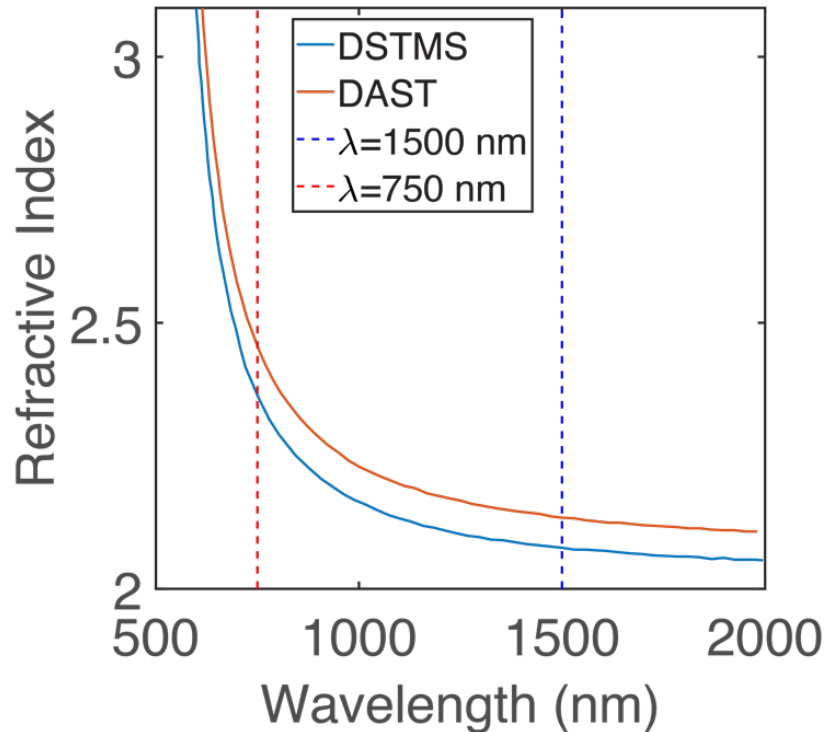


Figure 5-12: The refractive index of DSTMS (solid light blue line) and DAST (solid light red line) as a function of wavelength. The data was extracted from Fig. 5a from Ref. 39. The fundamental wavelength at 1500 nm (dotted blue line) with its respective SHG wavelength at 750 nm (dotted red line) are shown as an example to compare their respective refractive indices.

From Fig. 5-12, we can clearly see that the difference between the refractive indices at the fundamental and SHG wavelength is large for both DSTMS and DAST, which already suggests a nonideal phase matching condition. Additionally, we used this refractive index data to calculate the coherence length (L_c), according to Eqs. 5-3 and 5-4,⁴⁰

$$L_c = \frac{2}{\Delta k} \quad (5-3)$$

$$\Delta k = -\frac{2\pi n_{shg}}{\lambda_{shg}} + \frac{4\pi n_f}{\lambda_f} \quad (5-4)$$

where the wavevector $k = 2\pi n/\lambda_0$ (n is the refractive index and λ_0 is the wavelength of the light). The Δk is determined by taking the difference between the fundamental and SHG wavevectors. The coherence lengths at the signal and idler wavelengths for DSTMS range from 0.04 to 0.08 μm , while they range from 0.23 to 3.23 μm for DAST. This shows that the phase matching of the organic crystals is not ideal and that only a few microns at the back of the NLO organic crystals are responsible for generating SHG. Despite not having an ideal phase matching condition, Figs. 5-3 and 5-4 or Figs. 5-10 and 5-11 from this Appendix section show that DAST and DSTMS still outperform BBO in SHG efficiency. The BBO used for these measurements has a thickness of 100 μm , which also happens to also be its generation length. These figures also show that the thickness does not correlate to SHG efficiency, for example Fig. 5-11a shows that DSTMS 1, 2 and 3 seem to perform similarly despite having different thicknesses. We do not have the refractive index data for PNPA due to it being a more recent crystal but we assume it will behave similarly to DSTMS and DAST. Therefore, these organic crystals only require a few microns to generate SHG with a less optimal phase matching, while the BBO generates SHG along the 100 μm with ideal phase matching and yet it does not generate highly efficient SHG compared to the organic crystals.

5.7 References

1. L.-H. Hong, B.-Q. Chen, C.-Y. Hu, and Z.-Y. Li, “Spatial–temporal evolution of ultrashort laser pulse second harmonic generation in β -barium borate (β -BBO) crystal,” *Journal of Applied Physics* **129**, 233102 (2021).
2. G. C. Bhar, S. Das, and U. Chatterjee, “Noncollinear phase-matched second-harmonic generation in beta barium borate,” *Applied Physics Letters* **54**, 1383-1384 (1989).
3. G. Poberaj, R. Degl’Innocenti, C. Medrano, and P. Günter, “UV integrated optics devices based on beta-barium borate,” *Optical Materials* **31**, 1049-1053 (2009).
4. K. Stankevičiūtė, I. Pipinytė, J. Vengelis, A. Marcinkevičiūtė, R. Šuminas, R. Grigonis, R. C. Eckardt, and V. Sirutkaitis, “Optical parametric oscillators synchronously pumped by fundamental and second harmonic radiation of femtosecond Yb:KGW laser,” *Proc.SPIE* **8845**, 884519 (2013).
5. O. Gobert, G. Mennerat, R. Maksimenka, N. Fedorov, M. Perdrix, D. Guillaumet, C. Ramond, J. Habib, C. Prigent, D. Vernhet, T. Oksenhendler, and M. Comte, “Efficient broadband 400 nm noncollinear second-harmonic generation of chirped femtosecond laser pulses in BBO and LBO,” *Applied Optics* **53**, 2646-2655 (2014).
6. M. Kalmutzki, M. Ströbele, F. Wackenhut, A. J. Meixner, and H. J. Meyer, “Synthesis and SHG Properties of Two New Cyanurates: $\text{Sr}_3(\text{O}_3\text{C}_3\text{N}_3)_2$ (SCY) and $\text{Eu}_3(\text{O}_3\text{C}_3\text{N}_3)_2$ (ECY),” *Inorganic Chemistry* **53**, 12540-12545 (2014).
7. S. Hannig, J. Mielke, J. A. Fenske, M. Misera, N. Beev, C. Ospelkaus, and P. O. Schmidt, “A highly stable monolithic enhancement cavity for second harmonic generation in the ultraviolet,” *Review of Scientific Instruments* **89**, 013106 (2018).

8. C. Wu, X. Jiang, L. Lin, W. Dan, Z. Lin, Z. Huang, M. G. Humphrey, and C. Zhang, "Strong SHG Responses in a Beryllium-Free Deep-UV-Transparent Hydroxyborate via Covalent Bond Modification," *Angewandte Chemie International Edition* **60**, 27151-27157 (2021).
9. E. Rozenberg, and A. Arie, "Broadband and robust adiabatic second-harmonic generation by a temperature gradient in birefringently phase-matched lithium triborate crystal," *Optics Letters* **44**, 3358-3361 (2019).
10. M. Guido, S. Stefan, and W. Horst, "Influence of mechanical stress on the conversion efficiency of KTP and LBO," In *Proc.SPIE*, pp 289-297 (1999).
11. Z. Shuqing, H. Chaoen, and Z. Hongwu, "Crystal growth and properties of lithium triborate," *Journal of Crystal Growth* **99**, 805-810 (1990).
12. J. R. Michael, M. M. Stephen, A. T. Richard, M. A. Jerome, F. Randy, A. H.-F. Ruth, and K. B. Alan, "Effect of thermal annealing and second harmonic generation on bulk damage performance of rapid-growth KDP type-I doublers at 1064 nm," In *Proc.SPIE*, pp 389-399 (2001).
13. Z. Bai, Y. Wang, Z. Lu, H. Yuan, L. Jiang, T. Tan, Z. Liu, H. Wang, C. Cui, and W. Hasi, "Efficient KDP frequency doubling SBS pulse compressed 532nm hundred picosecond laser," *Optik* **127**, 9201-9205 (2016).
14. A. J. W. Brown, M. S. Bowers, K. W. Kangas, and C. H. Fisher, "High-energy, high-efficiency second-harmonic generation of 1064-nm radiation in KTP," *Optics Letters* **17**, 109-111 (1992).
15. H. Kiriya, S. Matsuoka, F. Nakano, and K. Yamakawa, "Quadrature Frequency Conversion Scheme Using CsLiB6O10 Crystals for the Efficient Second-Harmonic Generation of High Power Nd:YAG Laser," *Optical Review* **7**, 281-283 (2000).

16. H. Kiriya, N. Inoue, and K. Yamakawa, "High energy second-harmonic generation of Nd:glass laser radiation with large aperture CsLiB₆O₁₀ crystals," *Optics Express* **10**, 1028-1032 (2002).
17. A. Kokh, N. Kononova, G. Mennerat, P. Villeval, S. Durst, D. Lupinski, V. Vlezko, and K. Kokh, "Growth of high quality large size LBO crystals for high energy second harmonic generation," *Journal of Crystal Growth* **312**, 1774-1778 (2010).
18. T. Sekine, H. Sakai, Y. Takeuchi, Y. Hatano, T. Kawashima, H. Kan, J. Kawanaka, N. Miyanaga, and T. Norimatsu, "High efficiency 12.5 J second-harmonic generation from CsLiB₆O₁₀ nonlinear crystal by diode-pumped Nd:glass laser," *Optics Express* **21**, 8393-8400 (2013).
19. N. Dong, F. Chen, and J. R. Vázquez de Aldana, "Efficient second harmonic generation by birefringent phase matching in femtosecond-laser-inscribed KTP cladding waveguides," *physica status solidi (RRL) – Rapid Research Letters* **6**, 306-308 (2012).
20. AOTK. <http://www.aotk.com/product.aspx?mid=23&pcid=1&cid=4&childid=42> (accessed 2023 26 May).
21. U. Crystals. <https://www.unitedcrystals.com/BBOProp.html> (accessed 2023 26 May).
22. C. Rader, M. F. Nielson, B. E. Knighton, Z. B. Zaccardi, D. J. Michaelis, and J. A. Johnson, "Custom terahertz waveforms using complementary organic nonlinear optical crystals," *Optics Letters* **47**, 5985-5988 (2022).
23. H. Barhum, C. McDonnell, T. Alon, R. Hammad, M. Attrash, T. Ellenbogen, and P. Ginzburg, "Organic Kainate Single Crystals for Second-Harmonic and Broadband THz Generation," *ACS Applied Materials & Interfaces* **15**, 8590-8600 (2023).

24. Y. R. Shen, "Surface properties probed by second-harmonic and sum-frequency generation," *Nature* **337**, 519-525 (1989).
25. K. M. Ok, E. O. Chi, and P. S. Halasyamani, "Bulk characterization methods for non-centrosymmetric materials: second-harmonic generation, piezoelectricity, pyroelectricity, and ferroelectricity," *Chemical Society Reviews* **35**, 710-717 (2006).
26. Z. Xia, and K. R. Poeppelmeier, "Chemistry-Inspired Adaptable Framework Structures," *Accounts of Chemical Research* **50**, 1222-1230 (2017).
27. M. Mutailipu, K. R. Poeppelmeier, and S. Pan, "Borates: A Rich Source for Optical Materials," *Chemical Reviews* **121**, 1130-1202 (2021).
28. C. Chen, Y. Wang, B. Wu, K. Wu, W. Zeng, and L. Yu, "Design and synthesis of an ultraviolet-transparent nonlinear optical crystal $\text{Sr}_2\text{Be}_2\text{B}_2\text{O}_7$," *Nature* **373**, 322-324 (1995).
29. M. Mutailipu, M. Zhang, Z. Yang, and S. Pan, "Targeting the Next Generation of Deep-Ultraviolet Nonlinear Optical Materials: Expanding from Borates to Borate Fluorides to Fluorooxoborates," *Accounts of Chemical Research* **52**, 791-801 (2019).
30. C. Rader, Z. B. Zaccardi, S.-H. E. Ho, K. G. Harrell, P. K. Petersen, M. F. Nielson, H. Stephan, N. K. Green, D. J. H. Ludlow, M. J. Lutz, S. J. Smith, D. J. Michaelis, and J. A. Johnson, "A New Standard in High-Field Terahertz Generation: the Organic Nonlinear Optical Crystal PNPA," *ACS Photonics* **9**, 3720-3726 (2022).
31. T. Manaka, and M. Iwamoto, "Optical second-harmonic generation measurement for probing organic device operation," *Light: Science & Applications* **5**, e16040-e16040 (2016).
32. M. Reid, I. V. Cravetchi, and R. Fedosejevs, "Terahertz radiation and second-harmonic generation from InAs: Bulk versus surface electric-field-induced contributions," *Physical Review B* **72**, 035201 (2005).

33. J. Chen, C.-L. Hu, F. Kong, and J.-G. Mao, “High-Performance Second-Harmonic-Generation (SHG) Materials: New Developments and New Strategies,” *Accounts of Chemical Research* **54**, 2775-2783 (2021).
34. G. A. Valdivia-Berroeta, Z. B. Zaccardi, S. K. F. Pettit, S.-H. Ho, B. W. Palmer, M. J. Lutz, C. Rader, B. P. Hunter, N. K. Green, C. Barlow, C. Z. Wayment, D. J. Ludlow, P. Petersen, S. J. Smith, D. J. Michaelis, and J. A. Johnson, “Data Mining for Terahertz Generation Crystals,” *Advanced Materials* **34**, 2107900 (2022).
35. M. J. Lutz, Z. B. Zaccardi, E. S. H. Ho, D. J. Michaelis, and J. A. Johnson, “ZPAN: A New Organic Nonlinear Optical Crystal for THz Generation,” In *2022 Conference on Lasers and Electro-Optics (CLEO)*, pp 1-2 (2022).
36. B. Monoszlai, C. Vicario, M. Jazbinsek, and C. P. Hauri, “High-energy terahertz pulses from organic crystals: DAST and DSTMS pumped at Ti:sapphire wavelength,” *Optics Letters* **38**, 5106-5109 (2013).
37. B. W. H. Palmer, C. Rader, E. S.-H. Ho, Z. B. Zaccardi, D. J. Ludlow, N. K. Green, M. J. Lutz, A. Alejandro, M. F. Nielson, G. A. Valdivia-Berroeta, C. C. Chartrand, K. M. Holland, S. J. Smith, J. A. Johnson, and D. J. Michaelis, “Large Crystal Growth and THz Generation Properties of 2-Amino-5-Nitrotoluene (MNA),” *ACS Applied Electronic Materials* **4**, 4316-4321 (2022).
38. G. A. Valdivia-Berroeta, L. K. Heki, E. A. McMurray, L. A. Foote, S. H. Nazari, L. Y. Serafin, S. J. Smith, D. J. Michaelis, and J. A. Johnson, “Alkynyl Pyridinium Crystals for Terahertz Generation,” *Advanced Optical Materials* **6**, 1800383 (2018).
39. M. Jazbinsek, U. Puc, A. Abina, and A. Zidansek, “Organic Crystals for THz Photonics,” *Applied Sciences* **9**, 882 (2019).

40. R. W. Boyd. *Nonlinear Optics*; Elsevier Science & Technology, 2003.

CHAPTER 6: Vibrational Control Through THz Light

6.1 Introduction

Up to this point of this dissertation, we have primarily focused on how to generate, measure and characterize the THz light (chapters 2 and 3), and how to improve organic crystals to generate THz light more efficiently (chapter 4) or the use of organic crystals for second-harmonic generation (chapter 5). The remaining chapters of this dissertation will focus on using THz light to study nonlinear phenomena, such as coupling of vibrational modes in a molecular gas system (chapter 7) and in a crystal lattice (chapter 8). But before we can delve into those specific studies, we will need to understand key concepts related to vibrational motion and this will be the main focus of this chapter.

The important concepts that will be explained in this chapter include the vibrational motion inside molecules, the harmonic oscillator model, the potential energy surface (PES), classical equations of motion for coupled vibrational modes and anharmonic coupling. The understanding of these concepts will allow the reader to better understand the projects presented in chapters 7 and 8.

6.2 Vibrational Motion

As a starting point, we will use a simple molecule to talk about the degrees of freedom that govern atomic motion. The total number of degrees of freedom in a molecule can be determined by $3N$, where N is the number of atoms. There are three main degrees of freedom related to the different motions of the atoms in molecules: translational, rotational and vibrational degrees of freedom. Whether we are talking about a single atom or a molecule, there are usually

always three translational degrees of freedom because the molecule can move in the x -, y - or z -direction. Rotational degrees of freedom mostly exist in gas and liquid molecules due to their ability to move and not be tightly confined, and the number varies depending on whether the molecule is linear (two modes) or nonlinear (three modes). The number of the vibrational degrees of freedom, which will be the main focus in this section, is more complex as it increases with the increasing number of atoms (N) present in a polyatomic molecule. If a molecule is linear, then the number of vibrational modes can be determined by $3N - 5$; however, if the molecule is nonlinear, then we use $3N - 6$ to determine the number of vibrational modes.

When discussing vibrational modes, it is necessary to talk about them in two different frameworks: polyatomic molecules (gas-phase) and crystals (lattice/solids). In the former case, an isolated polyatomic molecule contains all three degrees of freedom because the molecule is not constrained and the vibrational modes can be determined by $3N - 6$. However, in the latter case, especially as we model a lattice structure as an infinite lattice, it does not contain any translational or rotational degrees of freedom, only vibrations, which we call phonons. As an example, Fig. 6-1 shows vibrational modes in a single isolated molecule (a) and phonons in a single unit cell for an inorganic crystal (b).

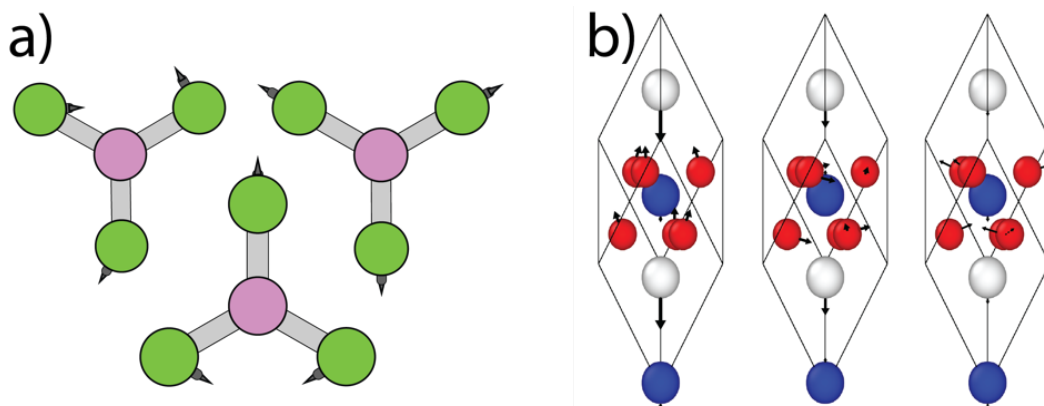


Figure 6-1: Vibrational modes and phonons. a) Three vibrational modes for a BF_3 molecule. b) Three phonons for a unit cell of LiNbO_3 . The arrows in both represent the direction of the eigenvectors of motion.

In crystalline systems there are acoustic and optical phonons. Acoustic phonons typically involve the vibrational motion of entire unit cells and optical phonons involve the motion of atoms within each unit cell. We decompose phonons into lattice waves that travel through the material, and the dispersion curve delineates specific phonon branches. There are three acoustic phonon branches for each direction in a 3-dimensional lattice structure, one longitudinal and two transverse, and the remaining phonon branches are optical phonons, originally named in this manner because of how certain branches could interact with light. Due to the lack of translational and rotational degrees of freedom and the three acoustic phonon branches, the number of optical phonon branches is determined by $3N - 3$, where N equals the number of atoms in the unit cell of the lattice. The work presented in chapter 7 of this dissertation will primarily focus on modeling the anharmonic coupling of vibrational modes of the organic molecule fluorobenzene, while chapter 8 will focus on measuring the coupling between optical phonons in the inorganic crystal CdWO_4 .

The vibrational motion of a molecule or of a crystal is crucial because several phenomena can be accessed and studied that have important applications in the scientific world. For example, studying the vibrational motion of molecules is crucial in understanding energy processes in liquids such as intramolecular vibrational relaxation (IVR),¹ vibrational energy relaxation (VER)²⁻⁴ or vibrational cooling (VC).^{2, 3} Vibrational motion is also important to study IVR or VER in gases,^{5, 6} or collisional energy transfer (CET).⁷⁻¹¹ In the case of motion between phonons, phenomena such as, anharmonic interactions between infrared- and Raman-active phonons,¹²⁻¹⁴ electron-phonon coupling,¹⁵ magnetophononic coupling,¹⁶ inducing magnetism through phonon motion,^{17, 18} and switching ferroelectric polarization in materials,¹⁹ have been studied in recent years.

6.3 The Harmonic Oscillator

A simple diatomic gas molecule only contains one vibrational mode and we can model its motion by using the harmonic oscillator approximation. To understand this model, we can picture a spring that is attached to a ceiling and can oscillate in one single direction without the interference of any other force (including the gravitational force) and at a constant acceleration (no damping). In this example, the restoring force of the spring (F) can be described by Eq. 6-1:

$$F = -kx \quad (6-1)$$

where k is the force constant and x is the displacement of the spring along the x-axis. From physics, we also know that the force is equal to the negative derivative of the potential energy along the x-axis, according to the following equation:

$$F = -\frac{\partial V}{\partial x} \quad (6-2)$$

We can then set both of these expressions equal to each other and follow the process shown in Eqs. 6-3 to 6-5 to obtain Eq. 6-6, which is an expression of the potential energy of a spring. It should be noted that Eq. 6-6 should also contain the addition of a constant when integrating but the constant is arbitrary and we have given it a value zero to set the zero point of the potential energy.

$$-kx = -\frac{\partial V}{\partial x} \quad (6-3)$$

$$\partial V = kx\partial x \quad (6-4)$$

$$\int \partial V = \int kx\partial x \quad (6-5)$$

$$V = \frac{1}{2}kx^2 \quad (6-6)$$

We can then use the equation

$$k = \omega^2 m, \quad (6-7)$$

where ω is the angular frequency and m is the mass of the spring, to modify Eq. 6-6 and get

$$V = \frac{1}{2} m \omega^2 x^2 \quad (6-8)$$

In this section, we have used the harmonic oscillator approximation to derive an equation that describes the potential energy for the motion of a spring. We can now use this model and apply it to vibrational modes (or phonons). To do this, we need to change the coordinate system that we use to describe motion. For the spring example, we assumed motion in only one direction (x-axis) in Cartesian coordinates but this is not the case when we are talking about vibrational modes. For instance, a single atom can move in three different directions (x-, y- or z-axis); however, when we are talking about a system with two or more atoms, like in molecules or crystals, the motion of each atom is not independent of the motion of the other atoms present in a vibrational mode. We can see that we would have to define an x-, y- and z-axis for each atom present in one vibrational mode. Additionally, we need to take into account that a molecule has more than one vibrational mode because the number of vibrational modes increase as the number of atoms increase. As we can see, these considerations make it difficult to work with Cartesian coordinates. It is for this reason, that we write Eq. 6-8 as

$$V = \frac{1}{2} \omega^2 Q^2 \quad (6-9)$$

where Q represents the motion of a vibrational mode along normal-mode coordinates, which are coordinates used to describe the relative movement all atoms within a vibrational mode. Eq. 6-9 describes the potential energy as one vibrational mode is displaced along its normal mode coordinate (like in a diatomic molecule), when the displacement is relatively small from the equilibrium position (see Eq. 6-6). In the following section, we will focus on a departure from the harmonic potential energy surface in Eq. 6-9 when the displacement is large. We also note that Q is mass weighted with units $\text{\AA} \text{ amu}^{1/2}$.

6.4 The Potential Energy Surface (PES)

In the previous section, we derived Eq. 6-9, which describes the harmonic potential energy surface of a single vibrational mode; however, molecules or crystals are far more complex due to having multiple vibrational modes (or phonons) and to accurately describe the potential energy we need to include information regarding all of the vibrational modes of the system of interest. This can be accomplished by using the potential energy surface (PES), which is an equation that describes all of the interatomic forces present in a system. So far Eq. 6-9 is only assuming that the system behaves as a harmonic oscillator because the displacement is small (see Eq. 6-6); however, that is not always the case due to the many attractive and repulsive forces present inside the molecules, and also the inclusion of the interactions between the multiple vibrational modes. We will first begin by using Eq. 6-6 and a Taylor series to expand this equation into

$$V = \frac{1}{2}kx^2 + \frac{\gamma_3}{6}x^3 + \frac{\gamma_4}{24}x^4 + \dots \quad (6-10)$$

From Eq. 6-10, we notice that the harmonic oscillator term is still present (first term on right-side of the equation) but we also now have additional terms with increasing powers multiplied by a constant γ_i . These additional terms are known as the anharmonic terms, which can become significant with large values of x . The constants γ_i are known as the anharmonic coupling constants. If the displacement x is small then the anharmonic terms in Eq. 6-10 are extremely small and only the first (harmonic) term is relevant for the potential energy, thus the equation simplifies to Eq. 6-6. Conversely, when the displacement is large, we need to apply Eq. 6-10 because it accounts for both the harmonic and anharmonic regions of the PES.

However, Eq. 6-10 only accounts for one vibrational mode (or phonon) and thus we need to modify this equation to account for several vibrational modes. This equation can become very

complex with the increasing number of vibrational modes; thus, we will limit ourselves to only include three vibrational modes and only a few anharmonic terms. With these two points in mind, we show the PES for a system containing three vibrational modes (Q_1 , Q_2 and Q_3) in the following equation, where for simplicity we have removed the mass from the harmonic terms:

$$V(Q_1, Q_2, Q_3) = \frac{1}{2}\omega_1^2 Q_1^2 + \frac{1}{2}\omega_2^2 Q_2^2 + \frac{1}{2}\omega_3^2 Q_3^2 + \phi_{111} Q_1^3 + \phi_{222} Q_2^3 + \phi_{333} Q_3^3 + \phi_{112} Q_1^2 Q_2 + \phi_{122} Q_1 Q_2^2 + \phi_{223} Q_2^2 Q_3 + \phi_{233} Q_2 Q_3^2 + \phi_{113} Q_1^2 Q_3 + \phi_{133} Q_1 Q_3^2 + \phi_{123} Q_1 Q_2 Q_3 + \dots (6-11)$$

Eq. 6-11 reveals the complexity of the PES for a system of three vibrational modes with harmonic and anharmonic considerations, compared to the simpler harmonic PES for a single vibrational mode in Eq. 6-9. In Eq. 6-11, the first three terms correspond to the harmonic oscillator terms ($\frac{1}{2}\omega^2 Q_i^2$, as seen in Eq. 6-9, where i denotes any vibrational mode) for each of the three modes Q_1 , Q_2 and Q_3 . The following three terms ($\phi_{iii} Q_i^3$) correspond to the first anharmonic term for each of the vibrational modes similar to the second term in Eq. 6-10 but in normal coordinates with their respective anharmonic coupling constant, ϕ_{iii} . For these terms, the anharmonic coupling constants are a measure of how these modes couple to themselves, which is equivalent to $\frac{\gamma_3}{6}$ in Eq. 6-10. The following six terms ($\phi_{ijj} Q_i^2 Q_j$, where j denotes another vibrational mode) are the cross-coupling terms between two vibrational modes, which we often call quadratic linear terms. The final term ($\phi_{ijk} Q_i Q_j Q_k$) in Eq. 6-11 is the cross-coupling term between three vibrational modes and the coupling constant represents the strength of the coupling between these modes. Since the last seven terms involve the coupling between three vibrational modes, they are also known as trilinear coupling terms (see chapter 8 of this dissertation).

Eq. 6-11 shows the complete PES for a system containing three vibrational modes and accounts for all the interatomic forces involved in this system including the coupling between

each of the three vibrational modes. It is important to note that not all of the cross-coupling terms will be part of the PES due to symmetry considerations depending on the molecule or crystal of interest; therefore, some of these terms can be excluded. Despite the removal of some terms in the PES, there will still be multiple energy flow pathways enabled by the cross-coupling terms. In Fig. 6-2, we show an example of the PES along (a) one and (b) two vibrational mode coordinates. This simple example in Fig. 6-2 shows that for more than two modes, the PES can become a really complex hypersurface.

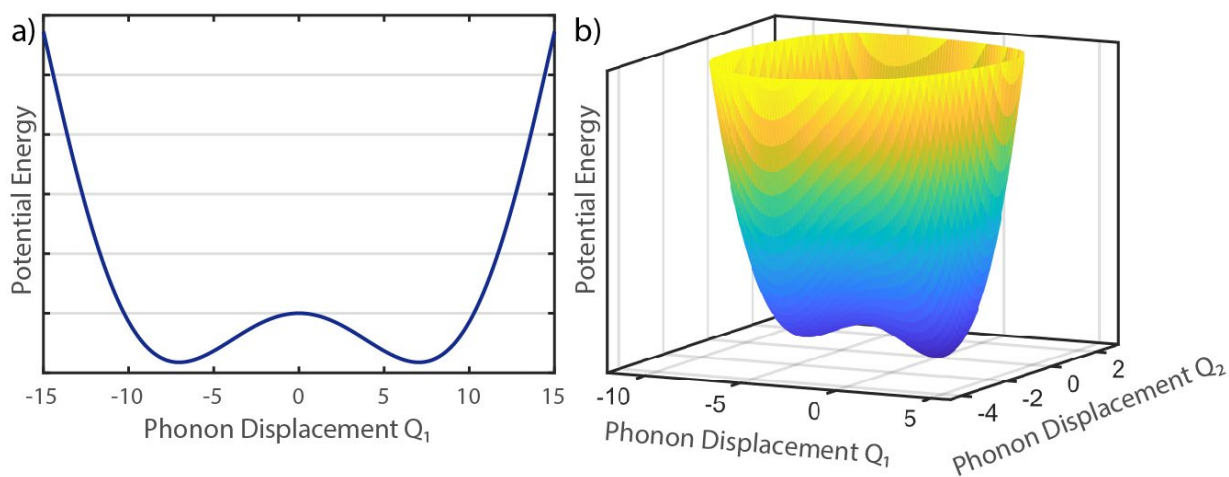


Figure 6-2: Potential energy surface. (a) Potential energy as a function of mode coordinate Q_1 and (b) as a function of mode coordinates Q_1 and Q_2 .

6.5 Equations of Motion

The PES offers additional insight about the displacement of the vibrational modes (or phonons) in a molecule (or crystal) by taking the (negative) first derivative with respect to each mode Q because of the relationship between force and potential energy (see Eq. 6-2). Due to the complexity of the PES (Eq. 6-11), we will take the derivative of the simple case involving only the harmonic term in Cartesian coordinates (Eq. 6-6), which results in

$$\mathbf{F}_p = -\frac{\partial V}{\partial \mathbf{x}} = -k\mathbf{x}. \quad (6-12)$$

Due to the vibrational modes also having a mass (m) component, we can use Newton's equation for force as the following expression:

$$F_m = ma = m\ddot{x}, \quad (6-13)$$

where a is the acceleration (\ddot{x}). We combine all the forces which is equivalent to setting Eqs. 6-12 and 6-13 equal to each other to get

$$m\ddot{x} = -kx, \quad (6-14)$$

We can then add all the terms in Eq. 6-14 to one side, divide by mass, use Eq. 6-7 and set it equal to zero to obtain a homogenous second-order differential equation, as follows:

$$\ddot{x} + \omega_0^2 x = 0 \quad (6-15)$$

where ω_0 denotes that the natural (angular) frequency of the harmonic oscillator. We can then add a damping term to Eq. 6-15, which denotes that the energy of the system can dissipate upon a disturbance to the system. We shall also replace the x with Q , since we want to apply this to the normal modes of a molecular or crystalline system, to obtain the following equation:

$$\ddot{Q} + 2\Gamma\dot{Q} + \omega_0^2 Q = 0 \quad (6-16)$$

Eq. 6-16 is the equation of motion for a single vibrational mode. In a molecule or crystal with multiple vibrational modes, there would be one equation of motion for each mode. Eq. 6-16, with the right-hand side equal to zero, is the equation of motion when no external force is acting on the vibrational mode. However, for the projects presented in chapters 7 and 8, we will have a THz pump pulse that acts as an external force that we can add to the right-side of equation 6-16. Additionally, anharmonic terms in the PES can also be included on the right-hand side of the equation of motion, providing an additional driving force that depends on the motion of other vibrational modes. For example, in chapter 7 we present studies of the vibrational modes in a gas molecule of fluorobenzene and how these modes are affected by a multi-THz pump electric field

and anharmonic coupling to other vibrational modes. In chapter 8, we present work on the inorganic crystal CdWO₄ and how the optical phonons react to a resonant THz electric field and anharmonic trilinear coupling. In chapters 7 and 8, we will discuss additional driving force terms and include them into the equations of motion. An example of an equation of motion with external forces looks as follows,

$$\ddot{Q}_i + 2\Gamma_i\dot{Q}_i + \omega_i^2 Q_i = Z_i^* E(t) - \phi_{ijk} Q_j Q_k, \quad (6-17)$$

where Z_i^* is the mode effective charge of a phonon, $E(t)$ is the THz electric field, and $\phi_{ijk} Q_j Q_k$ is an anharmonic coupling term between three vibrational modes.

The example of the equation of motion in Eq. 6-17 gives us an idea on how to interpret these types of equations. We can treat the right-hand side as the driving force and the left-hand side as what we are driving. In Eq. 6-17, we are driving mode Q_i through two external forces: a THz electric field, and anharmonic coupling between three modes. If there is enough amplitude at the resonant frequency ω_i in any of these two external forces, then mode Q_i will be excited. In chapter 7 and 8, we will cover the specifics of the equations of motion for the fluorobenzene molecule and the CdWO₄ crystal, respectively.

6.6 Conclusion

In conclusion, we have introduced the importance of vibrational motion in molecules and crystal lattices through their vibrational modes and phonons, respectively. Understanding how to control the vibrational modes inside a molecular system is crucial because their properties can be accessed and manipulated. We have also shown that the harmonic oscillator approximation can be used to model the vibrational motion of a molecular system and thus derive the PES equation for said molecular system. The PES describes how all the forces inside the molecular system

interact and affect the overall vibrational energy of the system. Finally, we show that the PES can be used to derive the equations of motion, which can be used to model how external forces drive vibrational modes inside a material.

6.7 References

1. B. C. Pein, Y. Sun, and D. D. Dlott, "Controlling Vibrational Energy Flow in Liquid Alkylbenzenes," *The Journal of Physical Chemistry B* **117**, 10898-10904 (2013).
2. J. C. Deak, L. K. Iwaki, and D. D. Dlott, "Vibrational Energy Redistribution in Polyatomic Liquids: Ultrafast IR-Raman Spectroscopy of Nitromethane," *The Journal of Physical Chemistry A* **103**, 971-979 (1999).
3. J. C. Deak, L. K. Iwaki, and D. D. Dlott, "Vibrational Energy Redistribution in Polyatomic Liquids: Ultrafast IR-Raman Spectroscopy of Acetonitrile," *The Journal of Physical Chemistry A* **102**, 8193-8201 (1998).
4. L. K. Iwaki, and D. D. Dlott, "Three-Dimensional Spectroscopy of Vibrational Energy Relaxation in Liquid Methanol," *The Journal of Physical Chemistry A* **104**, 9101-9112 (2000).
5. H. S. Yoo, M. J. DeWitt, and B. H. Pate, "Vibrational Dynamics of Terminal Acetylenes: I. Comparison of the Intramolecular Vibrational Energy Redistribution Rate of Gases and the Total Relaxation Rate of Dilute Solutions at Room Temperature," *The Journal of Physical Chemistry A* **108**, 1348-1364 (2004).
6. H. S. Yoo, D. A. McWhorter, and B. H. Pate, "Vibrational Dynamics of Terminal Acetylenes: III. Comparison of the Acetylenic C-H Stretch Intramolecular Vibrational-Energy Redistribution Rates in Ultracold Molecular Beams, Room-Temperature Gases, and Room-Temperature Dilute Solutions," *The Journal of Physical Chemistry A* **108**, 1380-1387 (2004).

7. V. Bernshtein, and I. Oref, "Gateway Modes for Collisional Energy Transfer between Benzene and Ar," *The Journal of Physical Chemistry A* **105**, 10646-10650 (2001).
8. J. A. Johnson, K. Kim, M. Mayhew, D. G. Mitchell, and E. T. Sevy, "Rotationally Resolved IR-Diode Laser Studies of Ground-State CO₂ Excited by Collisions with Vibrationally Excited Pyridine," *The Journal of Physical Chemistry A* **112**, 2543-2552 (2008).
9. K. Kim, A. M. Johnson, A. L. Powell, D. G. Mitchell, and E. T. Sevy, "High resolution IR diode laser study of collisional energy transfer between highly vibrationally excited monofluorobenzene and CO₂: The effect of donor fluorination on strong collision energy transfer," *The Journal of Chemical Physics* **141**, (2014).
10. D. G. Mitchell, A. M. Johnson, J. A. Johnson, K. A. Judd, K. Kim, M. Mayhew, A. L. Powell, and E. T. Sevy, "Collisional Relaxation of the Three Vibrationally Excited Difluorobenzene Isomers by Collisions with CO₂: Effect of Donor Vibrational Mode," *The Journal of Physical Chemistry A* **112**, 1157-1167 (2008).
11. G. Lendvay, "Gateway Modes in the Collisional Energy Transfer from Highly Vibrationally Excited CS₂," *The Journal of Physical Chemistry A* **101**, 9217-9223 (1997).
12. T. G. H. Blank, K. A. Grishunin, K. A. Zvezdin, N. T. Hai, J. C. Wu, S. H. Su, J. C. A. Huang, A. K. Zvezdin, and A. V. Kimel, "Two-Dimensional Terahertz Spectroscopy of Nonlinear Phononics in the Topological Insulator MnBi₂Te₄," *Physical Review Letters* **131**, 026902 (2023).
13. M. Först, C. Manzoni, S. Kaiser, Y. Tomioka, Y. Tokura, R. Merlin, and A. Cavalleri, "Nonlinear phononics as an ultrafast route to lattice control," *Nature Physics* **7**, 854-856 (2011).

14. C. L. Johnson, B. E. Knighton, and J. A. Johnson, “Distinguishing Nonlinear Terahertz Excitation Pathways with Two-Dimensional Spectroscopy,” *Physical Review Letters* **122**, 073901 (2019).
15. J. Choe, D. Lujan, M. Rodriguez-Vega, Z. Ye, A. Leonardo, J. Quan, T. N. Nunley, L.-J. Chang, S.-F. Lee, J. Yan, G. A. Fiete, R. He, and X. Li, “Electron–Phonon and Spin–Lattice Coupling in Atomically Thin Layers of MnBi_2Te_4 ,” *Nano Letters* **21**, 6139-6145 (2021).
16. H. Padmanabhan, M. Poore, P. K. Kim, N. Z. Koocher, V. A. Stoica, D. Puggioni, H. Wang, X. Shen, A. H. Reid, M. Gu, M. Wetherington, S. H. Lee, R. D. Schaller, Z. Mao, A. M. Lindenberg, X. Wang, J. M. Rondinelli, R. D. Averitt, and V. Gopalan, “Interlayer magnetophononic coupling in MnBi_2Te_4 ,” *Nature Communications* **13**, 1929 (2022).
17. O. H.-C. Cheng, D. H. Son, and M. Sheldon, “Light-induced magnetism in plasmonic gold nanoparticles,” *Nature Photonics* **14**, 365-368 (2020).
18. T. F. Nova, A. Cartella, A. Cantaluppi, M. Först, D. Bossini, R. V. Mikhaylovskiy, A. V. Kimel, R. Merlin, and A. Cavalleri, “An effective magnetic field from optically driven phonons,” *Nature Physics* **13**, 132-136 (2017).
19. R. Mankowsky, A. von Hoegen, M. Först, and A. Cavalleri, “Ultrafast Reversal of the Ferroelectric Polarization,” *Physical Review Letters* **118**, 197601 (2017).

CHAPTER 7: Modeling Ultrafast Anharmonic Vibrational Coupling in the Gas-Phase

7.1 Abstract

In this work, we study the energy flow through anharmonic coupling of vibrational modes after excitation of gas-phase fluorobenzene with a multi-THz pump. We show that to predict the efficiency of anharmonic energy transfer simple models that only include the anharmonic coupling coefficients and motion of modes at their resonant frequency are not adequate. The full motion of each mode is needed, including the time while the mode is being driven by the pump pulse, because all the frequencies present in the multi-THz pump contribute to the excitation of the non-resonantly excited vibrational modes. Additionally, the model gives us the insight that modes with either A_1 or B_2 symmetry are more actively involved in anharmonic coupling because these modes have more symmetry-allowed energy transfer pathways.

7.2 Introduction

Gas-phase chemical reactions can occur when reactant molecules with sufficient energy for reaction collide with one another in the proper orientation. The energy necessary for reaction is often made available to the reactants through collisions with other species present in the reaction environment.¹ However, these collisions can also remove energy from the reactants, hence limiting the rate of the overall reaction. Thus, understanding collisional energy transfer (CET) between reactant molecules and other surrounding molecules is key to understanding and predicting the rate of gas-phase reactions in complex environments, including atmospheric and combustion systems.^{2,3} Because understanding CET is key to an overall determination of gas

phase reaction rates in complex environments, intermolecular energy flow from donor molecules to bath molecules in collisions has been studied extensively.²⁻²⁰

A common method to study intermolecular and intramolecular vibrational energy transfer involves using quasi-classical trajectory (QCT) calculations, especially for molecules larger than a few atoms. QCT calculations model a molecular response using a quantum potential energy surface (PES) together with classical equations of motion. QCT methods have been utilized in a variety of settings and for different applications. For intermolecular energy transfer processes, QCT calculations have been used to study the gas-phase collisional energy transfer between different small molecules,^{21, 22} same type of small molecules,²³ and reaction dynamics.²⁴⁻²⁶ Some advanced studies of intermolecular vibrational energy transfer have included intramolecular energy transfer in the modeling.^{22, 27, 28} Intramolecular energy transfer in some molecules has been studied exclusively.²⁹ In these examples, QCT calculations have been used when a global PES is not available.^{27, 28} Comparisons between QCT and full-dimensional quantum calculations have also been performed on gas phase systems where minor differences have been observed.²⁶

QCT calculation studies of intramolecular energy transfer are few in number, and because intramolecular energy transfer may heavily influence CET processes, we present QCT modeling results in this work. Intramolecular energy transfer is important because it governs how energy flows into “gateway” modes, which energy transfer studies suggest are most efficient in intermolecular energy transfer.^{1, 30} Gateway modes appear to have two important characteristics: low vibrational frequency and out-of-plane motion;^{30, 31} however, it is unclear why low frequency and out-of-plane vibrational modes would result in large energy transfers. One possible aspect of this may be due to anharmonic coupling between gateway modes and other vibrational modes in the molecule. In fact, studies of fluorobenzene gas-phase molecules indicate

that low-frequency vibrational modes have strong anharmonic coupling to high-frequency modes, suggesting that the high-frequency modes act as an energy reservoir that funnels energy to the gateway modes, and the gateway modes can then transfer energy out to the bath molecules during collisions.³ This suggests that gateway modes may be efficient, in part, because they are continually replenished with energy from other molecular motions through anharmonic coupling.

In this work, we model the behavior of anharmonic coupling in the vibrational modes of fluorobenzene using QCT calculations in order to understand the flow of intramolecular vibrational energy. This classical trajectory modeling uses coupled equations of motion derived from classical mechanics to model the motion of the atoms after an external excitation.^{32,33} As an excitation source, a mid-IR or multi-THz pump is a great option because it can potentially reach high frequencies through the process of difference frequency generation³⁴⁻³⁷ and has been used successfully to excite high frequency modes in solid materials.³⁷⁻³⁹ This would be an ideal pumping source for fluorobenzene due to having several high frequency vibrational modes ranging from ~20 to ~95 THz. Essentially, we are modeling what we would expect to observe in a gas-phase, multi-THz pump, Raman probe experiment, where we would resonantly excite IR-active modes and then observe ultrafast anharmonic coupling to other modes probed via time-resolved femtosecond stimulated Raman scattering (FSRS). With this modeling, not only do we expand our understanding of anharmonic coupling to gateway modes, but it will also be used to support future ultrafast measurements of intramolecular vibrational energy transfer, which will aid in our understanding of energy flow prior to CET in gas-phase molecules. It is worth mentioning that other approaches have been taken when working with condensed matter systems, in particular liquids,^{40,41} however, our QCT approach on fluorobenzene seems

appropriate because these calculations are commonly performed on small molecule gas samples, and here we do not consider the influence of intermolecular collisions.

7.3 Methods

We calculate the angular harmonic frequencies (ω_i), the IR intensities (β_i^2), the eigenvectors that describe atomic motion, and the third (ϕ_{ijk}) and fourth (ϕ_{ijkl}) order anharmonic coupling constants using density functional theory (B3LYP) and a cc-pvqz basis set in Gaussian 09.⁴² The symmetry of the vibrational modes and the IR intensities along with their respective frequencies can be found in Table 7-1 in the Appendix section. The 1331 third order and 3817 fourth order coupling constants (unique, symmetry allowed) are included as separate files (see Appendix section for details on the coupling constants). These frequencies and coupling constants describe the shape of the anharmonic PES for the vibrational motion of a molecule, and the shape of the PES governs how energy flows within the molecule. These parameters were then incorporated into classical coupled equations of motion in the form of

$$\ddot{Q}_i + \omega_i^2 Q_i = \beta_i E(t) - \sum \phi_{ijk} Q_j Q_k - \sum \phi_{ijkl} Q_j Q_k Q_l, \quad (7-1)$$

where Q_i represents the motion of the i th vibrational mode, \ddot{Q}_i is the acceleration of the i th vibrational mode, and $E(t)$ is the pump electric field that acts as a driving force. The mid-IR pump field is modeled as

$$E(t) = E_0 \exp\{-((t - t_0)/\tau)^2\} \exp\{i(\omega_0(t - t_0) + \phi)\}, \quad (7-2)$$

where E_0 is the electric field amplitude, τ is the FWHM pulse duration, ω_0 is the center pump angular frequency and ϕ is the carrier-envelope offset phase (set to zero in our modeling).

These coupled equations of motion were used to model the classical trajectories of each vibrational mode on the PES after excitation with a multi-THz pump. In simple terms, the

equations of motion (Eq. 7-1) can be divided into two parts with the right side being the “driving force” and the left side as what is being excited, the vibrational mode of interest, Q_i . From the equations of motion, it can be noticed that any vibrational mode Q_i , can be excited by two driving forces: (1) directly by the THz electric field ($\beta_i E(t)$ from Eq. 7-1) if the mode is IR-active ($\beta_i \neq 0$) (see Fig. 7-1c) or (2) indirectly by anharmonic coupling ($\phi_{ijk} Q_j Q_k$ and/or $\phi_{ijkl} Q_j Q_k Q_l$ from Eq. 7-1) between non-resonant vibrational mode(s) and resonantly excited mode(s) (see Figs. 7-1b and 7-1d). The first driving force, represented as $\beta_i E(t)$ in Eq. 7-1, will be the most efficient if there is a large spectral amplitude of the THz pump at the frequency of mode Q_i . The second driving force, represented by the anharmonic terms $\phi_{ijk} Q_j Q_k$ and $\phi_{ijkl} Q_j Q_k Q_l$ from Eq. 7-1, depends on the product of motion of other modes and the resulting spectral amplitude at the resonant frequency of mode Q_i . As will be shown later, the equations of motion are a crucial part in understanding how the anharmonic-coupling driving force is related to the motion of all the vibrational modes in fluorobenzene.

In order to model the ultrafast, resonant excitation of vibrational modes, we modeled a 100 fs THz pump pulse set to specific frequencies (96, 49, 40, 33, 28, 21, 15, and 7 THz) with a bandwidth of ~ 5.3 THz to directly excite vibrational modes whose harmonic frequencies lie within the bandwidth of the THz pump pulse (see bandwidth represented in Fig. 7-1a). Fig. 7-1a shows the IR intensities as a function of mode frequency (THz on the lower axis and cm^{-1} on the upper axis) of the IR-active modes in fluorobenzene, with the line colors indicating the mode symmetry. Using coupled equations of motion, the motion of all the vibrational modes was modeled from -1 to 2 ps. Fig. 7-1b shows eigenvectors for a high frequency A_1 vibrational mode (95.7 THz) and a low frequency B_2 mode (12.2 THz) with an arrow to visualize energy flow between the modes. Figs. 7-1c and 7-1d show the actual modeled motion of these vibrational

modes. Fig. 7-1c shows the excitation waveform for a 96 THz pump pulse in black, and the resulting motions for the resonantly excited 95.7 THz mode and the non-resonantly excited 12.2 THz mode in red and blue, respectively. Meanwhile, Fig. 7-1d zooms in on the motion of the 12.2 THz mode from Fig. 7-1c, which was excited nonlinearly via anharmonic coupling to resonantly excited mode(s). We see that there is some initial motion while this mode is being non-resonantly driven by the incident field, and then after about 0.2 ps, we see the mode is oscillating at its own resonant frequency. The magnitude of the amplitude is a measure of intramolecular vibrational energy transfer between the resonant and the non-resonant vibrational modes, which occurs through anharmonic vibrational coupling.

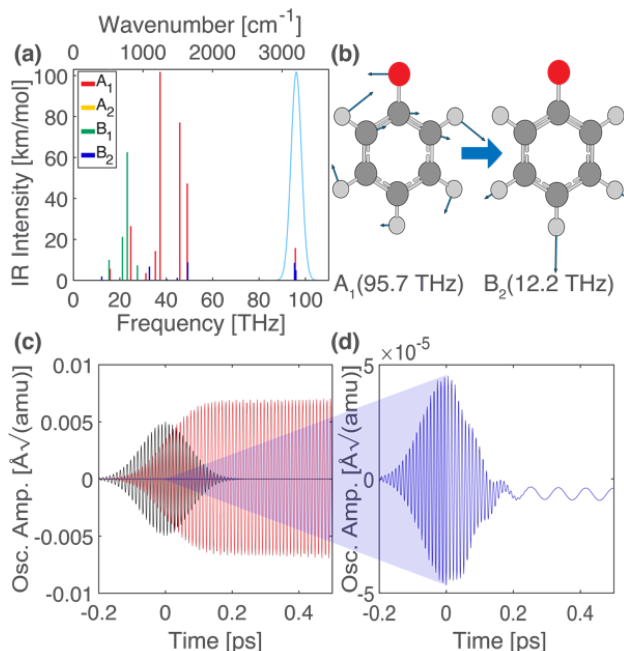


Figure 7-1: (a) The IR Intensity as a function of the harmonic frequency of each vibrational mode in fluorobenzene. The frequencies are listed in wavenumber (top axis) and in THz (bottom axis) units. The legend shows the symmetries of the vibrational modes: A₁ (red), A₂ (yellow), B₁ (green) and B₂ (blue). The light blue curve shows a scaled 96 THz pump excitation spectrum with a ~ 5.3 THz bandwidth. (b) Pictorial representation of a resonantly excited 95.7 THz vibrational mode (left) transferring energy to an anharmonically coupled non-resonant 12.2 THz mode (right). The vectors show the respective motion of the atoms. (c) Modeled time trace depicting a 96 THz pump pulse (black) that excites a resonant 95.7 THz vibrational mode (red) that lies within its pump bandwidth. The oscillations of the resonantly excited mode(s) anharmonically excite a 12.2 THz non-resonant mode (blue). (d) The oscillation motion of the non-resonant 12.2 THz mode (blue) from (c) is zoomed in because it is two orders of magnitude smaller in amplitude than the resonantly excited 95.7 THz mode.

7.4 Results

Resonant excitation of certain vibrational modes can lead to the transfer of energy to other, non-resonant modes through anharmonic coupling. This mechanism can be described by the equations of motion in which a driving force is introduced and used to resonantly excite a subset of vibrational modes at their respective frequency. By solving for the motion of each vibrational mode for a range of THz pump frequencies, we see large oscillations for modes that were directly pumped; and we also observe oscillations from non-resonant modes, which indicates that energy transfer has occurred through anharmonic coupling from resonantly excited modes.

The maximum peak-to-peak oscillation amplitude, after the resonant driving force ended, was extracted for each vibrational mode. For example, the mode amplitude in Figs. 7-1c and 7-1d was extracted from 0.3 to 0.5 ps. In Figs. 7-2a and 7-2b, we plot the mode amplitude as a function of mode frequency in THz, which shows the behavior of the vibrational modes subjected to a (a) 96 THz and (b) 49 THz pump (pump frequencies indicated by orange stripes); the behavior for other THz pump frequencies can be found in Figs. 7-7a to 7-7f of the Appendix section. Each non-resonant vibrational mode clearly differs in amplitude, thus showing that certain modes have more efficient anharmonic energy transfer pathways for a given pump frequency. We also show this in terms of energies by scaling the maximum oscillation amplitudes of each mode with their respective frequency in THz for both of these pumps in Figs. 7-2c and 7-2d (refer to Figs. 7-7g to 7-7l of the Appendix section to see plots for other pump frequencies in terms of energy as well). Due to the general trends in oscillation amplitudes and energy of the vibrational modes transferred almost being the same with a few minor shifts, we

will use the oscillation amplitude in subsequent discussions in accordance with the equations of motion (Eq. 7-1).

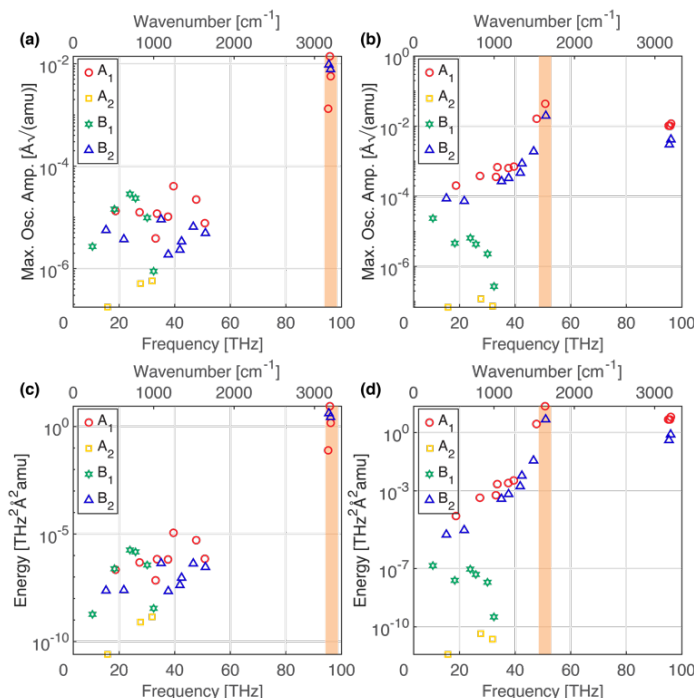


Figure 7-2: Maximum oscillation amplitude for each vibrational mode in fluorobenzene as a function of their mode frequency after excitation with a (a) 96 THz and (b) 49 THz pump. The maximum oscillation amplitudes were also converted in terms of energy for both the (c) 96 THz and (d) 49 THz pump. The center frequency for each pump is shown as an orange stripe. The width of the orange stripe was set to match the bandwidth of the THz pump (~5.3 THz). The frequencies are shown in both wavenumber (top axis) and in THz (bottom axis) units. The legend shows the symmetries of the vibrational modes: A₁ (circles, red), A₂ (squares, yellow), B₁ (stars, green) and B₂ (triangles, blue). A logarithmic amplitude scale was used to better distinguish the oscillation amplitudes of the non-resonant vibrational modes.

In order to understand why some modes are more efficient than others in the energy transfer process, different portions of the equation of motion were manipulated to determine the simplest form for contributing factors. In particular, we focused on determining the relationship and contribution between the maximum oscillation amplitude of a driven mode, which is related to the energy transfer, and the driving force terms containing the anharmonic coupling constants on the right-hand side of Eq. 7-1.

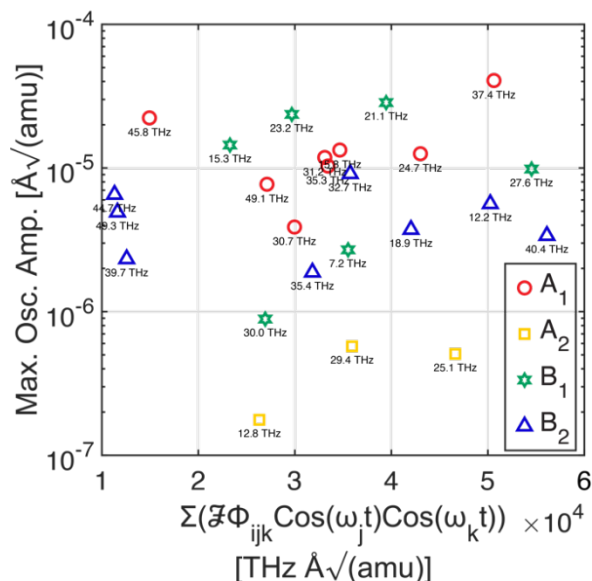
In one of our initial approaches, we took the product between the coupling constants and a simple sinusoidal model of the motion of each mode (oscillating at their respective resonant

frequencies). With the motion being modeled as cosine functions, the anharmonic coupling terms in Eq. 7-1 were modified as follows:

$$\sum \phi_{ijk} Q_j Q_k \rightarrow \sum \phi_{ijk} \cos(\omega_j t) \cos(\omega_k t), \quad (7-3)$$

$$\sum \phi_{ijkl} Q_j Q_k Q_l \rightarrow \sum \phi_{ijkl} \cos(\omega_j t) \cos(\omega_k t) \cos(\omega_l t). \quad (7-4)$$

These products include both the effects of the magnitude of the coupling constants and the motion at the resonant frequency of each vibrational mode. In the case of third-order anharmonic coupling, the product of cosine terms will give the expected largest amplitudes at the sums and differences of ω_j and ω_k frequencies. We model this combined motion for every mode and then extract the Fourier amplitude of this product at the frequency of the mode of interest Q_i and multiply the Fourier amplitude by the coupling constant. We then sum this amplitude for all possible couplings. Fig. 7-3 shows these sums over all the allowed terms along the x-axis compared to the modeled amplitude of each mode on the y-axis.



From Fig. 7-3, we note that there is no clear correlation between the x-axis and the y-axis: a high value in the summed amplitudes of the coupling terms along the x-axis does not necessarily show a high oscillation amplitude. Similar non-correlated behaviors were observed at the other THz pump frequencies and in the quartic coupling constant analysis (see Fig. 7-8 of the Appendix section for a few examples). Due to this lack of correlation, which we also saw in another approach where we only used the anharmonic coupling constants, it is clear that only accounting for coupling constants and motion at the resonant frequency of each mode is not adequate to explain why certain vibrational modes have higher or lower oscillation amplitudes upon excitation.

Subsequently, we removed the approximation that each mode only oscillates at its resonant frequency to more accurately explain the modeled intramolecular energy transfer efficiency. To improve upon the previous approach, we used the complete modeled motion of each vibrational mode (Q_i) (Eq. 7-1), rather than just cosine functions oscillating at the mode frequencies (Eq. 7-3 and Eq. 7-4). The benefit of using the complete motion is that Eq. 7-3 and Eq. 7-4 neglect the initial motion that each mode can experience. For example, while being driven by the multi-THz pump field, all IR-active modes include some initial motion that contains all the frequency components within the pump bandwidth (~5.3 THz). This is particularly apparent in Figs. 7-1c and 7-1d where, even when a mode is non-resonant with the pump, the initial motion follows the pump field (see early times in Fig. 7-1d). When we approximate the motion only at the resonant frequency of each mode (Eq. 7-3 and Eq. 7-4), we can only get frequency mixing caused by the sum and differences of the resonant frequencies and we neglect this initial motion. But when we include the entire motion, including the initial motion temporarily driven by the pump field, the coupled motion of two or more vibrational

modes (particularly those that are resonantly driven) can anharmonically drive motion of essentially every other mode.

To validate this more complete approach to understanding anharmonic energy flow, we multiplied each anharmonic coupling constant by the complete modeled motion of each mode, then take the Fourier transform of this product, and we extract the Fourier amplitudes of these new products at the frequency of the mode we were driving. The resulting values were summed to produce the x-axis in Fig. 7-4, and compared to the maximum oscillation amplitude as the y-axis for each vibrational mode. We note that this new x-axis is the sum of the Fourier amplitudes of each third-order anharmonic term from our coupled equation of motion (Eq. 7-1).

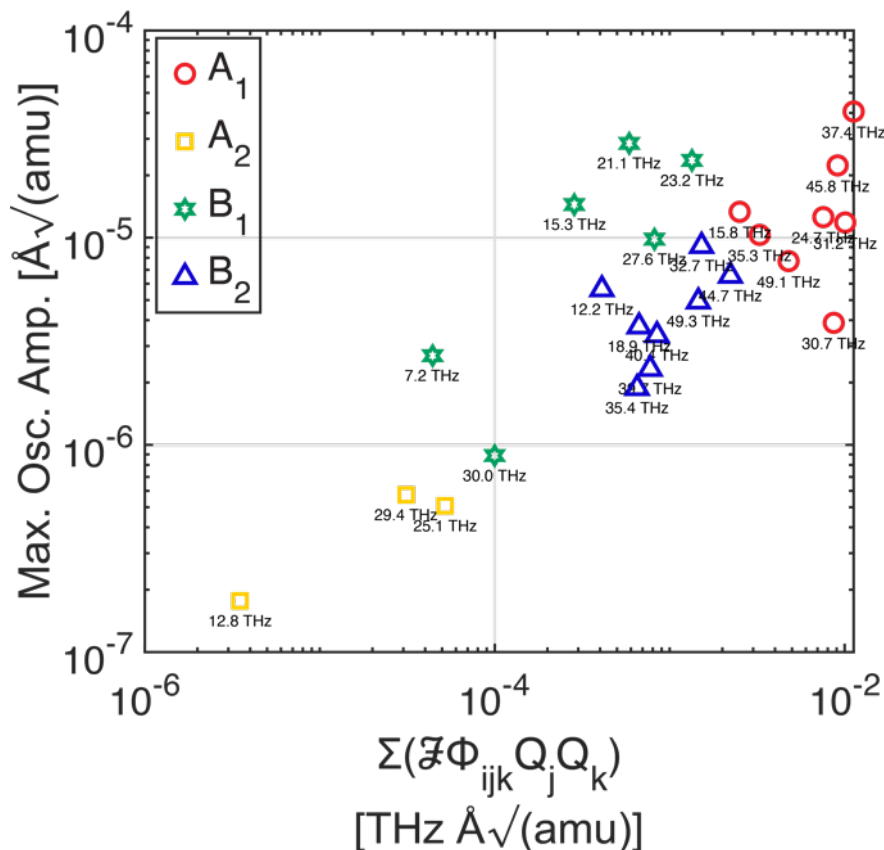


Figure 7-4: The maximum oscillation amplitude for each vibrational mode Q_i modeled as a function of the sum of the Fourier amplitude of each product ($\phi_{ijk}Q_jQ_k$) at a 96 THz pump frequency. The legend shows the symmetries of the vibrational modes: A₁ (circles, red), A₂ (squares, yellow), B₁ (stars, green) and B₂ (triangles, blue). The frequency of each vibrational mode is displayed under its respective marker.

In Fig. 7-4, we are only displaying the maximum oscillation amplitude behavior of the vibrational modes after being excited with a 96 THz pump and the x-axis only involves $\phi_{ijk}Q_jQ_k$ (third-order couplings). We observe a stronger positive trend as the maximum oscillation amplitude increases as a function of the sum of the Fourier amplitudes of each product of $\phi_{ijk}Q_jQ_k$. Although we are only showing the 96 THz pump, the same positive correlation was also observed for all other THz pumps frequencies, as seen in Figs. 7-9a, 7-9c and 7-9e of the Appendix section. This correlation was also observed for the plots involving only $\phi_{ijkl}Q_jQ_kQ_l$ (fourth-order couplings), as seen in Figs. 7-9b, 7-9d and 7-9f of the Appendix section, although not as pronounced as the plots that only involved third-order couplings. This approach does not account for potential phase differences due to signs of different coupling constants being opposite, and we expect this to account for the imperfections in the correlation. Regardless, this final approximation demonstrates that effects of the multi-THz driving force must be included to more completely understand ultrafast anharmonic energy flow.

Finally, we analyzed if any particular modes or mode symmetries consistently garnered more of the anharmonic energy flow (resulting in the largest oscillation amplitudes). Fig. 7-5 shows the oscillation amplitude for each mode, with the mode frequency along the x-axis, the pump frequency along the y-axis, and the oscillation amplitude along the vertical z-axis. Naturally, we see the largest amplitudes for many modes when the pump frequency is resonant with the probe frequency (light orange stripe along the diagonal, with many amplitudes larger than the depicted z-axis). Black arrows indicate some regions where the oscillation amplitudes are the largest, due to anharmonic coupling. Notably, this most often happens for A_1 and B_2 symmetry modes. We also note that several modes are most efficiently excited when pumped at $\sim 1/2$ their resonant frequency (light red stripe). This can be explained by looking at the products

of terms in Eq. 7-1 and 7-3, which lead to sum-frequency driving forces at twice the resonant frequency.

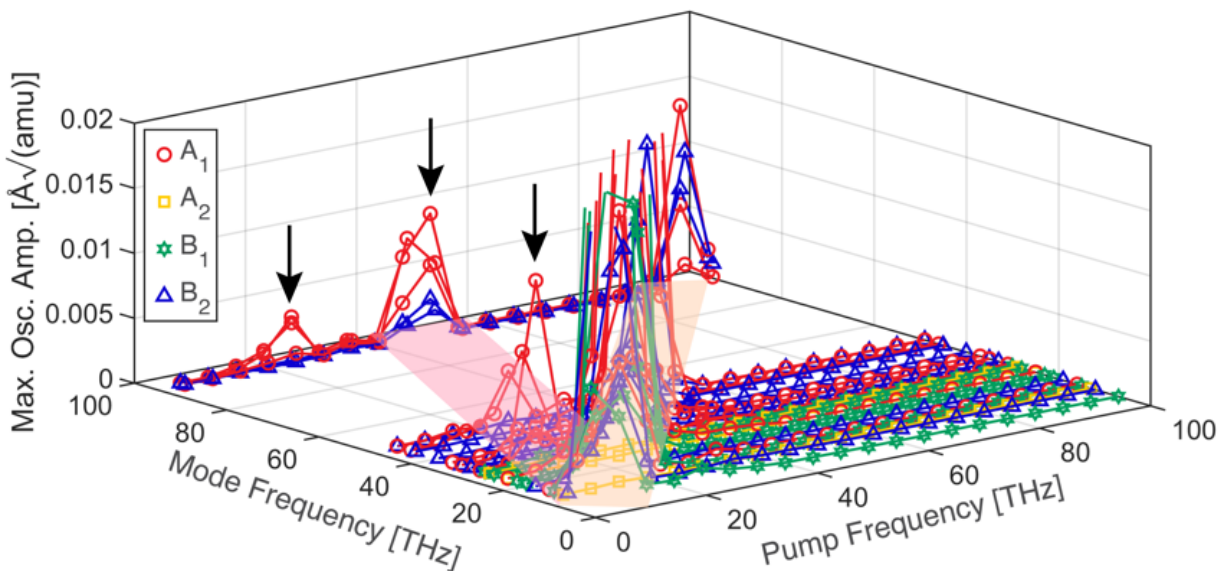


Figure 7-5: The maximum oscillation amplitude as function of mode and pump frequency in THz. A light orange stripe highlights the region where modes are resonantly excited and a light red stripe highlights where the mode frequency is equal to twice the pump frequency. Arrows are used to point out off-diagonal vibrational modes. The legend shows the symmetries of the vibrational modes: A₁ (circles, red), A₂ (squares, yellow), B₁ (stars, green) and B₂ (triangles, blue).

7.5 Discussion

In Fig. 7-5, we observe that modes with A₁ and B₂ symmetry are more frequently involved in efficient intramolecular anharmonic energy transfer. While both are efficient, the A₁ modes seem to be more efficient than the B₂ modes due to the observed larger amplitudes. This can be explained if we first take a closer look at the anharmonic coupling contributions in the equations of motion (Eq. 7-1).

The third order anharmonic coupling term in Eq. 7-1, $\phi_{ijk}Q_iQ_jQ_k$, describes the energy flow process associated with pumping both the Q_j and Q_k modes and then probing energy flow into the Q_i mode. Such third-order coupling is allowed if the direct product of the mode-

symmetries contains the fully-symmetric representation (A_1 for fluorobenzene) according to Eq. 7-5.

$$Q_j \otimes Q_k \otimes Q_i \tag{7-5}$$

Because of their involvement in energy transfer through anharmonic coupling (see Fig. 7-5), we only consider direct products where the probed modes, Q_i , were either of A_1 or B_2 symmetry. Using Eq. 7-5 to consider the direct products that allow energy transfer to the A_1 modes gives four direct products that contain the totally symmetric representation.

$$A_1 \otimes A_1 \otimes A_1 \subset A_1 \rightarrow A_1$$

$$A_2 \otimes A_2 \otimes A_1 \subset A_1 \rightarrow A_1$$

$$B_1 \otimes B_1 \otimes A_1 \subset A_1 \rightarrow A_1$$

$$B_2 \otimes B_2 \otimes A_1 \subset A_1 \rightarrow A_1$$

However, we only have two direct products that allow for energy transfer to B_2 modes.

$$A_1 \otimes B_2 \otimes B_2 \subset A_1 \rightarrow B_2$$

$$A_2 \otimes B_1 \otimes B_2 \subset A_1 \rightarrow B_2$$

This alone, suggests that A_1 modes can be more involved in anharmonic coupling than B_2 modes because they have more possible ways to interact as it is always possible to double-excite a single mode. For example, one of the A_1 modes at ~95-96 THz, seen in the off-diagonal region in Fig. 7-5, can be anharmonically pumped by either doubly exciting the 49.3 THz B_2 mode or the 49.1 THz A_1 mode (see Fig. 7-1a). In the case of B_2 , there are fewer options due to the requirement of two modes with different symmetries being simultaneously excited. For example, in the off-diagonal region of Fig. 7-5, we see that there are two B_2 modes at ~95-96 THz with significant anharmonic excitation. In order to pump either of these modes through anharmonic coupling, two modes (one with A_1 and one with B_2 symmetry) whose frequencies add up to ~95-

96 THz need to be pumped. In Fig. 7-1a, we see two modes of A_1 and B_2 symmetry with frequencies of 49.1 THz and 44.7 THz, respectively, that can work together to excite a B_2 mode at ~ 95 -96 THz.

We also compared the results of our energy transfer model through anharmonic coupling on gas-phase fluorobenzene with measurements performed on liquid fluorobenzene through the IR-Raman technique presented in Ref 43 by the Dlott group.⁴³ In their work, they used a 3068 cm^{-1} pump (~ 92 THz) to excite a high frequency vibrational mode in the mono-halogenated benzenes, including fluorobenzene, and observed the energy transfer to the other vibrational modes. In Fig. 4a of Ref 43, they show the initial resonant excitation of the 3075 cm^{-1} (~ 92 THz) vibrational mode in fluorobenzene and after a few picoseconds, they observe the increase in intensity of several non-resonant modes in the 500-1500 cm^{-1} (~ 15 -45 THz) region. Upon closer inspection of their Fig. 4a, evidence of energy flowing out of the resonant mode can be observed because its peak at the resonant frequency completely disappears after ~ 3 ps, which indicates interference from intermolecular energy transfer processes that may overshadow the intramolecular energy flow.

When working with liquid samples, intermolecular energy transfer processes occur more frequently than in gas samples due to the proximity of molecules to each other. Clear differences between the intramolecular energy transfer we model and the apparent intermolecular energy transfer in Ref. 43 are more apparent when we take a closer look at the energy transfer between vibrational modes of fluorobenzene. For comparison, we extracted the maximum of the occupation number and quantum yield of the fluorobenzene vibrational modes from Fig. 5 and Figs. 6-11 of Ref 43, respectively. The extracted quantum yield maximums were converted to occupation number and were then multiplied by their respective frequency in THz to express

them in terms of energy. We plotted the extracted energies as a function of mode frequency in Fig. 7-6. Fig. 7-6 only shows one resonant mode and six non-resonant vibrational modes because of the limitations with their detection, and it also shows their pump (~ 92 THz) as an orange line with a bandwidth of 25 cm^{-1} (~ 0.7 THz). Fig. 7-6 can then be compared to Fig. 7-2c of this work because they both show the resonant excitation of high frequency vibrational mode(s) with a high frequency pump (~ 95 THz or ~ 92 THz) and the subsequent energy flow to some non-resonant vibrational modes. Figs. 7-6 and 7-2c do not show the same energy transfer behaviors. In Fig. 7-6, the non-resonant modes in the liquid phase have much larger amount of energy transferred to them compared to our gas-phase modeling.

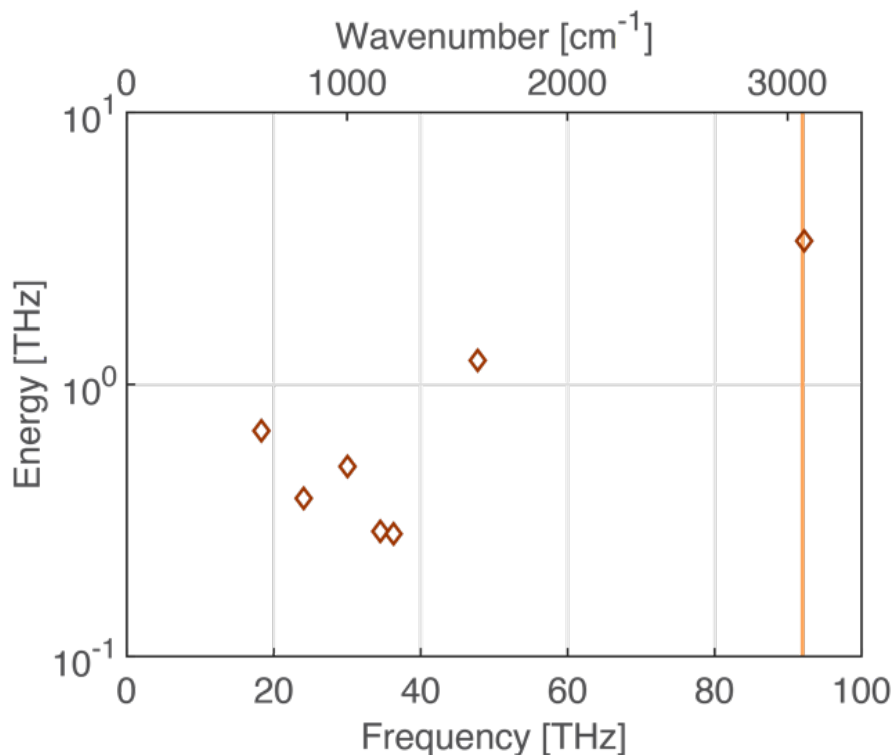


Figure 7-6: Extracted data from Ref 43. After resonantly exciting liquid fluorobenzene with a 3068 cm^{-1} pump (~ 92 THz), we show the energy deposited in the vibrational modes. The pump is shown as an orange line with a bandwidth of 25 cm^{-1} (~ 0.7 THz). The energy deposited in this liquid-phase fluorobenzene experiment from Ref 43 can be directly compared to Fig. 7-2c above showing differences in the modeled energy transfer for fluorobenzene in gas-phase.

The outcomes from this model have expanded our understanding of the role of anharmonic coupling in intramolecular energy transfer in gas-phase fluorobenzene, and provided more insight into the symmetry of the modes involved in this process. This modeling allows us to support future experiments involving FSRS measurements of energy transfer in gas-phase fluorobenzene molecules.

7.6 Conclusion

We have modeled anharmonic energy transfer after excitation with a multi-THz pump using first principles calculations to determine why certain vibrational modes are more efficient at receiving energy in intramolecular energy transfer. This QCT model shows that only including the motion of each mode at its resonant frequency together with the magnitude of the coupling constants is not sufficient to predict the anharmonic excitation of vibrational modes. To most accurately predict the amplitude of non-resonantly excited vibrational modes, we must account for the full motion of each mode, including the motion while it is being driven by the ultrafast pump pulse. In this manner, the spectral amplitude of the anharmonic driving force from the equation of motion has a linear one-to-one correspondence with the resulting amplitude of the mode desired to be non-resonantly excited. Our modeling also shows that the symmetry of the excited and probed modes is a key element, and that both A_1 or B_2 symmetry modes are strongly involved in anharmonic coupling, with A_1 modes being more efficiently excited due to multiple symmetry-allowed energy transfer pathways. This modeling helps us better understand factors that influence intramolecular vibrational energy flow, that is a crucial component in understanding collisional energy transfer.

7.7 Acknowledgments

This project was funded by the Simmons Research Fund and the Charles E. & Margaret P. Maw Fellowship (A. A.).

7.8 Appendix

We calculated important parameters of the quantum potential energy surface necessary to solve the equations of motion to model (with quasi-classical trajectories (QCT)) intramolecular vibrational anharmonic energy transfer in a fluorobenzene molecule. We used density functional theory (B3LYP) and a cc-pvqz basis set in Gaussian 09. In Table 7-1 below, we list the symmetry of the vibrational modes, the IR intensities and the frequencies in both cm^{-1} and THz. This work will be submitted to the Journal of Chemical Physics, and the cubic and quartic anharmonic coupling constants can be found in the attached CSV files once it is published.

Table 7-1. Quantum parameters used to model intramolecular vibrational energy transfer through anharmonic coupling in a fluorobenzene molecule.

Symmetry	IR Intensity (Km/mole)	Frequency (cm^{-1})	Frequency (THz)
A ₁	0.2542	3201.2373	95.97
B ₂	4.9289	3199.0785	95.91
A ₁	15.8107	3190.6568	95.65
B ₂	8.5635	3178.668	95.29
A ₁	0.1184	3170.1086	95.04
B ₂	8.8212	1643.4195	49.27
A ₁	47.2761	1636.1962	49.05
A ₁	77.0547	1529.2442	45.85
B ₂	1.2622	1492.3452	44.74
B ₂	0.4942	1347.0504	40.38
B ₂	0.2255	1325.7441	39.74
A ₁	101.7706	1246.1081	37.36
B ₂	0.2338	1181.349	35.42

Table 7-1. Continued

Symmetry	IR Intensity (Km/mole)	Frequency (cm ⁻¹)	Frequency (THz)
A ₁	14.2978	1178.4174	35.33
B ₂	6.7300	1092.314	32.75
A ₁	3.5438	1041.3863	31.22
A ₁	0.3268	1023.8341	30.69
B ₁	0.1057	999.3693	29.96
A ₂	0.0000	980.9546	29.41
B ₁	7.3403	919.2379	27.56
A ₂	0.0000	836.9171	25.09
A ₁	26.4939	824.6381	24.72
B ₁	62.6013	774.0221	23.20
B ₁	21.2486	704.9002	21.13
B ₂	0.1768	629.2287	18.86
A ₁	5.6382	526.5852	15.79
B ₁	10.0061	511.9745	15.35
A ₂	0.0000	425.9872	12.77
B ₂	1.9186	407.2158	12.21
B ₁	0.0827	238.9351	7.16

As shown in Fig. 7-2, we extracted the maximum oscillation amplitude for each vibrational mode after excitation with a resonant (a) 96 THz and (b) 49 THz pump and plotted them as a function of their mode frequency in THz. We also converted the maximum oscillation amplitude in terms of energy for the both of these THz pumps in Figs. 7-2c and 7-2d. In Fig. 7-7, we show the maximum oscillation amplitudes as a function of mode frequency for the additional THz pumps: (a) 40, (b) 33, (c) 28, (d) 21, (e) 15 and (f) 7 THz. Additionally, we show the maximum oscillation amplitude converted to energy for these six additional pumps in Figs. 7-7g to 7-7l.

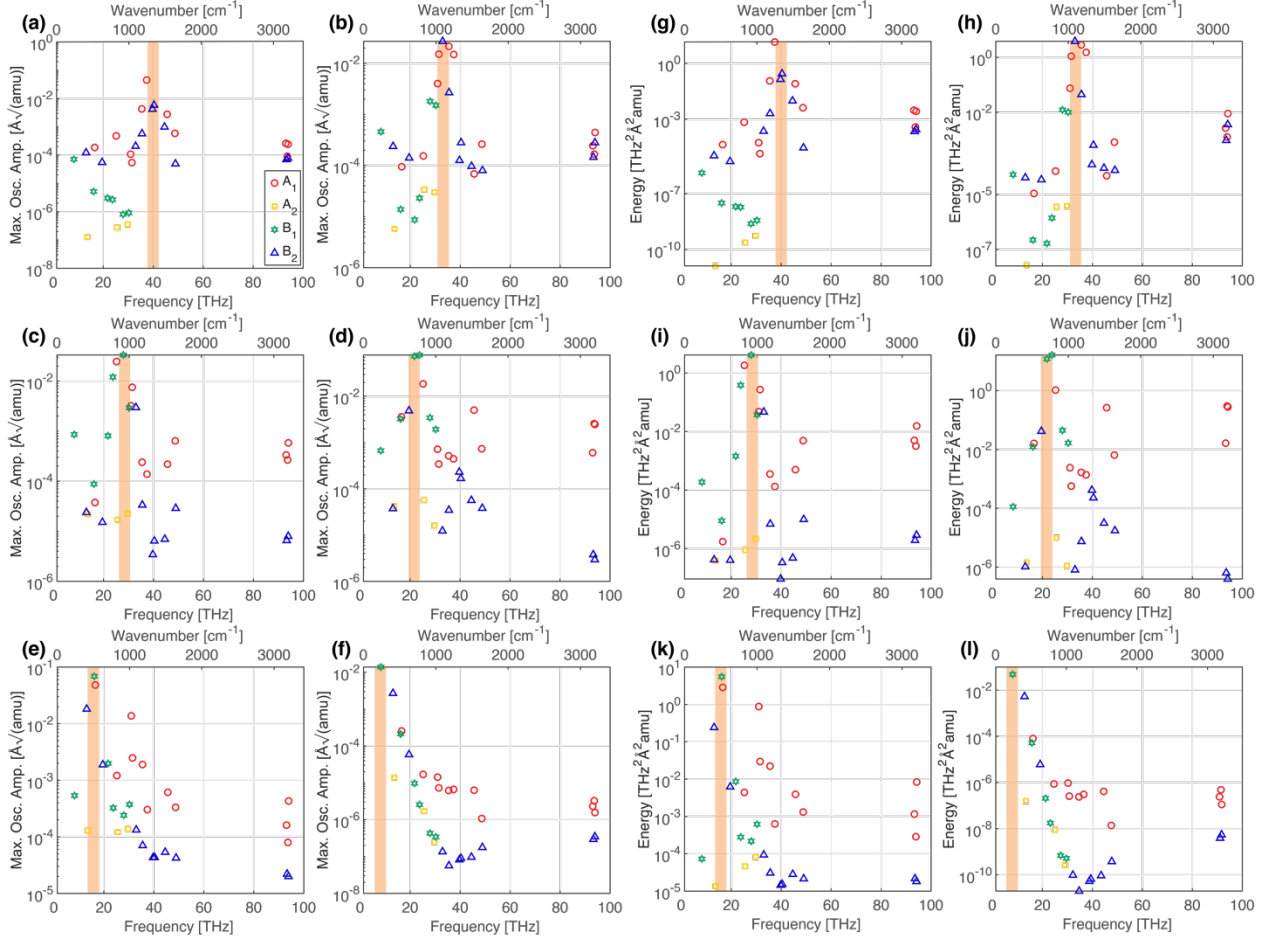


Figure 7-7: Maximum oscillation amplitude for each vibrational mode Q_i in fluorobenzene as a function of their respective harmonic frequencies after excitation with a (a) 40, (b) 33, (c) 28, (d) 21, (e) 15 and (f) 7 THz pump pulse. The maximum oscillation amplitude converted in terms of energy are shown for these same THz pumps in (g) 40, (h) 33, (i) 28, (j) 21, (k) 15 and (l) 7. The center frequency for each pump is shown as an orange stripe. The mode frequencies are shown in both wavenumber (top axis) and in THz (bottom axis) units. The legend in (a) shows the symmetries of the vibrational modes for each THz pump: A_1 (circles, red), A_2 (squares, yellow), B_1 (stars, green) and B_2 (triangles, blue). A logarithmic amplitude scale was used to better distinguish the oscillation amplitudes of the non-resonant vibrational modes.

In one of our initial approaches, we included the oscillation of each vibrational mode at its resonant frequency by using a sinusoidal model (see Eq. 7-3 and Eq. 7-4), in addition to including the anharmonic coupling constants, to explain the energy transfer between vibrational modes. This required us to multiply the anharmonic coupling constants by the modeled frequencies as cosine functions. In section 7.4, we only show the maximum oscillation amplitude as a function of $\sum \phi_{ijk} \cos(\omega_j t) \cos(\omega_k t)$ for the 96 THz pump. In Fig. 7-8, we show this modeling for the same

(a) 96 THz and for two additional pumps: (c) 28 and (e) 7 THz. We also include the modeling involving the quartic anharmonic coupling constants ($\sum \phi_{ijkl} \cos(\omega_j t) \cos(\omega_k t) \cos(\omega_l t)$) using these same pump pulses: (b) 96, (d) 28 and (f) 7 THz. As mentioned in section 7.4, we do not observe any correlation between the maximum oscillation amplitude and the quantity $\sum \phi_{ijk} \cos(\omega_j t) \cos(\omega_k t)$ or $\sum \phi_{ijkl} \cos(\omega_j t) \cos(\omega_k t) \cos(\omega_l t)$.

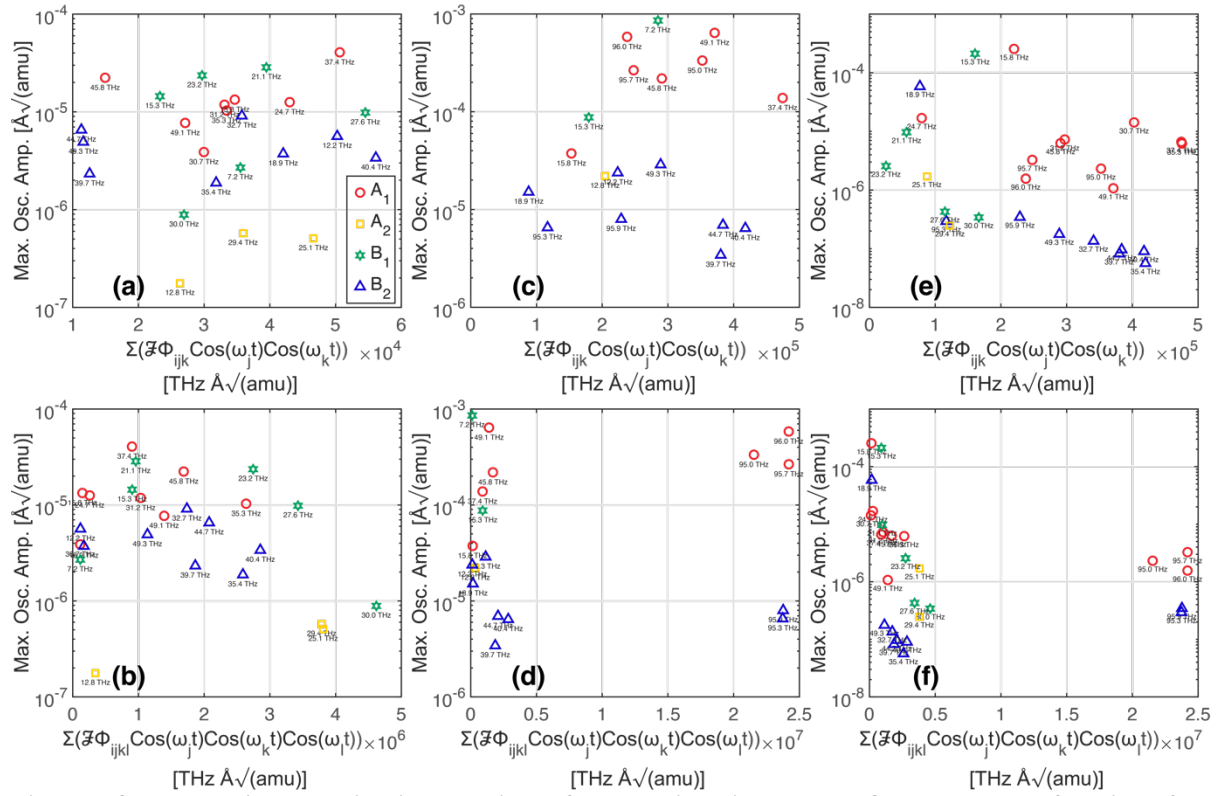


Figure 7-8: The maximum oscillation amplitude for each vibrational mode Q_i modeled as a function of the sum of the Fourier amplitude of each product $\phi_{ijk} \cos(\omega_j t) \cos(\omega_k t)$ at the mode frequency after excitation with a (a) 96, (c) 28 and (e) 7 THz pump pulse. The maximum oscillation amplitude was also modeled as a function of the sum of the Fourier amplitude of each product $\phi_{ijkl} \cos(\omega_j t) \cos(\omega_k t) \cos(\omega_l t)$ at the mode frequency after excitation with a (b) 96, (d) 28 and (f) 7 THz pump pulse. The legend in (a) shows the symmetries of the vibrational modes for each THz pump: A₁ (circles, red), A₂ (squares, yellow), B₁ (stars, green) and B₂ (triangles, blue). The frequency of each vibrational mode is displayed under the respective marker.

In our final approach, we used the actual modeled motion of each vibrational mode upon being anharmonically excited. The cosine functions from the previous attempt were replaced by

the motion of each vibrational mode. In section 7.4, we modeled the maximum oscillation amplitude as a function of the sum of the Fourier amplitude of $\phi_{ijk}Q_jQ_k$ for the 96 THz pump. In Fig. 7-9, we show the same (a) 96 THz pump with two additional pumps: (c) 28 and (e) 7 THz. We also include the model using quartic anharmonic coupling constants ($\phi_{ijkl}Q_jQ_kQ_l$) using these same pumps: (b) 96, (d) 28 and (f) 7 THz. As mentioned in section 7.4, this final approach showed a positive correlation between the maximum oscillation amplitude and the sum of the Fourier amplitudes of $\phi_{ijk}Q_jQ_k$ or $\phi_{ijkl}Q_jQ_kQ_l$.

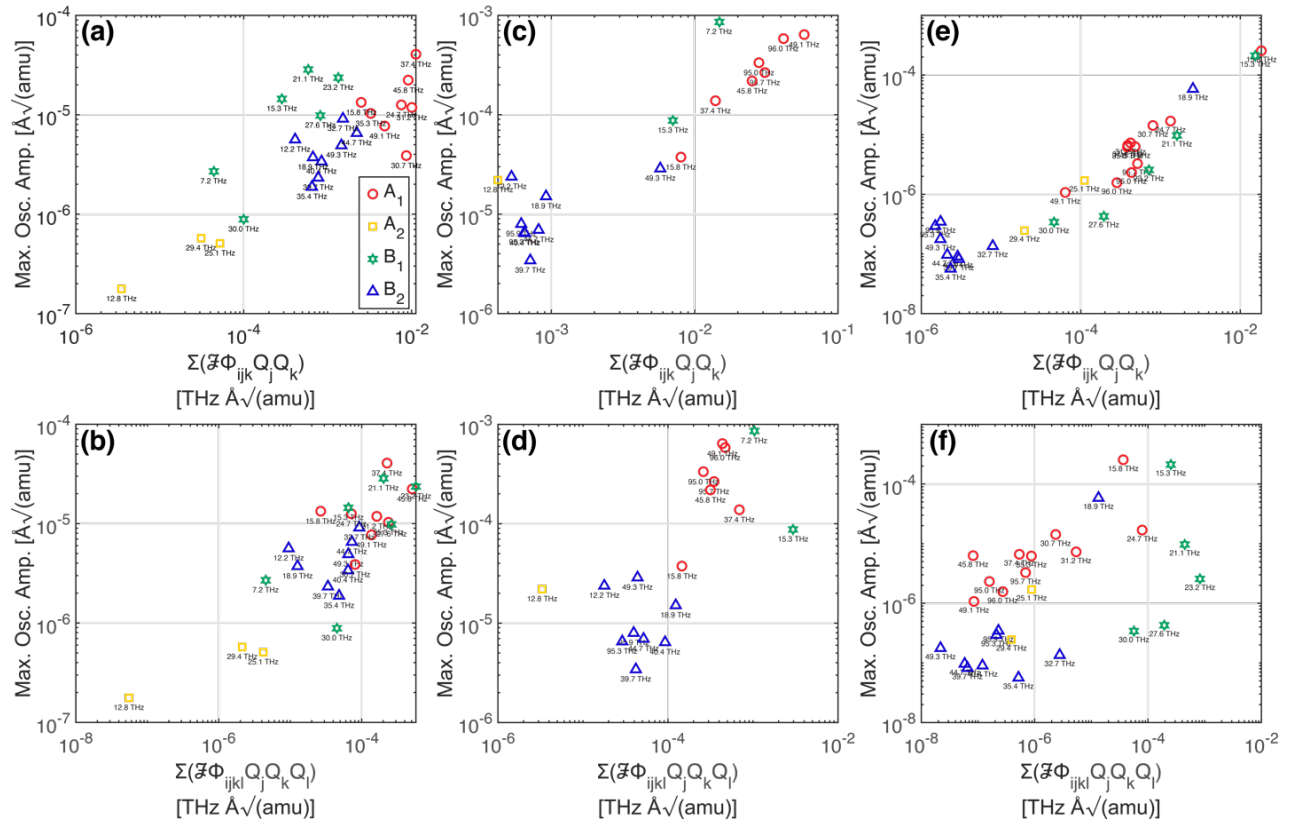


Figure 7-9: The maximum oscillation amplitude for each vibrational mode Q_i modeled as a function of the sum of the Fourier amplitude of each product $\phi_{ijk}Q_jQ_k$ after excitation with a (a) 96, (c) 28 and (e) 7 THz pump pulse. The maximum oscillation amplitude was also modeled as a function of the sum of the Fourier amplitude of each product $\phi_{ijkl}Q_jQ_kQ_l$ at the same pumps: (b) 96, (d) 28 and (f) 7 THz. The legend in (a) shows the symmetries of the vibrational modes: A_1 (circles, red), A_2 (squares, yellow), B_1 (stars, green) and B_2 (triangles, blue). The frequency of each vibrational mode is displayed under the respective marker.

7.9 References

1. V. Bernshtein, and I. Oref, "Gateway Modes for Collisional Energy Transfer between Benzene and Ar," *The Journal of Physical Chemistry A* **105**, 10646-10650 (2001).
2. J. A. Johnson, K. Kim, M. Mayhew, D. G. Mitchell, and E. T. Sevy, "Rotationally Resolved IR-Diode Laser Studies of Ground-State CO₂ Excited by Collisions with Vibrationally Excited Pyridine," *The Journal of Physical Chemistry A* **112**, 2543-2552 (2008).
3. K. Kim, A. M. Johnson, A. L. Powell, D. G. Mitchell, and E. T. Sevy, "High resolution IR diode laser study of collisional energy transfer between highly vibrationally excited monofluorobenzene and CO₂: The effect of donor fluorination on strong collision energy transfer," *The Journal of Chemical Physics* **141**, 234306 (2014).
4. D. G. Mitchell, A. M. Johnson, J. A. Johnson, K. A. Judd, K. Kim, M. Mayhew, A. L. Powell, and E. T. Sevy, "Collisional Relaxation of the Three Vibrationally Excited Difluorobenzene Isomers by Collisions with CO₂: Effect of Donor Vibrational Mode," *The Journal of Physical Chemistry A* **112**, 1157-1167 (2008).
5. J. Du, N. A. Sassin, D. K. Havey, K. Hsu, and A. S. Mullin, "Full State-Resolved Energy Gain Profiles of CO₂ from Collisions with Highly Vibrationally Excited Molecules. II. Energy-Dependent Pyrazine ($E = 32\,700$ and $37\,900\text{ cm}^{-1}$) Relaxation," *The Journal of Physical Chemistry A* **117**, 12104-12115 (2013).
6. D. K. Havey, J. Du, Q. Liu, and A. S. Mullin, "Full State-Resolved Energy Gain Profiles of CO₂ ($J = 2-80$) from Collisions of Highly Vibrationally Excited Molecules. 1. Relaxation of Pyrazine ($E = 37900\text{ cm}^{-1}$)," *The Journal of Physical Chemistry A* **114**, 1569-1580 (2010).

7. J. R. Barker, and R. E. Weston, Jr., "Collisional Energy Transfer Probability Densities $P(E, J; E', J')$ for Monatomics Colliding with Large Molecules," *The Journal of Physical Chemistry A* **114**, 10619-10633 (2010).
8. G. W. Flynn, C. S. Parmenter, and A. M. Wodtke, "Vibrational Energy Transfer," *The Journal of Physical Chemistry* **100**, 12817-12838 (1996).
9. E. T. Sevy, S. M. Rubin, Z. Lin, and G. W. Flynn, "Translational and rotational excitation of the $\text{CO}_2(0000)$ vibrationless state in the collisional quenching of highly vibrationally excited 2-methylpyrazine: Kinetics and dynamics of large energy transfers," *The Journal of Chemical Physics* **113**, 4912-4932 (2000).
10. X.-h. Cui, B.-x. Mu, Y.-f. Shen, and K. Dai, "Vibrational relaxation and vibration-rotation energy transfer between highly vibrationally excited $\text{KH}(X^1\Sigma^+, v=14-21)$ and CO_2 ," *Journal of Quantitative Spectroscopy and Radiative Transfer* **113**, 2081-2087 (2012).
11. S.-y. Wang, B. Zhang, D.-h. Zhu, K. Dai, and Y.-f. Shen, "Energy-dependence of vibrational relaxation between highly vibrationally excited $\text{KH}(X^1\Sigma^+, v''=14-23)$ and H_2 , and N_2 ," *Spectrochimica Acta Part A: Molecular and Biomolecular Spectroscopy* **96**, 517-525 (2012).
12. C.-L. Liu, H. C. Hsu, Y. C. Hsu, and C.-K. Ni, "Energy transfer of highly vibrationally excited naphthalene. I. Translational collision energy dependence," *The Journal of Chemical Physics* **127**, 104311 (2007).
13. C.-L. Liu, H. C. Hsu, Y. C. Hsu, and C.-K. Ni, "Energy transfer of highly vibrationally excited naphthalene. II. Vibrational energy dependence and isotope and mass effects," *The Journal of Chemical Physics* **128**, 124320 (2008).
14. C.-L. Liu, H. C. Hsu, and C.-K. Ni, "Energy transfer of highly vibrationally excited naphthalene. III. Rotational effects," *The Journal of Chemical Physics* **128**, 164316 (2008).

15. H. C. Hsu, C.-L. Liu, Y. C. Hsu, and C.-K. Ni, "Energy transfer of highly vibrationally excited 2-methylnaphthalene: Methylation effects," *The Journal of Chemical Physics* **129**, 044301 (2008).
16. Q. Liu, J. Du, D. K. Havey, Z. Li, E. M. Miller, and A. S. Mullin, "Alkylation Effects on Strong Collisions of Highly Vibrationally Excited Alkylated Pyridines with CO₂," *The Journal of Physical Chemistry A* **111**, 4073-4080 (2007).
17. E. M. Miller, L. Murat, N. Bennette, M. Hayes, and A. S. Mullin, "Relaxation Dynamics of Highly Vibrationally Excited Picoline Isomers ($E_{\text{vib}} = 38\,300\text{ cm}^{-1}$) with CO₂: The Role of State Density in Impulsive Collisions," *The Journal of Physical Chemistry A* **110**, 3266-3272 (2006).
18. M. S. Elioff, M. Fang, and A. S. Mullin, "Erratum: "Methylation effects in state resolved quenching of highly vibrationally excited azabenzenes ($E_{\text{vib}} \sim 38\,500\text{ cm}^{-1}$). I. Collisions with water" [*J. Chem. Phys.* 115, 6990 (2001)]," *The Journal of Chemical Physics* **117**, 6880-6880 (2002).
19. J. Park, Z. Li, A. S. Lemoff, C. Rossi, M. S. Elioff, and A. S. Mullin, "Energy-Dependent Quantum-State-Resolved Relaxation of Highly Vibrationally Excited Pyridine ($E_{\text{vib}} = 36\,990\text{--}40\,200\text{ cm}^{-1}$) through Collisions with CO₂," *The Journal of Physical Chemistry A* **106**, 3642-3650 (2002).
20. R. G. Gilbert, and S. C. Smith. *Theory of Unimolecular and Recombination Reactions*; 1990.
21. L. Guo, W. Wang, Y. Liu, D. Ma, C. Xu, and Y. Zhou, "Quasi-classical trajectory study of inelastic collision energy transfer between H₂CO and H₂ on a full-dimensional potential energy surface," *Chemical Physics Letters* **781**, 139014 (2021).

22. Y. Liu, Y. Huang, J. Ma, and J. Li, "Classical Trajectory Study of Collision Energy Transfer between Ne and C₂H₂ on a Full Dimensional Accurate Potential Energy Surface," *The Journal of Physical Chemistry A* **122**, 1521-1530 (2018).
23. J. Chen, J. Li, J. M. Bowman, and H. Guo, "Energy transfer between vibrationally excited carbon monoxide based on a highly accurate six-dimensional potential energy surface," *The Journal of Chemical Physics* **153**, 054310 (2020).
24. A. Caracciolo, D. Lu, N. Balucani, G. Vanuzzo, D. Stranges, X. Wang, J. Li, H. Guo, and P. Casavecchia, "Combined Experimental–Theoretical Study of the OH + CO → H + CO₂ Reaction Dynamics," *The Journal of Physical Chemistry Letters* **9**, 1229-1236 (2018).
25. J. Yuan, Z. Duan, S. Wang, J. Liu, and K. Han, "Significant effects of vibrational excitation of reactant in K + H₂ → H + KH reaction based on a new neural network potential energy surface," *Physical Chemistry Chemical Physics* **20**, 20641-20649 (2018).
26. J. Li, J. Chen, D. H. Zhang, and H. Guo, "Quantum and quasi-classical dynamics of the OH + CO → H + CO₂ reaction on a new permutationally invariant neural network potential energy surface," *The Journal of Chemical Physics* **140**, 044327 (2014).
27. J. Ree, Y. H. Kim, and H. K. Shin, "Intramolecular vibrational energy redistribution in nucleobases: Excitation of NH stretching vibrations in adenine–uracil + H₂O," *The Journal of Chemical Physics* **156**, 204305 (2022).
28. H. K. Shin, "Influence of a Methyl Group on the Unidirectional Flow of Vibrational Energy in an Adenine–Thymine Base Pair," *The Journal of Physical Chemistry B* **127**, 163-171 (2023).
29. J. Ree, K. C. Ko, Y. H. Kim, and H. K. Shin, "Excitation of NH Stretching Modes in Aromatic Molecules: o-Toluidine and α-Methylbenzylamine," *The Journal of Physical Chemistry B* **127**, 7276-7282 (2023).

30. G. Lendvay, "Gateway Modes in the Collisional Energy Transfer from Highly Vibrationally Excited CS₂," *The Journal of Physical Chemistry A* **101**, 9217-9223 (1997).
31. D. C. Clary, R. G. Gilbert, V. Bernshtein, and I. Oref, "Mechanisms for supercollisions," *Faraday Discussions* **102**, 423-433 (1995).
32. C. L. Johnson, B. E. Knighton, and J. A. Johnson, "Distinguishing Nonlinear Terahertz Excitation Pathways with Two-Dimensional Spectroscopy," *Physical Review Letters* **122**, 073901 (2019).
33. D. M. Juraschek, and S. F. Maehrlein, "Sum-frequency ionic Raman scattering," *Physical Review B* **97**, 174302 (2018).
34. A. Sell, A. Leitenstorfer, and R. Huber, "Phase-locked generation and field-resolved detection of widely tunable terahertz pulses with amplitudes exceeding 100 MV/cm," *Optics Letters* **33**, 2767-2769 (2008).
35. F. Junginger, A. Sell, O. Schubert, B. Mayer, D. Brida, M. Marangoni, G. Cerullo, A. Leitenstorfer, and R. Huber, "Single-cycle multiterahertz transients with peak fields above 10 MV/cm," *Optics Letters* **35**, 2645-2647 (2010).
36. I. M. Bayanov, R. Danielius, P. Heinz, and A. Seilmeier, "Intense subpicosecond pulses tunable between 4 μm and 20 μm generated by an all-solid-state laser system," *Optics Communications* **113**, 99-104 (1994).
37. A. Pashkin, F. Junginger, B. Mayer, C. Schmidt, O. Schubert, D. Brida, R. Huber, and A. Leitenstorfer, "Quantum Physics With Ultrabroadband and Intense Terahertz Pulses," *IEEE Journal of Selected Topics in Quantum Electronics* **19**, 8401608-8401608 (2013).
38. S. Maehrlein, A. Paarmann, M. Wolf, and T. Kampfrath, "Terahertz Sum-Frequency Excitation of a Raman-Active Phonon," *Physical Review Letters* **119**, 127402 (2017).

39. B. Mayer, C. Schmidt, A. Grupp, J. Bühler, J. Oelmann, R. E. Marvel, R. F. Haglund, T. Oka, D. Brida, A. Leitenstorfer, and A. Pashkin, “Tunneling breakdown of a strongly correlated insulating state in VO₂ induced by intense multiterahertz excitation,” *Physical Review B* **91**, 235113 (2015).
40. D. Sidler, and P. Hamm, “A Feynman diagram description of the 2D-Raman-THz response of amorphous ice,” *The Journal of Chemical Physics* **153**, 044502 (2020).
41. B. Sertcan, S. J. Mousavi, M. Iannuzzi, and P. Hamm, “Low-frequency anharmonic couplings in crystalline bromoform: Theory,” *The Journal of Chemical Physics* **158**, 014203 (2023).
42. M. J. Frisch, G. W. Trucks, H. B. Schlegel, G. E. Scuseria, M. A. Robb, J. R. Cheeseman, G. Scalmani, V. Barone, G. A. Petersson, H. Nakatsuji, X. Li, M. Caricato, A. V. Marenich, J. Bloino, B. G. Janesko, R. Gomperts, B. Mennucci, H. P. Hratchian, J. V. Ortiz, A. F. Izmaylov, J. L. Sonnenberg, Williams, F. Ding, F. Lipparini, F. Egidi, J. Goings, B. Peng, A. Petrone, T. Henderson, D. Ranasinghe, V. G. Zakrzewski, J. Gao, N. Rega, G. Zheng, W. Liang, M. Hada, M. Ehara, K. Toyota, R. Fukuda, J. Hasegawa, M. Ishida, T. Nakajima, Y. Honda, O. Kitao, H. Nakai, T. Vreven, K. Throssell, J. A. Montgomery Jr., J. E. Peralta, F. Ogliaro, M. J. Bearpark, J. J. Heyd, E. N. Brothers, K. N. Kudin, V. N. Staroverov, T. A. Keith, R. Kobayashi, J. Normand, K. Raghavachari, A. P. Rendell, J. C. Burant, S. S. Iyengar, J. Tomasi, M. Cossi, J. M. Millam, M. Klene, C. Adamo, R. Cammi, J. W. Ochterski, R. L. Martin, K. Morokuma, O. Farkas, J. B. Foresman, and D. J. Fox. *Gaussian 16 Rev. B.01*; Wallingford, CT, 2016.
43. B. C. Pein, N.-H. Seong, and D. D. Dlott, “Vibrational Energy Relaxation of Liquid Aryl-Halides X-C₆H₅ (X = F, Cl, Br, I),” *The Journal of Physical Chemistry A* **114**, 10500-10507 (2010).

CHAPTER 8: Pump-Pulse Bandwidth-Activated Nonlinear Phononic Coupling in CdWO₄

8.1 Abstract

This work was submitted for revision and can be found in arXiv with the following link: <https://doi.org/10.48550/arXiv.2310.08747>. In recent years, the capacity to employ light pulses to manipulate properties or create new functionality of materials^{1,2} is linked to the emerging realm of nonlinear phononics.³⁻¹² This new field is of great importance because the structure of materials plays a key role in the properties and functions of materials. If light is to be used to manipulate the properties of solid materials, it is crucial to understand the interatomic forces present inside the material. This can be done by studying the potential energy surface (PES) of the material, where anharmonic coupling constants are used to indicate the strength of the interaction or coupling between the vibrational modes. Ultrafast THz light pulses can be used to excite and drive the vibrational modes to access different states or properties of the material. In this work, we use two-dimensional (2D) THz spectroscopy to pump and probe vibrational modes present in CdWO₄, which allows us to isolate and measure nonlinear signal from trilinear coupling caused by two sets of mode couplings. It is commonly believed that trilinear coupling is the most efficient when the frequency combinations (sums or differences) of the resonantly driven modes match the frequency of a third mode (non-resonant). However, in this work we show that it is not always the case; when working with broadband THz pump pulses, the pump bandwidth can impart frequency content to the initial motion of each mode beyond the resonant frequency of the mode, leading to additional frequency combinations of the resonant modes. In this way, the THz pump bandwidth can activate trilinear coupling inside materials that would

otherwise not be efficient. This work is crucial as it gives additional insight into the ability to alter the properties or functions of materials with THz light in the field of nonlinear phononics.

8.2 Introduction

The growing field of nonlinear phononics is of great importance because it allows us to study and better understand the forces present inside materials, which are controlled by the positioning and movement of the atoms inside the material. Deeper understanding of these forces, can be achieved by controlling the motion of atoms with ultrafast spectroscopy. Ultrafast laser pulses can penetrate the material, excite the atoms and change their relative positions. The displacement of the atoms is linked to the properties of the material. For instance, ultrafast THz light and multi-THz (mid-infrared) light have been utilized to excite SrTiO_3 ^{4,11} to induce transient ferroelectricity, improve the superconductivity of materials,¹³ and temporarily reverse the ferroelectric polarization of LiNbO_3 .⁵

As described in chapter 6, the potential energy surface (PES) is an important concept crucial to understanding all the interatomic forces present inside a material. Understanding the PES enables us to consider how the structure and associated material properties can be controlled. The vibrational atomic motions inside the crystal lattice can be divided into individual normal vibrational modes for each unit cell, which are known as phonon modes. When the position of the atoms is changed from their equilibrium position at their respective normal-mode coordinates, whether it is due to an external or internal force, the potential energy changes and starts to increase quadratically, based on the harmonic oscillator approximation. However, if the motion of the atoms is large enough from their equilibrium position, the behavior of the motion can no longer be considered harmonic and it requires the PES to include

higher order terms. When this occurs, we say that the system behaves anharmonically. The PES becomes even more complex if external forces are acting upon the material, such as an electric field or a laser pulse. In section 6.4 of chapter 6, we show how to derive the PES equation for a system of three vibrational modes (Eq. 6-11). We can express the PES of any material according to Eq. 8-1 without the influence of any external forces, as

$$V(Q) = \sum_{i=1}^n \frac{1}{2} \omega_i^2 Q_i^2 + \sum_i \sum_j \sum_k \phi_{ijk} Q_i Q_j Q_k + \dots, \quad (8-1)$$

where V is the potential energy of a crystal with n vibrational modes (Q_i), $\omega_i = 2\pi\nu_i$ is the angular frequency (ν_i is the real frequency) and ϕ_{ijk} are the third-order anharmonic coupling constants that describe the interaction between multiple vibrational modes and help to describe the overall anharmonic shape of the PES. Before we show the derived equations of motion from Eq. 8-1, it is necessary to talk about certain properties of the material of interest for this work, which is CdWO₄.

The CdWO₄ crystal possess a centrosymmetric configuration, which means that its vibrational modes are IR (infrared) active or Raman active, but not both. CdWO₄ has four Raman-active (B_g) and three IR-active (A_u and B_u) phonon modes that lie within the THz range that we can excite and probe with our setup, which ranges from 0.5 to 4.5 THz. In Table 8-1,^{8, 14} we show the real frequencies, symmetries and types for the vibrational modes of CdWO₄.

Table 8-1: CdWO₄ Vibrational Modes

Band Index	ν_i (THz)	Symmetry	Raman/IR
1-3	-	Acoustic	Acoustic
4	2.33	B_g	R
5	2.90	A_g	R
6	2.94	B_u	IR
7	3.56	B_g	R

Table 8-1: Continued

Band Index	ν_i (THz)	Symmetry	Raman/IR
8	3.65	A _u	IR
9	4.04	B _g	R
10	4.47	B _u	IR
11	4.48	B _g	R

Again, following the process outlined in chapter 6, we can derive the equations of motion for each of the Raman and IR-active modes of CdWO₄ listed in Table 8-1 by taking the negative derivative of the PES with respect to Q_i . The general equations of motion for an IR-active and a Raman-active mode are shown below in Eq. 8-2 and Eq. 8-3, respectively. It should be mentioned that Appendix 8.6.1 at the end of this chapter shows all the equations of motion for the relevant CdWO₄ vibrational modes in this work.

$$\ddot{Q}_j + 2\Gamma_j\dot{Q}_j + \omega_j^2 Q_j = Z_{j\alpha}^* E_\alpha - \sum_i \sum_k \phi_{ijk} Q_i Q_k + \quad (8-2)$$

$$\ddot{Q}_i + 2\Gamma_i\dot{Q}_i + \omega_i^2 Q_i = -\epsilon_0 R_{i\alpha\beta} E_\alpha E_\beta - \sum_j \sum_k \phi_{ijk} Q_j Q_k + \dots \quad (8-3)$$

These equations of motion can be understood by treating the right-hand side as the driving force and left-hand side as what is being driven. In Eq. 8-2, an IR-active mode (Q_j) can be driven if there is a high oscillation amplitude from the resonant THz pump field ($Z_{j\alpha}^* E_\alpha$) or the third-order anharmonic coupling term ($\sum_i \sum_k \phi_{ijk} Q_i Q_k$). Similarly in Eq. 8-3, a Raman-active mode (Q_i) can be driven through Raman excitation ($-\epsilon_0 R_{i\alpha\beta} E_\alpha E_\beta$) or third-order anharmonic coupling as well. The remaining variables in these equations of motion are: the damping rate (Γ_j), the mode effective charge ($Z_{j\alpha}^*$, which equals a non-zero value for IR-active modes), the permittivity of free space (ϵ_0), the THz electric fields (E_α and E_β , where α and β represent the THz polarization direction), and the Raman tensor element ($R_{i\alpha\beta}$). From these

equations of motion, phonon excitation can happen through a variety of pathways.^{8, 15} IR-active modes can be directly excited by a resonant THz electric field; however, Raman-active modes can be excited by a Raman pathway consisting of a two-field interaction.¹⁶ Another pathway involves the excitation of other vibrational modes (Q_j and Q_k), which can then couple anharmonically to mode Q_i .^{15, 17} An important aspect that needs to be considered for anharmonic coupling is the symmetry of the modes involved in the coupling as well as the polarization of the incoming THz light. In the case of CdWO₄, third-order anharmonic coupling will occur in a B_g Raman-active mode, if the other two modes are IR-active and of the A_u and B_u symmetry. An in-depth discussion on the symmetry considerations on CdWO₄ can be found in Appendix 8.6.2.

The most efficient way to excite the mode of interest, Q_i , is by assuring that the magnitude of the amplitudes of the driving force terms on the right-hand side of the equations of motion (Eq. 8-2 or Eq. 8-3) are large enough at the frequency that is resonant with mode Q_i . In the case of a resonant excitation, which is the simplest case, the amplitude of the spectral components of the THz driving force must be strong enough at the resonant frequency (see Eq. 8-2). The more complicated case would be when the driving force involves processes that are of a third-order nature, such as the anharmonic coupling of modes and electronic Raman scattering (ERS), which are shown in Eq. 8-3 as products involving the electric fields of the THz pumps ($E_\alpha E_\beta$) or vibrational modes ($Q_j Q_k$). To accomplish an efficient excitation of a third-order process, the frequency components involving the driving force need to sum up or subtract down to the frequency of the mode of interest Q_i .^{15, 17} In the case of trilinear coupling, if one excites resonantly the phonon modes Q_j and Q_k , then they will start to oscillate at their respective resonant frequency. We can model the oscillatory response of the vibrational modes as cosine

waves and by applying a trigonometric identity, we can change the anharmonic coupling driving force from Eq. 8-3 to the following form

$$\phi_{ijk}Q_jQ_k = \phi_{ijk}\cos(\omega_j t)\cos(\omega_k t) = \phi_{ijk}\frac{1}{2}[\cos((\omega_j - \omega_k)t) + \cos((\omega_j + \omega_k)t)]. \quad (8-4)$$

Eq. 8-4 shows that if one desires to effectively drive mode Q_i through anharmonic coupling, then the sum or difference frequencies of the other two modes that are being directly excited need to match the frequency of mode Q_i . In a similar fashion for the ERS process, the sum or difference frequencies of the incoming fields (E_α and E_β) need to match the frequency of the mode that is being driven nonlinearly.¹⁵

In this work, we use two-dimensional (2D) THz spectroscopy^{8, 18-22} to isolate and measure a nonlinear anharmonic signal in CdWO₄ that is generated from two sets of third-order couplings. The couplings between modes 4, 6 and 8 ($\phi_{4,6,8}$) and between modes 4, 8 and 10 ($\phi_{4,8,10}$) are responsible for anharmonically driving the B_g mode 4 at a frequency of 2.33 THz. Unexpectedly, the sum or difference frequency combinations of the IR-active mode do not equal to the frequency of the B_g mode 4 that was anharmonically driven. Nonetheless, we demonstrate that excitation of Raman-active modes through anharmonic coupling can be activated by the bandwidth of the THz pump pulse. As it can be noticed, we are only focusing on third-order anharmonic coupling constants because field-strength dependence measurements suggested that contributions from fourth-order (or higher) are not significant (see Appendix 8.6.3).

8.3 Materials and Methods

The measurements performed in this work were done with 2D time-domain THz spectroscopy and the sample of interest was a (010) CdWO₄ crystal with a thickness of 500- μ m. The 2D measurements used two near IR light pulses, signal (1450 nm) and idler (1790 nm),

which were generated from our optical-parametric-amplifier (OPA). Both of these IR pulses have a 100 fs pulse duration and were guided to two separate organic DAST crystals to generate two THz light pump pulses through optical rectification with a frequency range of 0.5-5 THz. The THz pump pulses were directed and focused onto the CdWO₄ sample through a three-parabolic mirror scheme (see Fig. 8-2 or 8-4 below). The diameter for each THz pump beam is ~250 μm at the focus when overlapped.

The probe used to record the nonlinear signal from CdWO₄ was an 800 nm pulse with a 100 fs pulse duration that was produced from the output of our Ti:Sapphire laser, which was also focused and spatiotemporally overlapped onto the sample in the same spot that the THz pump pulses were focused on. The detection scheme used to measure the amplitude of the nonlinear vibrational signal consisted of a heterodyne detection with a configuration to perform sensitive detection that we have used in other works.^{8, 23, 24} Our setup also consisted of a delay stage with a step size of 0.005 mm because it allowed us to vary the timing of the idler THz pump pulse, referred in this work as the “variable delay” pulse, with respect to the signal THz pump pulse, which we referred in this work as the “stationary” pulse.

To properly excite the IR-active modes in CdWO₄, the azimuthal angle of the crystal was set to 0° to allow the variable delay THz pump pulse with horizontal polarization drive the A_u modes and simultaneously allow the stationary THz pump pulse with vertical polarization drive the B_u modes. In order to super-imposed the THz pump pulses in space we used a wire-grid polarizer. The configuration of the polarizer allows for the simultaneous transmission and reflection of horizontally polarized THz light and vertically polarized THz light, respectively.

The 2D THz spectroscopy setup uses a dual chopping scheme, which grants us the ability to isolate different portions of the nonlinear signal. Fig. 8-1a shows two perpendicularly

polarized THz pump pulses that are separated by a time delay (τ) and also by a delay (t) from the 800 nm Raman probe, which are then focused onto the CdWO₄ sample. Fig. 8-1b shows the dual chopping scheme used for separating and extracting the nonlinear signal generated by the THz pump pulses. Due to our laser having a repetition rate of 1 kHz, we use two choppers: a 500 Hz and a 250 Hz chopper that are set on the paths where the OPA signal output (stationary THz pulse) and the OPA idler output (variable delay pulse) travel prior to going through the THz generation crystals, respectively. By chopping the signal in this manner, we obtained four different combinations of our THz pump pulses: obstruction of both pump pulses, allowing both pump pulses, allowing only the variable delay pulse through while the stationary pulse is obstructed and vice versa, where the stationary pulse is the one allowed to go through.

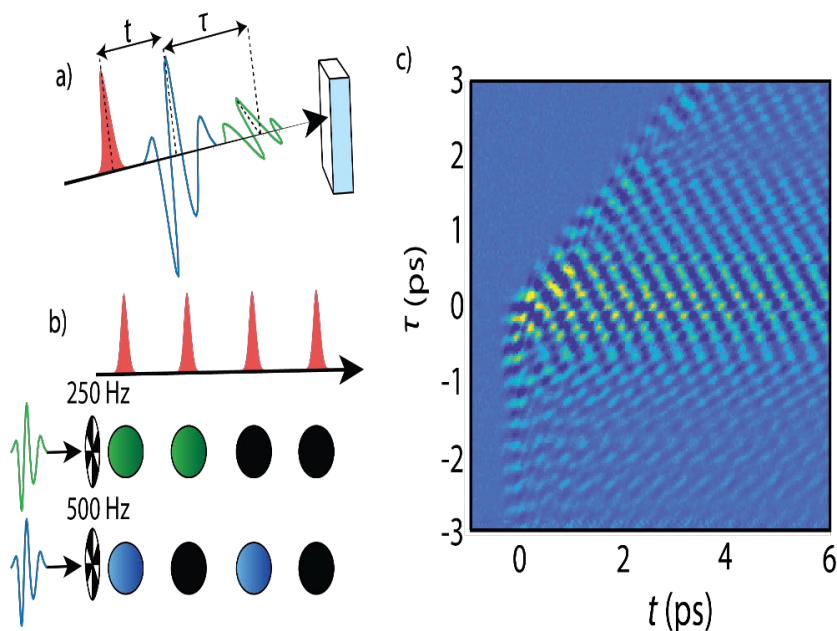


Figure 8-1: Important details of our 2D THz spectroscopy setup. a) The orthogonally polarized THz pump pulses, shown in blue and green, are separated by time delay (τ) and by delay (t) with respect to the 800 nm probe pulse, shown in red. b) Dual chopping scheme. The 250 Hz chopper (green) allows two pulses to go through and blocks two pulses; meanwhile, the 500 Hz chopper (blue) allows one pulse through and blocks one pulse. In the end, the chopping creates four different combinations of the THz pump pulses: both THz pulses allowed, the horizontal THz pulse allowed while the vertical pulse is blocked, the vertical THz pulse allowed while the horizontal pulse is blocked and finally both THz pulses blocked. c) The extracted nonlinear time signal from the 2D THz measurements, where the y-axis is the pump delay τ and the x-axis is the probe delay t .

We can then use Eq. 8-5 to simply obtain the desired nonlinear signal (See Fig. 8-1c) thanks to the different signals that we isolated through our chopping scheme,

$$\mathbf{S}_{\text{nonlinear}} = \mathbf{S}_{\text{both}} - \mathbf{S}_{\text{stationary pump}} - \mathbf{S}_{\text{variable pump}}. \quad (8-5)$$

In the following two subsections, we will go into the specific details that allow us to experimentally separate and measure the anharmonic coupling signal from that of the ERS process with 2D THz spectroscopy by having the polarization of the two THz pump pulses in two configurations: parallel and perpendicular.

8.3.1 Experimental Considerations: Parallel Polarization of the THz Pump Pulses

As mentioned before, we use an OPA to generate two IR pulses for the 2D THz spectroscopy setup: the signal and idler. The generated signal output, which is the stationary pulse, has a vertical polarization; however, the idler output, which is the variable delay pulse, has a horizontal polarization. In order to have both THz pulses in a parallel polarization configuration, a half-wave plate (HWP) is placed in the idler path prior to the THz generation crystal and set to 45° to change the polarization from horizontal to vertical. This setup with parallel THz pump pulses with vertically polarized light can be seen in Fig. 8-2. In Fig. 8-2, we show the use of a d-mirror to both redirect the stationary THz pump pulse towards the three off-axis parabolic mirror arrangement and to directly allow the variable delay pulse to travel above it to the parabolic mirrors. The alignment was optimized at the last parabolic mirror to ensure that both pulses were parallel after reflecting off of the parabolic mirror and then focusing into the CdWO₄ sample, where they are overlapped spatially. For optimal excitation of the IR-active modes in CdWO₄, the crystal was set 45° from the optical axis.

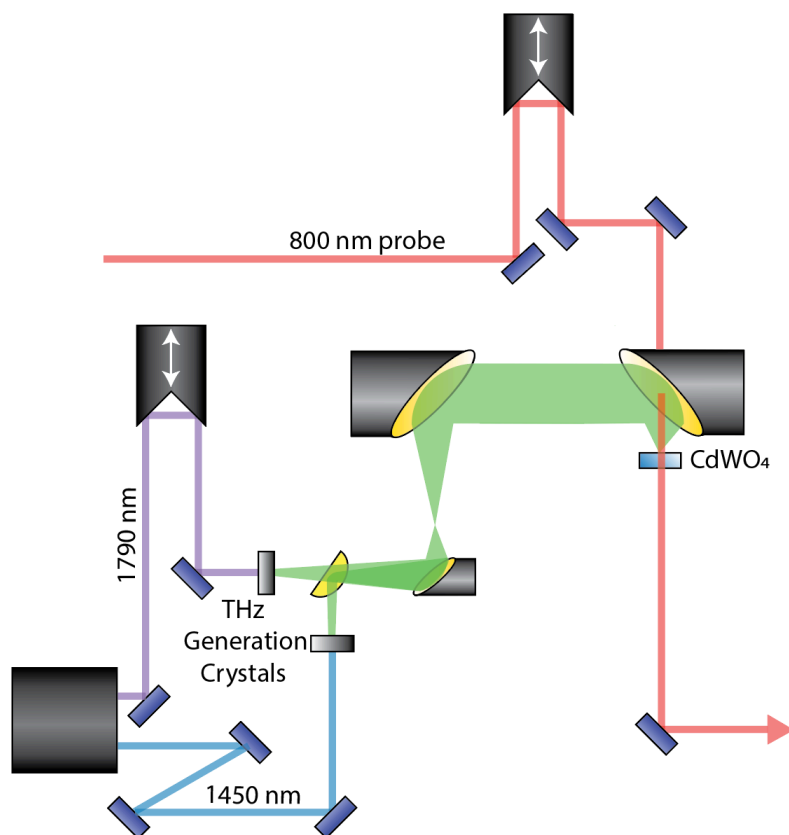


Figure 8-2: 2D THz setup with both THz pump pulses vertically polarized. The setup shows the 1450 nm output signal light (blue) and the 1790 nm output idler light (purple) generated from the OPA after being separated by a wavelength separator. A d-mirror reflects and allows the THz light that is generated from the signal and idler beam inputs to be directed to the parabolic mirror scheme, respectively. The parabolic mirror scheme focuses both THz beams onto the CdWO₄ sample. The 800 nm probe (red) focuses onto the sample through the back of the last parabolic mirror and is then guided to the heterodyne detection scheme.

By setting up the polarizations of the THz pump pulses parallel, the Raman-active phonons in CdWO₄ can be nonlinearly driven by the electric fields at all time delays by the ERS process due to each single pump pulse being composed of several photons that have the necessary orthogonal symmetries to drive a mode. This configuration also allows for the excitation of Raman-active modes through trilinear coupling between IR-active modes (A_u and B_u) because the vector components of the THz electric fields can excite the IR-active modes along their normal coordinates. Fig. 8-3 shows the resulting signal obtained from CdWO₄ in both the time and frequency domain through 2D THz spectroscopy. In Fig. 8-3a, the stationary pulse

is shown as vertical stripes, which are the responses generated from the CdWO₄ sample; meanwhile, the variable delay pulse response is shown as diagonal stripes. However, the sample response becomes more complicated when both THz pump pulses are overlapped in the sample and cannot simply be understood by the addition of the signals generated from both THz pulses. Fig. 8-3b shows the extracted nonlinear signal in the time domain that was obtained thanks to the chopping scheme previously mentioned and by using Eq. 8-5. The time domain response from Fig. 8-3b can be converted into the frequency domain by taking the Fourier transform along both pump and probe axis, which generates the frequency correlation spectrum, as seen in Fig. 8-3c.

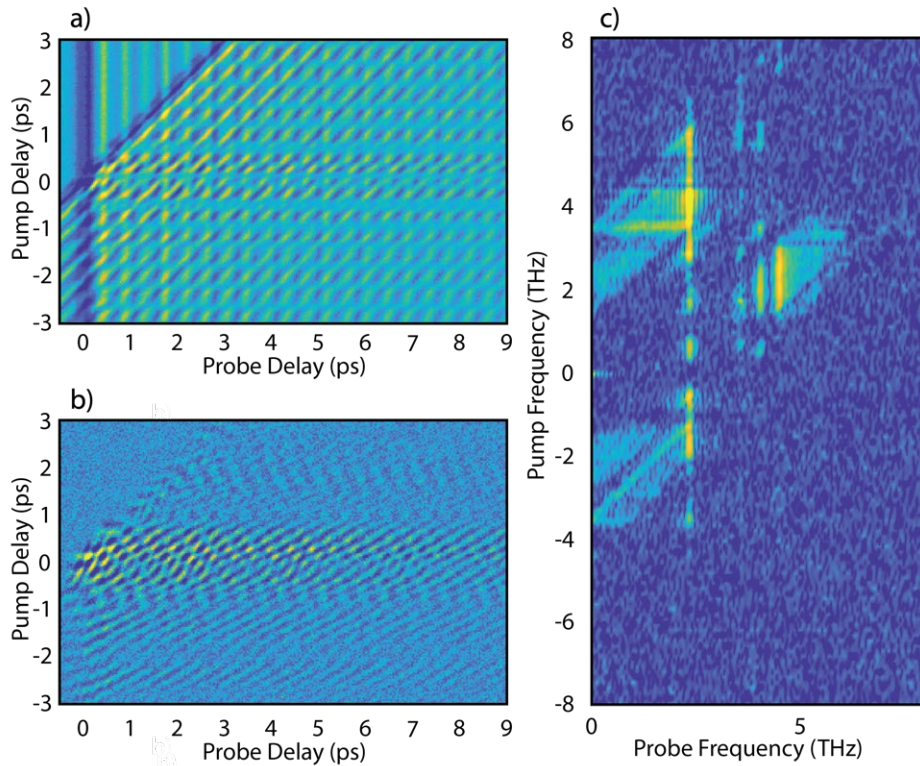


Figure 8-3: Time and frequency domain responses from CdWO₄ acquired through 2D THz spectroscopy with a parallel polarization setup of the THz pump pulses. (a) The time domain response, where the vertical stripes are the responses from the stationary THz pump pulse (signal) and the diagonal stripes are the responses from the variable delay THz pump pulse. (b) The isolated time domain nonlinear response from CdWO₄ after chopping the THz pump pulses and (c) the nonlinear response converted into the frequency domain, which are known as frequency correlation spectrum.

8.3.2 Experimental Considerations: Perpendicular Polarization of the THz Pump Pulses

In this work, we also performed 2D THz measurements by having both THz pump pulses perpendicularly polarized. As previously noted, the OPA output for the signal beam (stationary pulse) is vertically polarized, while the output from the idler beam (variable delay pulse) is horizontally polarized. In this regard, both pulses are already perpendicularly polarized when directed onto the THz generation DAST crystals, and there is no need to change the polarization of the variable delay pulse like in the parallel configuration. The 2D THz spectroscopy setup with perpendicularly polarized THz pump pulses is shown in Fig. 8-4.

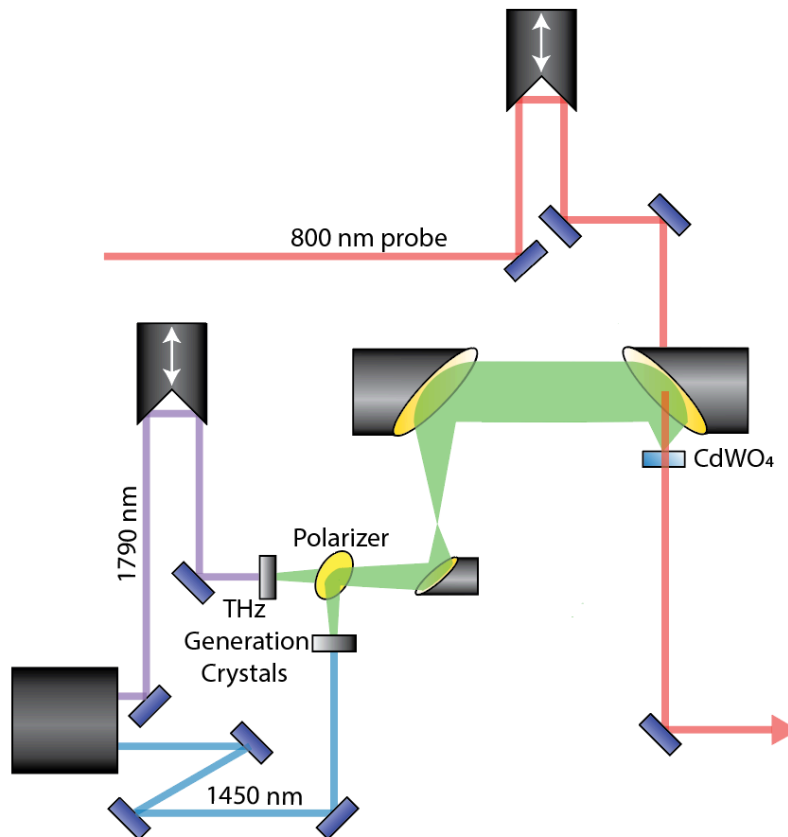


Figure 8-4: 2D THz setup with the THz pump pulses perpendicularly polarized. The setup shows the 1450 nm output signal light (blue) and the 1790 nm output idler light (purple) generated from the OPA after being separated by a wavelength separator. A polarizer reflects and transmits the THz light that is generated from the signal and idler beam inputs to be directed to the parabolic mirror scheme, respectively. The parabolic mirror scheme focuses both THz beams unto the CdWO₄ sample. The 800 nm probe (red) focuses unto the sample through the back of the last parabolic mirror and is then guided to the heterodyne detection scheme.

The setup in Fig. 8-4 is very similar to the one shown in Fig. 8-2 with the major difference that the d-mirror is replaced with a polarizer. The role of the polarizer is to reflect the vertically polarized THz pump pulse generated from the signal beam output and transmit the horizontally polarized THz pump pulse generated from the idler beam output unto the three parabolic mirror arrangement. To properly ensure the spatial overlap between both of the THz pump pulses, it is necessary to make sure that the variable delay pulse travels through the polarizer on the same spot that the stationary pulse is reflected off the polarizer. The CdWO₄ crystal is set at 0° and the optical axis is set vertically.

Similar to Fig. 8-3, the time and frequency responses obtained through 2D THz spectroscopy with perpendicularly polarized THz pulses are shown in Fig. 8-5. An interesting observation can be noticed when Figs. 8-5a and 8-5b are compared, which is the similarity between both time domain responses plots. On one hand Fig. 8-5a shows the combined response of the signal and idler, while Fig. 8-5b only shows the extracted nonlinear response. By having the THz pump pulses perpendicular to each other, the nonlinear response generated through ERS can only happen if both THz pump pulses are overlapped in time due to symmetry conditions in regard to two photons that are perpendicularly polarized. On the other hand, anharmonic coupling has the ability to happen over an extended time span. By having the THz pump pulses orthogonal to each other, they can each align along the normal mode coordinate of a different IR-active phonon (A_u or B_u) in CdWO₄. Symmetry considerations would only allow for Raman-active modes to be driving anharmonically when both modes IR-active modes (A_u and B_u) are vibrationally driven. Similar to ERS, this occurs at the highest amplitude when both THz pump pulses are overlapped in time; however, unlike ERS, driven phonons do not diminish immediately after the THz pump pulses are gone. In fact, both IR-active modes will continue to

be excited for a certain amount of time after the THz pump pulses are no longer overlapped in time, which permits anharmonic coupling to last for a longer period of time compared to ERS. It is for this reason that the time domain nonlinear responses in Figs. 8-5a and 8-5b are similar to each other. The smaller differences that are observed are due to small variations in the polarization of both THz pump pulses.

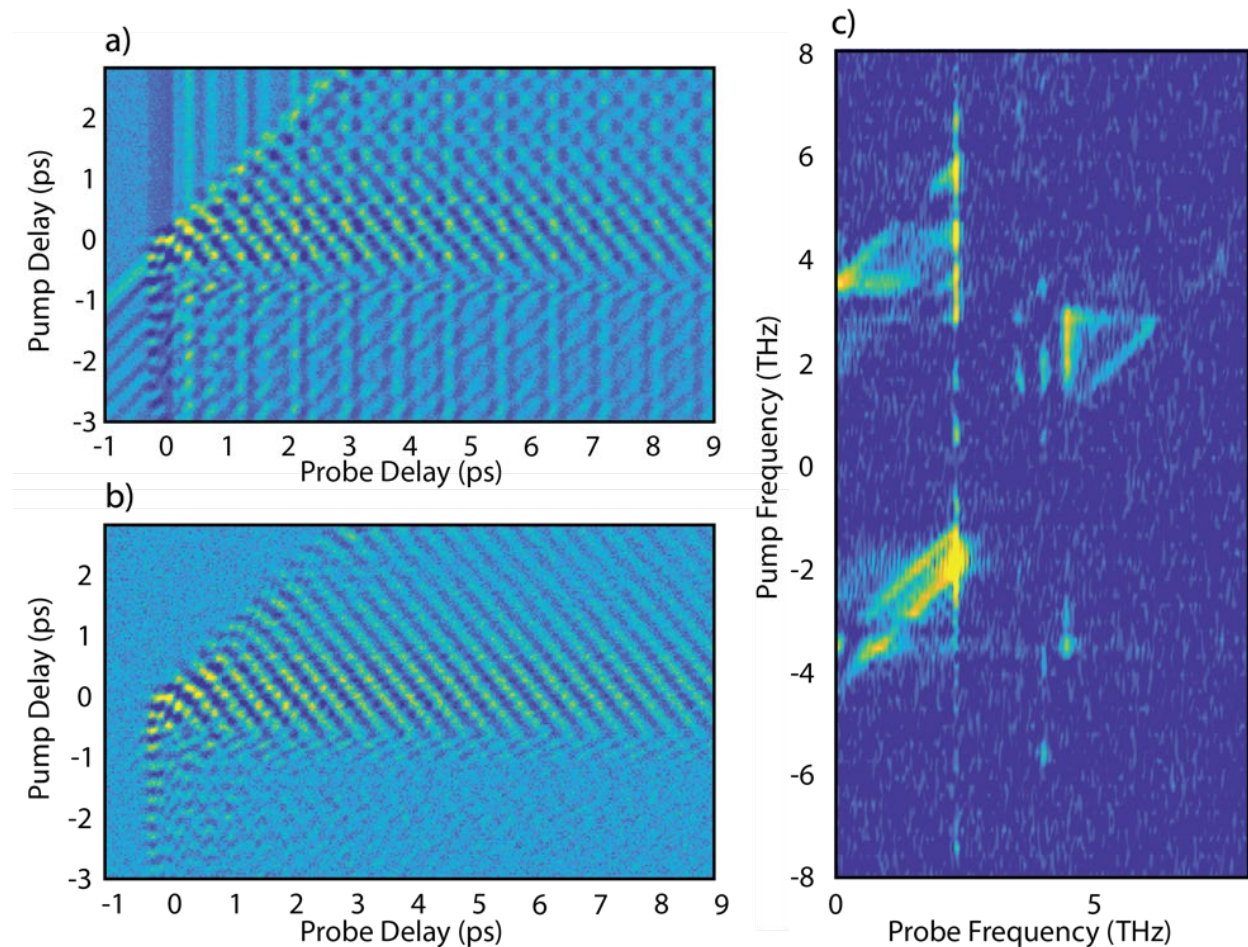


Figure 8-5: Time and frequency domain responses from CdWO₄ acquired through 2D THz spectroscopy with a perpendicular polarization setup of the THz pump pulses. a) The time domain response, where the vertical stripes are the responses from the stationary THz pump pulse (signal) and the diagonal stripes are the responses from the variable delay THz pump pulse. (b) The isolated time domain nonlinear response from CdWO₄ after chopping the THz pump pulses and (c) the nonlinear response converted into the frequency domain, which are known as frequency correlation spectrum.

Differences can be observed when comparing the frequency correlation plot in Fig. 8-5c to the one in Fig. 8-3c. To understand the observed differences, it is necessary to keep two things in mind in regard to performing 2D THz measurements with orthogonal THz pulses. First, nonlinear signal from ERS can only happen if both THz pulses are overlapped in time. Secondly, the polarization of the electric fields has been thoroughly refined to intensely drive them to high amplitudes, which in turn would strongly excite the IR-active modes engaged in the trilinear coupling. The strong excitation of the IR-active modes will in turn produce a strong nonlinear signal through trilinear coupling with the coupling to the Raman-active mode.

8.4 Results and Discussion

We performed 2D THz measurements using two different configurations of the THz pump pulses. In the first case, the THz pump pulses had a parallel polarization (see Fig. 8-2), while in the second case, the THz pump pulses had a perpendicular polarization (see Fig. 8-4). In the following two subsections, we will go over the specifics of the nonlinear signal that is generated by both ERS and anharmonic coupling. This will allow us to comprehend the nonlinear signal observed in Figs. 8-3c and 8-5c. In the third subsection, we will go over how to turn off the ERS signal and show the anharmonic coupling signal more strongly, which will be important to interpret the experimental 2D frequency correlation plot. In the fourth subsection, we will quantify the magnitude of the anharmonic coupling constants and compare those results to calculations performed through first-principles. Finally, in the fifth subsection we will show how the THz pump bandwidth can activate anharmonic coupling in CdWO₄, which is key to understanding why the nonlinear signal cannot be explained purely through trilinear coupling.

8.4.1 Electronic Raman Scattering (ERS) Signal in Frequency Correlation Spectrum

In 2D THz measurements performed with parallelly polarized THz pump pulses with the CdWO₄ oriented at a 45°,⁸ the Raman active modes can be driven through the ERS process at every time delay between the THz pump pulses because they each possess significant vector components of the THz electric field, which are needed for ERS to occur under the symmetry restrictions. In fact, an individual pulse is capable of providing the two photons needed to drive the Raman-active modes through ERS. However, when the 2D THz measurements are performed with perpendicularly polarized pump pulses, the ERS signal can only occur when the two perpendicularly polarized photons from both THz pump pulses are overlapped in space and time in order to fulfill the symmetry considerations. Due to this limitation, there is a high decrease in the nonlinear signal coming from the ERS process. The ERS response signal is still present at time delays where the THz pulses are overlapped; however, we can now appreciate concealed nonlinear responses at the other time delays where there is no direct overlap between the THz pump pulses. This basically allows us to shut off the nonlinear signal coming from ERS at certain time delays by using cross polarization, which in turn allows us to see the nonlinear signal coming from the trilinear phonon coupling process. Additionally, we modeled the THz pump pulses with a parallel and perpendicular polarization to show that it is possible to shut off ERS. This modeling can be appreciated in Appendix 8.6.4.

Although the contributions from ERS to the nonlinear signal are greatly reduced, some of the ERS signal is still present. We can model the ERS signal to more accurately interpret the frequency correlation plots (See Figs. 8-3c and 8-5c). As an example, we will show the modeling of the excitation of the B_g Raman-active mode 4 by the ERS process. To do this, we will assign a value of zero for the anharmonic coupling constants and the Raman tensors of the other Raman-

active modes in CdWO₄ to zero in the equation of motion, as seen in Eq. 8-6,

$$\ddot{Q}_{R_4} + 2\Gamma_{R_4}\dot{Q}_{R_4} + \omega_{R_4}^2 Q_{R_4} = -\varepsilon_0 R_{4\alpha\beta} E_\alpha(t) E_\beta(t). \quad (8-6)$$

In Fig. 8-6a, we show the modeled response from mode 4 being driven by ERS according to Eq. 8-6. The Raman excitation response shows up as a blue vertical band at 2.33 THz, which is the resonant frequency of the driven mode 4. The features present along the pump axis correspond to the frequency components of the THz pump pulses involved in the generation of the nonlinear response. The probe axis shows which modes were driven nonlinearly through ERS, which the 800 nm probe can observe and measure. In this modeled frequency correlation spectrum, the vertical band at 2.33 THz on the probe axis indicates that there are several combinations between the frequencies of the THz pump pulses responsible in driving the Raman-active mode 4. This vertical stripe is clearly seen in the actual data, which is shown in Fig. 8-6b. It can also be noticed that there are three more additional vertical stripes, which correspond to the other B_g Raman-active modes being driven by ERS and are located at their resonant frequencies (see Table 8-1).

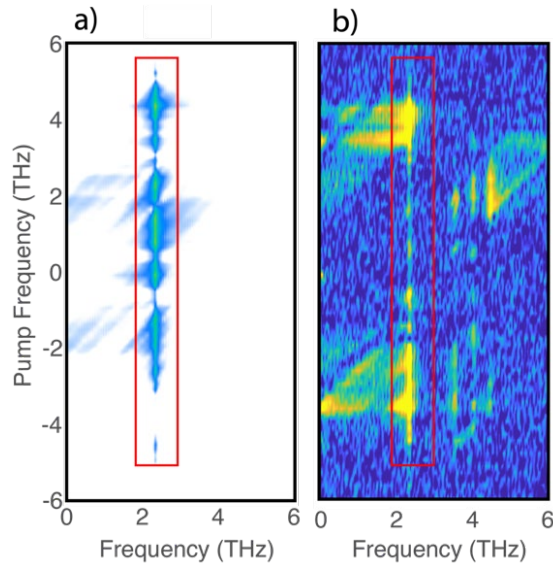


Figure 8-6: Modeled and experimental frequency correlation spectrum highlighting the ERS signals. a) Frequency correlation plot generated by only modeling mode 4 driven by ERS. b) Experimental frequency correlation plot generated from the isolated nonlinear signal. The red box highlights the ERS signal at the frequency of mode 4.

To understand the vertical stripes shown in Figs. 8-6a and 8-6b, we need to take a closer look at the THz spectrum from the pump pulses. Fig. 8-7a shows the normalized THz spectrum of one of the DAST crystals used for the generation of the THz pump pulses.

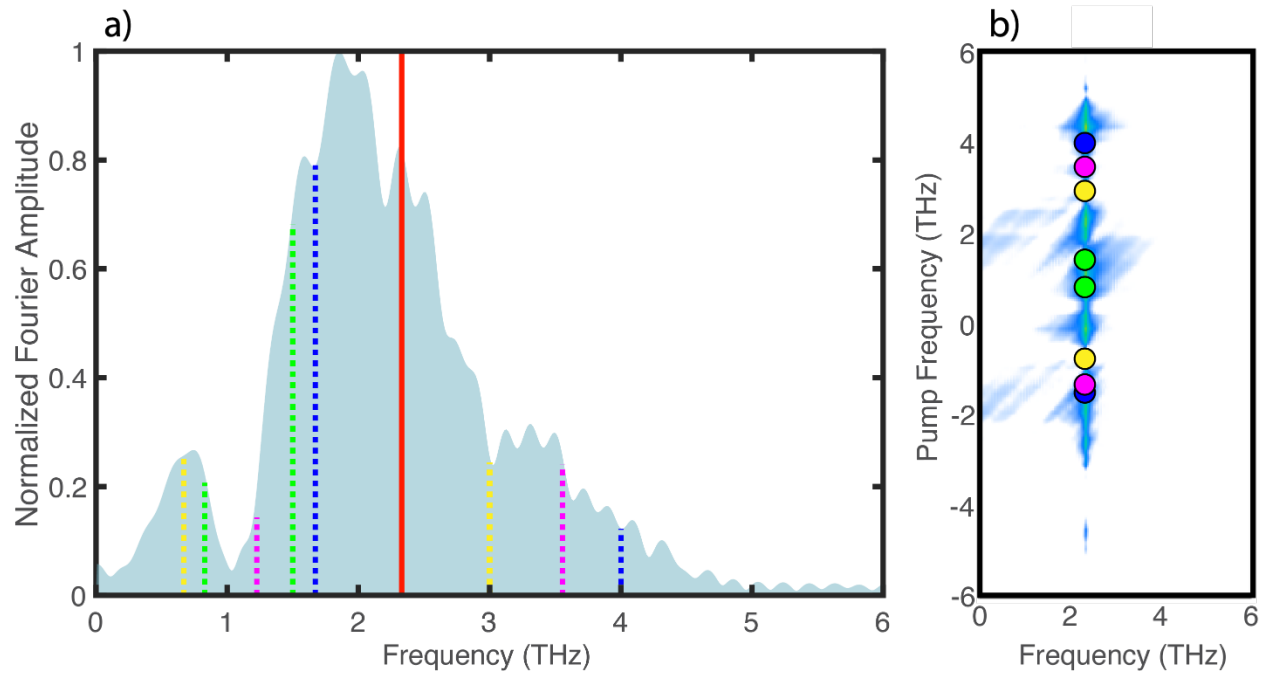


Figure 8-7: Contributions from ERS are observed as vertical bands in the 2D THz correlation spectrums. a) THz spectrum of the DAST crystal used for THz generation. The solid red line indicates the Raman-active mode 4 at its resonant frequency, while the dotted lines in pairs represent four possible combinations that can be mixed through addition or subtraction to match the frequency of the Raman-active mode that is being driven. b) Modeled frequency correlation spectrum by exciting mode 4 through ERS. Along the THz pump axis, the possible sum and difference combinations of the frequency pairs in a) are shown as circles that are found on the vertical band at the resonant frequency of the mode that is being drive at 2.33 THz in the THz probe axis.

To generate excitation through THz-ERS, it is necessary for either the sum or difference frequency combinations of the two photons involved in the process to match the frequency of the Raman-active mode that is being nonlinearly driven. Fig. 8-7a also shows a solid red vertical line at the resonant frequency of mode 4 and as example, four pairs of colored dotted lines at pump frequencies that can be combined through addition or subtraction to match the frequency of the Raman-active mode 4. The sum and difference frequency combinations for each of these four

pairs of frequencies are shown as circles of the corresponding color along the pump axis and at the frequency of the Raman-active mode 4 in the probe axis in the frequency correlation spectrum in Fig. 8-7b. In Fig. 8-7b, it can be noticed that the vertical band starts to become filled with spectral features corresponding the frequency combinations and we can visualize that by including all the frequency combinations present in the THz pump, that it would be possible to fill the remainder part of the vertical band. It can also be observed that some features are more pronounced than others, which is related to the intensities of the THz pump at certain frequencies, as seen in the THz spectrum of DAST. In the experimental spectrum, some of the other pronounced features that are present come from contributions due to anharmonic coupling.

8.4.2 Anharmonic Coupling Signal in Frequency Correlation Spectrum

In a similar way to the excitation through ERS, the anharmonic coupling process requires the simultaneous excitation of both phonons. However, a main difference is that unlike photons, phonons do not damp out after the THz pump is removed. The phonons can oscillate for a several picoseconds, which allows for the excitation through anharmonic coupling at all the delays between the THz pump pulses and thus generating a nonlinear phononic response.

The phononic response can also be modeled in a similar manner to the ERS response, like it was shown in the previous subsection. This is accomplished by using the Eq. 8-2 to model the nonlinear signal generated by driving Raman-active phonons through the coupling to IR-active phonons. The nonlinear features are observed in 2D frequency correlation plots (See Figs. 8-3c and 8-5c). The probed Raman-active mode that is involved in the anharmonic coupling, appears across the probe axis as vertical bands. Meanwhile, we see three types of features across the pump axis that are generated by the frequencies of the IR-active modes involved in the coupling:

1) at their resonant frequencies, 2) at the sum and 3) difference frequencies that result in the frequency of the Raman-active mode. In Fig. 8-8, we show an example of how to assign these particular frequencies to the nonlinear features observed in frequency correlation plots. To simplify this explanation, we have created an example with three phonons at 0.9 THz, 1.3 THz and 2.7 THz in Fig. 8-8a. In this case, the mode at 1.3 THz is the Raman-active mode and is being probed. The vertical band for this mode is located at its resonant frequency across the probe axis. Correspondingly, the frequency elements involving the coupling between the IR-active modes and the Raman-active mode are found across the pump axis in Fig. 8-8a as: 1) squares at the resonant frequencies of the IR-active modes (0.9 THz and 1.3 THz), 2) triangles at the sum frequencies ($1.3 + 0.9 = 2.2$ THz and $1.3 + 2.7 = 4$ THz) and 3) circles at the difference frequencies ($1.3 - 0.9 = 0.4$ THz and $1.3 - 2.7 = -1.4$ THz).

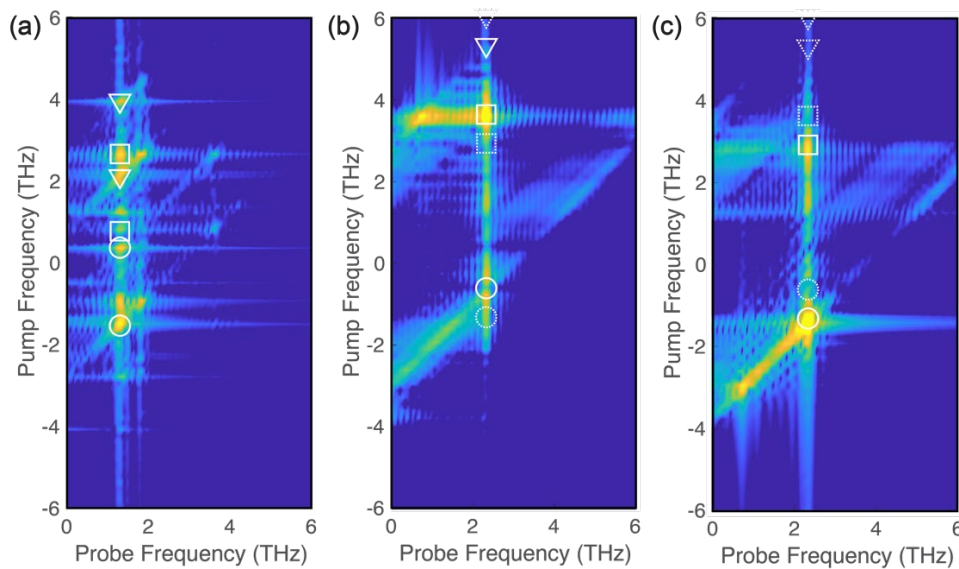


Figure 8-8: Modeled nonlinear features generated through anharmonic coupling and frequency assignments of the features. a) Example of spectrum generated through anharmonic coupling of three arbitrary phonons. b) Modeled spectrum of the coupling of phonons in CdWO₄ where the stationary pump pulse was model with a vertical polarization and the variable delay pump pulse with a horizontal polarization. c) The modeled CdWO₄ spectrum has the reverse order of the THz polarizations that were used to generate the spectrum in b). The frequency elements across the pump axis are found at: 1) the resonant frequencies of the IR-active modes (squares), 2) sum frequencies (triangles) and 3) difference frequencies (circles) that match the frequency of the Raman-active mode.

With the understanding from the created example in Fig. 8-8a, we show in Figs. 8-8b and 8-8c the actual model for CdWO₄ involving three of its phonons: the probed Raman-active B_g mode at 2.3 THz, and the IR-active B_u and A_u modes at 2.9 and 3.6 THz, respectively. Across the pump axis, the sum frequency features show up at 5.2 THz and 5.9 THz as triangles, while the difference frequency features show up at -1.3 THz and -0.6 THz as circles. The frequency correlation plot in Fig. 8-8b is modeled by setting the polarization vertical for the stationary THz pump pulse, while setting the polarization horizontal for the variable delay THz pump pulse. In Fig. 8-8c, the polarization of the THz pump pulses is the opposite, meaning that the stationary pulse is vertically polarized and the variable delay pulse is horizontally polarized. By changing the polarization of the THz pump pulses in Figs. 8-8b and 8-8c, the THz pump pulses can excite the IR-active modes in a different order and thus the correlation frequency plots can show different features due to the symmetry of the modes. In these frequency correlation plots, we show with dashed shapes features that are dimmer or that do not show up at all. Interestingly, if a feature is missing in one of the frequency correlation spectra, then it will usually show up in the other spectrum. The reason for modeling these two spectra in this manner will become more apparent when we begin to uncover the nonlinear signal from anharmonic coupling in the following two subsections.

By understanding how to properly identify features from the ERS and anharmonic coupling processes, we can now examine thoroughly the experimental frequency correlation spectrum obtained after nonlinearly exciting CdWO₄ with perpendicularly polarized THz pulses (see Fig. 8-5c). In the following subsection, we focus on interpreting the spectrum collected with perpendicularly polarized THz pulses because the nonlinear signal in the spectrum is mostly coming from anharmonic coupling due to the THz pulses shutting off the ERS signal.

8.4.3 Shutting off ERS to Isolate the Anharmonic Coupling Features in 2D THz Spectrum

By having the THz pump pulses orthogonal to each other, we can turn off the ERS signal and thus show nonlinear signal that is mostly originating from anharmonic coupling. The frequency correlation plot collected with this 2D THz configuration can be appreciated in Fig. 8-9. The nonlinear features observed that come from anharmonic coupling involve the excitation of a Raman-active mode that is driven by the motion of two IR-active modes that are driven by the perpendicularly THz pump pulses.

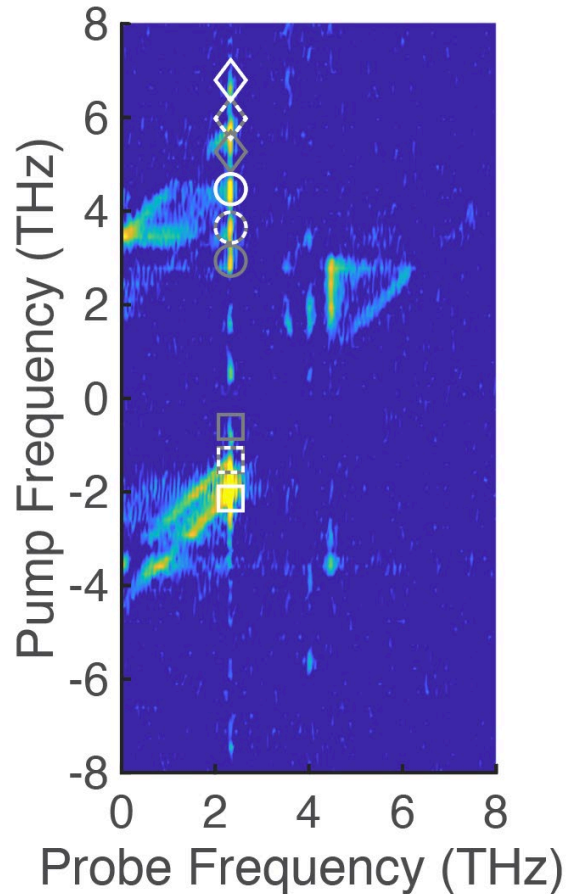


Figure 8-9: Frequency correlation plot of the nonlinear response in CdWO₄. The nonlinear features are highlighted with shapes depending on the following frequencies: 1) resonant frequency of the IR-active modes (circles), sum- (diamonds) and difference-frequencies (squares). Responses originating from the coupling of modes 4, 6, 8 and 4, 8, 10 are shown in gray and white, respectively. In the case that the signal is influence by both sets of couplings, the shape contains white lines with dashed gray lines.

We will take a closer look at the coupling between modes 4, 8 and 10. In the 2D frequency correlation spectrum, features appear at the resonant frequencies of the IR-active modes (3.65 THz and 4.47 THz) marked as white circles. Features corresponding to the sum frequency of the IR-active modes in the coupling show up at 5.98 THz (2.33 THz + 3.65 THz) and 6.80 THz (2.33 THz + 4.47 THz) marked as white diamonds; meanwhile, the features from difference frequency show up at -1.32 THz (2.33 THz – 3.65 THz) and -2.14 THz (2.33 THz – 4.47 THz) marked as white squares. Additionally, there is another coupling between the modes that fulfills the symmetry requirements and also appears in Fig. 8-9, which is the coupling involving modes 4, 6, and 8. The features have also been identified in a similar way to the previously mentioned coupling in the frequency correlation spectrum but they are marked in gray color instead. When the same feature is generated by both sets of mode coupling, the shapes are shown in a dashed manner in Fig. 8-9.

8.4.4 Comparison Between Experimental and First-Principles Anharmonic Coupling

To further support the anharmonic coupling features from Fig. 8-9, we extracted the magnitude of the coupling constants $\phi_{4,6,8}$ and $\phi_{4,8,10}$. This was done by first modeling the motion of the vibrational modes present in CdWO₄ to generate a model frequency correlation spectrum. The modeling involved solving the equations of motion for each vibrational mode, according to Eq. 8-2 and Eq. 8-3, by inputting the measured THz electric fields for E_α and E_β . It is then possible to construct a model of the different THz pump pulse combinations according to the chopping scheme presented in Fig. 8-1b, which allows us to generate and extract the nonlinear signal of interest. The nonlinear signal in the time domain can then be converted to the frequency domain by taking the Fourier transform along both the probe and pump axis and thus

generate a modeled frequency plot similar to the experimental one in Fig. 8-9. We can then use the modeled and experimental frequency correlation plots to extract the coupling constants and the Raman tensor of interest ($\phi_{4,6,8}$, $\phi_{4,8,10}$, R_{xz4}) through a manual chi-squared fitting process. In this fitting, the magnitudes for $\phi_{4,6,8}$, $\phi_{4,8,10}$ and R_{xz4} , along with ones of the other coupling constants and Raman tensors are adjusted to minimized the root-mean-square-error (RMSE) of the difference between both the experimental and modeled frequency correlation spectra. The chi-squared fitting is a long and tedious process that is explained in more detail in Appendix 8.6.5. Additionally, the coupling constants ($\phi_{4,6,8}$, $\phi_{4,8,10}$) were also calculated through first-principles calculations (see Appendix 8.6.6 for the specific details of these calculations).

One of the issues from the experimental frequency correlation spectrum is that the nonlinear features are generated due to the movement of the Raman-active modes and not due to the actual motion of the individual atoms. It is for this reason, that our chi-squared fitting cannot extract retrieve absolute values for the Raman tensor elements and the anharmonic coupling constants. We can only rely on obtaining relative values by comparing the ratio between the coupling constants, $\phi_{4,8,10}/\phi_{4,6,8}$. We were able to determine the ratio of the experimental value by chi-squared fitting and the calculated by first-principles calculations to be -0.67 and -1.23, respectively. Interestingly, the sign is the same for both of these ratios and they are also within the same order of magnitude.

8.4.5 The Inefficiency in Anharmonic Coupling can be Supplied by the THz Bandwidth

From the frequency correlation plots obtained with perpendicularly polarized THz pulses, we have shown the excitation of the Raman-active modes through anharmonic coupling. Despite this result, we notice that the sum and difference frequency (see Eq. 8-4) between the IR-active

modes do not match or come close to the frequency of the Raman-active mode for the ideal driving of the mode through anharmonic coupling. In Table 8-2 we show an analysis of the frequencies of the vibrational modes involved in the anharmonic coupling. The frequencies of the IR-active modes along with the frequency of the targeted Raman-active mode are shown. The determined sum and difference frequency combinations are also shown with the missing frequency requirement. It is clear that weather we are talking about the coupling between modes 4, 6 and 8, or, 4, 8 and 10, that there is a shortcoming of frequency content. We will now carefully inspect the coupling between modes 4, 8 and 10, to show that anharmonic coupling still occurs despite this discrepancy with the frequencies of the IR-active modes.

Table 8-2: Frequency Mixing of Relevant Anharmonic Coupling in CdWO₄

Coupled Modes	ν_j (mode IR ₁)	ν_k (mode IR ₂)	Sum	Diff.	Diff. needed	ν_i (mode R)
4, 6, 8	2.94 (mode 6)	3.65 (mode 8)	6.59	0.71	1.32	2.33 (mode 4)
4, 8, 10	3.65 (mode 8)	4.47 (mode 10)	8.12	0.82	2.14	2.33 (mode 4)

When we perform 2D THz spectroscopy, we can control the time delay (τ) between the variable delay THz pump pulse (horizontal polarization) and the stationary THz pump pulse (vertical polarization) as they approach the CdWO₄ sample. The polarization of the variable delay pulse is set to drive the A_u mode 8 at 3.65 THz; while, the polarization of the stationary pulse is set to drive the B_u mode 10 at 4.47 THz. In Fig. 8-10, we have selected a specific pump delay (τ) where the variable delay pulse approaches the sample to drive its respective IR-active mode a few ps before the stationary pulse can drive its respective mode. The modeled time traces a) and c) in Fig. 8-10 show the oscillations generated from the resonant movement of modes 8

and 10 with a suitable time delay. The dotted lines in these traces show the arrival of the two THz pump pulses.

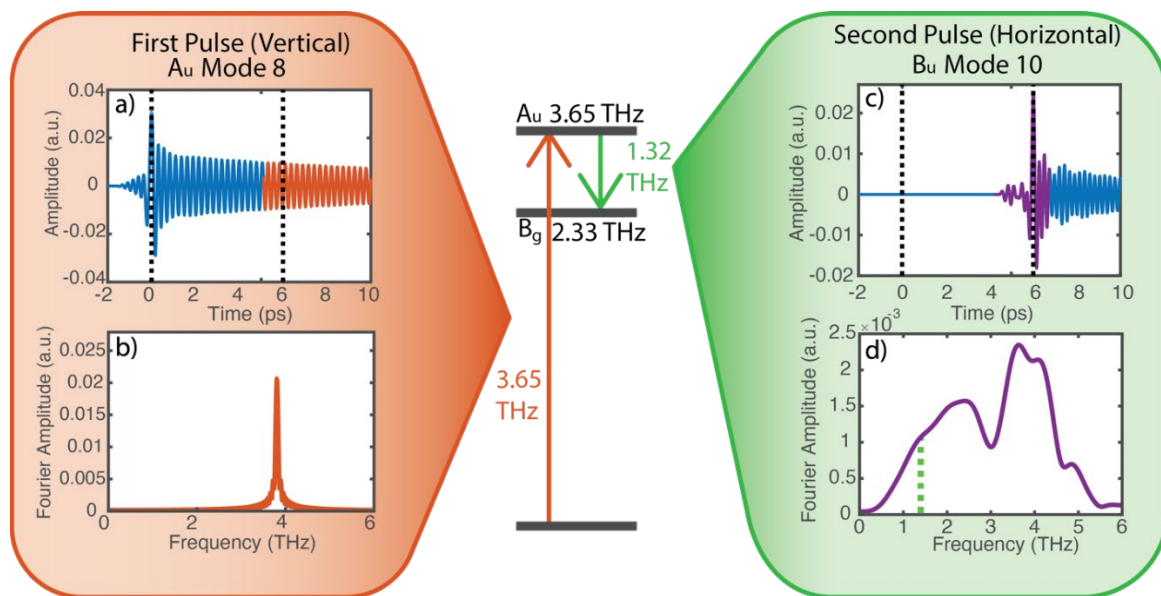


Figure 8-10: THz pump bandwidth adds additional frequency content to the motion of the vibrational modes, thus contributing to trilinear coupling. In the middle, the energy diagram shows the frequency difference (1.32 THz) needed from the coupling motion between the A_u mode 8 and B_u mode 10 to nonlinearly drive the B_g mode 4 at 2.33 THz. The orange box shows the motion of the A_u mode by the vertical THz pulse 6 ps prior to the excitation of the B_u mode by the horizontal THz pulse, which is shown in the green box. The vertical dotted lines in a) and c) show the arrival of the THz pump pulses. a) Shows the oscillations of the A_u mode, while b) shows the Fourier transform of the late motion of the A_u mode (oscillations in orange). c) Shows the early oscillation of the B_u mode when it is initially driven by the second THz pulse and d) shows the Fourier transform of that early motion (oscillations in purple), which shows more frequency content besides the resonant frequency of the B_u mode. The spectrum in d) shows frequency content from the THz pump bandwidth and the frequency content needed to drive the B_g mode is shown in a dotted green line at 1.32 THz.

Interestingly, we notice that there are more frequency components at the initial arrival of the THz pump than at subsequent times. In other words, when we are driving a vibrational mode, the THz driving force will introduce some of its frequency content as soon as it starts to interact with said mode, even if the frequency contents are not resonant to that particular mode. Once the driving force is gone, the mode will naturally move at its own resonant frequency. This can be clearly observed in frequency spectrum b) shown in Fig. 8-10, where the Fourier time was taken

after 6 ps and as result we only see a peak at the resonant frequency (3.65 THz) of mode 8 (spectrum in orange). However, we can see that when the second THz pulse arrives to excite mode 10 that at the spectrum of the initial motion (shown in purple in time trace c) contains broader frequency content (spectrum in purple) in d) that comes from the second THz pump pulse. It is this broad frequency range that contributes the missing frequency content of 1.32 THz (3.65 THz – 2.33 THz) needed to excite mode 4 at 2.33 THz. This complementary frequency can be noticed in spectrum d) as a dotted green line. Therefore, we show that mode 4 can be excited through anharmonic coupling by a combination between the resonant frequencies of mode 8 and 10, along with frequency content found within the THz pump pulse bandwidth when it initially excites mode 10, which ends up complimenting the missing frequency content from mode 10. We have only shown one example for one specific THz pump delay but activation of anharmonic coupling through the bandwidth of the THz pump does happen across the entire 2D THz data collection process and this also observed for both sets of mode coupling, $\phi_{4,6,8}$ and $\phi_{4,8,10}$.

8.5 Conclusions

In conclusion, we have shown in this work that we can use 2D THz spectroscopy to favorably drive Raman-active modes through third-order anharmonic coupling between IR-active modes in CdWO₄ by having the THz pump pulses perpendicularly polarized. The configuration of the THz pump pulses allows for the anharmonic coupling signal to be greatly increased because contributions from ERS are limited to time delays where both THz pulses are overlapped in time. We then were able to model the nonlinear signal from frequency correlation spectrum by solving the equations of motion, which allowed us to extract ratios between the coupling constants, $\phi_{4,6,8}$ and $\phi_{4,8,10}$, to make a direct comparison with coupling constants

determined through first-principles calculations. The experimental and calculated values of the ratio of coupling constants are in good agreement in magnitude and sign. We also discovered that missing frequency content that cannot be supplied by the IR-active phonons involved in the coupling can be provided by the THz pump bandwidth, allowing for the activation of anharmonic coupling.

An additional insight from this work is that to effectively model nonlinear excitation through anharmonic coupling, frequency content from the THz bandwidth needs to be included to generate a proper model, particularly in the case of using broadband THz pulses. The simple model of using sum and difference frequency combination should still work in the case of using narrowband THz pump pulses. Nonetheless, this work shows that a broadband THz pump can activate anharmonic coupling by supplying additional frequency content.

8.6 Appendix

8.6.1 Coupled Equations of Motion

The motion of the atoms along with the forces involved in said motion can be quantified by the coupled equations of motion, which can be derived by differentiating the potential energy surface equation (PES). The equations of motion could be understood by considering the right-hand side as the driving force and the left-hand side as the vibrational mode that is intended on being driven. In Eqs. 8-7, we show the derived equations of motion for the three IR-active modes in CdWO₄ with Q_j as the phonon mode normal coordinate, Γ_j as the damping rate of the phonon, ω_j as the angular mode frequency, $z_{j\alpha}^*$ as the mode effective charge that quantifies the interaction between the THz electric field (E_α) and Q_j , and $\phi_{i,j,k}$ as the anharmonic coupling constant. The

coupling constant quantifies the strength of the interaction between the modes that couple to mode Q_j . The polarization of electric fields, E_α and E_β , are set vertically and horizontally, respectively, and are set to drive the A_u and B_u modes, respectively. We can assume that the amplitude contributions of the Raman-active modes are smaller compared to the IR-active modes in the back-coupling terms (the summation elements in Eqs. 8-7) and thus we can ignore these terms when modeling the motion of these modes in the equations of motion.

$$\begin{aligned}\ddot{Q}_{IR_8} + 2\Gamma_{IR_8}\dot{Q}_{IR_8} + \omega_{IR_8}^2 Q_{IR_8} &= Z_{8\alpha}^* E_\alpha - \sum_{i=4,7,9,11} \phi_{i,6,8} Q_{IR_6} Q_{R_i} - \sum_{i=4,7,9,11} \phi_{i,8,10} Q_{IR_{10}} Q_{R_i} \\ \ddot{Q}_{IR_6} + 2\Gamma_{IR_6}\dot{Q}_{IR_6} + \omega_{IR_6}^2 Q_{IR_6} &= Z_{6\beta}^* E_\beta - \sum_{i=4,7,9,11} \phi_{i,6,8} Q_{IR_8} Q_{R_i} \\ \ddot{Q}_{IR_{10}} + 2\Gamma_{IR_{10}}\dot{Q}_{IR_{10}} + \omega_{IR_{10}}^2 Q_{IR_{10}} &= Z_{10\beta}^* E_\beta - \sum_{i=4,7,9,11} \phi_{i,8,10} Q_{IR_8} Q_{R_i}\end{aligned}\quad (8-7)$$

Similarly, the equations of motion for the Raman-active modes are shown in Eqs. 8-8. In this case, according to symmetry considerations and the magnitude of the motion amplitude of the IR-active modes, it is crucial to include both driving forces coming from ERS and trilinear coupling by the terms $R_{i\alpha\beta} E_\alpha E_\beta$ and $\phi_{i,j,k} Q_{IR_j} Q_{IR_k}$, respectively.

$$\begin{aligned}\ddot{Q}_{R_4} + 2\Gamma_{R_4}\dot{Q}_{R_4} + \omega_{R_4}^2 Q_{R_4} &= \epsilon_0 R_{4\alpha\beta} E_\alpha E_\beta - \phi_{4,6,8} Q_{IR_6} Q_{IR_8} - \phi_{4,8,10} Q_{IR_8} Q_{IR_{10}} \\ \ddot{Q}_{R_7} + 2\Gamma_{R_7}\dot{Q}_{R_7} + \omega_{R_7}^2 Q_{R_7} &= \epsilon_0 R_{7\alpha\beta} E_\alpha E_\beta - \phi_{7,6,8} Q_{IR_6} Q_{IR_8} - \phi_{7,8,10} Q_{IR_8} Q_{IR_{10}} \\ \ddot{Q}_{R_9} + 2\Gamma_{R_9}\dot{Q}_{R_9} + \omega_{R_9}^2 Q_{R_9} &= \epsilon_0 R_{9\alpha\beta} E_\alpha E_\beta - \phi_{9,6,8} Q_{IR_6} Q_{IR_8} - \phi_{9,8,10} Q_{IR_8} Q_{IR_{10}} \\ \ddot{Q}_{R_{11}} + 2\Gamma_{R_{11}}\dot{Q}_{R_{11}} + \omega_{R_{11}}^2 Q_{R_{11}} &= \epsilon_0 R_{11\alpha\beta} E_\alpha E_\beta - \phi_{11,6,8} Q_{IR_6} Q_{IR_8} - \phi_{11,8,10} Q_{IR_8} Q_{IR_{10}}\end{aligned}\quad (8-8)$$

From these equations, it can be noticed that the ERS process requires two electric fields rather than one, like in the case of simple resonant excitation. However, the polarization of both THz electric fields needs to be perpendicular, according to symmetry considerations. This can be accomplished by having both orthogonal THz pump pulses oriented diagonally with respect to the x and z axis of the CdWO₄ crystal or by orienting one THz pump pulse across the x-axis and the other one across the z-axis.

Regarding, the trilinear coupling, two IR-active modes (Q_{IR_j}, Q_{IR_j}) are coupled and drive the Raman-active mode, and the magnitude of such interaction depends on the individual motions of the IR-active modes along with the strength of the coupling constant, $\phi_{i,a,b}$. Symmetry considerations require one IR-active mode to be A_u and the other one to be B_u to drive the B_g mode through anharmonic coupling.

8.6.2 Group Theory and Pathways of Excitation

The THz crystal used in this work was DAST and it has a broad THz bandwidth (0.5 – 5 THz), which is an ideal bandwidth range because $CdWO_4$ has eight phonons whose frequencies lie in this range: three IR-active (Table 8-3) and five Raman active phonons (Table 8-4).

Table 8-3: Properties of IR-active Phonons in $CdWO_4$ ¹⁴

Band Index	Frequency	Symmetry
6	2.94 THz	B_u
8	3.65 THz	A_u
10	4.47 THz	B_u

Table 8-4: Properties of Raman-active Phonons in $CdWO_4$

Band Index	Frequency (Experimental)	Symmetry
4	2.33 THz	B_g
5	2.90 THz	A_g
7	3.56 THz	B_g
9	4.04 THz	B_g
11	4.48 THz	B_g

The 2D THz setup in this work, allows the THz pump pulses to drive the IR-active modes if the THz electric fields have enough energy and the proper polarization and the 800 nm probe to register the motion of Raman-active modes. For these measurements, the $CdWO_4$ is a y-cut crystal, which means that both the 800 nm Raman probe and the THz pump pulses, move

parallelly along the y-axis of the CdWO₄ crystal and that the x-z plane contains the important polarizations. The symmetry of the three IR-active modes is either A_u or B_u and according to the properties of the C_{2h} character table (see 6th column of Table 8-5), these types of modes can be excited if the polarization of THz pump pulse is along the z-axis of the crystal for A_u modes or if the polarization of the THz pump pulse is along the x- or y-axis for B_u modes.

Table 8-5: Character Table of C_{2h}

C_{2h}	E	C₂	i	σ		
A_g	1	1	1	1	R _z	x ² , y ² , z ² , xy
B_g	1	-1	1	-1	R _x , R _y	xz, yz
A_u	1	1	-1	-1	z	
B_u	1	-1	-1	1	x, y	

We then performed the mode symmetry multiplications, according to Table 8-6, to determine if certain combinations of modes are permitted through symmetry rules. For instance, if we wanted to excite an A_u symmetry mode, the oscillator would initially be as A_g in the fully symmetric ground state, then it would directly interact with a z-polarized THz electric field ($\hat{\mu}_z$) to finally be driven to an A_u excited state. Eq. 8-9 shows this symmetry product and it shows that the A_g symmetry is contained at the end, which means that it is an allowed transition.

Table 8-6: Symmetry Products

⊗	A _g	A _u	B _g	B _u
A _g	A_g	A_u	B_g	B_u
A _u		A_g	B_u	B_g
B _g			A_g	A_u
B _u				A_g

$$\psi_f | \hat{\mu} | \psi_i \rangle \propto \langle \mathbf{A}_u | \hat{\mu}_z | \mathbf{A}_g \rangle \propto \langle \mathbf{A}_u | \mathbf{A}_u | \mathbf{A}_g \rangle \supset \mathbf{A}_g \quad (8-9)$$

The symmetry multiplications for all the different types of symmetry of the vibrational modes in CdWO₄ were performed and multiple mechanisms were considered to be the acting driving forces to drive IR- and Raman-active modes, such as: single-photon, two-photon and anharmonic coupling (trilinear phonon coupling). Table 8-7 shows the results for all of these interactions and shows which transitions are allowed and which are forbidden according to symmetry rules. Interestingly, we noticed that both electronic Raman scattering (ERS) and trilinear coupling are permitted transitions and need to be taken into account as providers of the driving force. We modeled each of these mechanisms according to their own particular sets of equations of motion to properly model the 2D frequency correlation spectrum.

Table 8-7: Overview of all Symmetry Products and Driving Mechanisms

Mode Type	Excitation Type	Direct Products
IR-Active mode	Single Photon (Resonant Excitation)	$\langle A_u \hat{u}_z A_g \rangle \propto \langle A_u A_u A_g \rangle \supset A_g$ <i>Allowed</i> $\langle B_u \hat{u}_x A_g \rangle \propto \langle B_u B_u A_g \rangle \supset A_g$ <i>Allowed</i>
Raman-Active mode	Single Photon (Resonant Excitation)	$\langle A_g \hat{u}_z A_g \rangle \propto \langle A_g A_u A_g \rangle \not\supset A_g$ $\langle A_g \hat{u}_x A_g \rangle \propto \langle A_g B_u A_g \rangle \not\supset A_g$ <i>Forbidden: Product does not contain A_g</i> $\langle B_g \hat{u}_z A_g \rangle \propto \langle B_g A_u A_g \rangle \not\supset A_g$ $\langle B_g \hat{u}_x A_g \rangle \propto \langle B_g B_u A_g \rangle \not\supset A_g$ <i>Forbidden: Product does not contain A_g</i>

Table 8-7: Continued

Raman-Active mode	Single Photon (Hot Band Excitation)	$\langle B_g \hat{u}_z B_u \rangle \propto \langle B_g A_u B_u \rangle \supset A_g$ <i>Allowed</i>
Raman-Active mode	Two-Photon (Electronic Raman Scattering)	$\langle B_g \hat{u}_z \hat{u}_x A_g \rangle \propto \langle B_g A_u B_u A_g \rangle \supset A_g$ <i>Allowed</i> $\langle B_g \hat{u}_z \hat{u}_z A_g \rangle \propto \langle B_g A_u A_u A_g \rangle \not\supset A_g$ <i>Forbidden: Product does not contain A_g</i> $\langle B_g \hat{u}_x \hat{u}_x A_g \rangle \propto \langle B_g B_u B_u A_g \rangle \not\supset A_g$ <i>Forbidden: Product does not contain A_g</i>
Raman-Active mode	Trilinear phonon coupling	$\langle B_g A_u B_u \rangle \supset A_g$ <i>Allowed</i> $\langle B_g B_u B_u \rangle \not\supset A_g$ <i>Forbidden: Product does not contain A_g</i> $\langle B_g A_u A_u \rangle \not\supset A_g$ <i>Forbidden: Product does not contain A_g</i>

8.6.3 Dependence of the THz Field-Strength

To determine whether fourth-order anharmonic coupling constants needed to be considered in the equations of motion besides the trilinear coupling, we performed field-strength dependence measurements to generate 2D frequency correlation plots. This was accomplished by using the setup shown in Fig. 8-2. The generated 2D THz spectrum is shown in Fig. 8-11 at five increasing field strengths. It can be noticed that the nonlinear responses (yellow features) start to

increase as the field increase and they appear to be the strongest at the highest field strength (1.101 MV/cm).

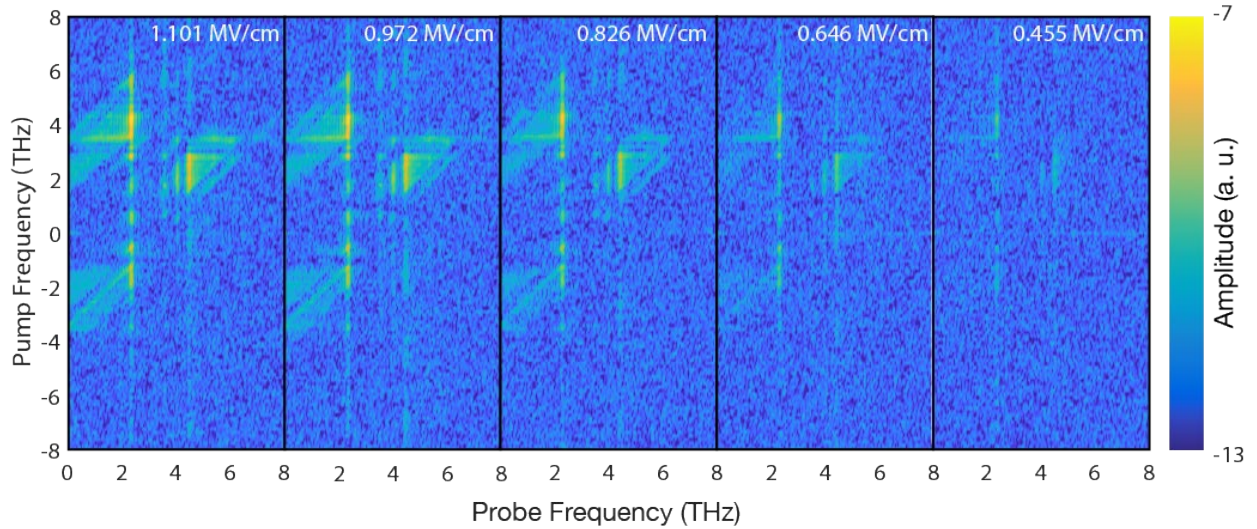


Figure 8-11: Frequency correlation spectrum with field strength dependence. 2D spectrum with parallel THz pump pulses were collected with increasing field strengths (right to left) of 0.455 MV/cm, 0.646 MV/cm, 0.826 MV/cm, 0.972 MV/cm and 1.101 MV/cm. The nonlinear response shows up as yellow features and start to increase with the increasing field strength.

We took the 2D frequency correlation plots and highlighted a portion of it with a red rectangle, as shown in Fig. 8-12a for the 1.101 MV/cm plot, to extract the average spectral amplitude of that region for all of the different field strengths to generate the plot shown in Fig. 8-12b. In Fig. 8-12b, we show the in red dots the increasing averaged spectral amplitude as a function of increasing field strength and it can be noticed that there is a quadratic dependence. This observation was also seen at other regions of the 2D frequency correlation plots. The quadratic dependence highly suggests that most of the signal depends on third-order and not so much from fourth-order (or higher) anharmonic coupling, and it is for this reason that in our equations of motion we omit those anharmonic coupling terms. Fourth-order coupling would require cubic dependence on the THz electric field ($E(t)^3$ or $\Phi_{abcd}Q_aQ_bQ_cQ_{R_d} \propto E(t)^3$), which is clearly not observed in Fig. 8-12b.

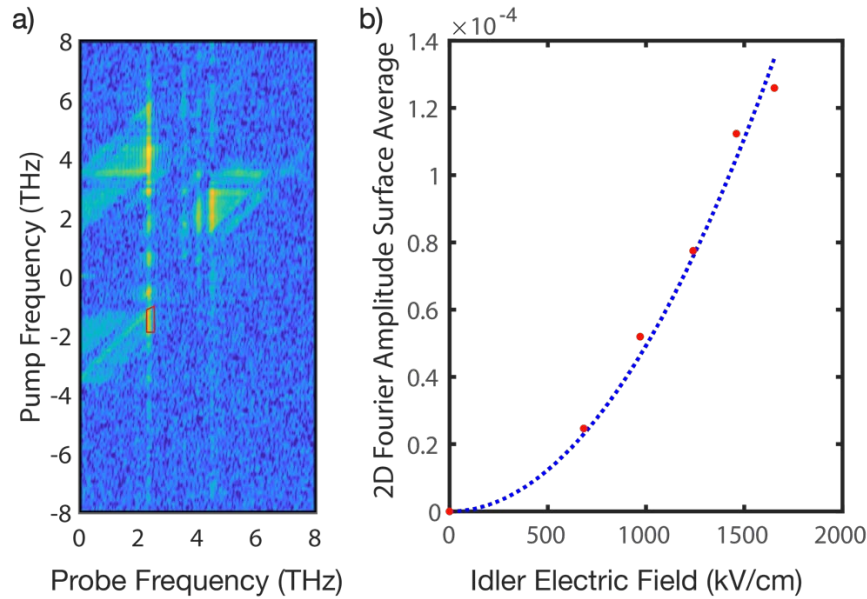


Figure 8-12: Quadratic dependence of nonlinear signal of 2D frequency correlation spectrum. a) Frequency correlation spectrum at 1.101 MV/cm, where a region is highlighted in a red box. b) Extracted average of the Fourier amplitude spectral signal from the region in red in a) as a function of electric field strength of idler THz pump pulse.

8.6.4 Turning off Electronic Raman Scattering Signal

The setup used in Ref. 8 with a proper modification on the polarization of THz pump pulses can be used to isolate nonlinear signal coming from the trilinear phonon coupling. As mentioned in section 8.3, the polarization of the THz pump pulses can be set to parallel or perpendicular by changing a few optics in the setups (see Figs. 8-2 and 8-4) and the nonlinear signal can be extracted by obtaining a different combination of the THz pump pulses through the chopping scheme. ERS can basically be removed by having the THz pump pulses in a perpendicular configuration and modeling shows that this indeed does happen orthogonal THz pump pulses at all time delays except when both pulses are overlapped in time. We modeled the excitation of mode 4 by both processes, ERS and trilinear coupling, with both configurations of the THz pump pulses, as seen in Fig. 8-13. For the parallelly polarized THz pump pulses (top panels of Fig. 8-13), the pump pulses are vertically polarized and the orientation of the sample is

set to 45° . It can be noticed that there is nonlinear signal present under ERS and trilinear coupling at time delays where the pump pulses are not overlapped in time. In the case of perpendicularly polarized THz pump pulses (bottom panels in Fig. 8-13), the pump pulses are orthogonally polarized and the sample is set to 0° . Unlike the parallel configuration, ERS signal from the mode 4 is not observed at time delays where the pump pulses are not overlapped; however, signal is observed by trilinear coupling. Interestingly, the signal from the Raman-active mode 4 is stronger for trilinear coupling under trilinear coupling with a perpendicular configuration of the THz pump pulses compared to the parallel one. The modeling shows that we can shut off ERS and isolate the trilinear coupling signal more effectively by having both THz pump pulses orthogonal to each other, which we were unable to observe before.⁸

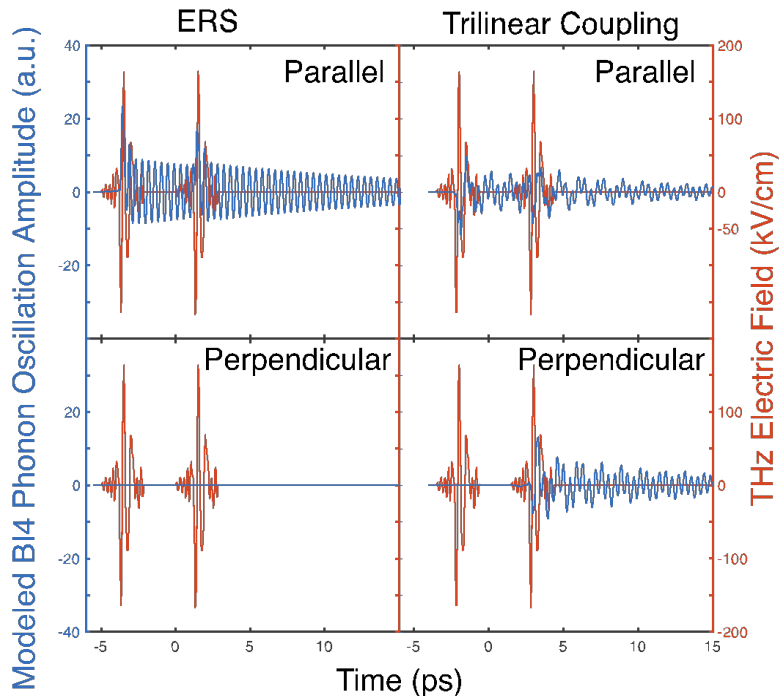


Figure 8-13: Modeled nonlinear signal from the Raman-active mode 4 of CdWO₄ generated by ERS and trilinear coupling with different polarization of the THz pulses. The top panels show the modeled oscillation amplitude of mode 4 driven by ERS (left) and trilinear coupling (right) with parallel THz pump pulses. The bottom panels show the modeled oscillation amplitude by ERS (left) and trilinear coupling (right) with perpendicular THz pump pulses. Mode 4 is basically not driven by ERS when both THz pulses are orthogonal and the pulses are not overlapped in time.

8.6.5 Chi-Squared Fitting

A manual Chi-squared fitting was carried out to obtain key ERS and anharmonic phononic coupling parameters from our experimental frequency correlation spectrum. We adjusted and extracted four Raman scattering tensors ($R_{i\alpha\beta}$) and eight coupling constants ($\phi_{i,6,8}$ and $\phi_{i,8,10}$, where $i=4, 7, 9$ and 11) for CdWO_4 . Due to the stronger contributions from the anharmonic coupling process to the nonlinear signal, we used the coupling constant $\phi_{4,6,8}$, as the reference with a value of 1 during the entire fitting process, which can be seen throughout all the tables of Fig. 8-14. We then generated modeled spectra for a wide range of values for its coupling constant sister, $\phi_{4,8,10}$, while having all the other ERS and coupling constants parameters as zeroes. We then used the modeled 2D spectrum along with the experimental spectrum to determine the root-mean-square error (RMSE) of the Fourier amplitude with respect to our 2D data. This allowed us to find the minimum RMSE of the Fourier amplitude as a function of $\phi_{4,8,10}$, as seen in Fig. 8-14a and thus find an optimal value of -2.2 for coupling constant for our model (Fig. 8-14b). This value of $\phi_{4,8,10}$, was retained along with the reference value of $\phi_{4,6,8}$, while keeping all the other parameters as zeroes, to then fit its corresponding Raman scattering tensor, $R_{4\alpha\beta}$.

Similar to the fit of the anharmonic coupling constant, a wide range of values for the Raman tensor (Table II of Fig. 8-14) was set to find an optimal value of the tensor (-10, see Fig. 8-14c) by minimizing the RMSE of the Fourier amplitude. The values for the coupling constants $\phi_{4,6,8}$ and $\phi_{4,8,10}$, along with their corresponding Raman tensor, $R_{4\alpha\beta}$, were used to generate a model 2D frequency spectrum, as seen in Fig. 8-14d.

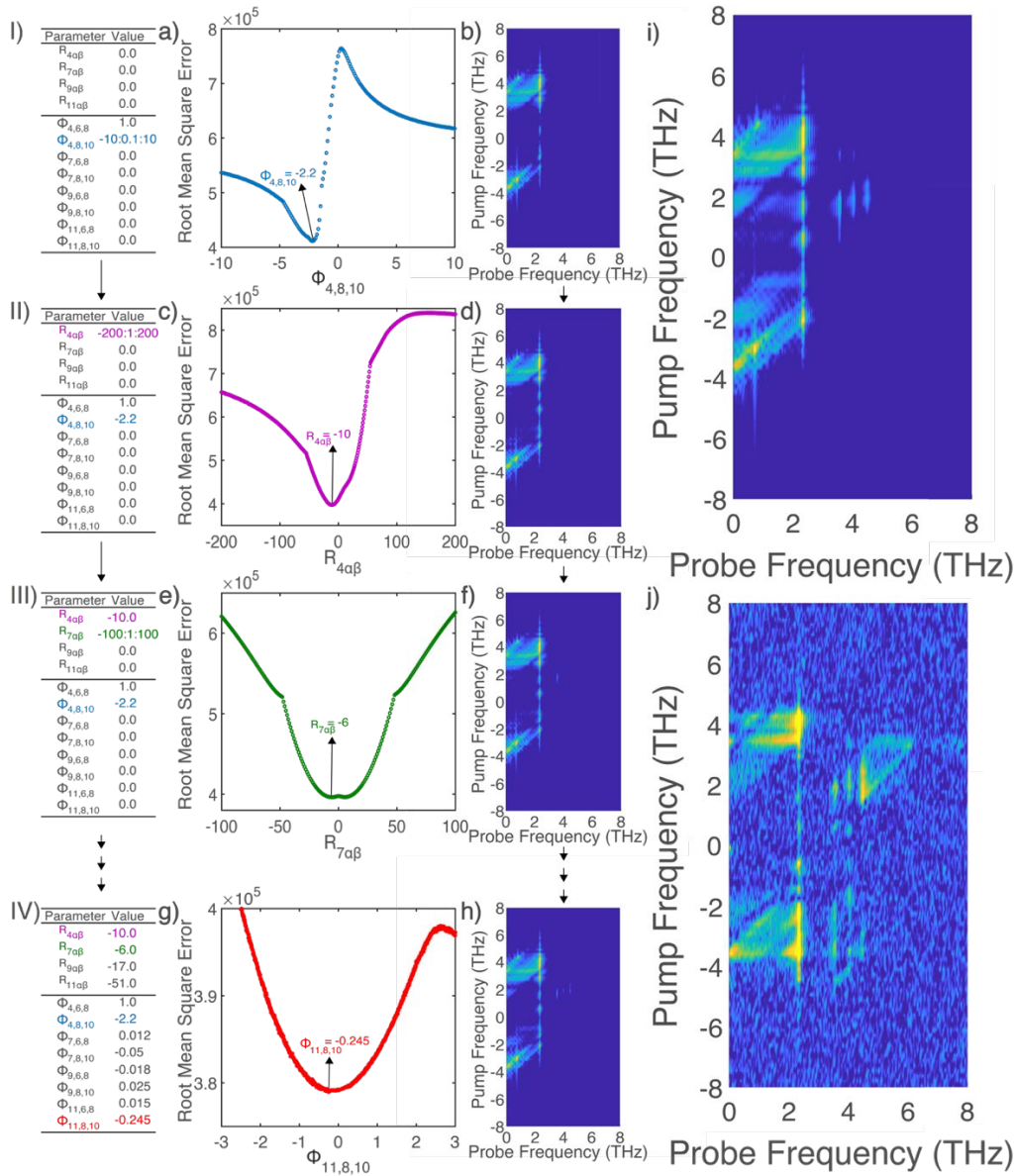


Figure 8-14: Summary of Chi-squared fitting process. (I) Values for the ERS and the anharmonic coupling parameters of CdWO₄, with the range of $\phi_{4,8,10}$ magnitudes used to find the minimum RMSE for $\phi_{4,8,10}$ shown in A). **(B)** The modeled frequency correlation spectrum according to the values of I and the optimal $\phi_{4,8,10}$. **(II)** Values of fit parameters with the range of $R_{4\alpha\beta}$ magnitudes used to find the minimum RMSE for $R_{4\alpha\beta}$ shown in C). **(D)** The modeled frequency correlation spectrum with the values of II and the optimal $R_{4\alpha\beta}$. **(III)** Values of fit parameters with the range of $R_{7\alpha\beta}$ magnitudes used to find the minimum RMSE for $R_{7\alpha\beta}$ shown in E). **(F)** The modeled frequency correlation spectrum with the values of III and the optimal $R_{7\alpha\beta}$. The multiple small arrows after III, E) and F) shows multiple steps that are not shown. **(IV)** Final values of all fit parameters after one round of fitting. **(G)** The minimization of the RMSE to find the optimal value of the last parameter, $\phi_{11,8,10}$. **(H)** Final modeled frequency correlation plot after one round of adjusting all the parameters, which are shown in IV. **(I)** Final modeled frequency correlation spectrum after two rounds of adjusting all the parameters. **(J)** Experimental frequency correlation plot.

The pattern that was just described about fitting the anharmonic coupling constants along with their corresponding Raman tensor was followed for the remainder of the fitting process and the initial values of zero were replaced each time that the optimal value of a parameter was determined. The only difference was that for all the other pairs of parameters, the Raman tensor was first determined and then its corresponding coupling constants. For example, after finding the parameters $\phi_{4,6,8}$, $\phi_{4,8,10}$, and $R_{4\alpha\beta}$, we determined the Raman tensor $R_{7\alpha\beta}$ to have an optimal value of -6 as seen in Fig. 8-14e and modeled its 2D frequency correlation spectrum in Fig. 8-14f with the parameters shown in Table III of Fig. 8-14. A round of fitting would be over after determining the last parameter (Fig. 8-14g) and in the end we were able to determine the optimal value for each Raman tensor and its corresponding anharmonic coupling constants as seen in Table IV of Fig. 8-14. With a full set of optimal parameters, we were able to produce a complete modeled frequency correlation plot (Fig. 8-14h).

The whole Chi-squared fitting process involved two entire rounds of fitting. In the first round, we determined the RMSE solely based on the absolute value of the Fourier amplitude to influence all the nonlinear features at the same time. However, during the second round, we determined the RMSE based on the natural log of the absolute value of the Fourier amplitude to primarily influence the smaller nonlinear features in the frequency correlation plots. The second round of fitting, used as its initial values, the values determined from the first round of fitting (see Table IV of Fig. 8-14). Fig. 8-14h is the modeled frequency correlation spectrum after the first round of fitting, while Fig. 8-14i is the modeled spectrum after the second round of fitting. Fig. 8-14i can then be compared to the experimental frequency correlation plot in Fig. 8-14j. In this comparison of 2D THz spectra, it can be noticed that features are shared between both plots. The optimal values of the averaged Raman scattering tensors and the coupling constants can be

found in Table 8-8, which were then compared to those determined through first-principles calculations in the next section.

Table 8-8: Extracted values of the anharmonic coupling constants along with their corresponding Raman scattering tensors for CdWO₄

Parameter	Value
$R_{4\alpha\beta}$	-22.5 ± 12.5
$R_{7\alpha\beta}$	-2.8 ± 9.9
$R_{9\alpha\beta}$	4.5 ± 65.3
$R_{11\alpha\beta}$	-39.0 ± 142.9
$\phi_{4,6,8}$	1.00
$\phi_{4,8,10}$	-1.2 ± 0.6
$\phi_{7,6,8}$	0.4 ± 0.2
$\phi_{7,8,10}$	-0.8 ± 0.5
$\phi_{9,6,8}$	1.9 ± 1.2
$\phi_{9,8,10}$	-4.1 ± 3.4
$\phi_{11,6,8}$	1.7 ± 1.4
$\phi_{11,8,10}$	-3.0 ± 1.5

8.6.6 First-Principles Calculations

We carried out first-principles calculations to compute values for the Raman scattering tensors and the anharmonic coupling constants of the significant vibrational modes of CdWO₄ involved in this work. We used the Vienna ab initio simulation package (VASP) to determine the relevant first-principles variables needed for CdWO₄. For the remainder of this paragraph, all of

the INCAR tags utilized in VASP will be specified with uppercase letters inside parenthesis. The process began by making sure that the crystal structure was relaxed up to the point where 1) the norms of all the Hellmann-Feynman forces had a value lower than 0.0001 eV (-EDIFFG) and 2) the ions were determined to be in their instantaneous ground state, which was all accomplished with the assistance of a conjugate gradient algorithm (IBRION = 2). In regards of the plane-wave-basis, the energy limit was arranged to be 1000 eV (ENCUT). Additionally, the Brillouin zone was probed by using an 8x8x8 k-point Monkhorst-Pack mesh, which was concentrated at the gamma point. For the exchange-correlation functional, the generalized gradient approximation (GGA) was used but it was necessary to use its solid Perdew-Burke-Ernzerhof (PBEsol) form. Once the relaxation process of the structure was completed, the finite difference method (IBRION = 6) was used to compute the forces of both the relaxed and shifted unit cell structure, as seen in Fig. 8-15.

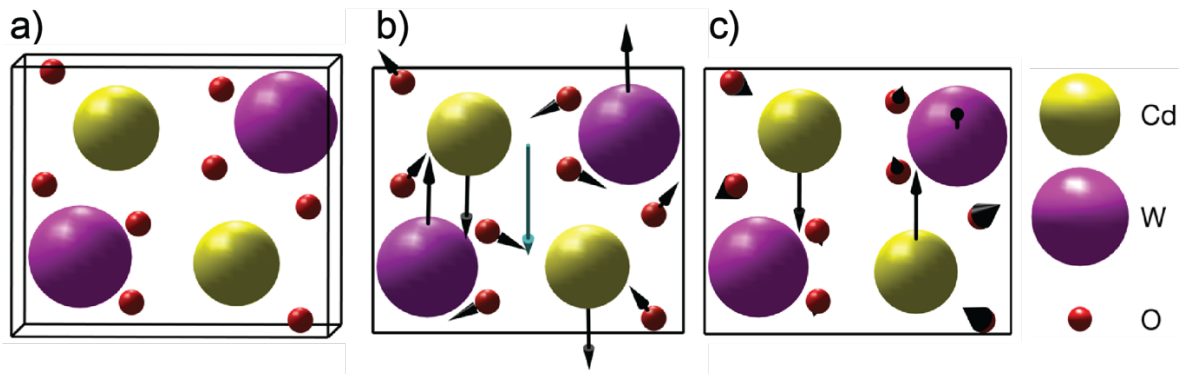


Figure 8-15: Unit cells of CdWO₄. a) The unit cells with all the atomic positions at rest. b) The unit cell showing an excited IR-active mode along with eigenvectors of each atom and the mode effective charge vector (blue arrow). c) The unit cell showing an excited Raman-active mode along with the eigenvectors of each atom.

A major advantage of performing the calculations with our method is that unlike the finite difference method, which would require a large number of calculations just to determine an individual mode coupling, we only need to perform a total of $2n+1$ computations to determine all

the potential third- and fourth-order mode couplings (n is the number of vibrational modes in the material). This is done by 1) carrying out finite difference computations on the structure that was previously relaxed and 2) carrying out finite difference computations on the structure after being shifted in the positive and negative direction across each normal mode coordinate (2n+1 computations). These computations generate the following information: Hessian matrices, eigenvectors along with their eigenfrequencies (see Figs. 8-15b and 8-15c), Born effective charges and CdWO₄'s static dielectric constants. The frequencies determined through first-principles calculations along with the experimental frequencies and damping rates for the modes relevant to this work are listed in Table 8-9.

Table 8-9: Frequencies from first-principles and literature along with experimental damping rates^{8, 14}

Band Index	Calculated (THz)	Experimental (THz)	Type	Axis	Exp. Damping Rate (THz)
1-3	-	-	Acoustic	-	-
4	2.27	2.33	R (B _g)	-	0.061
5	3.01	2.90	R (A _g)	-	-
6	3.07	2.94	IR (B _u)	x, y	0.1049
7	3.45	3.56	R (B _g)	-	0.05
8	3.83	3.65	IR (A _u)	z	0.06
9	3.95	4.04	R (B _g)	-	0.207
10	4.35	4.47	IR (B _u)	x, y	0.27
11	4.44	4.48	R (B _g)	-	0.1709

The Hessian matrices (Φ_{ijk}) contain the necessary information of the anharmonic coupling constants and Eqs. 8-10-11 are used to extract them. It should be noted that the Hessian matrices were determined in mode coordinates and not atomic coordinates.

$$\Phi_{ijk} = \frac{1}{3} \left(\frac{\phi_{jk}(\delta Q_i) - \phi_{jk}(-\delta Q_i)}{2\delta Q_i} + \frac{\phi_{ki}(\delta Q_j) - \phi_{ki}(-\delta Q_j)}{2\delta Q_j} + \frac{\phi_{ij}(\delta Q_k) - \phi_{ij}(-\delta Q_k)}{2\delta Q_k} \right) \quad (8-10)$$

$$\phi_{ijkk} = \frac{\phi_{ij}(\delta Q_k) + \phi_{ij}(-\delta Q_k) - 2\phi_{ij}(0)}{\delta Q_k^2} \quad (8-11)$$

$$\phi_{iikk} = \frac{1}{2} \left(\frac{\phi_{ii}(\delta Q_k) + \phi_{ii}(-\delta Q_k) - 2\phi_{ii}(0)}{\delta Q_k^2} + \frac{\phi_{kk}(\delta Q_i) + \phi_{kk}(-\delta Q_i) - 2\phi_{kk}(0)}{\delta Q_i^2} \right) \quad (8-12)$$

A few experimental conditions that were taken into account when using first-principles calculations to determine the anharmonic coupling constants and the Raman scattering tensor components of CdWO₄ will be discussed. Initially, we performed several corrections to our THz pump pulses, which are the driving force. Prior to the THz pulses going through the sample, there are reflective losses at the surface of the material and it is for this reason that we determined the dielectric constant. We can then determine the field transmission coefficient in CdWO₄ according to its specific orientation with the dielectric constant. Once the THz pulses have penetrated the material, we needed to determine the frequencies of the IR-active modes along with their respective effective charge. All this information was crucial to generate a more correct THz pump pulse to input into our model. The finite difference method was used to determine the magnitude of the coupling constants, which are a measure of the energy efficiency transfer between the phonons. The Raman tensor elements were also determined at THz frequencies, which served as a measure of the nonlinear driving force of Raman-active modes by a two-photon absorption process. Additionally, the Raman tensor elements were also computed at 800 nm (probe frequency) to aware of the sensitivity of our probe to each of the Raman-active phonons. Likewise, we also used the finite difference approach on a relaxed structure to compute the mode effective charge and frequencies. Finally, the we performed numerical derivatives on the forces generated from the shifted structures to find the Raman tensors and coupling constants and manually included the experimental damping rates.

8.7 References

1. K. G. Yager, and C. J. Barrett, "Novel photo-switching using azobenzene functional materials," *Journal of Photochemistry and Photobiology A: Chemistry* **182**, 250-261 (2006).

2. V. A. Stoica, N. Laanait, C. Dai, Z. Hong, Y. Yuan, Z. Zhang, S. Lei, M. R. McCarter, A. Yadav, A. R. Damodaran, S. Das, G. A. Stone, J. Karapetrova, D. A. Walko, X. Zhang, L. W. Martin, R. Ramesh, L. Q. Chen, H. Wen, V. Gopalan, and J. W. Freeland, “Optical creation of a supercrystal with three-dimensional nanoscale periodicity,” *Nature Materials* **18**, 377-383 (2019).
3. M. Kozina, M. Fechner, P. Marsik, T. van Driel, J. M. Glowina, C. Bernhard, M. Radovic, D. Zhu, S. Bonetti, U. Staub, and M. C. Hoffmann, “Terahertz-driven phonon upconversion in SrTiO₃,” *Nature Physics* **15**, 387-392 (2019).
4. T. F. Nova, A. S. Disa, M. Fechner, and A. Cavalleri, “Metastable ferroelectricity in optically strained SrTiO₃,” *Science* **364**, 1075-1079 (2019).
5. R. Mankowsky, A. von Hoegen, M. Först, and A. Cavalleri, “Ultrafast Reversal of the Ferroelectric Polarization,” *Physical Review Letters* **118**, 197601 (2017).
6. A. Subedi, A. Cavalleri, and A. Georges, “Theory of nonlinear phononics for coherent light control of solids,” *Physical Review B* **89**, 220301 (2014).
7. L. Luo, D. Cheng, B. Song, L.-L. Wang, C. Vaswani, P. M. Lozano, G. Gu, C. Huang, R. H. J. Kim, Z. Liu, J.-M. Park, Y. Yao, K. Ho, I. E. Perakis, Q. Li, and J. Wang, “A light-induced phononic symmetry switch and giant dissipationless topological photocurrent in ZrTe₅,” *Nature Materials* **20**, 329-334 (2021).
8. C. L. Johnson, B. E. Knighton, and J. A. Johnson, “Distinguishing Nonlinear Terahertz Excitation Pathways with Two-Dimensional Spectroscopy,” *Physical Review Letters* **122**, 073901 (2019).

9. B. E. Knighton, R. Tanner Hardy, C. L. Johnson, L. M. Rawlings, J. T. Woolley, C. Calderon, A. Urrea, and J. A. Johnson, "Terahertz waveform considerations for nonlinearly driving lattice vibrations," *Journal of Applied Physics* **125**, (2019).
10. B. S. Dastrup, J. R. Hall, and J. A. Johnson, "Experimental determination of the interatomic potential in LiNbO₃ via ultrafast lattice control," *Applied Physics Letters* **110**, (2017).
11. X. Li, T. Qiu, J. Zhang, E. Baldini, J. Lu, A. M. Rappe, and K. A. Nelson, "Terahertz field-induced ferroelectricity in quantum paraelectric SrTiO₃," *Science* **364**, 1079-1082 (2019).
12. P. Hamm, M. Meuwly, S. L. Johnson, P. Beaud, and U. Staub, "Perspective: THz-driven nuclear dynamics from solids to molecules," *Structural Dynamics* **4**, (2017).
13. K. Isoyama, N. Yoshikawa, K. Katsumi, J. Wong, N. Shikama, Y. Sakishita, F. Nabeshima, A. Maeda, and R. Shimano, "Light-induced enhancement of superconductivity in iron-based superconductor FeSe_{0.5}Te_{0.5}," *Communications Physics* **4**, 160 (2021).
14. A. Mock, R. Korlacki, S. Knight, and M. Schubert, "Anisotropy, phonon modes, and lattice anharmonicity from dielectric function tensor analysis of monoclinic cadmium tungstate," *Physical Review B* **95**, 165202 (2017).
15. D. M. Juraschek, and S. F. Maehrlein, "Sum-frequency ionic Raman scattering," *Physical Review B* **97**, 174302 (2018).
16. S. Maehrlein, A. Paarmann, M. Wolf, and T. Kampfrath, "Terahertz Sum-Frequency Excitation of a Raman-Active Phonon," *Physical Review Letters* **119**, 127402 (2017).
17. D. M. Juraschek, M. Fechner, and N. A. Spaldin, "Ultrafast Structure Switching through Nonlinear Phononics," *Physical Review Letters* **118**, 054101 (2017).
18. K. Reimann, M. Woerner, and T. Elsaesser, "Two-dimensional terahertz spectroscopy of condensed-phase molecular systems," *The Journal of Chemical Physics* **154**, (2021).

19. J. Lu, X. Li, Y. Zhang, H. Y. Hwang, B. K. Ofori-Okai, and K. A. Nelson, “Two-Dimensional Spectroscopy at Terahertz Frequencies,” *Topics in Current Chemistry* **376**, 6 (2018).
20. I. A. Finneran, R. Welsch, M. A. Allodi, T. F. Miller, III, and G. A. Blake, “2D THz-THz-Raman Photon-Echo Spectroscopy of Molecular Vibrations in Liquid Bromoform,” *The Journal of Physical Chemistry Letters* **8**, 4640-4644 (2017).
21. S. Houver, L. Huber, M. Savoini, E. Abreu, and S. L. Johnson, “2D THz spectroscopic investigation of ballistic conduction-band electron dynamics in InSb,” *Optics Express* **27**, 10854-10865 (2019).
22. J. Savolainen, S. Ahmed, and P. Hamm, “Two-dimensional Raman-terahertz spectroscopy of water,” *Proceedings of the National Academy of Sciences* **110**, 20402-20407 (2013).
23. F. D. J. Brunner, J. A. Johnson, S. Grübel, A. Ferrer, S. L. Johnson, and T. Feurer, “Distortion-free enhancement of terahertz signals measured by electro-optic sampling. I. Theory,” *Journal of the Optical Society of America B* **31**, 904-910 (2014).
24. J. A. Johnson, F. D. J. Brunner, S. Grübel, A. Ferrer, S. L. Johnson, and T. Feurer, “Distortion-free enhancement of terahertz signals measured by electro-optic sampling. II. Experiment,” *Journal of the Optical Society of America B* **31**, 1035-1040 (2014).